



# Carbon nanomaterials as antibacterial and antiviral alternatives

Aleksandra Loczechin

## ► To cite this version:

Aleksandra Loczechin. Carbon nanomaterials as antibacterial and antiviral alternatives. Other. Université de Lille; Ruhr-Universität, 2019. English. NNT : 2019LILUI117 . tel-03622608

**HAL Id: tel-03622608**

**<https://theses.hal.science/tel-03622608>**

Submitted on 29 Mar 2022

**HAL** is a multi-disciplinary open access archive for the deposit and dissemination of scientific research documents, whether they are published or not. The documents may come from teaching and research institutions in France or abroad, or from public or private research centers.

L'archive ouverte pluridisciplinaire **HAL**, est destinée au dépôt et à la diffusion de documents scientifiques de niveau recherche, publiés ou non, émanant des établissements d'enseignement et de recherche français ou étrangers, des laboratoires publics ou privés.

**THESE EN COTUTELLE**

présentée à

**L'UNIVERSITE DE LILLE**

Ecole Doctorale Régionale Sciences Pour l'Ingénieur Lille Nord-de-France

Et

**RUHR-UNIVERSITÄT BOCHUM**

Graduate school of Chemistry and Biochemistry

Pour obtenir le grade de

**DOCTEUR EN SCIENCES**

Dans la spécialité

Micro et Nano Technologies, Acoustique et Télécommunications

par

**ALEKSANDRA ŁOCZECHIN**

**LES NANOMATERIAUX EN CARBONE:  
DES ALTERNATIVES ANTIBACTERIENNES ET  
ANTIVIRALES**

Soutenue le 16 DÉCEMBRE 2019 devant le jury composé de :

Prof. Chantal PICHON  
Prof. Kevin BRAECKMANS  
Prof. Nils METZLER-NOLTE  
Prof. Sabine SZUNERITS

Rapportrice  
Rapporteur  
Co-Directeur de thèse  
Co-Directrice de these //  
Président du jury

CNRS & Université d'Orléans  
Ghent University  
Ruhr Universität Bochum  
Université de Lille

Prof. Axel ROSENHAHN  
Dr. Emerson GIOVANELLI

Invité  
Invité

Ruhr Universität Bochum  
Université de Lille

## COTUTELLE THESIS

Presented at

University of Lille

Ecole Doctorale Régionale Sciences Pour l'Ingénieur Lille Nord-de-France

and

RUHR-UNIVERSITÄT BOCHUM

Graduate school of Chemistry and Biochemistry

For the degree of

### DOCTOR OF SCIENCE

In specialization

Micro and Nano Technologies, Acoustique and Telecommunications

by

ALEKSANDRA ŁOCZECHIN

## **CARBON NANOMATERIALS AS ANTIBACTERIAL AND ANTIVIRAL ALTERNATIVES**

Defended on the 16th of December 2019 before the following PhD committee :

Prof. Chantal PICHON  
Prof. Kevin BRAECKMANS  
Prof. Nils METZLER-NOLTE  
Prof. Sabine SZUNERITS

Reviewer  
Reviewer  
Co-director  
Co-director //  
President

CNRS & Orleans University  
Ghent University  
Ruhr University Bochum  
University of Lille

Prof. Axel ROSENHAHN  
Dr. Emerson GIOVANELLI

Invited  
Invited

Ruhr University Bochum  
University of Lille

## ACKNOWLEDGEMENT

Preparing my PhD thesis has been a wonderful experience. During this period, I have had the opportunity to meet a lot of remarkable people. I have received support and encouragement from a great number of individuals that made my stay in France and Germany an unforgettable experience.

First, I would like to express my sincere gratitude to my PhD supervisors. Prof. Sabine Szunerits, for her support, guidance and scientific discussions throughout my study period and also for the suggestions during the writing process of this thesis and the patience while correcting it. Prof. Nils Metzler-Nolte, also, for his guidance, scientific ideas and discussions for the past three years. I am especially grateful for your confidence and the freedom you gave me to do this work. I would never have come this far without your support, encouragement and possibility you both created initiating this co-tutelle project.

My sincere thanks go to Dr. Rabah Boukherroub for his suggestions and sharpening my scientific thinking. To Dr. Alexandre Barras for his valuable advice during my research work and guidance while exploring new areas that I was not familiar with and to Dr. Emerson Giovanelli for his useful suggestions and corrections throughout the process of writing this thesis.

A special thank goes to Dr. Jean Dubuisson for his generosity and letting me experience the research of human coronavirus and helping me to develop my background in this field. I would also like to express my special thanks to Dr. Karin Seron, who had helped me with the viral assays experiments.

I want to thank all the NanoBioInterfaces group (NBI, France) and Inorganic chemistry I group (AC1, Germany) for providing a stimulating research environment and for their friendship, support and company during the past three years.

My heartfelt thanks go to Ioana Silvia Hosu and Milica Budimir for always being there during the good and bad days, listening to my problems and providing possible solutions. Without you, life in Lille would not have been the same. I will always cherish all those humour, stupid jokes and meaningful discussions. To VEDI without whom we would be just the fantastic trio instead of magnificent four. Anna, Vlad and Mathias thank you for being a great company (Slavic

power), especially during the karaoke evenings. Many thanks to Quentin without whom my coffee breaks would not be the same.

I would like to thank Sugina for always remembering me when buying a coffee. Without you, my mornings would be miserable, especially when the day was starting earlier than usual. Also, many thanks to all the girls who were sharing the lab space with me for maintaining the ambience and peaceful working environment in the lab. Especially to Nicole for always entertaining me throughout the day. I would also like to express my thanks to Carsten and Matt who had helped me a lot with HPLC, often sacrificing their free time.

I would like to thank all the lab members from both groups, which I did not mention for stimulating research environment. I truly appreciate the nature of sharing the ideas among lab mates.

I extend my sincere thanks to all members of the Department of Chemistry at Ruhr University Bochum, all members of the NBI team and all those who contributed directly or indirectly to the dissertation. Especially to Dr. Laura Chambre and Prof. Amitav Sanyal for providing the cryogels.

Special thanks go to Université de Lille and Ruhr Universität Bochum for funding my PhD fellowship.

I would like to thank all the people I met on my way during the past three years who believed in me and make my PhD experience even more valuable as well as all my friends who supported my decision of studying abroad even if that meant being miles away from them.

I have no words to explain my gratitude to Antoine for his encouragement, continuous support and help he had offered me for the past 3 years.

Finally, I owe my deepest gratitude to my mother, grandmother and my two sisters for their unconditional love, encouragement and support in my decision for studying miles away from my hometown.

Aleksandra Łoczechin

October 2019

# TABLE OF CONTENTS

<b>ACRONYMS</b>	<b>a</b>
<b>RESUME/ABSTRACT/ZUSAMMENFASSUNG</b>	<b>I</b>
<b>OBJECTIVES</b>	<b>III</b>
<b>CHAPTER 1 Nanoparticles for biomedical application</b>	<b>1</b>
1.1. Introduction	1
1.2. Inorganic nanoparticles	5
1.3. Organic nanoparticles	10
1.4. Carbon nanoparticles	12
1.4.1. Carbon quantum dots- CQDs	12
1.4.2 Nanodiamonds	17
1.4.3. Graphene, graphene oxide and reduced graphene oxide	20
1.5. References	22
<b>CHAPTER 2 Carbon nanomaterials as antibacterial alternatives</b>	<b>34</b>
2.1. Introduction	34
2.2. Synthesis of short synthetic antimicrobial peptides (synAMPs) and their antibacterial activity	38
2.3. Synthesis and surface modifications of nanoparticles prior to formation of bioconjugates	40
2.4. Subsequent post functionalization of carbon nanostructures:	
Nanoparticles- peptide bioconjugates	46
2.5. Antibacterial activity of carbon- based conjugates	50
2.6. Conclusions	53
2.7. References	54
<b>CHAPTER 3 On-demand antimicrobial releasing platform triggered by near-infrared light</b>	<b>57</b>
3.1. Introduction	57
3.2. Fabrication and photothermal properties of furan- modified cryogels with and without embedded rGO	59
3.3. Loading of cryogels with antimicrobial agents	62
3.3.1. Loading of the antimicrobial drug via absorption and subsequent release	62
3.3.2. Loading of the antibacterial agent via Diels-Alder reaction and subsequent release	63

3.4. Conclusions	67
3.5. References	68
<b>CHAPTER 4 Functional carbon quantum dots as a medical countermeasure to human coronavirus (HCoV)</b>	<b>70</b>
4.1. Introduction	70
4.2. First- generation of CQDs inhibitors of host cell infections by HCoV-229E coronavirus:	
Boronic acid- modified CQDs	72
4.2.1. Formation, functionalization and characterisation	72
4.2.2. Cytotoxicity assay	77
4.2.3. Antiviral assay of first- generation CQDs	79
4.3. Second- generation of CQDs inhibitors of host cell infections by HCoV-229E coronavirus	80
4.3.1. Formation and characterisation of CQDs-6, -7, -8	80
4.3.2. Antiviral assay of seconds generation CQDs-6, -7, -8	87
4.4. Mechanism of action	89
4.5. Conclusions	91
4.6. References	92
<b>CHAPTER 5 Conclusions and perspectives</b>	<b>94</b>
<b>APPENDIX</b>	<b>97</b>
<b>EXPERIMENTAL PART</b>	<b>97</b>
6.1. Materials	97
6.2. Synthesis	98
6.2.1. General procedure for solid-phase peptide synthesis (SPPS)	98
6.2.1.1. Synthesis of <i>H-RWRWRW-NH<sub>2</sub>: 1a</i>	99
6.2.1.2. Synthesis of <i>H-WRWRWR-NH<sub>2</sub>: 1b</i>	100
6.2.1.3. Synthesis of <i>FcCO-WRWRW-NH<sub>2</sub>: 2a</i>	101
6.2.1.4. Synthesis of <i>FcCO-RWRWR-NH<sub>2</sub>: 2b</i>	102
6.2.1.5. Synthesis of <i>RcCO-WRWRW-NH<sub>2</sub>: 3a</i>	103
6.2.1.6. Synthesis of <i>RcCO-RWRWR-NH<sub>2</sub>: 3b</i>	104
6.2.1.7. Synthesis of <i>CHCCH<sub>2</sub>CH<sub>2</sub>C(O)-RWRWR-NH<sub>2</sub>: 4a</i>	105
6.2.1.8. Synthesis of <i>CHCCH<sub>2</sub>CH<sub>2</sub>C(O)-WRWRW-NH<sub>2</sub>: 4b</i>	106
6.2.1.9. Synthesis of <i>H-RWRWRWG(CH<sub>2</sub>CCH)-NH<sub>2</sub>: 5a</i>	107
6.2.1.10. Synthesis of <i>H-WRWRWRG(CH<sub>2</sub>CCH)-NH<sub>2</sub>: 5b</i>	108

6.2.1.11. Synthesis of $\text{FcCO-WRWRWG}(\text{CH}_2\text{CCH})\text{-NH}_2$ : 6a	109
6.2.1.12. Synthesis of $\text{FcCO-RWRWRG}(\text{CH}_2\text{CCH})\text{-NH}_2$ : 6b	110
6.2.1.13. Synthesis of $\text{RcCO-WRWRWG}(\text{CH}_2\text{CCH})\text{-NH}_2$ : 7a	111
6.2.1.14. Synthesis of $\text{RcCO-RWRWRG}(\text{CH}_2\text{CCH})\text{-NH}_2$ : 7b	112
6.2.1.15. Synthesis of $\text{H-WRWRWC-NH}_2$ : 8	113
6.2.2. Organic compounds	114
6.2.2.1. Synthesis of $\text{H-WRWRWC-maleimide}$	114
6.2.2.2. Ruthenocenecarboxylic acid	114
6.2.2.3. 4-[(1-oxo-4-pentyn-1-yl)amino]phenylboronic acid	115
6.2.3. Nanoparticles	116
6.2.3.1. Carbon dots: CQDs	116
6.2.3.1.1. CQDs-1: $\text{NH}_2$ -rich CQDs	116
6.2.3.1.2. CQDs-2: CQDs-COOH	116
6.2.3.1.3. CQDs-3: CQDs- $\text{N}_3$	116
6.2.3.1.4. CQDs-4: CQDs-BA	116
6.2.3.1.5. CQDs-5	117
6.2.3.1.6. CQDs-6	117
6.2.3.1.7. CQDs-7	117
6.2.3.1.8. CQDs-8	118
6.2.3.1.9. Fluorescently labelled CQDs-7	118
6.2.3.1.10. CQDs-peptide conjugates: CQDs-2.1a; -2.1b; -2.2a; -2.2b; -2.3a; -2.3b	118
6.2.3.1.11. CQDs-peptide conjugates: CQDs-3.4a; -3.4b; -3.5a; -3.6b; -3.7a; -3.7b	119
6.2.3.2. Nanodiamonds: ND	119
6.2.3.2.1. ND-3: ND- $\text{N}_3$	119
6.2.3.2.2. Nanodiamonds-peptide conjugates: ND-1.1a; -1.1b; -1.2a; -1.2b; -1.3a; -1.3b	119
6.2.3.2.3. Nanodiamonds- peptide conjugates: ND-3.4a; -3.4b; -3.5a; -3.5b; -3.6a; -3.6b; -3.7a; -3.7b	120
6.2.3.3. Reduced graphene oxide: rGO	120
6.2.4. Preparation of flexible patch photothermal heaters	120
6.2.5. Fabrication of furfuryl- containing cryogels	120
6.2.6. Synthesis of rGO embedded furfuryl containing cryogels	121
6.3. Swelling of cryogels	121



6.4. Drug loading	121
6.4.1. Non- covalent interaction with ampicillin	121
6.4.2. Diels-Alder reaction	121
6.4.2.1. Conjugation of N-(5-fluoresceinyl)maleimide	121
6.4.2.2. Conjugation of maleimide-functionalized antibacterial peptides	122
6.5. High- Performance Liquid Chromatography for quantification	122
6.5.1. AMP loading and release	122
6.5.2. Quantification of peptides incorporated into the nanostructures of carbon nanoparticles	122
6.6. Fluorescent plate reader for quantification of dye loading and release	122
6.7. Purification and purity assessment of peptides: 1a-8	123
6.8. Quantification of the amino group by modified Keiser test	123
6.9. Quantum yield measurements	124
6.10. Photothermal release studies	125
6.11. Biological assays	125
6.11.1. Cytotoxicity assay – Huh-7 cells	125
6.11.2. Cytotoxicity assay – HeLa cells	125
6.11.3. Uptake mechanism: fluorescently labelled CQDs-7	126
6.11.4. Antiviral assay: HCoV-229E-Luc	126
6.11.5. Time-of-addition assay	127
6.11.6. Virus-nanoparticles interaction assay	127
6.11.7. Competitive assay with mannose	127
6.11.8. Susceptibility testing – MIC values determination	128
6.12. Instrumentation	129
6.12.1. NMR Spectroscopy	129
6.12.2. Mass Spectrometry	129
6.12.3. High-Performance Liquid Chromatography (HPLC)	129
6.12.4. Fourier Transform Infrared (FTIR) Spectroscopy	130
6.12.5. X-ray Photoelectron Spectroscopy (XPS)	130
6.12.6. Raman Spectroscopy	130
6.12.7. UV-Vis Spectroscopy	130
6.12.8. X-Ray Diffraction (XRD)	130
6.12.9. Transmission Electron Microscopy (TEM)	131

6.12.10. Scanning Electron Microscopy (SEM)	131
6.12.11. Emission fluorescence Spectroscopy	131
6.12.12. Particle Size and Zeta Potential Measurements	131
6.12.13. Photothermal Effect Measurements	131
6.13. References	132
<b>SCIENTIFIC ACTIVITY</b>	<b>133</b>

---

---

## ACRONYMS

<i>ACN</i>	<i>Acetonitrile</i>
<i>AMP</i>	<i>Antimicrobial peptide</i>
<i>APBA</i>	<i>4-aminophenylboronic acid</i>
<i>ARG, R</i>	<i>Arginine</i>
<i>ATP</i>	<i>Adenosine triphosphate</i>
<i>BA</i>	<i>Boronic acid</i>
<i>CDCl<sub>3</sub></i>	<i>Chloroform</i>
<i>CG</i>	<i>Cryogel</i>
<i>CCK-8</i>	<i>Cell counting kit 8</i>
<i>CuAAC</i>	<i>Copper(I)-catalysed azide-alkyne cycloaddition</i>
<i>CQDs</i>	<i>Carbon dots</i>
<i>DA</i>	<i>Diels-alder</i>
<i>DAPI</i>	<i>4'-6-diamidino-phenylindole</i>
<i>DCC</i>	<i>N,N'-dicyclohexylcarbodiimide</i>
<i>DCM</i>	<i>Dichloromethane</i>
<i>DIC</i>	<i>N,N'-Diisopropylcarbodiimide</i>
<i>DiPEA</i>	<i>N,N-Diisopropylethylamine</i>
<i>DMAP</i>	<i>4-Dimethylaminopyridine</i>
<i>DMEM</i>	<i>Dulbecco modified Eagle medium</i>
<i>DMF</i>	<i>Dimethylformamide</i>
<i>EC<sub>50</sub></i>	<i>Half maximal effective concentration</i>
<i>E.coli</i>	<i>Escherichia coli</i>
<i>EDTA</i>	<i>Ethylenediaminetetraacetic acid</i>
<i>EDC</i>	<i>N-(3-dimethylaminopropyl)-N'-ethylcarbodiimide</i>
<i>EtOAc</i>	<i>Ethyl acetate</i>
<i>ESI</i>	<i>Electron spray ionisation</i>
<i>FA</i>	<i>Formic acid</i>
<i>FBS</i>	<i>Fetal bovine serum</i>
<i>Fc</i>	<i>Ferrocene</i>
<i>FITC</i>	<i>Fluorescein isothiocyanate</i>

<i>fluorescein- NHS</i>	<i>5/6-carboxyfluorescein succinimidyl ester</i>
<i>FTIR</i>	<i>Fourier-transform infrared spectroscopy</i>
<i>FMOC</i>	<i>Fluorenylmethyloxycarbonyl</i>
<i>GO</i>	<i>Graphene oxide</i>
<i>HCoV</i>	<i>Human corona virus</i>
<i>HCoV 229E</i>	<i>Human corona virus 229E</i>
<i>HOBt</i>	<i>1-Hydroxybenzotriazole hydrate</i>
<i>Huh-7</i>	<i>Hepatocyte derived cellular carcinoma cell line</i>
<i>HPLC</i>	<i>High performance liquid chromatography</i>
<i>IPA</i>	<i>Isopropanol</i>
<i>KCN</i>	<i>Potassium cyanide</i>
<i>KOtBu</i>	<i>Potassium tert-butoxide</i>
<i>LB</i>	<i>Luria-bertani</i>
<i>MERS</i>	<i>Middle east respiratory syndrome</i>
<i>MHA</i>	<i>Muller Hinton agar</i>
<i>MHB</i>	<i>Muller Hinton Broth</i>
<i>MIC</i>	<i>Minimal inhibitory concentration</i>
<i>MOI</i>	<i>Multiplicity of infection</i>
<i>MRSA</i>	<i>Methicillin-resistant Staphylococcus aureus</i>
<i>MWCO</i>	<i>Molecular weight cut off</i>
<i>ND, NDs</i>	<i>Nanodiamonds</i>
<i>NHS</i>	<i>N-hydroxysuccinimide</i>
<i>NIR</i>	<i>Near-infrared</i>
<i>NP, NPs</i>	<i>Nanoparticles</i>
<i>NMR</i>	<i>Nuclear magnetic resonance</i>
<i>OD600</i>	<i>Optical density at 600nm</i>
<i>PBA</i>	<i>Phenylboronic acid</i>
<i>PBS</i>	<i>Phosphate buffer saline</i>
<i>PEG</i>	<i>Polyethylene glycol</i>
<i>Rc</i>	<i>Ruthenocene</i>
<i>rDA</i>	<i>Retro-Diels-Alder</i>
<i>rGO</i>	<i>Reduced graphene oxide</i>
<i>PDI</i>	<i>Polydispersity index</i>

<i>Ppm</i>	<i>Part per million</i>
<i>PTT</i>	<i>Photothermal therapy</i>
<i>ROS</i>	<i>Reactive oxygen species</i>
<i>RPM</i>	<i>Revolutions per minute</i>
<i>t<sub>R</sub></i>	<i>Retention time</i>
<i>S.aureus</i>	<i>Staphylococcus aureus</i>
<i>SARS</i>	<i>Severe acute respiratory syndrome</i>
<i>SEM</i>	<i>Scanning electron microscope</i>
<i>SPPS</i>	<i>Solid phase peptide synthesis</i>
<i>synAMP</i>	<i>Synthetic antimicrobial peptide</i>
<i>TBTU</i>	<i>2-(1H-Benzotriazole-1-yl)-1,1,3,3-tetramethylaminiumtetrafluoroborate</i>
<i>TEM</i>	<i>Transmission electron microscopy</i>
<i>TFA</i>	<i>Trifluoroacetic acid</i>
<i>TIS</i>	<i>Triisopropylsilane</i>
<i>TRP, W</i>	<i>Tryptophan</i>
<i>VISA</i>	<i>Vancomycin resistant Staphylococcus aureus</i>
<i>WHO</i>	<i>World Health Organisation</i>
<i>XPS</i>	<i>X-ray photoelectron spectroscopy</i>
<i>XRD</i>	<i>X-ray powder diffraction</i>
<i>QY</i>	<i>Quantum yield</i>

## RESUME

La résistance croissante aux antibiotiques et les limitations dans le développement de nouveaux médicaments nécessitent la recherche de stratégies alternatives afin d'éradiquer les infections bactériennes. Des problèmes semblables apparaissent dans le développement de thérapeutiques antivirales, en raison de l'émergence constante de nouveaux virus et leur capacité à contourner les thérapies par des mutations génétiques.

Ce travail de recherche examine la potentielle activité antibactérienne et/ou antivirale de nanostructures à base de carbone telles que les nanoparticules de diamant et les points quantiques carbonés (*carbon quantum dots*, CQDs), ainsi que l'oxyde de graphène réduit (*reduced graphene oxide*, rGO) combiné à des cryogels. Les CQDs produits par synthèse hydrothermale à partir de l'acide 4-aminophénylboronique comme précurseur carboné se sont montrés efficace en tant qu'inhibiteurs de l'attachement du coronavirus humain HCoV-229E-Luc aux cellules avec une  $EC_{50}$  de  $5,2 \pm 0,7 \mu\text{g mL}^{-1}$ . Les études mécanistiques suggèrent que les CQDs agissent lors des tout premiers stades de l'infection virale ainsi que lors de l'étape de réplication du virus. En parallèle, nous avons tiré parti du caractère multivalent des CQDs et des nanodiamants pour les modifier en y fixant de courts peptides synthétiques antimicrobiens (*antimicrobial peptides*, AMPs). Ces nanostructures ont été testées contre des bactéries pathogènes à Gram positif *Staphylococcus aureus* et à Gram négatif *Escherichia coli* et ont montré une activité antibactérienne plus élevée que celle des AMPs seuls. Dans le cas du rGO combiné à des cryogels chargés en AMPs, l'éradication des bactéries a été réalisée efficacement et à la demande en utilisant une irradiation infrarouge comme activateur externe permettant le relargage des AMPs.

## ABSTRACT

Increasing antibiotic resistance and limited development of new drugs necessitate the search for alternative strategies to eradicate bacterial infections. Similar problems are faced in the development of antiviral therapeutics, due to the constant emergence of new viruses and their ability to escape therapy by genetic mutations.

This work investigates the potential antibacterial and/or antiviral activity of carbon-based nanostructures such as diamond nanoparticles and carbon quantum dots (CQDs) as well as reduced graphene oxide (rGO) in combination with cryogels. CQDs formed by hydrothermal synthesis from 4-aminophenylboronic acid as the carbon precursor showed to be efficient in the inhibition of the viral attachment of human coronavirus HCoV-229E-Luc to cells with an  $EC_{50}$  of  $5.2 \pm 0.7 \mu\text{g mL}^{-1}$ . Mechanistic studies suggest that the CQDs are acting at the early stage of virus infection as well at the viral replication step. In parallel, we took advantage of the multivalent character of CQDs as well as nanodiamonds and modified them with short synthetic antimicrobial peptides (AMPs). Tests of these nanostructures against Gram-positive *Staphylococcus aureus* and Gram-negative *Escherichia coli* pathogens showed increased antibacterial activity when compared to AMPs alone. In the case of rGO combined with cryogels loaded with AMPs, bacterial eradication was achieved efficiently and on-demand using near-infrared light as external trigger to release AMPs.

## ZUSAMMENFASSUNG

Die zunehmende Antibiotikaresistenz und die begrenzte Entwicklung neuer Medikamente erfordern die Suche nach alternativen Strategien zur Ausrottung bakterieller Infektionen. Ähnliche Probleme stellen sich bei der Entwicklung antiviraler Therapeutika, da stetig neue Viren auftauchen und diese durch genetische Mutationen der Therapie entgehen können.

In dieser Arbeit wurde die potenzielle antibakterielle und/oder antivirale Aktivität von Nanostrukturen auf Kohlenstoffbasis wie Diamantnanopartikeln und Kohlenstoff-Quantenpunkten (CQDs) sowie reduziertem Graphenoxid (rGO) in Kombination mit Kryogelen untersucht. CQDs, die durch hydrothermale Synthese aus 4-Aminophenylboronsäure als Kohlenstoffvorläufer gebildet wurden, erwiesen sich als effizient bei der Hemmung der viralen Anheftung des humanen Coronavirus HCoV-229E-Luc an Zellen mit einem  $EC_{50}$  von  $5,2 \pm 0,7 \mu\text{g mL}^{-1}$ . Mechanistische Studien deuten darauf hin, dass die CQDs sowohl im frühen Stadium der Virusinfektion als auch im viralen Replikationsschritt wirken. Parallel dazu nutzten wir den multivalenten Charakter der CQDs sowie der Nanodiamanten und modifizierten diese mit kurzen synthetischen antimikrobiellen Peptiden (AMPs). Analysen dieser Nanostrukturen gegen gram-positive *Staphylococcus aureus* und gram-negative *Escherichia coli*-Erreger zeigten eine erhöhte antibakterielle Aktivität im Vergleich zu AMPs allein. Im Falle von rGO in Kombination mit AMPs beladenen Kryogelen wurde die bakterielle Eradikation effizient erreicht. Bei Bedarf wurde Nahes Infrarot Licht als externer Auslöser für die Freisetzung von AMPs verwendet.

## OBJECTIVES

Both, the increasing antibiotic resistance and the limited development of new antibacterial drugs, make imperative the search for alternative strategies to eradicate bacterial infections. Similar problems are faced in the development of antiviral therapeutics, due to the continued emergence of new viruses and their ability to escape therapy by genetic mutations. Nanoparticles have attracted tremendous interest for the treatment of bacterial and viral infections mainly due to either their intrinsic antibacterial properties (*e.g.* silver nanoparticles) or their multivalent nature. Indeed, multivalent interactions are omnipresent in biology and confer on biological systems dramatically enhanced affinities towards determined receptors. Such multivalent binding interactions have lately been considered for the development of new therapeutic strategies against bacterial and viral infections. While a high synthetic effort is often needed for the development of such therapeutics, the integration of several molecules (otherwise named ligands) onto nanostructures turned out to be a viable alternative. Particles modified with numerous ligands have the additional advantage of giving rise to high local concentrations of the corresponding bound molecules.

In this thesis, different surface modification strategies have been applied and developed with the goal of obtaining nanostructures with antibacterial and antiviral properties. Carbon-based nano scaffolds, notably diamond nanoparticles (often also referred to as nanodiamonds), carbon quantum dots (CQDs) and 2D carbon nanomaterials such as reduced graphene oxide (rGO), were chosen herein as they possess unique biological and physicochemical properties. Each nanostructure exhibits inimitable features and can be exploited in diverse biological applications, including antiviral and antibacterial applications.

The thesis is divided into two parts: the first part is devoted to the screening of a large number of peptide nanostructures and nanostructures against Gram-positive *Staphylococcus aureus* and Gram-negative *Escherichia coli*; the second part is an in-depth study of the possibility of functionalised CQDs to work as inhibitors for the interaction of the human coronavirus HCoV-229E with the cell membrane. After a general overview of the use of nanoparticles for biological applications, a brief description of the surface modification strategies of carbon nanomaterials towards biomedical applications is provided in **Chapter 1**.



**Chapter 2** reports the design of effective carbon-based nano scaffolds working as nanobiotics with inhibitory concentrations below that of synthetic antibacterial peptides. The synthesis, characterisation and functionalisation of CQDs and nanodiamonds with short synthetic antimicrobial peptides (synAMP) are described first. The antibacterial activity of these particles, conjugated with or without organometallic moieties, against *Staphylococcus aureus* and *Escherichia coli* is then investigated. We show that the multivalent character of the treatment when combined with synAMP, has a positive effect on the eradication of bacterial cells. **Chapter 3** describes another nanotechnological concept aimed at killing bacteria. It is based on the development of an on-demand antimicrobial peptide delivery platform and consists in incorporation synAMP into photothermally active cryogels, from which the drugs can be released as a result of an external light trigger.

**Chapter 4** is dedicated to the study of the potential of CQDs as inhibitors of host cells infections caused by HCoV-229E. Therapeutic options for the highly pathogenic human coronavirus (HCoV) infections are urgently needed. Anti-coronavirus therapy is, however, challenging, as coronaviruses are biologically diverse and mutate rapidly. The antiviral activity of seven different CQDs for the treatment of human coronavirus HCoV-229E infections is investigated in this chapter. The first generation of antiviral CQDs derives from the hydrothermal carbonisation of ethylenediamine/citric acid as carbon precursors and subsequent modification with ligands bearing a boronic acid function. These nanostructures show a concentration-dependent virus inactivation with an estimated  $EC_{50}$  of  $52 \pm 8 \mu\text{g mL}^{-1}$ . CQDs derived from 4-aminophenylboronic acid without any further modification resulted in the second generation of anti-HCoV nanomaterials with an  $EC_{50}$  lowered down to  $5.2 \pm 0.7 \mu\text{g mL}^{-1}$ . The underlying mechanism of action of these CQDs proved to be the inhibition of HCoV-229E entry which can be explained by a favourable interaction of the functional groups of the CQDs towards HCoV-229E entry receptors; surprisingly, an equally significant inhibition activity was observed at the viral replication step.

**Chapter 5** summarises the results and gives some perspectives on the work.

## CHAPTER 1

### Nanoparticles for biomedical application

#### 1.1. Introduction

Nanotechnology, introduced almost half a century ago, is an active research area with both novel science and useful applications that has gradually established itself in the past two decades. Much of nanoscience and nanotechnology is concerned with producing new or enhanced materials in the form of nanoparticles (NPs) and nanostructured materials and represents an active area of research and a techno-economic sector with full expansion in many application domains. These nanostructures have gained prominence in technological advancements due to their tunable physicochemical characteristics (**Figures 1.1**) such as melting point, wettability, electrical and thermal conductivity, catalytic activity, light absorption and scattering resulting in enhanced performance over their bulk counterparts.

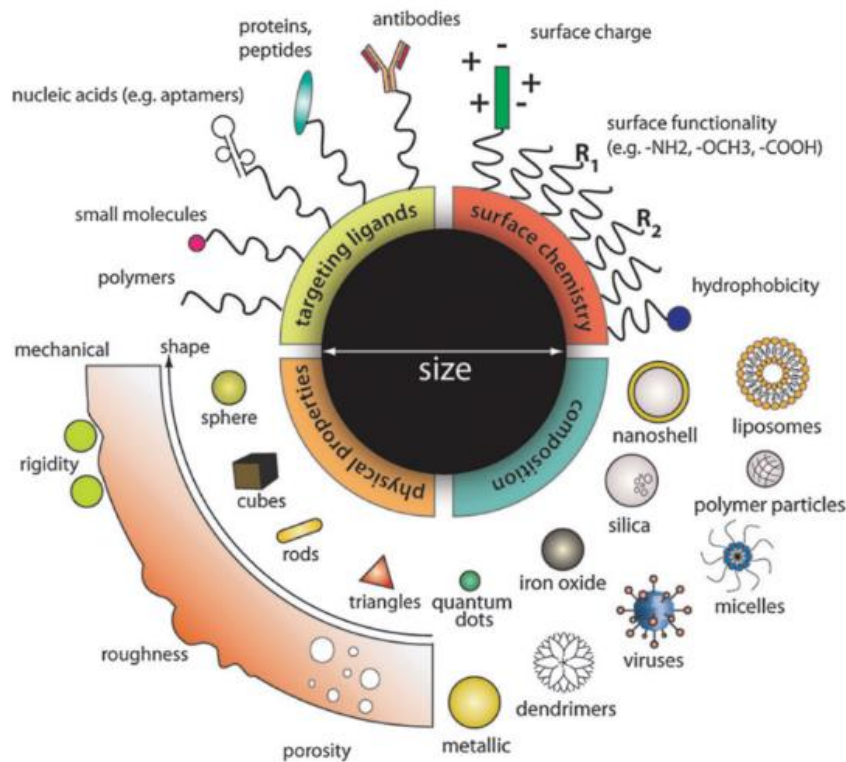


**Figure 1.1:** Design strategies and properties of nanoparticles for biomedical applications (image is taken from ref [1]).

The implementation and rapid development of chemical functionalization strategies on nanomaterials have, in addition, greatly increased the variety of available nanomaterials and their application. Through the manipulation of size, surface characteristics and the material used, the nanoparticles can be developed into smart systems, encasing therapeutic and imaging agents as well as bearing stealth property. Nanometre-sized materials are thus gaining massive attention for various application areas ranging from their use in energy devices and as catalytic scaffolds to their interest for biomedical applications (Figure 1.2) [2-4]. This is due to their unique physical and chemical properties which are barely found in bulk materials.

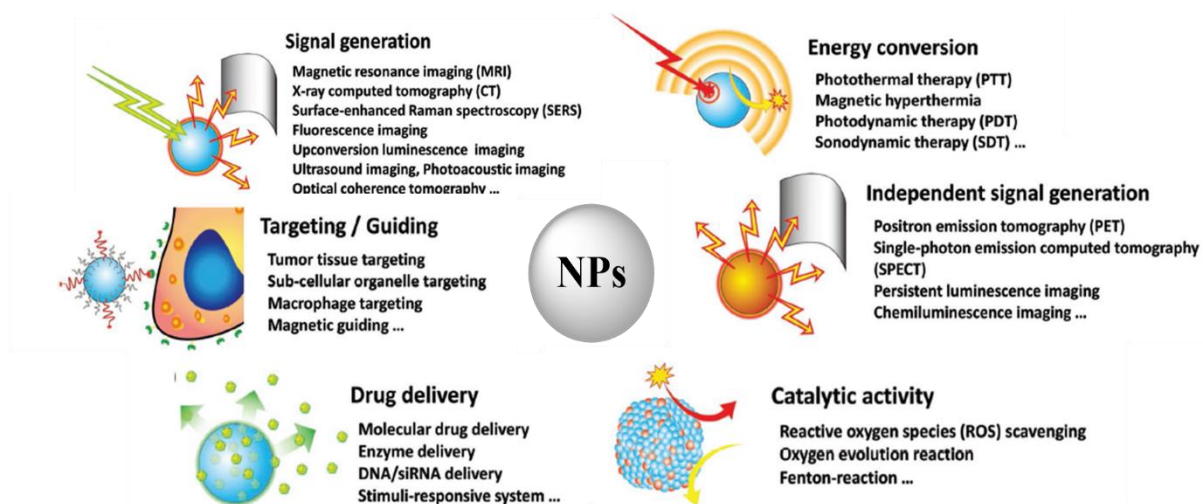


**Figure 1.2:** Different classes of the properties and functions of NPs utilised for biomedical applications (image is taken from ref [5]).

In the biomedical field, the large surface-to-volume ratio of NPs is of value when engineering drug delivery systems, diagnostic platforms and nanotechnology-based imaging strategies. The high surface-to-volume ratio allows the integration of different molecules allowing the target delivery of drugs [6, 7] and is responsible for the multivalent character of these nanostructures. A series of experiments and theoretical studies have also shown that the multivalent nature of nanoparticles allows distinguishing surfaces (cells) on the basis of their receptor concentration, rather than just on the basis of the presence of a suitable receptor [8, 9]. The use of multivalent particles coated with a single type of ligand is very effective, provided that a cognate receptor has been identified that is sufficiently overexpressed in targeted cells. There are various other reasons why using nanoparticles for therapeutic and diagnostic agents, as well as the advancement of drug delivery, is important and much needed. One of them is that that hydrophobic character of many drugs limits their oral or injectable administration, as they are not manufactured as the optimal formulation for each product. Products containing proteins or nucleic acids require a more innovative type of carrier system to enhance their efficacy and

protect them from unwanted degradation. It is notable that the efficiency of most drug delivery systems is directly related to particle size (excluding intravenous and solution). Due to their small size and large surface area, drug nanoparticles show increase solubility and thus enhanced ability to cross the blood-brain barrier (BBB), enter the pulmonary system and be absorbed through the tight junctions of endothelial cells of the skin [10-14]. Additionally, the use of multifunctional theranostic agents with targeted delivery can solve problems associated with an increase in the drug doses and the resulting toxicity [15-17].

While a high surface-to-volume ratio is a fundamental characteristic of NPs for drug delivery, the ability of some NPs (e.g. gold nanorods, rGO) to convert light energy into heat also allows the remote manipulation of their environment. Such a capacity can cause intentional damages to the targeted tissues and/or favour the interaction with determined bioactive compounds. For example, thermosensitive drug delivery vehicles can be activated by photothermal therapy (PTT), allowing the on-demand drug release at a target site [18-20].

Understanding how the body handles the exogenous particulate matter is warranted. Once, they enter systemic circulation, particle-protein interaction is the first phenomenon taking place before distribution into various organs. Absorption from the blood capillaries allows the lymphatic system to further distribute and eliminate the particles. If something is recognised as foreign, macrophages will engulf and clear it from the body. This tends to be the struggle with nanoparticle-based nanomedicines; however, clearance can be influenced by the size and surface characteristics of particles.

Currently, several therapeutic agents and technologies based on nanotechnology have been approved for clinical use (**Table 1.1**) or are under clinical trials, which underlines the already high interest in this field.

**Table 1.1:** Clinically approved intravenous nanoparticle therapies and diagnostics. [21]

Name	Particle type	Approved application	Year of approval
Doxil/Caelyx	Liposomal doxorubicin (PEGylated)	Cancer treatment	1995 (FDA); 1996 (EMA)
Abraxane	Albumin-particle bound paclitaxel	Cancer treatment	2005 (FDA); 2008 (EMA)
Onivyde MM-398	Liposomal irinotecan (PEGylated)	Cancer treatment	2015 (FDA)
Injectafter	Iron carboxymaltose colloid	Iron- replacement nanoparticle therapies	2013 (FDA)
Definity	Perflutren lipid microspheres	Imaging agents	2001 (FDA)
Epaxal	Liposome with hepatitis A virus	Nano vaccines	Some of Europe(Discontinued)
Inflexal V	Liposome with trivalent- influenza	Nano vaccines	Some of Europe (Discontinued)
AmBisome	Liposomal amphotericin B	Fungal treatment	1997 (FDA); Most of Europe
Diprivan	Liposomal propofol	anaesthetics	1989 (FDA)

NPs typically used for biomedical applications fall into three categories (**Figure 1.3**): i) inorganic nanoparticles (gold, silica, iron oxide, metal quantum dots); ii) organic nanoparticles (polymeric liposomes, micelles, dendrimers); iii) carbon nanoparticles (fullerene, nanodiamonds, carbon nanotubes, carbon dots, graphene).

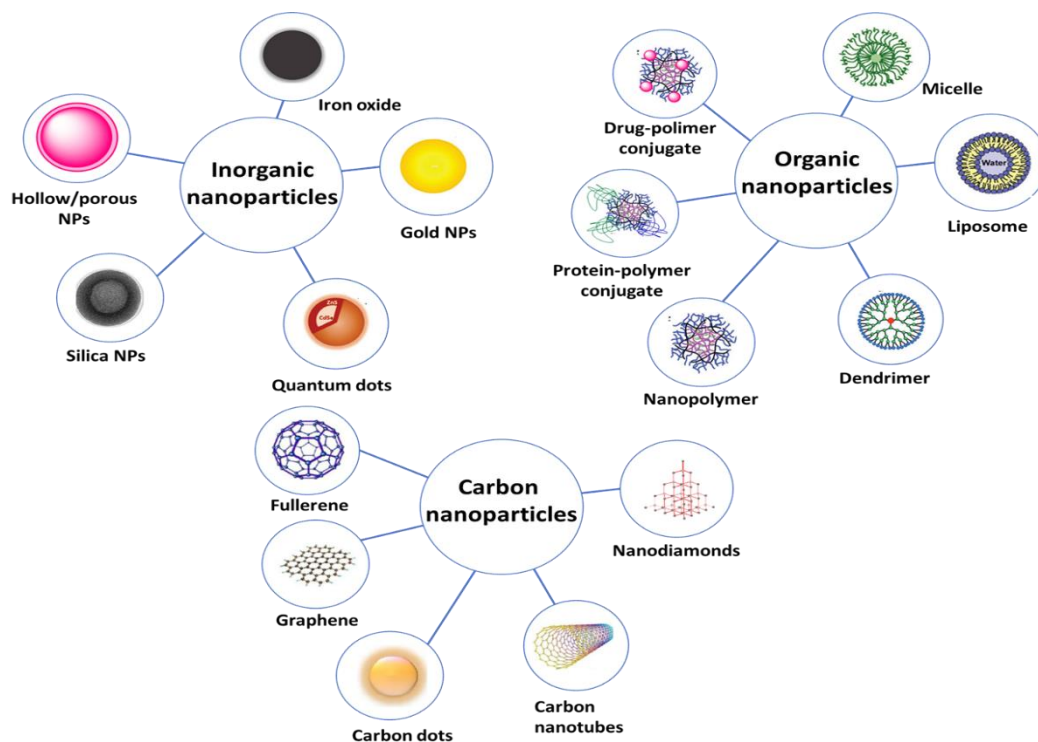


**Figure 1.3:** Classification of nanomaterials commonly used in nanomedicine. Sketch inspired from ref [22].

In this thesis work, we have exploited different strategies for the surface modification of carbon nanoparticles. Our goal was to obtain nanostructures with antibacterial and antiviral properties. Therefore, carbon-based nanoparticles, notably carbon dots, nanodiamonds, and 2D-materials such as graphene oxide were chosen. Before discussing our results on the application of these nanomaterials, a general outline about a different class of nanomaterials focusing on carbon based materials is given below.

## **1.2. Inorganic nanoparticles**

Inorganic particles comprise metal, metal oxides and semiconductors. One of the main reasons for their use in biomedicine is their intrinsic physical properties. As a few examples, we can cite iron oxide magnetic NPs, gold NPs exhibiting surface plasmon resonance, luminescent semiconductor quantum dots, and upconverting luminescent lanthanide-doped NPs [23-28]. All of these properties can be fine-tuned during the synthesis by engineering the size, shape, composition and structure of the inorganic core.

Basic requirements for biomedical applications of such nanostructures include water solubility and colloidal stability under physiological conditions while keeping their physicochemical properties steady. Another critical factor is their biocompatibility [29]. Biocompatible surface modifications enable water solubility and endow NPs with stability and biocompatibility. Surface modifications can modulate the pharmacokinetics and medical functions of NPs aiming at different tissue or organ lesions [30].

Synthetic strategies to obtain biocompatible NPs include in situ “one-pot” synthesis of hydrophilic particles [31, 32] or post surface modification of hydrophobic NPs. Most common coating materials are polymers, zwitterionic molecules and biomolecules [33-35]. For improving solubility and biocompatibility among polymers, the most commonly used is PEG and PEG-copolymers [36]. PEG-based modifications can be roughly categorized into i) encapsulation strategies [36] ii) ligand exchange by coordinating with the anchoring groups strategies [37]. Apart from PEG molecules, zwitterions are another class of materials often used for coating of inorganic particles to increase their biocompatibility. The advantage compared to the PEG molecule is little apparent increase of hydrodynamic size under physiological conditions [38, 39]. Zwitterions and other biomolecules such as proteins, nucleic acids, peptides can be coated onto the particle surface upon covalent or non-covalent interactions (**Figure 1.4**).



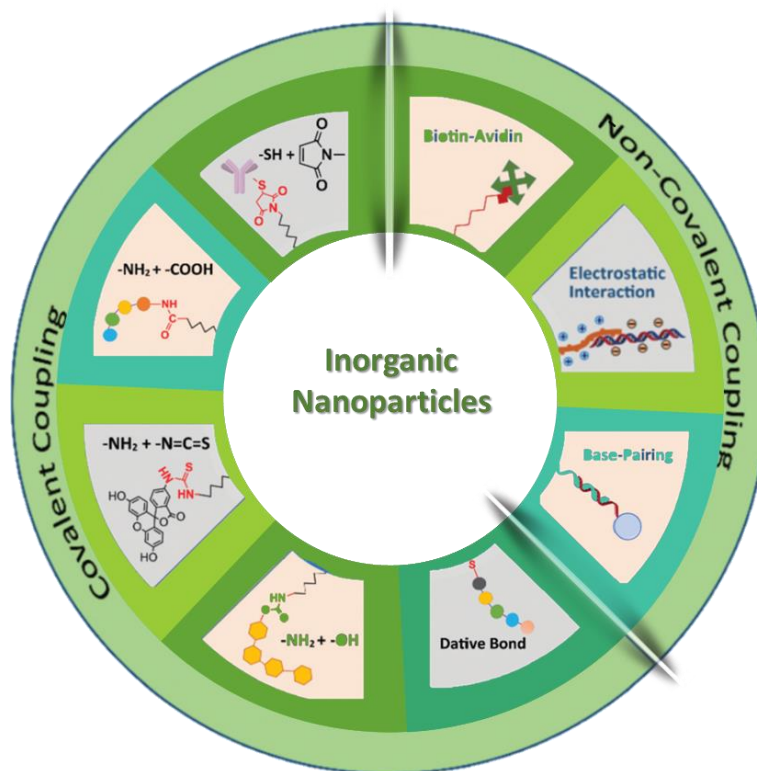


**Figure 1.4:** Schematic summary of bioconjugation strategies for inorganic nanoparticles [40].

The covalent coupling can be achieved by creating the bond directly or through cross-linker coupled with biomolecules with functional groups like  $\text{-COOH}$ ,  $\text{-NH}_2$ ,  $\text{-SH}$ , maleimide [41, 42]. The non-covalent attachment includes electrostatic interactions [43] which depend on the affinity of two differently charged species, biotin-avidin system [44] allowing incorporation of biomolecules as well as non-biomolecules such as DNA, antibodies, fluorescent dyes, hydrophobic interactions and base-pairing interactions [45, 46].

Inorganic nanoparticles found their application in many different biomedical fields. They have been extensively studied for their potential use as antimicrobial agents due to their direct and indirect antimicrobial properties (**Table 1.2**). Their mode of action varies between particles, but they exhibit bactericidal properties mostly through the generation of reactive oxygen species (ROS) although some are effective due to their physical structure and metal ion release (**Table 1.2**).

One of the major types of NPs with antimicrobial properties that have been utilized for decades is metals/metal oxides NPs [47, 48]. This group of NPs include silver (Ag), iron oxide ( $\text{Fe}_3\text{O}_4$ ), titanium oxide ( $\text{TiO}_2$ ), copper oxide ( $\text{CuO}$ ), zinc oxide ( $\text{ZnO}$ ), and gold NPs.

Silver nanoparticles possess unique physicochemical properties that have a significant impact on their biological properties. It has been shown that silver nanoparticles can effectively prevent the growth of bacteria on the surface of agar plates but are becoming less effective in a liquid medium [49]. The difference is associated with the aggregation of colloidal silver in the presence of high salts concentration and other media components. These results suggest that the antimicrobial efficacy depends on the surface oxidation state of NPs and particles dispersion [49]. Next to that, size and shape play a significant role in their ability to interact with the bacterial surface [50, 51]. Small and spherical NPs show higher affinity towards the surface of a cell membrane [52, 53]. Although silver NPs are known to researchers for decades and have been extensively studied. Their bactericidal mechanism of action is not yet fully understood. In AgNPs there might be three sources of bactericidal activity: Ag, Ag<sup>+</sup>, AgNPs. All three of them can interlacing, making it difficult to determine what effect comes from each of them [52, 54]. Impregnation of medical devices and wound dressing significantly reduced the infections rate in hospital settings [55], but the toxicity of the particles on mammalian cells is still in dispute [56-58].

Titanium oxide, similarly to silver NPs, has been studied for its antibacterial and antiviral activities [59, 60]. Their optical, dielectric, and photo-catalytic properties resulting from size quantization makes them promising structures which can be utilized as a self-cleaning and self-disinfecting material for surface coating in many application, e.g. self-cleaning or self-sterilizing surfaces for places such as medical centres. Their bactericidal properties are associated mostly with the formation of ROS [61].

Zinc oxide NPs show broad-spectrum bactericidal activity. The particles show to successfully inhibit the growth of methicillin-sensitive *S. aureus* (MSSA), methicillin-resistant *S. aureus* (MRSA), and methicillin-resistant *S. epidermidis* (MRSE) strains and proved to be effective bactericidal agents that were not affected by the drug-resistant mechanisms of MRSA and MRSE [62, 63]. These inexpensive NPs proved to be effective in size dependency against a wide range of bacteria species. They possess the highest photocatalytic efficiency among all inorganic photocatalytic materials and are more biocompatible than TiO<sub>2</sub> [64]. Their white colour and ability to absorb UV light enhances its conductivity which significantly activates the interaction with bacteria. It has been proven that zinc oxide NPs have the ability to prevent the biofilm formation [65] making them suitable coating material designated for medical and other application like, e.g. potential antibacterial agent in food preservation and packaging [66].



Iron oxide in its bulk form is considered inert and has lack of any antimicrobial properties. However, when synthesized as nanosized particles, iron oxide NPs demonstrate anti-adherent properties and significantly reduce both Gram-negative and Gram-positive bacterial colonization [67]. For biomedical applications, iron and iron oxide magnetic NPs with nanocrystalline magnetite ( $\text{Fe}_3\text{O}_4$ ) cores is preferable because of its biocompatibility profile, biodegradability and facile synthesis. Roughly iron oxide can be divided into two classes, superparamagnetic iron oxide nanoparticles (SPIONs) and ultra-small superparamagnetic iron oxide nanoparticles (USPIONs), each with different mean hydrodynamic diameters, as well as different relaxometry properties. It has been shown that FeO-NPs can improve the stability and solubility of the encapsulated drug [68], and no toxicity effect has been observed after cell uptake. Additionally, nano-therapy with smartly coated MPs possess a broad scope in diagnostic and therapeutic applications [69-72].

Gold NPs possess effective antimicrobial properties due to its large surface area, high chemical stability, optical properties, oxidation resistance and biocompatibility [73-75]. The key characteristics that distinguish AuNPs from other nanostructures are their unique optical properties resulting from a physical phenomenon known as localised surface plasmon resonance (LSPR). LSPR is known to be highly sensitive to the geometric parameter (e.g. size, shape, symmetry) and material composition. In the case of spherical gold NPs, LSPR occurs in the visible region and can be shifted to the NIR region. As a result, the optical properties of gold nanostructures can be tuned and adjust to suit specific biomedical application [76]. Besides their surface can be easily modified by a wide variety of ligands via thiol or amine functions which allows the incorporation of biomolecules that can tailor their properties as well as introduce new functionalities to NPs [77, 78]. AuNPs, when decorated with antibiotics, show bactericidal properties to many multidrug- drug-resistant pathogens [79]. Additionally, their activity can be enhanced by binding to nonantibiotic molecules and together with light energy can induce ROS production and mutation extensively use in therapy against cancer cells [80, 81].

Another group of inorganic particles which thanks to their properties found an application in the diverse biomedical field are quantum dots (QDs). They possess superior photo-stability, bright photoluminescence, narrow emission and broad absorption spectra. They are nanometer-scale semiconductor crystals composed of groups II to VI or III to V elements. Their ability to absorb white light and then remit specific colour depends on the bandgap of the

material. QDs usually consist of a semiconductor core, overcoated by a shell to improve optical properties and a cap enabling improved solubility in aqueous buffers. Their use for the biological application has cast some doubts due to their potential toxicity. There have been several studies reported that size, charge, coating ligands, oxidative, photolytic and mechanical stability each could contribute to the toxicity of cadmium containing QDs [82]. In addition, the potential leakage of heavy metal ions from the core of the particles caused by photolysis and oxidation has a significant impact on the toxicity of QDs [82, 83]. The additional layer on the surface of QDs (usually ZnS or CdS) not only protect the core from photo-oxidation minimizing cytotoxicity but also enhancing photostability [84]. However, even with advances in synthesis, obtaining medically useful QDs is still problematic due to differences in optical properties from batch to batch. Moreover, additional functionalization is required for incorporation of biologically active molecules [85, 86].

**Table 1.2:** Examples of antimicrobial inorganic nanoparticles and their mechanism of action.

Nanoparticles	Targeted microorganism	Mechanism of action	Ref.
Ag	<i>E. coli, B. subtilis, S. aureus</i>	Release of Ag <sup>+</sup> ions	[87]
	<i>C. albicans</i>	Cell membrane disruption and electron transport, DNA damage	[88]
TiO <sub>2</sub>	<i>E. coli, B. megaterium</i>	Production of reactive oxygen species	[89]
		Cell membrane and cell wall damage	
	<i>C. albicans</i>	Generation of electron-hole pairs by visible light excitation with low recombination rate	[90]
	<i>E. coli, S. aureus</i>	Intracellular accumulation of NPs	
		Cell membrane damage	[91-93]
Au	<i>B. cinerea, P. expansum</i>	H <sub>2</sub> O <sub>2</sub> production	
		Release of Zn <sup>2+</sup> ions	
	<i>P. aeruginosa, E. coli</i>	Sequestration of Mg <sup>2+</sup> or Ca <sup>2+</sup> ions to disrupt bacterial cell membrane	[94]
	<i>E. coli, K.pneumonia, S. aureus, and B.subtilis</i>	Changed the membrane potential and reduced adenosine triphosphate (ATP) synthase activities	[95]
		Declined the subunit of the ribosome for tRNA binding	
QDs	<i>E.coli</i>	Increased antibacterial activity, higher therapeutic indices	[96]

### 1.3. Organic nanoparticles

Another class of nanomaterials used for biomedical purposes includes organic NPs. They consist of a wide range of different materials like liposomes, polymers, lipids, capsules, gels [97, 98]. These kinds of NPs are mostly made from organic matter, and their synthesis and design rely on non-covalent interactions that convert them into desired structures via self-assembly. The most important feature of these nanostructures is their ability to encapsulate other materials, such as hydrophobic drugs. The material used for their fabrication is by nature biodegradable, which makes them an attractive system for drug delivery.

Methods used for the preparation of organic nanoparticles can be divided into three categories [99, 100]: i) procedure based emulsification ii) nano-precipitation iii) drying process. The first method is based on two steps process. The first step involves the preparation of nanodroplets of specific size wherein organic compound are formerly solubilized. In the second step, nanoparticles are formed by a different mechanism such as precipitation, gelation or polymerization. The second method is based on the nanoprecipitation where the organic compound is precipitating out of the solution through solvent displacement, self-assembly mechanism induced by ionic gelation or by the formation of polyelectrolyte complexes.

One of the most extensively used organic nanoparticles for drug delivery is liposomes. Liposomes are spherical in shape particles that contain one or more lipid or phospholipids bilayer with the spacing in between the bilayers. Their structure contains lipophilic as well as hydrophobic and amphiphilic molecules which makes them suitable for incorporation of many different molecules with different solubility [101].

Another NPs that consists of the lipid-based formulation are nanoparticles/nanoemulsions, solid-lipid nanoparticles (SLNs), and nanostructured lipid carriers (NLCs). Solid lipid nanoparticles (SLNs) consists of the lipid solid core such as glycerides, which can solubilize lipophilic molecules. SLNs are physiologically well tolerated, protect labile drugs from chemical degradation, control the release of the drug due to the solid state of the lipid matrix. Nanostructured lipid carriers consist of a matrix composed of solid and liquid lipids stabilized by a surfactant solution. Other than that, we can distinguish lipid, protein and polysaccharides based systems that belong to the group called “generally recognized as safe (GRAS) nanoparticles” [102]. These systems are often made from natural products and therefore are much safer than their chemically synthesized counterpart.

Micelles and dendrimers are another class of organic nanoparticles which are used as drug delivery vehicles. Micelles are polymeric structures that consist of monomer joined together; it is the bipolarity of the monomer molecules that causes the formation of micelles. Dendrimers, on the other hand, are highly branched molecules that combine the properties of polymers as well as small discrete entities. In comparison to micelles, their structure does not have a completely hollow core, but the polymeric network of repeating units is expanding inside-out. Drugs can be incorporated into the dendrimer structure by three different ways: i) covalent linkage to outer boundary ii) ionically joined to functional groups on the periphery iii) encapsulated inside the dendrimer. Some examples of different drug delivery systems together with delivered substance and targeted microorganism are collected in the **Table 1.3**.

**Table 1.3:** Organic nanoparticle-based systems for drug delivery.

NPs	Drug	Targeted microorganism	Activity and features	Ref.
Liposomes	-	<i>S.epidermidis</i>	Inhibition of biofilm formation	[103]
	Vancomycin	<i>S.aureus</i>	Inhibition of biofilm formation	[104]
	Amikacin	<i>P.aeruginosa</i>	Inhibition of biofilm formation	[105]
	Tobramycin	<i>P.aeruginosa</i>	Liposome fusion with bacterial cells	[106]
	Vancomycin/ rifampin	<i>S.epidermidis</i>	Enhanced biofilm eradication	[107]
	Gentamycin	<i>S.aureus</i>	Significantly increased efficacy as compared to liposomal gentamicin; complete sterilization of bone tissues; prolonged drug release	[108]
	Diclofenac sodium	-	Improved drug delivery through skin	[109]
	Peptides	Cancer cells	Improved pharmacokinetics and pharmacodynamics of the drug	[110, 111]
	Dox	Cancer cells	Enhanced antitumor efficacy	[112, 113]
	Vancomycin	<i>P.aeruginosa</i>	Decrease bacterial colonization	[114]
Micelles	Piperacillin/ Tazobactam	<i>P.aeruginosa</i>	Enhanced inhibition of biofilm formation	[115]
	Hypocrellin A	<i>S.aureus</i>	increase the antibacterial activity	[116]
	Rifampicin	<i>Mycobacterium tuberculosis</i>	Enhanced antibacterial activity for non-resistant bacterial strain	
	PTX	Cancer cells	Enhanced antibacterial activity	[117]
	Dox/ cRGDfK	Cancer cells (human Kaposi's sarcoma)	Enhanced accumulation in tumor tissue and significant tumor weight decrease	[118]
	Dox	Cancer cells	Enhanced internalization in tumor endothelial cells	[119]
	Dox	Cancer cells	Increased therapeutic activity better cytotoxicity in vitro and low systemic toxicity with superior anti-tumor metastasis activity in vivo	[120]

**Table 1.3:** Continued

NPs	Drug	Targeted microorganism	Activity and features	Ref.
Dendrimers	1-hexadecyl-azoniabicyclo [2.2.2] octane (C <sub>16</sub> -DABCO)	<i>E.coli</i> <i>B.cereus</i> <i>P.aeruginosa</i> <i>S.aureus</i> <i>S.oralis</i>	Increased antibacterial activity against gram positive bacteria	[121]
	PAMAM dendrimer/ nadifloxacin and prulifloxacin	<i>E.coli</i>	Increased solubility of quinolones and antibacterial activity	[122]
	PEI/silver NPs	-	Used as imaging agent, antimicrobial agent	[123, 124]
SLNs	Hyaluronic acid/PTX	Cervical breast tumor	Sustained drug release profiles, increased tumor drug concentration	[125]
	Floxuridine	Cancer cells	Higher efficacy on cancer cells	[126]
	Curcumin	Skin disorders	Controlled drug delivery	[127]
	Squalane	Yiest vaccines	squalene-based adjuvants with excellent biocompatibility and provided immune stimulating properties comparable to Freund's adjuvant.	
	Tretinoin	<i>Propionibacterium acnes</i> , <i>S. aureus</i>	Improved drug loading capacity Greater stability	[128]
	Tobramycin	<i>P.aeruginosa</i>	Increased drug bioavailability	[129]
	Atazanavir	HIV	Improved drug loading capacity	[130]
SLN/NLC	penciclovir	-	Improved targeting	[131]
	clotrimazole	fungi	Greater stability Improved drug loading capacity Improved drug penetration through stratum corneum	[132]

## 1.4. Carbon nanoparticles

In the field of biomedicine, carbon-based materials are becoming more and more attractive [133-137]. The existence of different carbon allotropes, from well-known and characterised allotropic phases such as amorphous carbon, graphite and diamonds to more lately discovered carbon nanotubes, graphene (and graphene oxide) or carbon dots, has recently attracted a lot of attention. Each of these structures exhibits distinctive features and has been extensively exploited in diverse biological applications [138, 139]. NPs from this group show unique mechanical, electrical and structural characteristics which find their application in sensing, medical diagnosis, and disease treatment [140, 141].

### 1.4.1. Carbon quantum dots- CQDs

Carbon quantum dots (CQDs) have attracted significant attention since their accidental discovery in 2004 [142]. They show an overall size diameter below 10 nm and with [143] and

can exist as amorphous or crystalline nanostructures commonly with an  $sp^2$  carbon hybridisation, even if cases of  $sp^3$  hybridisation have also been reported [144]. The large number of oxygen-based functional groups they bear is responsible for their excellent water dispersibility and fluorescent properties [143]. In addition, the presence of these different reactive groups on their surface makes further functionalization possible. The diversity of surface functional groups on CQDs is related to the carbon precursor used for the synthesis as well as to the synthesis method itself. In general, the synthetic methods for the development of CQDs can be classified into two main categories commonly found in all nanotechnological approaches, namely top-down and bottom-up. Top-down processes are based on breaking down larger carbon structures while bottom-up processes rely on synthesis from small molecular precursors. **Table 1.4** shows different methods corresponding to each approach. Depending on the synthesis route chosen for the preparation of the carbon nanomaterial, their properties may differ significantly.

**Table 1.4:** Top-down and bottom-up methods for the synthesis of CQDs.

Top-down	Bottom-up
Laser ablation [145]	Hydrothermal/Solvothermal [146, 147]
Ultrasonic synthesis [148]	Microwave-hydrothermal
Electrochemical/chemical oxidation [149]	Plasma hydrothermal [150]
Arc discharge [142]	Chemical Vapor Deposition [151]
Ball milling [152]	Pyrolysis [153]

In biomedical application, the optical properties of CQDs are of great importance. Next to the absorption and fluorescence properties, size-dependent photoluminescence is an exciting feature of the particles [154, 155]. This phenomenon can be explained by the core-state emission induced by perfect carbon crystal with fewer defects, surface- state emission-determined by the hybridisation of the carbon backbone and/or molecular fluorescence- induced by fluorescence impurities. The quantum confinement effect occurs when the particles decrease in size, and their radius approaches the exciton Bohr radius. The quantisation of the energy levels occurs according to Pauli's exclusion principle (**Figure 1.5A**), which relates them more closely to the atoms than in the bulk material. A decrease in size results in an increase in the energy difference between the top of the valence band and the bottom of the conduction band so that more energy is needed to excite the dot. Consequently, more energy is released when it returns to its ground state (**Figure 1.5B**). In terms of application, it means that changing the size of the dots (controlling the size during the synthesis), any emission wavelength can be

obtained from the same material (in a determined wavelength range depending on the material) [156], which is a very useful property especially for bioimaging [157].

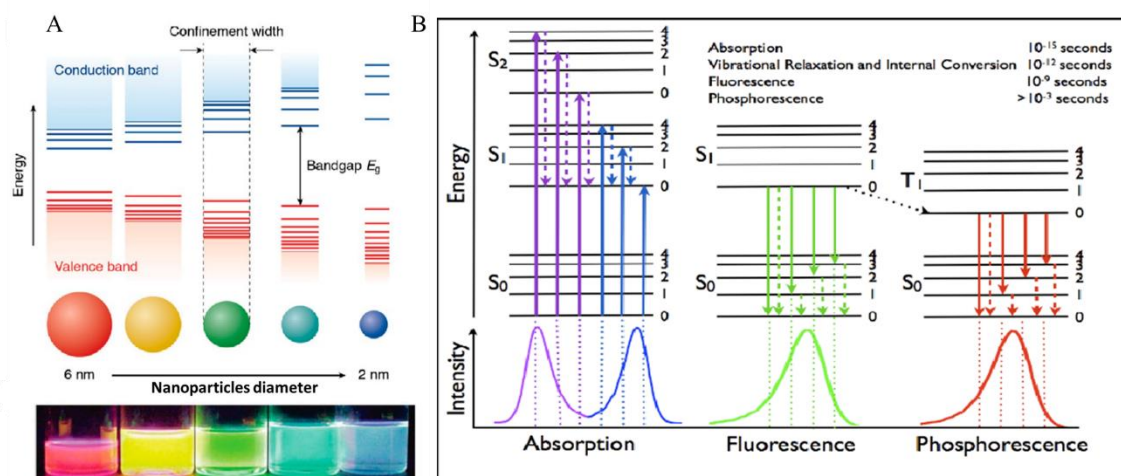


**Figure 1.5:** **A)** Schematic representation of quantum confinement effects (image is taken from ref [158]); **B)** Jablonski diagram (image is taken from ref [159]).

However, not only the size but also the surface functionalization can tailor the optical properties of carbon based quantum dots: modifying the nanoparticles with either electron-donating or electron-accepting molecules will cause the photoluminescence wavelength to shift.

Another important feature of CQDs for biomedical application is their cell cytotoxicity [160] which is, in contrast to metallic nanoparticles for example, significantly lower due to their hydrophilic character and to the “green” reagents involved in their process of fabrication which does not include any metals. Comprehensive studies of *in vitro* cytotoxicity have already been conducted by many research groups [161]. As for *in vivo* studies, **Figure 1.6c** shows a biodistribution of CQDs used in this thesis labelled with a NIR-fluorescent dye. It shows that the fluorescence signal can be observed in the bladder after already 2.5 h after injection, indicating that the CQDs are removed from the body of mice through an excretion pathway (via urine) which is in accordance to other studies carried out in this direction [162, 163]. Additional tests of hemolytic activity of such nanostructures still need to be performed as there is only a little information available up to date. These properties of make CQDs promising candidates in the biomedical field (**Figure 1.6**).



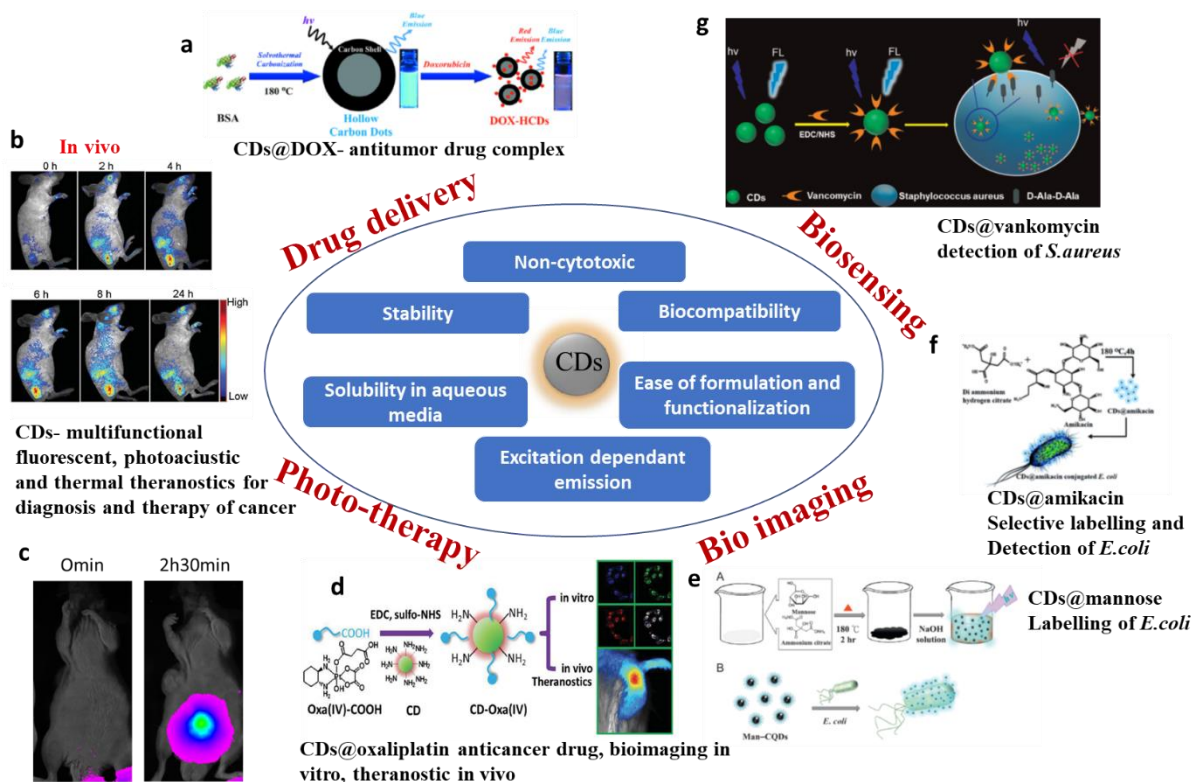


**Figure 1.6.** Schematic illustration of the properties and applications of CQDs (image **a** is taken from [164]; image **b** is taken from [165]; **c** bio-distribution of CF-790-CQDs after intravenous injection (via tail) in five-week-old swiss nude mice; image **d** is taken from [166]; image **e** is taken from [167]; image **f** is taken from [168]; image **g** is taken from [169]).

The choice of the precursor or passivation agent used for the synthesis already defines which functional groups will (potentially) be exhibited at their surface. Carboxylic acid, hydroxyl or amino groups give us a possibility to covalently link biologically active material. Next to covalent functionalization, non-covalent modification based on  $\pi$ - $\pi$  interaction as well as van der Waals forces have been reported [170]. **Figure 1.7** shows some of the most common functionalization approaches used in biomedicine for CQDs. The majority of CQDs contain abundant carboxyl or amino groups on their surface, which allow grafting the molecules via condensation reactions either via an amine- or a carboxy-group-containing agent. Condensation reactions (mainly peptide-coupling-like reactions) usually use EDC/NHS chemistry due to the high solubility of the material in aqueous media. Next to carboxylic and amino functions, hydroxyl groups allow modifications by silylation which is the reaction between silane and active hydrogen at the surface. The resulting alkoxysilane derivative is a biocompatible and nontoxic material which can act as a protective silicon shell, encapsulating the CQDs inside. Other classes of widely used covalent modifications are the esterification and sulfonylation reactions. The second reaction introduces a sulphur atom close to the surface which may



provide energy or emissive trap states for a photoexcited electron capture. As a consequence, it can potentially alter the electronic structure of CQDs. Another kind of reaction that is becoming increasingly attractive for biological purposes is the copper(I) azide-alkyne cycloaddition reaction. It relies on the reaction between an azide function which can be grafted onto the surface of the NPs by EDC/NHS chemistry and an alkyne group born by the molecule to be linked to the CQDs. An example, recently described by us, utilisation of the click reaction for the inhibition of viral infection [171]. Carbon dots rich in amino groups prepared from citric acid and ethylenediamine were first functionalized with an azide moiety and further reacted with the boronic acid molecule, as prepared conjugate show a moderate activity towards Human coronavirus-229E (HCoV-229E). A group of Huang [172] reported the synthesis of carboxyl rich CQDs and further amidation with propargylamine, which in consequence, was further reacted with azido beacon DNA, as prepared conjugate was then bonded to gold nanoparticles and applied to the recognition of single-base-mismatched target. The advantage of such a “click” reaction is its high selectivity and shows great potential in the fields of biomedicine.

Apart from covalent modifications, non-covalent functionalization is another approach. Compared to covalent bonding,  $\pi$ - $\pi$  interactions, complexation or non-covalent interactions have a lesser impact on the surface of NPs and also provide new targeting molecules.

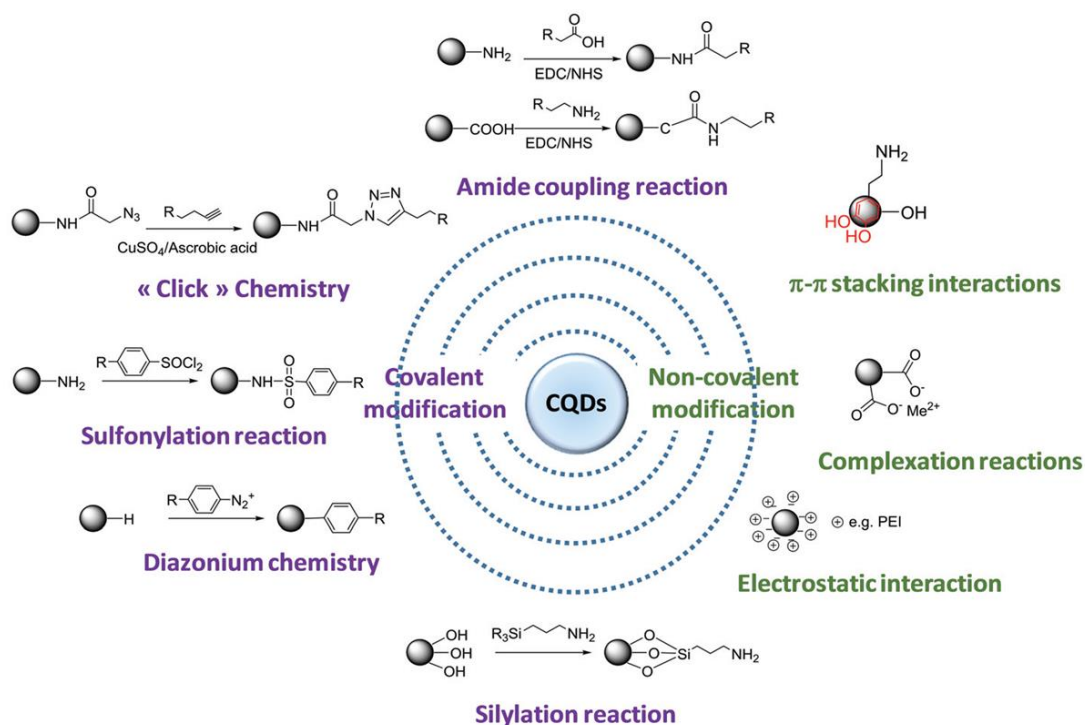


**Figure 1.7:** Covalent and non-covalent approaches for the surface functionalization of CQDs (image is taken from ref [173]).

### 1.4.2. Nanodiamonds

In contrast to CQDs, the carbon atoms in diamond all possess  $sp^3$  hybridisation. The average size of these structures is 4-5 nm, and their quality and surface chemistry can be influenced by the considered synthetic approaches. The most popular synthesis conditions or processes include the detonation (D-NDs), the high pressure/temperature (HPHT-NDs) and the chemical vapour deposition (CVD-NDs). All NDs share the same core structure, which confers them properties similar to bulk diamond which are: excellent stability in harsh conditions, high refractive index and excellent thermal conductivity. They also provide versatile surface chemistry which allows to tailor them as a function of the desired application. In addition, they can undergo processes which can modify their  $sp^3$  core. Bombarding them with high-energy ions implants defects inside the diamond lattice [174]. These defects are commonly called “coloured centres” because the creation of vacancies in the lattice of the material leads to fluorescence properties. This makes the corresponding NDs especially suitable for bioimaging.

Like previously mentioned for CQDs, nanodiamonds can be produced by a variety of bottom-up and top-down methods [175]. Bottom-up processes include the formation of detonated NDs: there, the carbon lattice is built from a molecular precursor. During this process, a mixture of 2,4,6-trinitrotoluene (TNT) and 1,3,5-trinitroperhydro-1,3,5-triazine (hexogen) is exploded, and nanodroplets of liquid carbon are converted into D-NDs by fast cooling (**Figure 1.8**). Detonated NDs contain metal impurities and  $sp^2$  carbon; therefore, the material is subjected to an intense oxidative purification process [175]. During the pre-treatment/purification process, the surface of particles covers itself with various functional groups which are further oxidised and eventually lead to hydroxyl, anhydride or carboxylic groups. Such NDs subjected to strong acid oxidation exhibit a significant affinity for proteins, easily form stable conjugates under different conditions through adsorption [176].

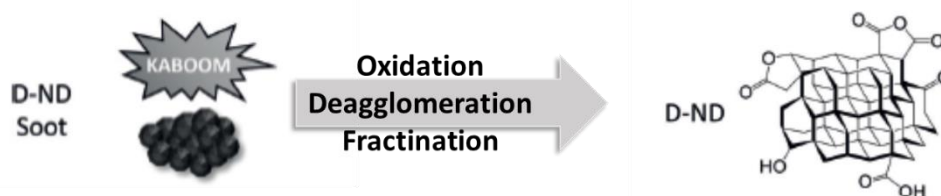


**Figure 1.8:** Illustration of the synthesis and post-synthetic treatment in the preparation of D-NDs (image is taken from ref [85]).

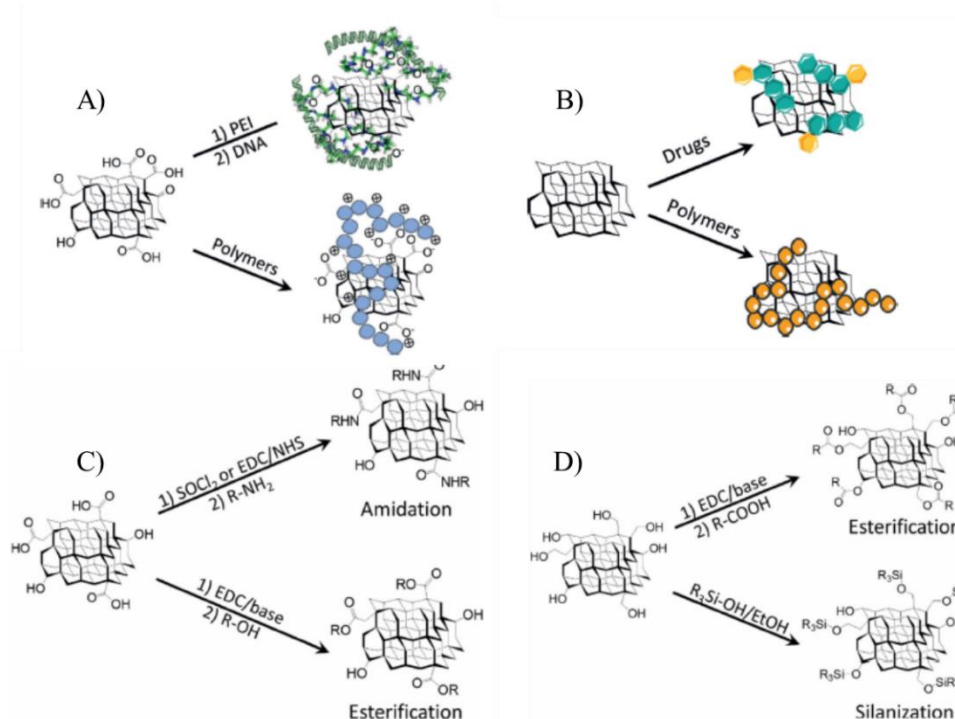
Even after the intense purification process,  $sp^2$  carbon impurities might be still present in the cleaned D-NDs, causing a significant tendency to agglomeration [175]. Therefore, prior to utilisation, they need to undergo deagglomeration and fractionation. This step is usually achieved by high energy ball milling [177] followed by a fractionation which separates the different agglomerates according to their size.

To make nanodiamonds applicable, they very often need to undergo additional surface functionalization. These modifications will tune their future interaction with the surrounding media. The presence of hydroxyls, carboxylic acids, epoxides, as well as lactones, has been identified at the surface of NDs [178]. Various kinds of NDs have been commercialised up to date. However, we must not forget that the composition might differ as a function of the producer.

The main strategies used to modify of NDs' surface can be divided into covalent and non-covalent approaches (**Figure 1.9**). Non-covalent functionalisation includes mostly electrostatic (highly negatively charged surface of NDs) and hydrophobic interactions (adsorption onto the surface via apolar interactions) [179]. This approach found a successful application in drug delivery, where an adsorbed molecule can be released upon a specific stimulus, e.g. the pH [180, 181]. The group of Ho and co-workers applied non-covalent adsorption of doxorubicin (DOX) onto the surface of NDs. The composite led to a significant increase in cell apoptosis compared to conventional treatment [182, 183]. Another example of successful non-covalent adsorption is the adsorption of cell-penetrating peptide TAT onto NDs improving its delivery [184]. It is worth to notice that incorporating a peptide or protein can provide additional binding sites for other molecules to be linked covalently, leading to improved and more effective penetration and delivery abilities [185].

Main covalent modifications are similar to the one described for carbon dots. The presence of abundant carboxylic groups onto the surface allows condensation-type reactions between the NPs and the drug. Another popular response is the esterification reaction between the carboxylic groups on the particles and molecules bearing an alcohol moiety (or the other way around). Barras and co-workers created azido- or alkynyl-modified NDs by coupling 4-azidobenzoic acid or 4-pentynoic acid with hydroxyl groups present at the ND surface [186]. This connection creates another possibility for grafting molecules by applying the copper(I) catalysed azide-alkyne cycloaddition. The esterification reaction is commonly used for grafting

biopolymers with the aim of improving colloidal stability and blood circulation [187]. Another approach consists in the reaction with siloxanes which exhibits several advantages such as the use of mild reaction conditions and an extended versatility. The product after the reaction is covered with a uniform shell, the thickness of which depends on the amount of precursor. This reaction is often used to enhance the surface area, hence to increase the loading capacity or to introduce amine functions which later will be used in a condensation reaction with a carboxylic-group-bearing biomolecule [186]. The derivatisation of the hydroxyl group has been found to be an excellent method for modification and has been intensively explored. Barras and co-workers reported the direct functionalisation of NDs-OH with dopamine derivatives bearing an azide function [188]. Such an approach creates new possibilities for preparing multifunctional particles. In addition, Turcheniuk and co-workers created pre-modified NDs with perfluorophenylazide ligands and linked them photochemically with unmodified polysaccharides to obtain NDs showing a pronounced affinity towards lectins in pathogenic UTI *E. coli* [189]. The group conducted further studies in the direction of biofilm disruption



and the particles were tested against *S. aureus* and *E. coli* [190]. It has also been reported that NDs upon thiolation can be successfully conjugated with gold nanoparticles which provide a new platform for NDs applications [191].

**Figure 1.9: Common surface functionalization methods used in the chemistry of NDs:** **A)** non-covalent electrostatic interactions; **B)** non-covalent hydrophobic interactions; **C)** covalent functionalization via carboxylic acid groups; **D)** covalent functionalization via hydroxyl groups. The image is taken from ref [192].

NDs can be used as co-adjuvants, stimulating the pro-inflammatory or anti-inflammatory signalling pathway [193, 194]. They found their application not only as a platform for the delivery of antibodies but also as enhancers of host immune response. Recently it has been reported that NDs have been used in an influenza vaccine in conjugation with trimeric H-7 antigen (viral protein). This nanoconjugate resulted in a virus-like particle vaccine suspension which showed increased efficiency *in vitro* [194]. In addition, NDs can show an intrinsic bactericidal activity [195, 196]. Ong and co-workers demonstrated that these bactericidal properties depend on the bacteria type, concentration, size and structure [197, 198].

The toxicity of nanodiamonds is doubtful [199]. Indeed, NDs undergo various cleaning processes, and each of them depends on the considered producer. This induces multiple variants as far as the surface modifications are concerned. *In vivo* and *in vitro* studies have been carried out in order to test their features such as cell vitality, *in vivo* physiological and mechanistic behaviour [200]. It has been reported that even at high doses, NDs conjugates did not increase systemic immune response nor increase or modify the serum indicators of liver toxicity [201].

Nanodiamonds, due to their excellent properties, biocompatible nature and their easy-to-modify surface, are excellent candidates as nanocarriers for biomolecules. In addition, nitrogen-vacancy defects centre in NDs makes them fluorescent. Therefore, they found their application as a non-photobleaching fluorescent probe for bioimaging experiments [202].

### **1.4.3. Graphene, Graphene oxide and reduced graphene oxide**

Graphene and its derivatives such as graphene oxide (GO) and reduced graphene oxide (rGO) (**Figure 1.10**) have also attracted attention for biomedical applications [203, 204]. Graphene is a two-dimensional material, consisting of carbon atoms with the  $sp^2$  hybridisation. Ever since its discovery in 2004, a vast number of studies has been performed followed up its exceptional properties [205-208]. Structurally graphene is considered the basic material with the ability to fold in a different way or aggregate thus resulting in carbon allotropes like 0D- fullerene, 1D- carbon nanotubes, 2D- graphene itself, 3D- graphite [209]. It exists as few layers of graphite with the crystal structure of a tightly packed honeycomb-like structure [210]. The family of graphene includes members such as graphene oxide (GO) and its reduced form reduced graphene oxide (rGO) (**Figure 1.10**).

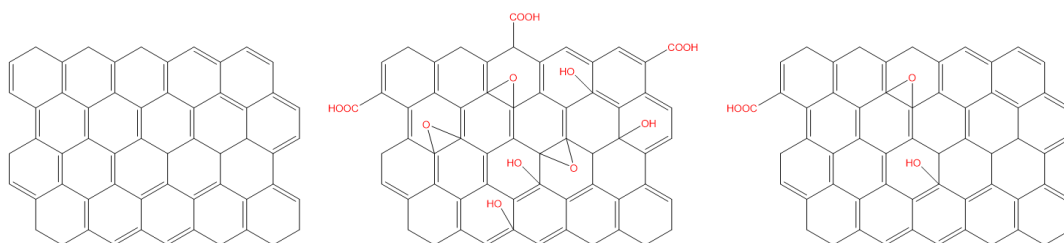


**Figure 1.10:** Schematic illustration of graphene (left), graphene oxide (middle), reduced graphene oxide (right).

Graphene can be formed in a bottom-up or top-down approaches, the most widely used being chemical vapour deposition (CVD) on catalytic interfaces such as Ni or Cu. The main drawback of using this graphene for biomedical applications is that it is a time-consuming process of low yield and high cost. An alternative method scalable, cost-effective with an excessive yield is the chemical exfoliation of graphite resulting in graphene oxide (GO) [211]. The most widely applied method used for fabrication of GO is a Hummer's method, which consists of oxidation of graphite accomplished by use of sulfuric acid and potassium permanganate [212]. GO bears a variety of oxygen-containing functional groups like carboxylic, hydroxyl, carbonyl or epoxy groups. Their presence makes GO a chemically complex inhomogeneous 2D system of hydrophilic character [213]. Reduction of GO by thermal, chemical, microwave or chemical means reduces the oxygen amount on its surface results in reduced graphene oxide (rGO) nanosheets of hydrophobic character, with good electrical conductivity and possibility to convert absorbed light into heat. Typically to improve the hydrophilic character of rGO, poly(ethylene glycol) (PEG) chains are integrated [214].

The possibility of non-covalent functionalization via van der Waals forces and  $\pi$ - $\pi$  interactions with organic molecules or polymers is an easy manner to modify these nanosheets. The first one applied to molecules with high hydrophobic character while the other to the molecules with short or highly extended  $\pi$  system. In addition to that, the presence of oxygen groups on the surfaces and edges of GO allow ionic interactions and hydrogen bonding. Electrostatic interactions employ two opposite charged materials commonly used as a convenient tool in the preparation of composites via self-assembly as such GO/rGO composites with biocompatible materials have been reported. For example, successful anchoring of lactoferrin, lactoferrin protected gold nanoclusters, chitosan has been reported and as prepared material enhances the antibacterial property of GO/rGO [215]. Non-covalent occurs without interrupting the extended  $\pi$  system of graphenic nanostructures.  $\pi$ - $\pi$  stacking can be comparable to covalent interactions where two aromatic rings have overlapping  $\pi$  orbitals. They provide more stable alternatives to above mention interactions. One of the strategies incorporates



modification of molecules with pyrene which is a  $\pi$ -orbital rich group [216]. Recently a group of Liu and co-workers synthesised thermoresponsive graphene/polymer by first preparing well defined thermoresponsive pyrene- poly(N-isopropylacrylamide) followed by the attachment onto the basal plane of graphene sheets [217]. In addition to that, Zhou et al. recently showed that the solubility of a very poor soluble drug could be increased by its interaction with GO surface. They incorporated hypocrellins onto the surface via  $\pi$ - $\pi$  interaction/hydrogen bonds and the in vitro studies showed an effective uptake of the hybrid into the tumour, which subsequently was irradiated and damaged [218]. Another example of improving the solubility of the molecule is the incorporation of quercetin which resulted in stable hybrid in physiological solution with no toxicity in vitro [219]. Another example of successful surface loading of the drugs is doxorubicin [220]. Recently described by some of us, showed the potential of drug loading onto the surface of rGO with the combination of photothermal therapy. rGO was incorporated into the matrix of a hydrogel and further loaded with insulin. The release was achieved upon near-infrared irradiation thanks to the good photothermal properties of rGO. Another example developed by our group was the non-covalent functionalization of rGO with maleimide containing dopamine which further can undergo “click” reaction with sulphur containing molecules like the one used in the studies- c(RGDfC) peptide (cancer cell targeting peptide). It was shown that such a construct could work as a targeted drug delivery system for doxorubicin [221]

## 1.5. References

1. Chou, L.Y.T., K. Ming, and W.C.W. Chan, *Strategies for the intracellular delivery of nanoparticles*. Chemical Society Reviews, 2011. **40**(1): p. 233-245.
2. Aricò, A.S., et al., *Nanostructured materials for advanced energy conversion and storage devices*. Nature Materials, 2005. **4**(5): p. 366-377.
3. Talapin, D.V., et al., *Prospects of Colloidal Nanocrystals for Electronic and Optoelectronic Applications*. Chemical Reviews, 2010. **110**(1): p. 389-458.
4. Pelaz, B., et al., *The State of Nanoparticle-Based Nanoscience and Biotechnology: Progress, Promises, and Challenges*. ACS Nano, 2012. **6**(10): p. 8468-8483.
5. Kim, D., et al., *Synthesis and Biomedical Applications of Multifunctional Nanoparticles*. Advanced Materials, 2018. **30**(49): p. 1802309.
6. Byrne, J.D., T. Betancourt, and L. Brannon-Peppas, *Active targeting schemes for nanoparticle systems in cancer therapeutics*. Advanced Drug Delivery Reviews, 2008. **60**(15): p. 1615-1626.
7. Choi, H.S., et al., *Design considerations for tumour-targeted nanoparticles*. Nature Nanotechnology, 2010. **5**(1): p. 42-47.
8. Turcheniuk, V., et al., *Affinity of Glycan-Modified Nanodiamonds towards Lectins and Uropathogenic Escherichia Coli*. ChemNanoMat, 2016. **2**.

9. Khanal, M., et al., *Inhibition of type 1 fimbriae-mediated Escherichia coli adhesion and biofilm formation by trimeric cluster thiomannosides conjugated to diamond nanoparticles*. Nanoscale, 2015.
10. Shilo, M., et al., *The effect of nanoparticle size on the probability to cross the blood-brain barrier: an in-vitro endothelial cell model*. Journal of nanobiotechnology, 2015. **13**: p. 19-19.
11. Barua, S. and S. Mitragotri, *Challenges associated with Penetration of Nanoparticles across Cell and Tissue Barriers: A Review of Current Status and Future Prospects*. Nano today, 2014. **9**(2): p. 223-243.
12. Doroudian, M., et al., *Nanotechnology based therapeutics for lung disease*. Thorax, 2019. **74**(10): p. 965.
13. Teleanu, D.M., et al., *Blood-Brain Delivery Methods Using Nanotechnology*. Pharmaceutics, 2018. **10**(4): p. 269.
14. Zhou, Y., et al., *Crossing the blood-brain barrier with nanoparticles*. Journal of Controlled Release, 2018. **270**: p. 290-303.
15. Miller, M.A., et al., *Predicting therapeutic nanomedicine efficacy using a companion magnetic resonance imaging nanoparticle*. Science translational medicine, 2015. **7**(314): p. 314ra183-314ra183.
16. Danhier, F., *To exploit the tumor microenvironment: Since the EPR effect fails in the clinic, what is the future of nanomedicine?* Journal of Controlled Release, 2016. **244**: p. 108-121.
17. Mura, S. and P. Couvreur, *Nanotheranostics for personalized medicine*. Advanced Drug Delivery Reviews, 2012. **64**(13): p. 1394-1416.
18. Biesso, A., et al., *Gold Nanoparticles Surface Plasmon Field Effects on the Proton Pump Process of the Bacteriorhodopsin Photosynthesis*. Journal of the American Chemical Society, 2009. **131**(7): p. 2442-2443.
19. Lee, H., et al., *An endoscope with integrated transparent bioelectronics and theranostic nanoparticles for colon cancer treatment*. Nature Communications, 2015. **6**(1): p. 10059.
20. Di Corato, R., et al., *Combining Magnetic Hyperthermia and Photodynamic Therapy for Tumor Ablation with Photoresponsive Magnetic Liposomes*. ACS Nano, 2015. **9**(3): p. 2904-2916.
21. Anselmo, A.C. and S. Mitragotri, *Nanoparticles in the clinic*. Bioengineering & translational medicine, 2016. **1**(1): p. 10-29.
22. Tang, L. and J. Cheng, *Nonporous silica nanoparticles for nanomedicine application*. Nano Today, 2013. **8**(3): p. 290-312.
23. Lee, N. and T. Hyeon, *Designed synthesis of uniformly sized iron oxide nanoparticles for efficient magnetic resonance imaging contrast agents*. Chemical Society Reviews, 2012. **41**(7): p. 2575-2589.
24. Lynch, J., et al., *Gas-Bubble Effects on the Formation of Colloidal Iron Oxide Nanocrystals*. Journal of the American Chemical Society, 2011. **133**(32): p. 12664-12674.
25. Cheng, X., et al., *Light-Triggered Assembly of Gold Nanoparticles for Photothermal Therapy and Photoacoustic Imaging of Tumors In Vivo*. Advanced Materials, 2017. **29**(6): p. 1604894.
26. Zhao, E., et al., *Surface engineering of gold nanoparticles for in vitro siRNA delivery*. Nanoscale, 2012. **4**(16): p. 5102-5109.
27. Ding, K., et al., *Magnetically engineered Cd-free quantum dots as dual-modality probes for fluorescence/magnetic resonance imaging of tumors*. Biomaterials, 2014. **35**(5): p. 1608-1617.



28. Gao, J., et al., *Ultrasmall near-infrared non-cadmium quantum dots for in vivo tumor imaging*. Small (Weinheim an der Bergstrasse, Germany), 2010. **6**(2): p. 256-261.
29. Giner-Casares, J.J., et al., *Inorganic nanoparticles for biomedicine: where materials scientists meet medical research*. Materials Today, 2016. **19**(1): p. 19-28.
30. Bruns, O.T., et al., *Next-generation in vivo optical imaging with short-wave infrared quantum dots*. Nature Biomedical Engineering, 2017. **1**(4): p. 0056.
31. Reiss, P., et al., *Synthesis of Semiconductor Nanocrystals, Focusing on Nontoxic and Earth-Abundant Materials*. Chemical Reviews, 2016. **116**(18): p. 10731-10819.
32. Bilan, R., et al., *Quantum Dot Surface Chemistry and Functionalization for Cell Targeting and Imaging*. Bioconjugate Chemistry, 2015. **26**(4): p. 609-624.
33. Li, Z., et al., *One-Pot Reaction to Synthesize Biocompatible Magnetite Nanoparticles*. Advanced Materials, 2005. **17**(8): p. 1001-1005.
34. Kroll, A.V., R.H. Fang, and L. Zhang, *Biointerfacing and Applications of Cell Membrane-Coated Nanoparticles*. Bioconjugate Chemistry, 2017. **28**(1): p. 23-32.
35. Fang, R.H., et al., *Cell membrane-derived nanomaterials for biomedical applications*. Biomaterials, 2017. **128**: p. 69-83.
36. Palui, G., et al., *Strategies for interfacing inorganic nanocrystals with biological systems based on polymer-coating*. Chemical Society Reviews, 2015. **44**(1): p. 193-227.
37. Huang, J., et al., *Chemical Spacer Design for Engineering the Relaxometric Properties of Core-Shell Structured Rare Earth Nanoparticles*. Chemistry of Materials, 2015. **27**(23): p. 7918-7925.
38. Wang, W., et al., *Multifunctional and High Affinity Polymer Ligand that Provides Bio-Orthogonal Coating of Quantum Dots*. Bioconjugate Chemistry, 2016. **27**(9): p. 2024-2036.
39. García, K.P., et al., *Zwitterionic-Coated "Stealth" Nanoparticles for Biomedical Applications: Recent Advances in Countering Biomolecular Corona Formation and Uptake by the Mononuclear Phagocyte System*. Small, 2014. **10**(13): p. 2516-2529.
40. Jiao, M., et al., *Recent advancements in biocompatible inorganic nanoparticles towards biomedical applications*. Biomaterials Science, 2018. **6**(4): p. 726-745.
41. Sapsford, K.E., et al., *Functionalizing Nanoparticles with Biological Molecules: Developing Chemistries that Facilitate Nanotechnology*. Chemical Reviews, 2013. **113**(3): p. 1904-2074.
42. Hou, Y., et al., *Protease-Activated Ratiometric Fluorescent Probe for pH Mapping of Malignant Tumors*. ACS Nano, 2015. **9**(3): p. 3199-3205.
43. Miao, X., et al., *Sensitive detection of miRNA by using hybridization chain reaction coupled with positively charged gold nanoparticles*. Scientific Reports, 2016. **6**(1): p. 32358.
44. Jain, A. and K. Cheng, *The principles and applications of avidin-based nanoparticles in drug delivery and diagnosis*. Journal of Controlled Release, 2017. **245**: p. 27-40.
45. Tiwari, A.P., S.J. Ghosh, and S.H. Pawar, *Biomedical applications based on magnetic nanoparticles: DNA interactions*. Analytical Methods, 2015. **7**(24): p. 10109-10120.
46. Li, L.-L., et al., *An Exceptionally Simple Strategy for DNA-Functionalized Up-Conversion Nanoparticles as Biocompatible Agents for Nanoassembly, DNA Delivery, and Imaging*. Journal of the American Chemical Society, 2013. **135**(7): p. 2411-2414.
47. Zhao, G. and S.E. Stevens, *Multiple parameters for the comprehensive evaluation of the susceptibility of Escherichia coli to the silver ion*. Biometals, 1998. **11**(1): p. 27-32.

48. Ansari, M., et al., *Evaluation of antibacterial activity of silver nanoparticles against MSSA and MRSA on isolates from skin infections*. Biology and Medicine, 2011. **3**: p. 141-146.
49. Lok, C.-N., et al., *Silver nanoparticles: partial oxidation and antibacterial activities*. JBIC Journal of Biological Inorganic Chemistry, 2007. **12**(4): p. 527-534.
50. Pal, S., Y.K. Tak, and J.M. Song, *Does the antibacterial activity of silver nanoparticles depend on the shape of the nanoparticle? A study of the Gram-negative bacterium Escherichia coli*. Applied and environmental microbiology, 2007. **73**(6): p. 1712-1720.
51. Sondi, I. and B. Salopek-Sondi, *Silver nanoparticles as antimicrobial agent: a case study on E. coli as a model for Gram-negative bacteria*. Journal of Colloid and Interface Science, 2004. **275**(1): p. 177-182.
52. Morones, J.R., et al., *The bactericidal effect of silver nanoparticles*. Nanotechnology, 2005. **16**(10): p. 2346-2353.
53. Yamanaka, M., K. Hara, and J. Kudo, *Bactericidal Actions of a Silver Ion Solution on Escherichia coli, Studied by Energy-Filtering Transmission Electron Microscopy and Proteomic Analysis*. Applied and Environmental Microbiology, 2005. **71**(11): p. 7589.
54. He, W., et al., *Mechanisms of the pH dependent generation of hydroxyl radicals and oxygen induced by Ag nanoparticles*. Biomaterials, 2012. **33**(30): p. 7547-7555.
55. Politano, A.D., et al., *Use of silver in the prevention and treatment of infections: silver review*. Surgical infections, 2013. **14**(1): p. 8-20.
56. Carlson, C., et al., *Unique Cellular Interaction of Silver Nanoparticles: Size-Dependent Generation of Reactive Oxygen Species*. The Journal of Physical Chemistry B, 2008. **112**(43): p. 13608-13619.
57. Xia, T., et al., *Comparison of the Abilities of Ambient and Manufactured Nanoparticles To Induce Cellular Toxicity According to an Oxidative Stress Paradigm*. Nano Letters, 2006. **6**(8): p. 1794-1807.
58. Lekamge, S., et al., *The Toxicity of Silver Nanoparticles (AgNPs) to Three Freshwater Invertebrates With Different Life Strategies: Hydra vulgaris, Daphnia carinata, and Paratya australiensis*. Frontiers in Environmental Science, 2018. **6**(152).
59. Akhtar, S., et al., *Antibacterial and antiviral potential of colloidal Titanium dioxide (TiO<sub>2</sub>) nanoparticles suitable for biological applications*. Materials Research Express, 2019. **6**.
60. Baek, S., et al., *Effects of coating materials on antibacterial properties of industrial and sunscreen-derived titanium-dioxide nanoparticles on Escherichia coli*. Chemosphere, 2018. **208**: p. 196-206.
61. Huang, Z., et al., *Bactericidal mode of titanium dioxide photocatalysis*. Journal of Photochemistry and Photobiology A: Chemistry, 2000. **130**(2): p. 163-170.
62. Ansari, M.A., et al., *Characterization of clinical strains of MSSA, MRSA and MRSE isolated from skin and soft tissue infections and the antibacterial activity of ZnO nanoparticles*. World Journal of Microbiology and Biotechnology, 2012. **28**(4): p. 1605-1613.
63. Kadiyala, U., et al., *Unexpected insights into antibacterial activity of zinc oxide nanoparticles against methicillin resistant Staphylococcus aureus (MRSA)*. Nanoscale, 2018. **10**(10): p. 4927-4939.
64. Fan, Z. and J. Lu, *Zinc Oxide Nanostructures: Synthesis and Properties*. Journal of nanoscience and nanotechnology, 2005. **5**: p. 1561-73.
65. Mahamuni-Badiger, P.P., et al., *Biofilm formation to inhibition: Role of zinc oxide-based nanoparticles*. Materials Science and Engineering: C, 2020. **108**: p. 110319.

66. Espitia, P.J.P., C.G. Otoni, and N.F.F. Soares, *Chapter 34 - Zinc Oxide Nanoparticles for Food Packaging Applications*, in *Antimicrobial Food Packaging*, J. Barros-Velázquez, Editor. 2016, Academic Press: San Diego. p. 425-431.
67. Gabrielyan, L., et al., *Antibacterial effects of iron oxide (Fe<sub>3</sub>O<sub>4</sub>) nanoparticles: distinguishing concentration-dependent effects with different bacterial cells growth and membrane-associated mechanisms*. *Applied Microbiology and Biotechnology*, 2019. **103**(6): p. 2773-2782.
68. Cheng, K.-W. and S.-H. Hsu, *A facile method to prepare superparamagnetic iron oxide and hydrophobic drug-encapsulated biodegradable polyurethane nanoparticles*. *International journal of nanomedicine*, 2017. **12**: p. 1775-1789.
69. Ebrahimi, E., et al., *Novel drug delivery system based on doxorubicin-encapsulated magnetic nanoparticles modified with PLGA-PEG1000 copolymer*. *Artificial Cells, Nanomedicine, and Biotechnology*, 2016. **44**(1): p. 290-297.
70. Ji, F., et al., *A Dual pH/Magnetic Responsive Nanocarrier Based on PEGylated Fe<sub>3</sub>O<sub>4</sub> Nanoparticles for Doxorubicin Delivery*. *Journal of Nanoscience and Nanotechnology*, 2018. **18**: p. 4464-4470.
71. Attia, M.F., et al., *One-step synthesis of iron oxide polypyrrole nanoparticles encapsulating ketoprofen as model of hydrophobic drug*. *International Journal of Pharmaceutics*, 2016. **508**(1): p. 61-70.
72. Ivashchenko, O., et al., *Synthesis and characterization of magnetite/silver/antibiotic nanocomposites for targeted antimicrobial therapy*. *Materials Science and Engineering: C*, 2015. **55**: p. 343-359.
73. Giljohann, D.A., et al., *Gold Nanoparticles for Biology and Medicine*. *Angewandte Chemie International Edition*, 2010. **49**(19): p. 3280-3294.
74. Dykman, L. and N. Khlebtsov, *Gold nanoparticles in biomedical applications: recent advances and perspectives*. *Chemical Society Reviews*, 2012. **41**(6): p. 2256-2282.
75. Kim, H., et al., *Multifunctional Photonic Nanomaterials for Diagnostic, Therapeutic, and Theranostic Applications*. *Advanced Materials*, 2018. **30**(10): p. 1701460.
76. Wiley, B., Y. Sun, and Y. Xia, *Synthesis of Silver Nanostructures with Controlled Shapes and Properties*. *Accounts of Chemical Research*, 2007. **40**(10): p. 1067-1076.
77. Singh, R., et al., *Dual functionality nanobioconjugates targeting intracellular bacteria in cancer cells with enhanced antimicrobial activity*. *Scientific Reports*, 2017. **7**(1): p. 5792.
78. Rattanata, N., et al., *Gallic acid conjugated with gold nanoparticles: antibacterial activity and mechanism of action on foodborne pathogens*. *International journal of nanomedicine*, 2016. **11**: p. 3347-3356.
79. Silvero C, M.J., et al., *Selective Photoinduced Antibacterial Activity of Amoxicillin-Coated Gold Nanoparticles: From One-Step Synthesis to in Vivo Cytocompatibility*. *ACS omega*, 2018. **3**(1): p. 1220-1230.
80. Farooq, M.U., et al., *Gold Nanoparticles-enabled Efficient Dual Delivery of Anticancer Therapeutics to HeLa Cells*. *Scientific Reports*, 2018. **8**(1): p. 2907.
81. Singh, P., et al., *Gold Nanoparticles in Diagnostics and Therapeutics for Human Cancer*. *International journal of molecular sciences*, 2018. **19**(7): p. 1979.
82. Zhang, T., et al., *Cellular Effect of High Doses of Silica-Coated Quantum Dot Profiled with High Throughput Gene Expression Analysis and High Content Cellomics Measurements*. *Nano Letters*, 2006. **6**(4): p. 800-808.
83. Fang, T.-T., et al., *Toxicity evaluation of CdTe quantum dots with different size on Escherichia coli*. *Toxicology in Vitro*, 2012. **26**(7): p. 1233-1239.
84. Vasudevan, D., et al., *Core-shell quantum dots: Properties and applications*. *Journal of Alloys and Compounds*, 2015. **636**: p. 395-404.

85. Medintz, I.L., H. Mattoussi, and A.R. Clapp, *Potential clinical applications of quantum dots*. International journal of nanomedicine, 2008. **3**(2): p. 151-167.
86. Matea, C.T., et al., *Quantum dots in imaging, drug delivery and sensor applications*. International journal of nanomedicine, 2017. **12**: p. 5421-5431.
87. Jung, W.K., et al., *Antibacterial Activity and Mechanism of Action of the Silver Ion in <em>Staphylococcus aureus</em> and <em>Escherichia coli</em>*. Applied and Environmental Microbiology, 2008. **74**(7): p. 2171.
88. Vazquez-Muñoz, R., M. Avalos-Borja, and E. Castro-Longoria, *Ultrastructural analysis of Candida albicans when exposed to silver nanoparticles*. PloS one, 2014. **9**(10): p. e108876-e108876.
89. Darbari, S., et al., *Investigating the antifungal activity of TiO<sub>2</sub> nanoparticles deposited on branched carbon nanotube arrays*. Journal of Physics D: Applied Physics, 2011. **44**: p. 245401.
90. Gopalu, K., et al., *Impact of nano and bulk ZrO<sub>2</sub>, TiO<sub>2</sub> particles on soil nutrient contents and PGPR*. Journal of nanoscience and nanotechnology, 2013. **13**: p. 678-85.
91. He, L., et al., *Antifungal activity of zinc oxide nanoparticles against Botrytis cinerea and Penicillium expansum*. Microbiological Research, 2011. **166**(3): p. 207-215.
92. Liu, Y., et al., *Antibacterial activities of zinc oxide nanoparticles against Escherichia coli O157:H7*. Journal of Applied Microbiology, 2009. **107**(4): p. 1193-1201.
93. Jones, N., et al., *Antibacterial activity of ZnO nanoparticle suspensions on a broad spectrum of microorganisms*. FEMS Microbiology Letters, 2008. **279**(1): p. 71-76.
94. Zhao, Y., et al., *Small Molecule-Capped Gold Nanoparticles as Potent Antibacterial Agents That Target Gram-Negative Bacteria*. Journal of the American Chemical Society, 2010. **132**(35): p. 12349-12356.
95. Shamaila, S., et al., *Gold Nanoparticles: An Efficient Antimicrobial Agent against Enteric Bacterial Human Pathogen*. Nanomaterials (Basel, Switzerland), 2016. **6**(4): p. 71.
96. Williams, D.N., et al., *Poly(oxanorbornene)-Coated CdTe Quantum Dots as Antibacterial Agents*. ACS Applied Bio Materials, 2020. **3**(2): p. 1097-1104.
97. Doshi, N. and S. Mitragotri, *Designer Biomaterials for Nanomedicine*. Advanced Functional Materials, 2009. **19**(24): p. 3843-3854.
98. Mattu, C., G. Brachi, and G. Ciardelli, *2 - Smart Polymeric Nanoparticles*, in *Smart Nanoparticles for Biomedicine*, G. Ciofani, Editor. 2018, Elsevier. p. 15-29.
99. *Emulsion: Theory and practice*. By Paul Becher. Reinhold Publishing Corporation, N. Y., 1957. ix + 392 pp. 15 × 23 cm. Price \$12.50. Journal of the American Pharmaceutical Association, 1958. **47**(10): p. 762-762.
100. Grumezescu, A., *Nano- and microscale drug delivery systems: Design and fabrication*. 2017. 1-491.
101. Jesorka, A. and O. Orwar, *Liposomes: Technologies and Analytical Applications*. Annual Review of Analytical Chemistry, 2008. **1**(1): p. 801-832.
102. Amini, S.M., *Safety of Nanotechnology in Food Industries*. Electronic physician, 2014. **6**: p. 964-968.
103. Sanderson, N.M., et al., *The interaction of cationic liposomes with the skin-associated bacterium Staphylococcus epidermidis: effects of ionic strength and temperature*. Biochimica et Biophysica Acta (BBA) - Biomembranes, 1996. **1283**(2): p. 207-214.
104. Kim, H.-J., E.L. Michael Gias, and M.N. Jones, *The adsorption of cationic liposomes to Staphylococcus aureus biofilms*. Colloids and Surfaces A: Physicochemical and Engineering Aspects, 1999. **149**(1): p. 561-570.



105. Meers, P., et al., *Biofilm penetration, triggered release and in vivo activity of inhaled liposomal amikacin in chronic Pseudomonas aeruginosa lung infections*. Journal of Antimicrobial Chemotherapy, 2008. **61**(4): p. 859-868.
106. Sachetelli, S., et al., *Demonstration of a fusion mechanism between a fluid bactericidal liposomal formulation and bacterial cells*. Biochimica et Biophysica Acta (BBA) - Biomembranes, 2000. **1463**(2): p. 254-266.
107. Moghadas-Sharif, N., et al., *The effect of nanoliposomal formulations on Staphylococcus epidermidis biofilm*. Drug Development and Industrial Pharmacy, 2015. **41**(3): p. 445-450.
108. Hui, T., et al., *Treatment of osteomyelitis by liposomal gentamicin-impregnated calcium sulfate*. Archives of Orthopaedic and Trauma Surgery, 2009. **129**(10): p. 1301-1308.
109. Manconi, M., et al., *Ex vivo skin delivery of diclofenac by transcutol containing liposomes and suggested mechanism of vesicle-skin interaction*. European Journal of Pharmaceutics and Biopharmaceutics, 2011. **78**(1): p. 27-35.
110. Chang, D.-K., et al., *Antiangiogenic targeting liposomes increase therapeutic efficacy for solid tumors*. The Journal of biological chemistry, 2009. **284**(19): p. 12905-12916.
111. Lee, T.-Y., et al., *Peptide-Mediated Targeting to Tumor Blood Vessels of Lung Cancer for Drug Delivery*. Cancer Research, 2007. **67**(22): p. 10958.
112. Pastorino, F., et al., *Enhanced Antitumor Efficacy of Clinical-Grade Vasculature-Targeted Liposomal Doxorubicin*. Clinical Cancer Research, 2008. **14**(22): p. 7320.
113. Sugano, M., et al., *Antibody Targeting of Doxorubicin-loaded Liposomes Suppresses the Growth and Metastatic Spread of Established Human Lung Tumor Xenografts in Severe Combined Immunodeficient Mice*. Cancer Research, 2000. **60**(24): p. 6942.
114. Chen, M., et al., *Antibacterial Micelles with Vancomycin-Mediated Targeting and pH/Lipase-Triggered Release of Antibiotics*. ACS Applied Materials & Interfaces, 2018. **10**(43): p. 36814-36823.
115. Morteza, M., et al., *Synthesis and evaluation of polymeric micelle containing piperacillin/tazobactam for enhanced antibacterial activity*. Drug delivery, 2019. **26**(1): p. 1292-1299.
116. Guo, L.-Y., et al., *Evaluation of hypocrellin A-loaded lipase sensitive polymer micelles for intervening methicillin-resistant Staphylococcus Aureus antibiotic-resistant bacterial infection*. Materials Science and Engineering: C, 2020. **106**: p. 110230.
117. Tripodo, G., et al., *Drug delivery of rifampicin by natural micelles based on inulin: Physicochemical properties, antibacterial activity and human macrophages uptake*. European Journal of Pharmaceutics and Biopharmaceutics, 2019. **136**: p. 250-258.
118. Torchilin, V.P., et al., *Immunomicelles: Targeted pharmaceutical carriers for poorly soluble drugs*. Proceedings of the National Academy of Sciences, 2003. **100**(10): p. 6039.
119. Nasongkla, N., et al., *cRGD-Functionalized Polymer Micelles for Targeted Doxorubicin Delivery*. Angewandte Chemie International Edition, 2004. **43**(46): p. 6323-6327.
120. Wei, X., et al., *Stability Influences the Biodistribution, Toxicity, and Anti-tumor Activity of Doxorubicin Encapsulated in PEG-PE Micelles in Mice*. Pharmaceutical Research, 2012. **29**(7): p. 1977-1989.
121. VanKoten, H.W., et al., *Synthesis and Biological Activity of Highly Cationic Dendrimer Antibiotics*. Molecular Pharmaceutics, 2016. **13**(11): p. 3827-3834.

122. Cheng, Y., et al., *Polyamidoamine (PAMAM) dendrimers as biocompatible carriers of quinolone antimicrobials: An in vitro study*. European Journal of Medicinal Chemistry, 2007. **42**(7): p. 1032-1038.
123. Aymonier, C., et al., *Hybrids of silver nanoparticles with amphiphilic hyperbranched macromolecules exhibiting antimicrobial properties*. Chemical Communications, 2002(24): p. 3018-3019.
124. Tülü, M. and A.S. Ertürk, *Dendrimers as Antibacterial Agents*. 2012.
125. Wang, F., et al., *Hyaluronic acid decorated pluronic P85 solid lipid nanoparticles as a potential carrier to overcome multidrug resistance in cervical and breast cancer*. Biomedicine & Pharmacotherapy, 2017. **86**: p. 595-604.
126. Chirio, D., et al., *Lipophilic Prodrug of Floxuridine Loaded into Solid Lipid Nanoparticles: In Vitro Cytotoxicity Studies on Different Human Cancer Cell Lines*. Journal of Nanoscience and Nanotechnology, 2018. **18**: p. 556-563.
127. Gonzalez, M.L., et al., *Curcumin-loaded cationic solid lipid nanoparticles as a potential platform for the treatment of skin disorders*. Pharmazie, 2017. **72**: p. 721-727.
128. Ridolfi, D.M., et al., *Chitosan-solid lipid nanoparticles as carriers for topical delivery of tretinoin*. Colloids and Surfaces B: Biointerfaces, 2012. **93**: p. 36-40.
129. Cavalli, R., et al., *Solid lipid nanoparticles (SLN) as ocular delivery system for tobramycin*. International Journal of Pharmaceutics, 2002. **238**(1): p. 241-245.
130. Chattopadhyay, N., et al., *Solid Lipid Nanoparticles Enhance the Delivery of the HIV Protease Inhibitor, Atazanavir, by a Human Brain Endothelial Cell Line*. Pharmaceutical Research, 2008. **25**(10): p. 2262-2271.
131. Lv, Q., et al., *Development and evaluation of penciclovir-loaded solid lipid nanoparticles for topical delivery*. International Journal of Pharmaceutics, 2009. **372**(1): p. 191-198.
132. Souto, E.B., et al., *Development of a controlled release formulation based on SLN and NLC for topical clotrimazole delivery*. International Journal of Pharmaceutics, 2004. **278**(1): p. 71-77.
133. Cha, C., et al., *Carbon-Based Nanomaterials: Multifunctional Materials for Biomedical Engineering*. ACS Nano, 2013. **7**(4): p. 2891-2897.
134. Wang, L., et al., *Carbon-Dot-Based Two-Photon Visible Nanocarriers for Safe and Highly Efficient Delivery of siRNA and DNA*. Advanced Healthcare Materials, 2014. **3**(8): p. 1203-1209.
135. Tiwari, J.N., et al., *Engineered Carbon-Nanomaterial-Based Electrochemical Sensors for Biomolecules*. ACS Nano, 2016. **10**(1): p. 46-80.
136. Lin, G., et al., *Inorganic Nanocarriers Overcoming Multidrug Resistance for Cancer Theranostics*. Advanced science (Weinheim, Baden-Wurttemberg, Germany), 2016. **3**(11): p. 1600134-1600134.
137. Zhang, D.-Y., et al., *Graphene Oxide Decorated with Ru(II)-Polyethylene Glycol Complex for Lysosome-Targeted Imaging and Photodynamic/Photothermal Therapy*. ACS Applied Materials & Interfaces, 2017. **9**(8): p. 6761-6771.
138. Hong, G., et al., *Carbon Nanomaterials for Biological Imaging and Nanomedicinal Therapy*. Chemical Reviews, 2015. **115**(19): p. 10816-10906.
139. Maiti, D., et al., *Carbon-Based Nanomaterials for Biomedical Applications: A Recent Study*. Frontiers in pharmacology, 2019. **9**: p. 1401-1401.
140. Kumar, S., et al., *Graphene, carbon nanotubes, zinc oxide and gold as elite nanomaterials for fabrication of biosensors for healthcare*. Biosensors and Bioelectronics, 2015. **70**: p. 498-503.

141. Wu, H.-C., et al., *Chemistry of carbon nanotubes in biomedical applications*. Journal of Materials Chemistry, 2010. **20**(6): p. 1036-1052.
142. Xu, X., et al., *Electrophoretic Analysis and Purification of Fluorescent Single-Walled Carbon Nanotube Fragments*. Journal of the American Chemical Society, 2004. **126**(40): p. 12736-12737.
143. Yuan, F., et al., *Shining carbon dots: Synthesis and biomedical and optoelectronic applications*. Nano Today, 2016. **11**(5): p. 565-586.
144. Zheng, X.T., et al., *Glowing Graphene Quantum Dots and Carbon Dots: Properties, Syntheses, and Biological Applications*. Small, 2015. **11**(14): p. 1620-1636.
145. Reyes, D., et al., *Laser Ablated Carbon Nanodots for Light Emission*. Nanoscale Research Letters, 2016. **11**(1): p. 424.
146. Barras, A., et al., *High Efficiency of Functional Carbon Nanodots as Entry Inhibitors of Herpes Simplex Virus Type 1*. ACS Applied Materials & Interfaces, 2016. **8**(14): p. 9004-9013.
147. Qian, Z., et al., *Highly Luminescent N-Doped Carbon Quantum Dots as an Effective Multifunctional Fluorescence Sensing Platform*. Chemistry – A European Journal, 2014. **20**(8): p. 2254-2263.
148. Li, H., et al., *Synthesis of fluorescent carbon nanoparticles directly from active carbon via a one-step ultrasonic treatment*. Materials Research Bulletin, 2011. **46**(1): p. 147-151.
149. Wang, C.-I., et al., *Electrochemical synthesis of photoluminescent carbon nanodots from glycine for highly sensitive detection of hemoglobin*. Green Chemistry, 2014. **16**(5): p. 2509-2514.
150. Wang, J., C.-F. Wang, and S. Chen, *Amphiphilic Egg-Derived Carbon Dots: Rapid Plasma Fabrication, Pyrolysis Process, and Multicolor Printing Patterns*. Angewandte Chemie International Edition, 2012. **51**(37): p. 9297-9301.
151. Yan, L., et al., *Synthesis of carbon quantum dots by chemical vapor deposition approach for use in polymer solar cell as the electrode buffer layer*. Carbon, 2016. **109**: p. 598-607.
152. Wang, L., et al., *Carbon quantum dots displaying dual-wavelength photoluminescence and electrochemiluminescence prepared by high-energy ball milling*. Carbon, 2015. **94**: p. 472-478.
153. Pan, D., et al., *Observation of pH-, solvent-, spin-, and excitation-dependent blue photoluminescence from carbon nanoparticles*. Chemical Communications, 2010. **46**(21): p. 3681-3683.
154. Zhu, S., et al., *The photoluminescence mechanism in carbon dots (graphene quantum dots, carbon nanodots, and polymer dots): current state and future perspective*. Nano Research, 2015. **8**(2): p. 355-381.
155. Lim, S.Y., W. Shen, and Z. Gao, *Carbon quantum dots and their applications*. Chemical Society Reviews, 2015. **44**(1): p. 362-381.
156. Gao, D., et al., *Exploring of multicolor emissive carbon dots with novel double emission mechanism*. Sensors and Actuators B: Chemical, 2018. **277**: p. 373-380.
157. Boakye-Yiadom, K.O., et al., *Carbon dots: Applications in bioimaging and theranostics*. International Journal of Pharmaceutics, 2019. **564**: p. 308-317.
158. Berends, A.C. and C. de Mello Donega, *Ultrathin One- and Two-Dimensional Colloidal Semiconductor Nanocrystals: Pushing Quantum Confinement to the Limit*. The journal of physical chemistry letters, 2017. **8**(17): p. 4077-4090.
159. Lee, J., *Bioluminescence, the Nature of the Light*. 2017.

160. Havrdova, M., et al., *Toxicity of carbon dots – Effect of surface functionalization on the cell viability, reactive oxygen species generation and cell cycle*. Carbon, 2016. **99**: p. 238-248.
161. Yan, J., et al., *The effect of surface charge on the cytotoxicity and uptake of carbon quantum dots in human umbilical cord derived mesenchymal stem cells*. Colloids and Surfaces B: Biointerfaces, 2018. **171**: p. 241-249.
162. Yang, S.-T., et al., *Carbon dots for optical imaging in vivo*. Journal of the American Chemical Society, 2009. **131**(32): p. 11308-11309.
163. Choi, H.S., et al., *Renal clearance of quantum dots*. Nature biotechnology, 2007. **25**(10): p. 1165-1170.
164. Wang, Q., et al., *Hollow luminescent carbon dots for drug delivery*. Carbon, 2013. **59**: p. 192-199.
165. Ge, J., et al., *Red-Emissive Carbon Dots for Fluorescent, Photoacoustic, and Thermal Theranostics in Living Mice*. Advanced Materials, 2015. **27**(28): p. 4169-4177.
166. Zheng, M., et al., *Integrating Oxaliplatin with Highly Luminescent Carbon Dots: An Unprecedented Theranostic Agent for Personalized Medicine*. Advanced Materials, 2014. **26**(21): p. 3554-3560.
167. Weng, C.-I., et al., *One-step synthesis of biofunctional carbon quantum dots for bacterial labeling*. Biosensors and Bioelectronics, 2015. **68**: p. 1-6.
168. Chandra, S., et al., *One-step synthesis of amikacin modified fluorescent carbon dots for the detection of Gram- negative bacteria like Escherichia coli*. RSC Adv., 2016. **6**.
169. Zhong, D., et al., *Employing carbon dots modified with vancomycin for assaying Gram-positive bacteria like Staphylococcus aureus*. Biosensors and Bioelectronics, 2015. **74**: p. 546-553.
170. Yan, F., et al., *Surface modification and chemical functionalization of carbon dots: a review*. Microchimica Acta, 2018. **185**(9): p. 424.
171. Loczechin, A., et al., *Functional Carbon Quantum Dots as Medical Countermeasures to Human Coronavirus (HCoV)*. ACS Applied Materials & Interfaces, 2019.
172. Gao, M.X., et al., *“Click” on Alkynylated Carbon Quantum Dots: An Efficient Surface Functionalization for Specific Biosensing and Bioimaging*. Chemistry – A European Journal, 2017. **23**(9): p. 2171-2178.
173. Nekoueian, K., et al., *Carbon-based quantum particles: an electroanalytical and biomedical perspective*. Chemical Society Reviews, 2019. **48**(15): p. 4281-4316.
174. Chipaux, M., et al., *Nanodiamonds and Their Applications in Cells*. Small, 2018. **14**(24): p. 1704263.
175. Turcheniuk, K. and V.N. Mochalin, *Biomedical applications of nanodiamond (Review)*. Nanotechnology, 2017. **28**(25): p. 252001.
176. Kong, X.L., et al., *High-Affinity Capture of Proteins by Diamond Nanoparticles for Mass Spectrometric Analysis*. Analytical Chemistry, 2005. **77**(1): p. 259-265.
177. Krüger, A., et al., *Unusually tight aggregation in detonation nanodiamond: Identification and disintegration*. Carbon, 2005. **43**(8): p. 1722-1730.
178. Neburkova, J., J. Vavra, and P. Cigler, *Coating nanodiamonds with biocompatible shells for applications in biology and medicine*. Current Opinion in Solid State and Materials Science, 2017. **21**(1): p. 43-53.
179. Shuai, C., et al., *Surface modification of nanodiamond: Toward the dispersion of reinforced phase in poly-l-lactic acid scaffolds*. International Journal of Biological Macromolecules, 2019. **126**: p. 1116-1124.
180. Wang, P., W. Su, and X. Ding, *Control of nanodiamond-doxorubicin drug loading and elution through optimized compositions and release environments*. Diamond and Related Materials, 2018. **88**: p. 43-50.



181. Tinwala, H. and S. Wairkar, *Production, surface modification and biomedical applications of nanodiamonds: A sparkling tool for theranostics*. Materials Science and Engineering: C, 2019. **97**: p. 913-931.
182. Huang, H., et al., *Active Nanodiamond Hydrogels for Chemotherapeutic Delivery*. Nano Letters, 2007. **7**(11): p. 3305-3314.
183. Chow, E.K., et al., *Nanodiamond Therapeutic Delivery Agents Mediate Enhanced Chemoresistant Tumor Treatment*. Science Translational Medicine, 2011. **3**(73): p. 73ra21.
184. Li, J., et al., *Nanodiamonds as intracellular transporters of chemotherapeutic drug*. Biomaterials, 2010. **31**(32): p. 8410-8418.
185. Huang, S., et al., *Adsorption of Cathepsin B-sensitive peptide conjugated DOX on nanodiamonds*. Applied Surface Science, 2011. **257**(20): p. 8617-8622.
186. Barras, A., et al., *Functionalization of Diamond Nanoparticles Using "Click" Chemistry*. Langmuir, 2010. **26**(16): p. 13168-13172.
187. Zhao, L., et al., *Chromatographic Separation of Highly Soluble Diamond Nanoparticles Prepared by Polyglycerol Grafting*. Angewandte Chemie, 2011. **123**(6): p. 1424-1428.
188. Barras, A., et al., *Direct Functionalization of Nanodiamond Particles Using Dopamine Derivatives*. Langmuir, 2011. **27**(20): p. 12451-12457.
189. Turcheniuk, V., et al., *Affinity of Glycan-Modified Nanodiamonds towards Lectins and Uropathogenic Escherichia Coli*. ChemNanoMat, 2016. **2**(4): p. 307-314.
190. Khanal, M., et al., *Selective Antimicrobial and Antibiofilm Disrupting Properties of Functionalized Diamond Nanoparticles Against Escherichia coli and Staphylococcus aureus*. Particle & Particle Systems Characterization, 2015. **32**(8): p. 822-830.
191. Hsu, M.-H., et al., *Directly Thiolated Modification onto the Surface of Detonation Nanodiamonds*. ACS Applied Materials & Interfaces, 2014. **6**(10): p. 7198-7203.
192. Reina, G., et al., *Chemical Functionalization of Nanodiamonds: Opportunities and Challenges Ahead*. Angewandte Chemie International Edition, 2019. **0**(0).
193. Zhao, L., et al., *Polyglycerol-coated nanodiamond as a macrophage-evading platform for selective drug delivery in cancer cells*. Biomaterials, 2014. **35**(20): p. 5393-5406.
194. Zhao, L., et al., *Multi-level control of conductive nano-filament evolution in HfO<sub>2</sub> ReRAM by pulse-train operations*. Nanoscale, 2014. **6**(11): p. 5698-5702.
195. Wehling, J., et al., *Bactericidal Activity of Partially Oxidized Nanodiamonds*. ACS Nano, 2014. **8**(6): p. 6475-6483.
196. Jira, J., et al., *Inhibition of E. coli Growth by Nanodiamond and Graphene Oxide Enhanced by Luria-Bertani Medium*. Nanomaterials (Basel, Switzerland), 2018. **8**(3): p. 140.
197. Ong, S.Y., et al., *Interaction of nanodiamonds with bacteria*. Nanoscale, 2018. **10**(36): p. 17117-17124.
198. Szunerits, S., A. Barras, and R. Boukherroub, *Antibacterial Applications of Nanodiamonds*. International journal of environmental research and public health, 2016. **13**(4): p. 413-413.
199. Tsai, L.-W., et al., *Nanodiamonds for Medical Applications: Interaction with Blood in Vitro and in Vivo*. International journal of molecular sciences, 2016. **17**(7): p. 1111.
200. Schrand, A.M., et al., *Are Diamond Nanoparticles Cytotoxic?* The Journal of Physical Chemistry B, 2007. **111**(1): p. 2-7.
201. Chow, E., et al., *Nanodiamond Therapeutic Delivery Agents Mediate Enhanced Chemoresistant Tumor Treatment*. Science translational medicine, 2011. **3**: p. 73ra21.
202. Mochalin, V.N., et al., *The properties and applications of nanodiamonds*. Nature Nanotechnology, 2012. **7**(1): p. 11-23.

203. Wu, S.-Y., S.S.A. An, and J. Hulme, *Current applications of graphene oxide in nanomedicine*. International journal of nanomedicine, 2015. **10 Spec Iss**(Spec Iss): p. 9-24.
204. Wang, Y., et al., *Graphene and graphene oxide: biofunctionalization and applications in biotechnology*. Trends in Biotechnology, 2011. **29**(5): p. 205-212.
205. Peigney, A., et al., *Specific surface area of carbon nanotubes and bundles of carbon nanotubes*. Carbon, 2001. **39**(4): p. 507-514.
206. Bolotin, K.I., et al., *Ultrahigh electron mobility in suspended graphene*. Solid State Communications, 2008. **146**(9): p. 351-355.
207. Lee, C., et al., *Measurement of the Elastic Properties and Intrinsic Strength of Monolayer Graphene*. Science, 2008. **321**(5887): p. 385.
208. Bonaccorso, F., et al., *Graphene photonics and optoelectronics*. Nature Photonics, 2010. **4**(9): p. 611-622.
209. Geim, A.K. and K.S. Novoselov, *The rise of graphene*. Nature Materials, 2007. **6**(3): p. 183-191.
210. Allen, M.J., V.C. Tung, and R.B. Kaner, *Honeycomb Carbon: A Review of Graphene*. Chemical Reviews, 2010. **110**(1): p. 132-145.
211. Park, S. and R.S. Ruoff, *Chemical methods for the production of graphenes*. Nature Nanotechnology, 2009. **4**(4): p. 217-224.
212. Smith, A.T., et al., *Synthesis, properties, and applications of graphene oxide/reduced graphene oxide and their nanocomposites*. Nano Materials Science, 2019. **1**(1): p. 31-47.
213. Dreyer, D.R., et al., *The chemistry of graphene oxide*. Chemical Society Reviews, 2010. **39**(1): p. 228-240.
214. Liu, Z., et al., *PEGylated Nanographene Oxide for Delivery of Water-Insoluble Cancer Drugs*. Journal of the American Chemical Society, 2008. **130**(33): p. 10876-10877.
215. Sreeprasad, T.S., et al., *Transparent, Luminescent, Antibacterial and Patternable Film Forming Composites of Graphene Oxide/Reduced Graphene Oxide*. ACS Applied Materials & Interfaces, 2011. **3**(7): p. 2643-2654.
216. Zhao, H., et al., *Enhanced dispersion of nanotubes in organic solvents by donor-acceptor interaction between functionalized poly(phenylacetylene) chains and carbon nanotube walls*. Journal of Polymer Science Part A: Polymer Chemistry, 2009. **47**(19): p. 4995-5005.
217. Liu, J., et al., *Thermosensitive graphene nanocomposites formed using pyrene-terminal polymers made by RAFT polymerization*. Journal of Polymer Science Part A: Polymer Chemistry, 2010. **48**(2): p. 425-433.
218. Zhou, L., et al., *High-efficiency loading of hypocrellin B on graphene oxide for photodynamic therapy*. Carbon, 2012. **50**: p. 5594-5604.
219. Rahmanian, N., et al., *Nano graphene oxide: A novel carrier for oral delivery of flavonoids*. Colloids and Surfaces B: Biointerfaces, 2014. **123**: p. 331-338.
220. Balcioglu, M., M. Rana, and M. Yigit, *"Doxorubicin loading on graphene oxide, iron oxide and gold nanoparticle hybrid"*. Journal of Materials Chemistry, 2013.
221. Oz, Y., et al., *Functionalization of Reduced Graphene Oxide via Thiol-Maleimide "Click" Chemistry: Facile Fabrication of Targeted Drug Delivery Vehicles*. ACS Applied Materials & Interfaces, 2017. **9**(39): p. 34194-34203.

## CHAPTER 2

### Carbon nanomaterials as antibacterial alternatives

#### 2.1. Introduction

Increasing antibiotic resistance and the limited development of new drugs make the search for alternative strategies to eradicate bacterial infections imperative. Although the last class of antibiotics was introduced on the market in 2000 (**Figure 2.1**), its discovery dates from the 1970s, which shows that no significant progress has been made in the development of new classes of antibacterial agents. Certainly, a lot of “new” products approved for clinical use have been released as 2<sup>nd</sup>, 3<sup>rd</sup>, 4<sup>th</sup> generation antibiotics, but they are mostly derivatives of existing compounds, and their mode of action remains the same. The shortage of newly developed drugs in the past years, together with overusing and abusing current antibacterial agents, led to the increasing development of resistance in pathogenic bacteria. This continued evolution of antimicrobial resistance brings a real threat to human health by seriously compromising our ability to treat infections [1]. The annual deaths worldwide caused by pathogenic bacteria are estimated to reach 10 million by 2050 [2]. Thus, the development of new antibacterial agents becomes an urgent and crucial task to overcome this growing problem.

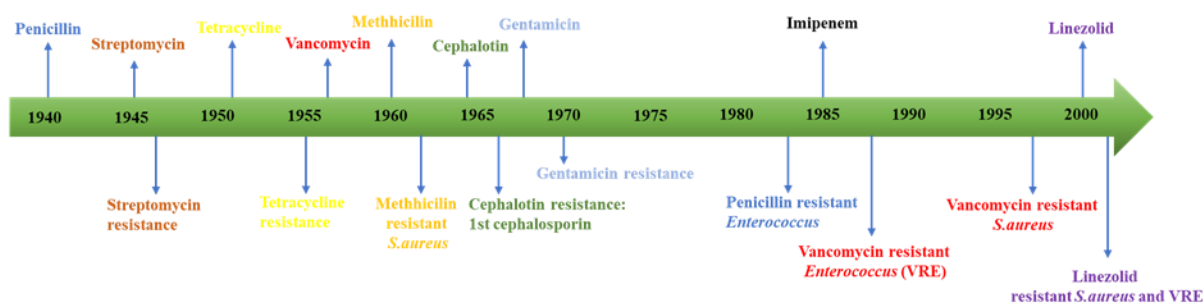


**Figure 2.1:** History of antimicrobial agent development vs subsequent acquisition of resistance by microorganisms [3].

In recent years, a new approach has been intensively explored as a promising alternative to nowadays antibiotic-based treatments. It focuses on antimicrobial nanomaterials and nanosized platforms for efficient and targeted drug delivery. Antimicrobial nanoparticles (NPs) or nanosized drug carriers present many distinct advantages over conventional antibiotics,

including improved pharmacokinetics (higher solubility, controlled release, site-targeted delivery) and accumulation while reducing the side effects proper to antibiotic therapy. Additionally, nanocarriers can improve the stability of antibacterial agents in various physiological environments, and it is believed that it can help to overcome the antimicrobial drug resistance [4, 5].

Antibacterial NPs are made up of metals, metal oxides, carbon-based materials, surfactant-based emulsions or naturally occurring compounds with antibacterial activity[6]. Their unique physicochemical properties and high surface-to-volume ratio make them successful and effective alternatives [4, 7]. The different pathways through which NPs can act against pathogens include the disruption of the cell membrane, the perturbation of energy transduction mechanisms, the inhibition of enzyme activity and/or synthesis, and the photocatalysed production of reactive oxygen species (**Figure 2.2**) [4, 8-11].

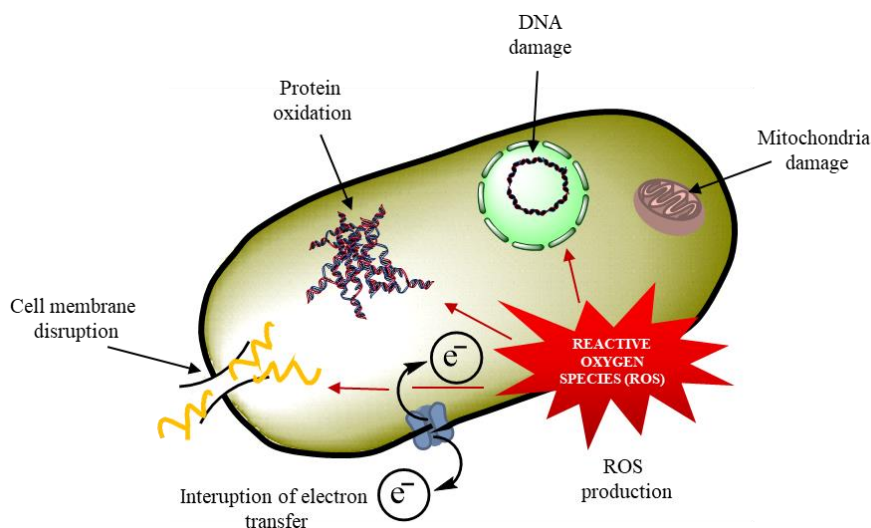


**Figure 2.2:** Various antimicrobial mechanisms due to nanomaterials. The form was inspired by the sketch in [3].

To maximise the therapeutic effect, the therapeutic index and adverse reactions need to be optimised [12]. Additionally, the acquired resistance of infectious pathogens is another challenge in the discovery of new drugs. The exceptional properties of NPs such as their small and controllable size, or their structural/functional versatility, make them very promising platforms to overcome those limitations [12, 13]. The use of NPs as delivery platforms show huge advantages over traditional antibiotics. Incorporating poorly water-soluble drugs onto the NPs may increase their solubility, extend their half-life, as well as their constant and stimuli-responsive release, which would ultimately lead to lower the corresponding administration

frequency and dose [12-14]. Targeted delivery, together with the synergistic effect due to the co-delivery of multiple antimicrobials achieved by NP carriers, can also minimise the side effects resulting from the taken antibiotics [12, 13].

For the past decade, several studies have significantly contributed to the development of novel nanoparticle-based platforms with different compositions and biological properties. Amongst them, carbon-based materials like nanodiamonds (NDs) [15, 16] and carbon dots (CQDs) [17, 18] became a viable alternative as nanocarriers.

NDs have attracted increasing attention due to their large specific surface area, good biocompatibility [19, 20], non-toxicity [21, 22], high drug loading capacity [23], and inexpensive large-scale synthesis. Some of the advantages of NDs over other carbon vehicles such as carbon nanotubes are their optical transparency, their complete inertness and the scope of their functionalization possibilities, which make them highly adaptive as a function of the considered application [23-25].

CQDs, as another group of carbon materials, have attracted tremendous attention due to their chemical stability, very good dispersibility in aqueous media, biocompatibility, low toxicity, high cell membrane permeability, fluorescent properties [26, 27], and facile surface functionalization [28, 29]. Their low cytotoxicity, as well as their good photostability, are key advantages over other quantum dots. Furthermore, the presence of different functional groups on the CQD surface, together with fluorescent properties, makes them excellent drug delivery tools [18, 29, 30]. Surprisingly, there are only a few studies about the antibacterial use of CQDs as nanocarriers for antibiotic delivery [29, 31-33].

The work described in this chapter concerns the synthesis and functionalization of CQDs and NDs with short, cationic and synthetic antimicrobial peptides (synAMP), to investigate their antibacterial activity and to compare them to that of the free peptide. Peptides were modified in two distinct ways, which allowed to incorporate them by two different methods:

- a) an amide bond formation via a condensation reaction;
- b) a copper(I)-catalysed azide-alkyne cycloaddition (CuAAC).

Antibacterial peptides are mostly cationic and target bacterial cell membrane causing the disintegration of the lipid bilayer structure [34, 35]. Most of them are also amphipathic, i.e. they contain both a hydrophobic and a hydrophilic part [36]. Such a peculiar structure helps them to bind to lipid components and phospholipid groups. Some other peptides can kill bacteria without interacting with the membrane. Instead, they do inhibit some of the important pathways inside the cells [37]. It was also reported that some antimicrobial peptides (AMPs) were able to kill resistant strains of bacteria [38].

There are several limitations to the clinical application of naturally occurring AMP including, e.g. their toxicity, their sensitivity to proteases, as well as their isolation and purification, associated with high costs. This underlines the search for smaller synthetic AMPs that have no natural counterparts and low minimal inhibitory concentration (MIC). One of the advantages of using synAMP over naturally occurring peptides is the possibility to introduce chemical modifications that are not accessible through natural biosynthetic pathways, increased yield during the synthesis and reduced production cost.

In this work, we chose to synthesise a hexapeptide based on arginine (Arg, R) and tryptophan (Trp, W) with the sequence H-RWRWRW-NH<sub>2</sub> (**Figure 2.3**), where arginine brings the charged moiety and tryptophan serves as a lipophilic bulk [39]. We also synthesised some derivatives by altering the described sequence. It is worth to notice that amongst synAMPs, the one chosen for these studies is one of the smallest candidates that prove to show antibacterial activity [40, 41].

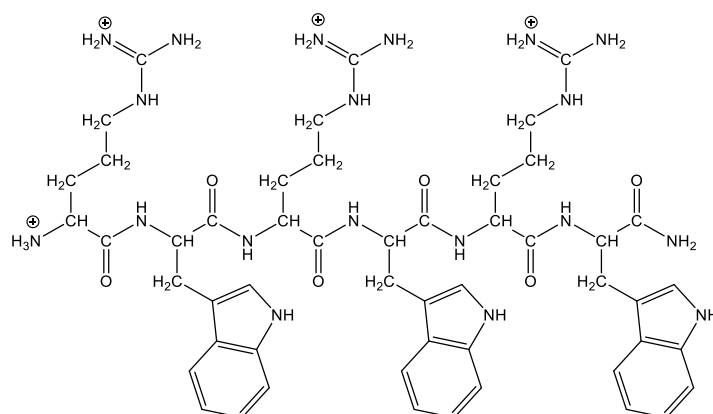


**Figure 2.3:** Structure of the synthesised synAMPs being an arginine- and tryptophan-rich hexapeptide.

The mechanism of action of this peptide has already been investigated by Wenzel et al.[42]. Shortly, the hexapeptide incorporates into the bacterial cytoplasmic membrane, which



contains negatively charged phospholipids. When attached to the cell membrane, it causes the detachment of cytochrome C (a protein involved in the respiratory chain) and MurG (an enzyme involved in the synthesis of the cell wall). The indifference of cytochrome C affects the synthesis of adenosine triphosphate (ATP) and consequently, the cellular energy, whereas the indifference of MurG affects the cell wall integrity.

The choice of this peptide was driven by its already recognised activity against some methicillin-resistant *S. aureus* (MRSA) and vancomycin-intermediate-resistant *S. aureus* (VISA) [43]. As it is also known to cause bacteria death through the disruption of a broad range of cellular processes, such a peptide can be envisioned as a key structure to address the issue of growing antimicrobial resistance.

Together with the multivalent character of nanoparticles which potentially can significantly increase the affinity to appropriate target compared to the monovalent reference, the conjugates might be a promising alternative to nowadays antibiotics by improving their antibacterial activity and stability against protease degradation. The antibacterial activity of peptides and carbon-peptides conjugates was investigated against two strains of pathogenic bacteria: *E.coli* and *S.aureus*.

## **2.2. Synthesis of short synthetic antimicrobial peptides (synAMPs) and their antibacterial activity**

All the peptides were prepared by standard Fmoc/tBu solid-phase peptide synthesis (SPPS). To increase the overall positive charge on the peptides and their organometallic conjugates, they were synthesised as peptide amides. All the structures were purified by reverse-phase high-pressure liquid chromatography (RP-HPLC), analytical HPLC established their purity and the composition of the final product was confirmed by electron ionisation mass spectrometry (ESI-MS) (**Table 2.1**). Additionally, their antibacterial activity was assessed by determining their MIC values by the microdilution method (**Table 2.1**).

We decided to use the H-RWRWRW-NH<sub>2</sub> as a model structure, that amongst short cationic peptides showed the highest antibacterial activity [40, 41]. Another factor that determined our choice was the ease of preparation and sequence modification without losing the antibacterial activity. In general, a set of 14 differently modified peptides was prepared.

The modifications were made in order to improve the antibacterial activity of the peptides (introduction of organometallic moiety on the N terminal end (**2a-3b**; **6a-7b**) [44-46] and introduce the necessary linkage for the CuAAC reactions between the nanoparticles (introduction of propargyl group on the N terminal end (**4a-4b**), the addition of extra amino acid with propargyl group on the C terminal end (**5a-7b**). Small cationic synAMPs owe their antibacterial activity mainly to charge and lipophilic bulk. These two factors were taken into consideration while designing the sequences to avoid eukaryotic toxicity.

**Table 2.1:** Summary of HPLC retention times ( $t_R$ ), ESI-MS data and MIC values for the peptides 1a-7b

Compound	Sequence	$t_R^1$ [min]	Molecular mass		MIC [ $\mu\text{g/ml}$ ]	
			Calc.	Exp. <sup>1</sup>	<i>E.coli</i> DSM 30083	<i>S.aureus</i> (MRSA) ATCC 43300
<b>1a</b>	H-RWRWRW-NH <sub>2</sub>	6.28	1044.24	1044.79	32	16
<b>1b</b>	H-WRWRWR-NH <sub>2</sub>	6.36	1044.24	1044.75	32	16
<b>2a</b>	FcCO-WRWRW-NH <sub>2</sub>	7.4	1100.08	1100.53	32	16
<b>2b</b>	FcCO-RWRWR-NH <sub>2</sub>	6.63	1070.06	1070.75	256	32
<b>3a</b>	RcCO-WRWRW-NH <sub>2</sub>	7.43	1145.31	1146.04	32	8
<b>3b</b>	RcCO-RWRWR-NH <sub>2</sub>	6.66	1115.28	1116.05	64	16
<b>4a</b>	CHCCH <sub>2</sub> CH <sub>2</sub> C(O)-RWRWRW-NH <sub>2</sub>	6.61	1124.33	1124.8	32	16
<b>4b</b>	CHCCH <sub>2</sub> CH <sub>2</sub> C(O)-WRWRWR-NH <sub>2</sub>	6.68	1124.33	1124.8	32	16
<b>5a</b>	H-RWRWRWG(CH <sub>2</sub> CCH)-NH <sub>2</sub>	6.36	1139.34	1139.86	32	16
<b>5b</b>	H-WRWRWRWG(CH <sub>2</sub> CCH)-NH <sub>2</sub>	6.5	1139.34	1139.93	32	16
<b>6a</b>	FcCO-WRWRWG(CH <sub>2</sub> CCH)-NH <sub>2</sub>	7.43	1195.18	1195.68	64	32
<b>6b</b>	FcCO-RWRWRWG(CH <sub>2</sub> CCH)-NH <sub>2</sub>	6.83	1165.16	1165.98	128	32
<b>7a</b>	RcCO-WRWRWG(CH <sub>2</sub> CCH)-NH <sub>2</sub>	7.51	1240.41	1240.9	128	8
<b>7b</b>	RcCO-RWRWRWG(CH <sub>2</sub> CCH)-NH <sub>2</sub>	7.41	1210.39	1211.01	128	32
<b>ref</b>	ciprofloxacin	-	-	-	2<	4

<sup>1</sup>For more details see appendix 6.2.1.1.- 6.2.1.14.

All peptides were prepared in high purity and satisfying yield. The activity against pathogenic microbes was as expected, higher for Gram-positive bacteria than Gram-negative. In the case of peptides (**1a-1b**; **4a-5b**) which have a balanced content of charged and bulky lipophilic groups, there is no difference in the activity irrespective of the order of the amino acids. Peptides with the structure  $\text{McC(O)-WRWRW-NH}_2$  showed higher activity than  $\text{McC(O)-RWRWR-NH}_2$  where the one with ruthenocene showed an increase in antibacterial activity over the one that contained ferrocene.



### 2.3. Synthesis and surface modifications of nanoparticles prior to the formation of bioconjugates

Two different kinds of carbon particles were used as a scaffold to incorporate previously prepared peptides (**1a-7b**). Commercially available nanodiamonds (NDs) and carbon dots (CQDs). Both particles have hydroxyl, carboxy or amino groups on their surface, which enable to create amid bond between the peptides and create azido groups, necessary for the “click” reaction.

In this work, we synthesised amine rich carbon dots (**CQDs-1**), which surface was modified in two ways (**Figure 2.4**). First, to enable the incorporation of peptide amides, amine groups were reacted with  $\text{ClCH}_2\text{COONa}$  under strong alkaline conditions resulting in carboxyl capped CQDs (**CQDs-2**). The second modification includes grafting 2-azidoacetic acid onto the surface in the presence of EDC/NHS (**CQDs-3**). In case of nanodiamonds, for the coupling of peptide amides, we used commercially available NDs-COOH, and for the “click” reactions ND-NH<sub>2</sub> was directly modified with 4-azidobenzoic acid in the presence of N, N'-dicyclohexylcarbodiimide (DCC) and a catalytic amount of 4-dimethyl aminopyridine (DMAP) (ND-3) (**Figure 2.4**).

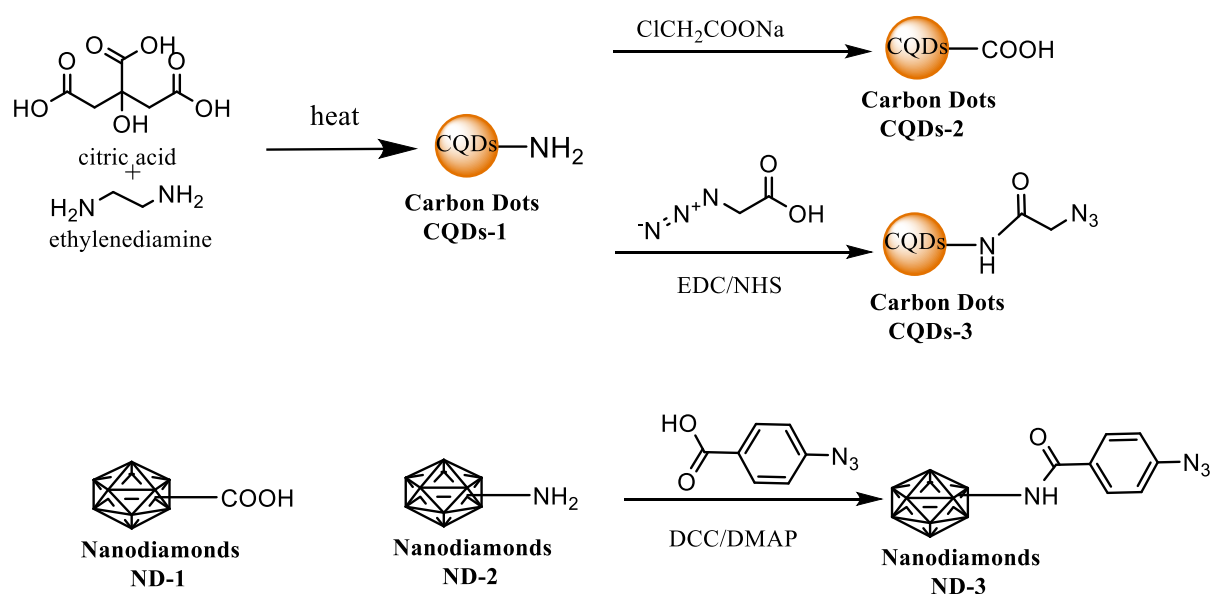


**Figure 2.4:** Schematic illustration of synthesis and surface functionalization used for carbon nanoparticles.

**CQDs-1** were prepared by a hydrothermal method previously reported by Zhu et al.[47] with small modifications. The reaction was conducted by carbonisation of the organic precursor with a sealed Teflon lined autoclave chamber at elevated temperature under reduced pressure

for 5 h. The obtained product was left to cool down to be further purified by dialysis for 24 h, resulting in a dark brown solution with the yield of the reaction- around 60%.

The morphology and structure of **CQDs-1** were examined. **Figure 2.5** shows transmission electron microscopy (TEM) of as-prepared material confirming their spherical shape with an average diameter of  $4.5 \pm 0.2$  nm. From the image, most of the observed particles are of a crystalline character possessing well-resolved lattice fringes.

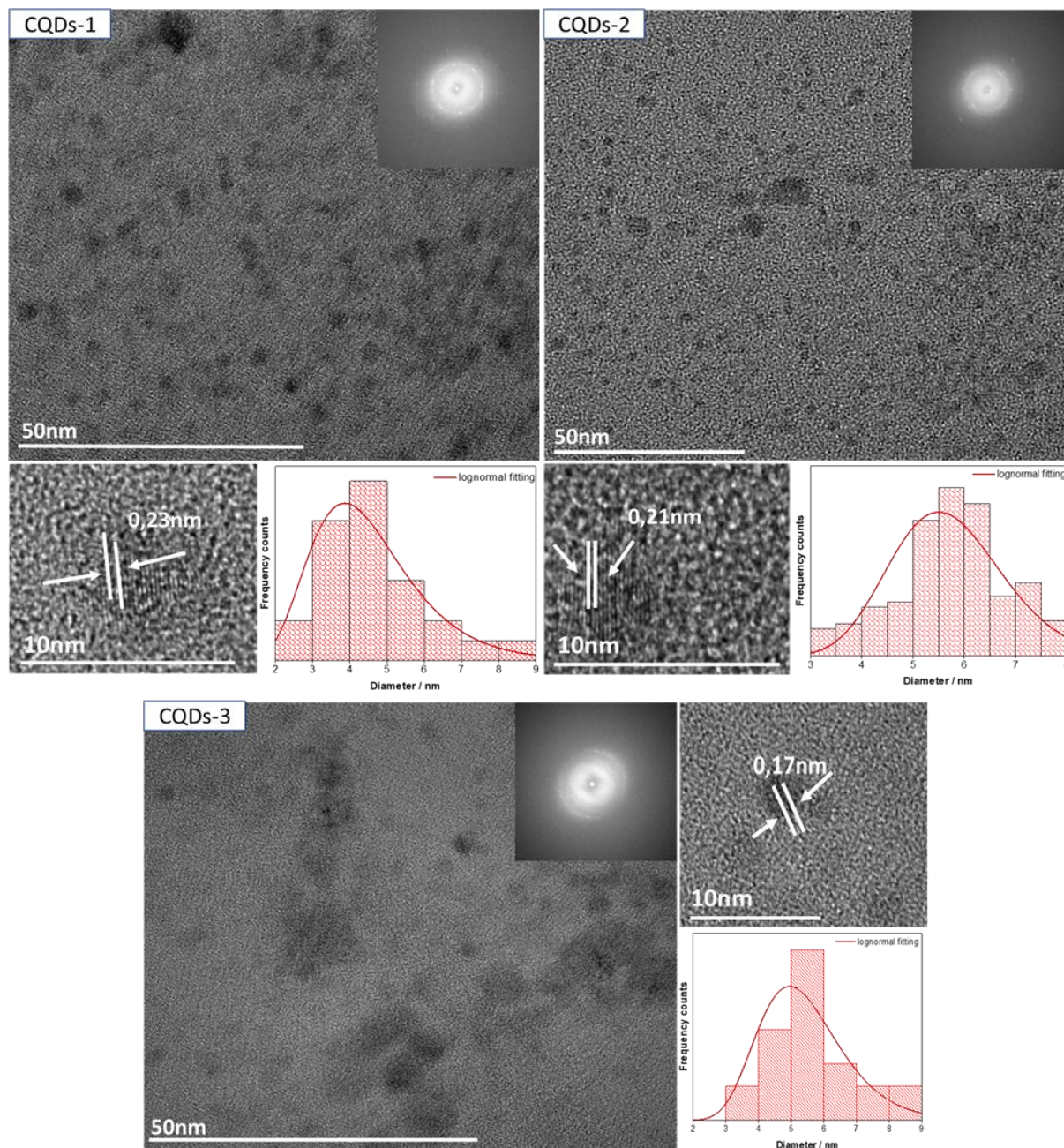


**Figure 2.5:** TEM image, magnified TEM, FFT images and size distribution histograms for CQDs-1, CQDs-2, and CQDs-3.

With such a high carbon lattice structure content, D and G band were detected in the Raman spectra of CQDs-1 (**Figure 2.6A**). G band at  $1570\text{ cm}^{-1}$  related to in-plane vibration of  $\text{sp}^2$  carbon, and the D band at  $1350\text{ cm}^{-1}$  attributed to the presence of  $\text{sp}^3$  defects. The intensity ratio of the D and G band ( $I_D/I_G$ ) is  $0.85\pm 0.12$ . Also, a broad peak centred at around  $2800\text{ cm}^{-1}$  corresponding to the 2D component of graphitic structures is observed. The XRD diffractogram (**Figure 2.6B**) displays a broad diffraction peak centred at  $25.5^\circ$  corresponding to an interlayer spacing of  $0.35\text{ nm}$ , larger than the spacing between (100) planes in bulk graphite ( $0.23\text{ nm}$ ) due to the incorporation of functional groups along the edges of the CQDs.

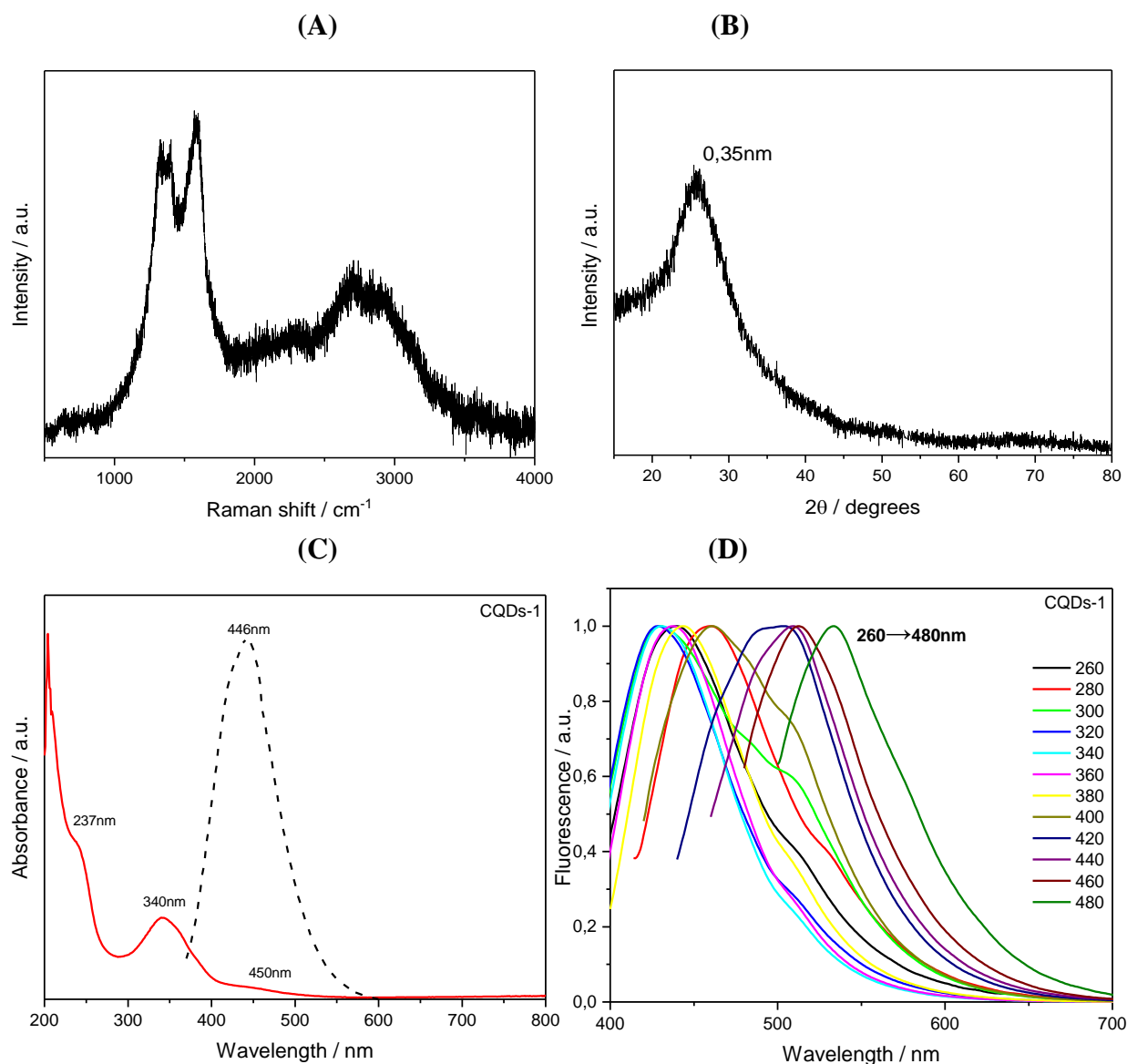


**Figure 2.6: Characterisation of CQDs-1:** (A) Raman spectrum of CQDs-1; (B) XRD diffractogram of CQDs-1; (C) UV-Vis absorption (solid lines) and fluorescence spectra (dash-dot,  $\lambda_{\text{ex}} = 350\text{ nm}$ ) of the CQDs-1; (D) wavelength-dependent fluorescent emission properties of CQDs-1.

The UV/Vis of **CQDs-1 (Figure 2.6C)** reveals an absorption maximum at  $\approx 242$  nm attributed to  $\pi$ - $\pi^*$  transition of C=C and a band at 344 nm attributed to n- $\pi^*$  transition of C=O and C=N bonds.[48, 49] Furthermore, the QY of as-prepared carbon dots was as high as 61% (0,33) (using quinine sulphate as a reference; QY, 0.54 in 0.12 M H<sub>2</sub>SO<sub>4</sub>). Additionally, upon increasing the excitation wavelength, the emission gradually shifts to the red region with an increase in fluorescence intensity (**Figure 2.6D**). The phenomenon of excitation-dependent emission is typical for these nanostructures.

To get more information about the chemical composition FTIR and XPS measurements were performed. XPS data revealed the presence of oxygen, nitrogen, and carbon on the surface of the particles. The deconvolution of the high-resolution spectrum of C1s confirms the existence of three different types of carbon atoms graphitic or aliphatic (C=C and CC), oxygenated, and nitrous (**Figure 2.7A**) on the surface. The high-resolution XPS spectrum of N1s displays one peak at 399,7eV, which corresponds to C-NH (**Figure 2.7B**).

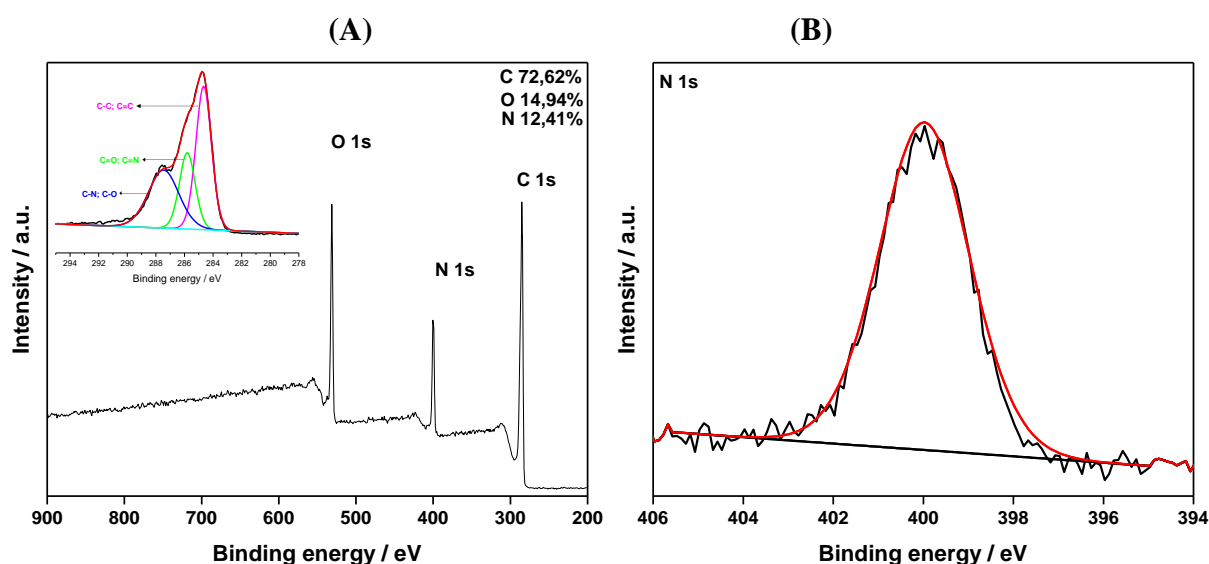


**Figure 2.7:** Characterisation of CQDs-1: (A) XPS survey of CQDs-1 with inset of high resolution C1s spectrum; (B) N1s spectrum of CQDs-1.

The FTIR spectrum of as-prepared dots exhibits a distinct band at 3432 cm<sup>-1</sup> attributed to stretching vibration of -OH. Another absorption band corresponding to stretching vibrations are the one of NH (3262cm<sup>-1</sup>), C=CH (3018cm<sup>-1</sup>), CH (2923cm<sup>-1</sup>), C=O (1771cm<sup>-1</sup> and 1645cm<sup>-1</sup>), C-C (1297cm<sup>-1</sup>). The existence of the amine functional groups is confirmed by the presence of a band at around 1567cm<sup>-1</sup> and 1396cm<sup>-1</sup>(**Figure 2.8**).

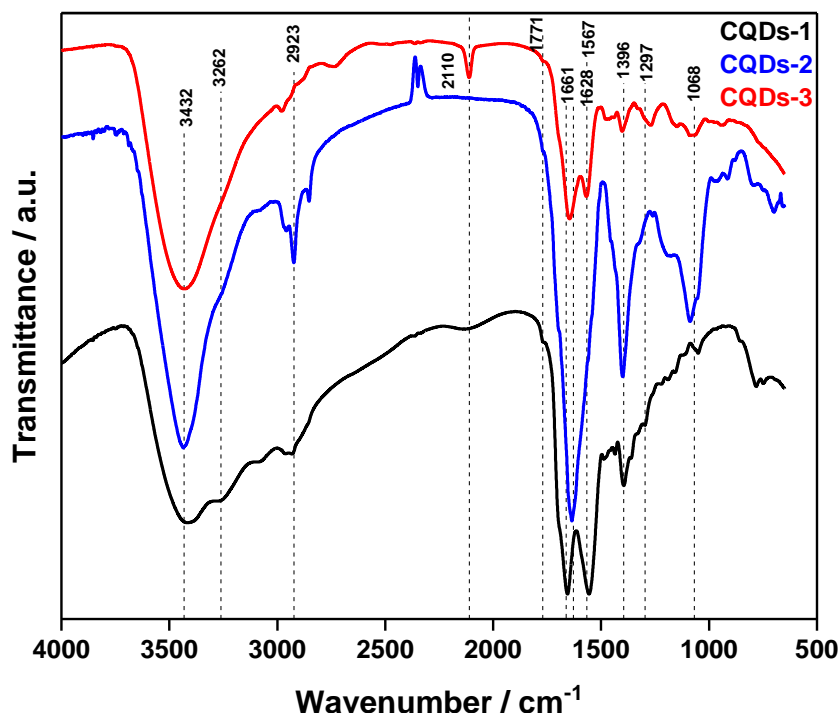


**Figure 2.8: Characterisation of CQDs:** FTIR spectra of as-prepared CQDs-1 (black), CQDs-2 (blue), CQDs-3 (red).

Modifications that have been made in order to enable the incorporation of peptide amides on the surface of as-prepared carbon dots were verified by FTIR and XPS. First one includes the conversion of amine groups presented on the surface into carboxyl capped carbon dots [50, 51]. Briefly, the amino groups reacted with  $\text{ClCH}_2\text{COONa}$  under strongly alkaline conditions. The suspension was further neutralised, resulting in CQDs-COOH (**CQDs-2**). As observed in the FTIR spectra, the sharp peak at around  $1650\text{ cm}^{-1}$  was enhanced, which indicates that plenty of carboxyl groups were introduced after the treatment of **CQDs-1**. The increase in the oxygen content for **CQDs-2** compared to **CQDs-1** is 26.87% and 14.94% respectively, strongly indicating the successful introduction of additional carboxyl groups. Additionally, we can observe an increase in negative zeta potential and hydrodynamic diameter (**Table 2.2**). Moreover, the quantum yield decreased significantly which can be attributed to the increase of electron withdrawing carboxyl groups (QY= 7% (0.038) using quinine sulphate as a reference; QY, 0.54 in 0.12 M  $\text{H}_2\text{SO}_4$ ).

In case of **CQDs-3**, the successful formation of azide groups on the surface of nanoparticles was confirmed by the appearance of the band at  $2110\text{ cm}^{-1}$  corresponding to  $\nu_{\text{as}}(\text{N}_3)$  (**Figure 2.8**) and further verified by XPS which revealed the presence of the peak  $405.2\text{ eV}$  ( $-\text{N}=\text{N}^+=\text{N}^-$ ) and  $401.6\text{ eV}$  ( $\text{N}=\text{N}^+=\text{N}^-$ ) in a ratio of 1:2, as theoretically expected



(Figure 2.9B). In addition, we can observe the increase in the atomic percentage of the N1s component as well as the increase in the potential on the surface from -9.9 for CQDs-1 to +7 for CQDs-3 (Table 2.2). Furthermore, we decided to quantify the free amino group on the surface of CQDs before and after the modification with the technique of so-called Keiser test. The Keiser test makes the use of the formation of Ruhemann's Blue by the reaction of ninhydrin with the primary amino groups. The successful implementation of this colorimetric assay on the nanoparticles has been already reported [52]. We can see than the modification made on CQDs-1 caused a decrease in the amount of free amino groups in both CQDs-2 and CQDs-3. It may indicate the success of converting the surface from amino into carboxyl groups and successful coupling of azido moieties. It is also giving us more information about possible loading efficiency.

**Table 2.2:** Physicochemical properties of nanostructures

Particles	$\zeta$ (mV) <sup>1</sup>	Size (nm)	Hydrodynamic size (nm) <sup>2</sup>	PDI	C1s	O1s	N1s	Surface loading mmol/g Keiser test
CQDs-1	-9.9 ± 3.4	4.5±0.2	11 ± 0.1	0.22±0.11	72.62	14.94	12.43	0.144
CQDs-2	-27 ±2.1	5.75±0.78	17± 2	0.357±0.2	68.89	26.87	4.23	0.0445
CQDs-3	7.14±3	5.5 ± 0.3	12 ± 0.1	0.23 ± 0.11	68.8	13.9	17.3	0.055

<sup>1</sup> $\zeta$ : zeta potential, PDI Polydispersity index; <sup>2</sup>the hydrodynamic size was recorded at 37°C

The modification of nanodiamonds with azide moiety was based on the same principle as CQDs with the use of different coupling reagents. The successful coupling was confirmed by FTIR and XPS. (Figure 2.9A) shows the transmission FTIR spectra of commercially available ND-NH<sub>2</sub> (ND-2) and modified nanodiamonds (ND-3). The presence of the broadband between 3000-3600 cm<sup>-1</sup> corresponds to the vibrational mode of amino groups presented on the surface and adsorbed water molecules. The peak at 1632 cm<sup>-1</sup> can be assigned to a superposition of N-H scissoring mode and OH deformation mode of adsorbed water. After the surface modification, an intense peak at 2124cm<sup>-1</sup> appears, which is characteristic for  $\nu_{as}(N_3)$  stretching mode. Additionally, new bands appeared at 1600, 1376, 1286, and 1174 cm<sup>-1</sup> that correspond to the same observed bands present in an FTIR spectrum of neat 4-azidobenzoic acid (data not shown). In addition to FTIR, XPS analysis was performed to characterise and confirm the modification. Deconvolution of high resolution N1s spectrum (Figure 2.7B) reveals the presence of azide function by the signals at 405.2eV and 401.6eV in a 1:2 ration, comparable to the XPS spectra generated for CDots-3.

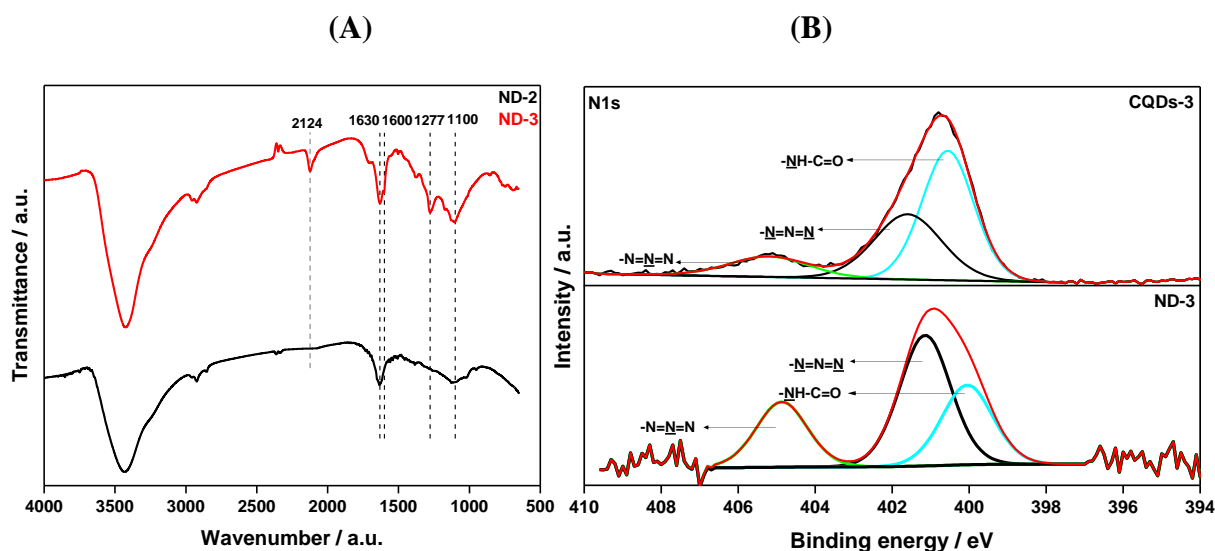


**Figure 2.9:** (A) FTIR of ND-2, ND-3; (B) High resolution N1s XPS spectrum of CQDs-3 (up) and ND-3 (down).

**Table 2.2:** Physical properties of nanodiamonds (ND-2; ND-3)

Particles	$\zeta$ (mV) <sup>1</sup>	Hydrodynamic size (nm) <sup>2</sup>	PDI
ND-2	18 ± 3	134 ± 7	0.35 ± 0.02
ND-3	24 ± 3	183 ± 5	0.34 ± 0.10

<sup>1</sup> $\zeta$ : zeta potential, PDI Polydispersity index;

## 2.4. Subsequent post functionalization of carbon nanostructures: Nanoparticles- peptide bioconjugates

We decided to use two different approaches to prepare nanoparticle-peptide conjugates (**Figure 2.10**). First, consists of a standard coupling reaction using carboxyl groups presented on the surface of carbon nanomaterial and creation of amide bond between the peptides. As prepared peptides comprised of 2 or 3 arginine residues and C-terminal was created as amid. Which gives us multiple binding sites on the peptide chain. Therefore, to gain more control of the reaction, we decided to introduce an alkyne in the sequence of the peptides which together with an azide moiety presented on nanoparticles allow us to “click” the molecules together. Cu(I) catalysed azide-alkyne cycloaddition (CuAAC- click reaction) is stereospecific forming 1,4-substituted 1,2,3-triazole and is relatively fast even at low temperature resulting in high yield products.



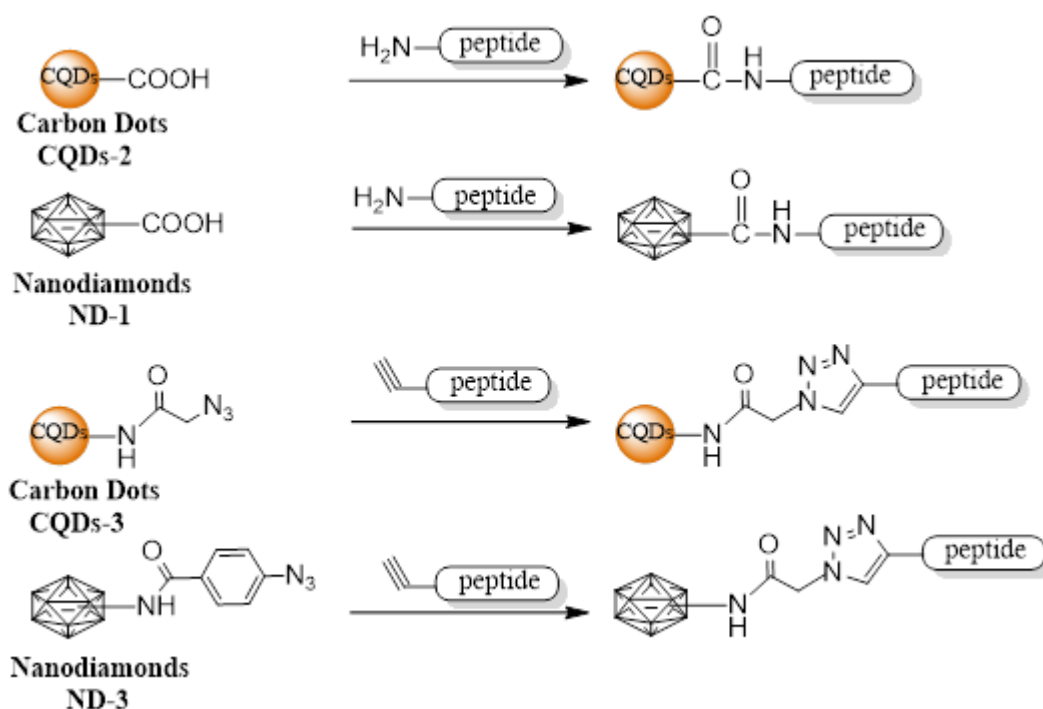


**Figure 2.10:** Schematic illustration of surface functionalization used in this section.

The preparation of **CQDs-peptides (1a-3b)** is based on a two-step process. The first step was the conversion of the amino coated surface into carboxyl capped **CQDs-2**. **CQDs-2** has further reacted with peptide amide with the use of N-Ethyl-N'-(3-dimethyl aminopropyl)carbodiimide hydrochloride (EDC•HCl) and N-hydroxysuccinimide (NHS) as coupling reagents. The reaction was carried out in a buffer solution at physiological pH and resulted in well dispersible carbon-conjugates. On the FTIR spectra (**Figure 2.11A**) we can see the peak at  $3450\text{ cm}^{-1}$  has broadened due to additional symmetric stretching vibration mode of -NH. Additionally, a new band appears at  $1530\text{ cm}^{-1}$  which corresponds to the symmetric bending vibration of -NH commonly presented in amino acids. In the (**Table 2.3**), we can see the changes in zeta potential and hydrodynamic diameter of as-prepared particles. Charge of the modified carbon dots, changes towards more positive values in the case of all the compounds. However, the changes are not as significant as expected. The hydrodynamic diameter increases from  $68\pm 2.1$  to be within the range of 137-157nm, which is probably the result of the formation of aggregated structures. Surprisingly the calculated quantum yields do not differ significantly from **CQDs-2** reflecting that the modifications barely altered the inherent emission features of **CQDs-COOH**.

For the preparation of ND-peptides, we decided to use commercially available **ND-COOH**. For the coupling of the peptides, we chose N,N'-Diisopropylcarbodiimide (DIC) and

Hydroxybenzotriazole (HOBt). The FTIR spectrum (**Figure 2.11B**) of as-prepared NDs conjugates show similar features to the one of CQDs. The band at around  $3450\text{cm}^{-1}$  is broadened due to appearance of the stretching mode of  $-\text{NH}$ . Additionally, new bands appeared at  $1534\text{ cm}^{-1}$ ,  $1200\text{cm}^{-1}$ ,  $1135\text{ cm}^{-1}$  which are attributed to stretching vibration and stretching rocking mode of  $-\text{NH}$ . For the conjugates **ND-1.2a** and **ND-1.3a** we can observe an appearance of additional bands at  $837\text{cm}^{-1}$  and  $802\text{cm}^{-1}$  which might be attributed to the presence of metallocenoyl group on the surface of the particles. Similarly, to CQDs, the surface potential of nanodiamonds changes towards less negative values but remaining negative. The hydrodynamic diameter increases from  $78\pm 2.3$  to ranging between  $147\text{-}167\text{nm}$ .

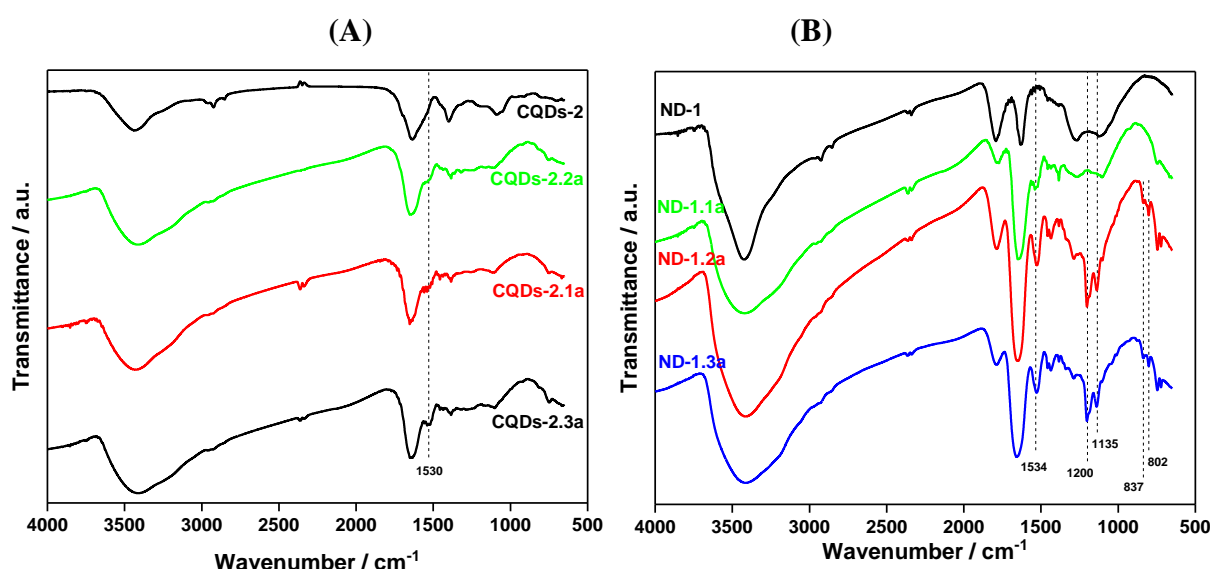


**Figure 2.11:** (A) FTIR spectra of CQDs-peptides (CQDs-2.1a, CQDs-2.2a, CQDs-2.3a); (B) FTIR spectra of ND-peptides (ND-1.1a, ND-1.2a, ND-1.3a) bioconjugates.

**Table 2.3:** Physicochemical properties of carbon-conjugates

Particles	$\zeta$ (mV) <sup>1</sup>	Hydrodynamic size (nm)	PDI	Loading $\mu\text{g}/\text{mg}$	QY (%)
CQDs-2	$-27 \pm 2$	$68 \pm 2.1$	$0.24 \pm 0.13$	-	7
CQDs-2.1a	$2 \pm 0.4$	$141 \pm 2.5$	$0.21 \pm 0.09$	134	6.54
CQDs-2.1b	$2 \pm 0.5$	$137 \pm 1.7$	$0.17 \pm 0.10$	115	6.72
CQDs-2.2a	$-2 \pm 0.3$	$153 \pm 2.4$	$0.14 \pm 0.04$	98	6.1
CQDs-2.2b	$0.5 \pm 0.3$	$157 \pm 3.6$	$0.51 \pm 0.09$	103	6.3
CQDs-2.3a	$-2 \pm 0.8$	$149 \pm 3.2$	$0.42 \pm 0.02$	95	6.41
CQDs-2.3b	$-0.4 \pm 0.7$	$147 \pm 4.6$	$0.33 \pm 0.41$	97	6.44
ND-1	$-45 \pm 2$	$78 \pm 3$	$0.19 \pm 0.02$	-	-
ND-1.1a	$-25 \pm 2$	$154 \pm 2$	$0.14 \pm 0.02$	284	-
ND-1.1b	$-17 \pm 3$	$147 \pm 3.5$	$0.16 \pm 0.03$	292	-
ND-1.2a	$-19 \pm 3$	$161 \pm 4.1$	$0.17 \pm 0.02$	266	-
ND-1.2b	$-15 \pm 3$	$167 \pm 3$	$0.17 \pm 0.02$	268	-
ND-1.3a	$-20 \pm 2$	$159 \pm 2$	$0.18 \pm 0.02$	275	-
ND-1.3b	$-15 \pm 3$	$160 \pm 2.7$	$0.18 \pm 0.02$	267	-

<sup>1</sup> $\zeta$  : zeta potential, PDI Polydispersity index;

The formation of the click conjugates for both carbon structure was performed in the same way using copper sulphate pentahydrate and ascorbic acid as catalysts for the reaction. In both cases, the process was accomplished in two steps. The first step consists of the introduction of the azide molecule on the surface of the nanoparticles, and the second step was achieved by using a previously prepared “clickable” peptides. The successful modification can be easily followed by the disappearance of the band at  $2100\text{ cm}^{-1}$  for CQDs (**Figure 2.12A**) and  $2123\text{ cm}^{-1}$  for ND (**Figure 2.12B**). Additionally, for CQDs containing metallocene moieties, the characteristic band at  $3071\text{ cm}^{-1}$  was observed. The band at  $1200\text{ cm}^{-1}$  and  $1130\text{ cm}^{-1}$  are attributed to stretching rocking mode of  $\text{-NH}$ . For ND, the band assigned to stretching vibrations of  $\text{-NH}$  appears at  $1540\text{ cm}^{-1}$ .

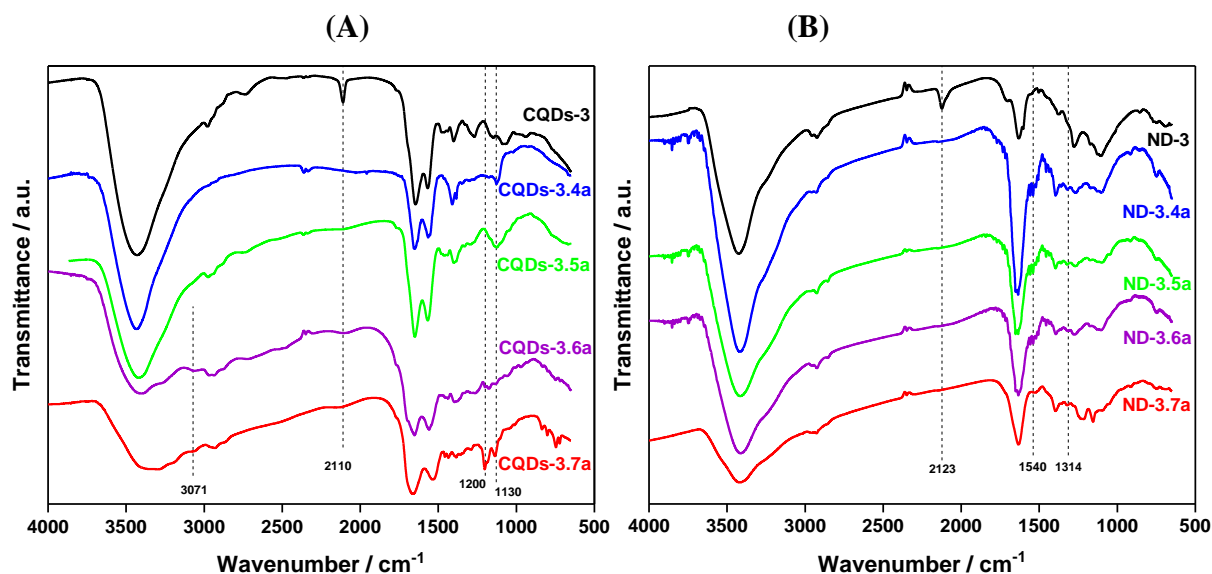


**Figure 2.12:** (A) FTIR spectra of CQDs-peptides (CQDs-3.4a, CQDs-3.5a, CQDs-3.6a, CQDs-3.7a); (B) FTIR spectra of ND-peptides (ND-3.4a, ND-3.5a, ND-3.6a, ND-3.7a) bioconjugates.

Following the changes in the zeta potential of the particles (**Table 2.4**), we can assume that the cationic peptide is incorporated on the surface, and its charge is not altered by additional interactions. For CQDs, the potential changes from  $7\pm3$  up to  $26\pm1$  and for all the particles stay in the same range. ND showed a higher charge on the surface, which is influenced by higher loading of the cationic peptide on the surface. As expected, the hydrodynamic diameter increases for all prepared nanoconjugates indicating the successful incorporation of peptides. In the case of CQDs click particles, another factor indicating the success of the reaction is the decrease in the quantum yield. The changes are quite significant, decreasing from 33% for CQDs-3 to get as low as 9.8% after the modification. It is worth to notice that the peptides “b” are the reverse sequence of peptides “a” showing the same FTIR spectra.

**Table 2.4:** Physicochemical properties of carbon conjugates: “clicked” nanoparticles

Particles	$\zeta$ (mV) <sup>1</sup>	Hydrodynamic size (nm)	PDI	Loading $\mu\text{g}/\text{mg}$	QY (%)
CQDs-3	7 $\pm$ 3	71 $\pm$ 4	0.24 $\pm$ 0.13	-	34
CQDs-3.4a	21 $\pm$ 2	181 $\pm$ 2	0.28 $\pm$ 0.09	94	10
CQDs-3.4b	26 $\pm$ 1	175 $\pm$ 3	0.22 $\pm$ 0.08	95	13
CQDs-3.5a	23 $\pm$ 1	179 $\pm$ 4	0.19 $\pm$ 0.05	101	14
CQDs-3.5b	25 $\pm$ 2	158 $\pm$ 2	0.20 $\pm$ 0.10	103	11
CQDs-3.6a	19 $\pm$ 2	198 $\pm$ 3	0.34 $\pm$ 0.09	100	9.8
CQDs-3.6b	22 $\pm$ 2	191 $\pm$ 4	0.32 $\pm$ 0.13	97	10
CQDs-3.7a	21 $\pm$ 3	193 $\pm$ 3	0.31 $\pm$ 0.11	99	15
CQDs-3.7b	24 $\pm$ 1	190 $\pm$ 3	0.34 $\pm$ 0.15	96	14.7
ND-2	18 $\pm$ 3	134 $\pm$ 7	0.35 $\pm$ 0.02	-	-
ND-3	24 $\pm$ 3	183 $\pm$ 5	0.34 $\pm$ 0.10	-	-
ND-3.4a	34 $\pm$ 3	213 $\pm$ 4	0.36 $\pm$ 0.02	243	-
ND-3.4b	33 $\pm$ 3	234 $\pm$ 6	0.36 $\pm$ 0.02	239	-
ND-3.5a	33 $\pm$ 3	219 $\pm$ 2	0.34 $\pm$ 0.04	257	-
ND-3.5b	29 $\pm$ 3	229 $\pm$ 3	0.39 $\pm$ 0.10	256	-
ND-3.6a	28 $\pm$ 3	261 $\pm$ 5	0.41 $\pm$ 0.09	261	-
ND-3.6b	29 $\pm$ 3	267 $\pm$ 7	0.40 $\pm$ 0.07	273	-
ND-3.7a	31 $\pm$ 2	253 $\pm$ 6	0.39 $\pm$ 0.15	269	-
ND-3.7b	30 $\pm$ 2	249 $\pm$ 8	0.4 $\pm$ 0.11	258	-

<sup>1</sup> $\zeta$ : zeta potential, PDI Polydispersity index;

## 2.5. Antibacterial activity of carbon-based conjugates

The antibacterial activity of all the compounds was assessed by determining their MIC values by microdilution assay. MIC value is the lowest concentration of an antimicrobial that will inhibit the visible growth of a microorganism after overnight incubation. In this work, one Gram-negative (*E.coli* DSM 30038) and one Gram-positive (*S.aureus* ATCC 43300), the bacterial strain was used.

The first group of compounds where the peptides were covalently linked showed no antibacterial activity against studied bacterial strains (conjugates: **1a-3b**) (Table 2.5). Peptides used in this study owe their antibacterial properties to charge and lipophilic bulk. The unprotected guanidine groups on the arginine side chain could react with the nanoparticles during the coupling, resulting in the loss of the positive charge and increase lipophilicity. This indicates the importance of preserving these groups during the reaction.

**Table 2.5:** Antibacterial properties of carbon nanomaterials (CQDs-1; CQDs-2; ND-1) and covalently modified carbon-peptides conjugates (CQDs-2.1a- CQDs-2.3b; ND-1.1a- ND-1.3b).

Compound	Sequence	MIC [ $\mu\text{g/ml}$ ]	MIC [ $\mu\text{g/ml}$ ]
		<i>E.coli</i> DSM 30083	<i>S.aureus</i> (MRSA) ATCC 43300
CQDs-1	-	n.a.	n.a.
CQDs-2	-	n.a.	n.a.
CQDs-2.1a	H-RWRWRW-NH <sub>2</sub>	n.a.	n.a.
CQDs-2.1b	H-WRWRWR-NH <sub>2</sub>	n.a.	n.a.
CQDs-2.2a	FcCO-WRWRW-NH <sub>2</sub>	n.a.	n.a.
CQDs-2.2b	FcCO-RWRWR-NH <sub>2</sub>	n.a.	n.a.
CQDs-2.3a	RcCO-WRWRW-NH <sub>2</sub>	n.a.	n.a.
CQDs-2.3b	RcCO-RWRWR-NH <sub>2</sub>	n.a.	n.a.
ND-1	-	n.a.	n.a.
ND-1.1a	H-RWRWRW-NH <sub>2</sub>	n.a.	n.a.
ND-1.1b	H-WRWRWR-NH <sub>2</sub>	n.a.	n.a.
ND-1.2a	FcCO-WRWRW-NH <sub>2</sub>	n.a.	n.a.
ND-1.2b	FcCO-RWRWR-NH <sub>2</sub>	n.a.	n.a.
ND-1.3a	RcCO-WRWRW-NH <sub>2</sub>	n.a.	n.a.
ND-1.3b	RcCO-RWRWR-NH <sub>2</sub>	n.a.	n.a.

n.a.: not active

To overcome this problem and protect the positive charge of the peptides, click chemistry was developed to link AMPs to the nanostructures. Increased antibacterial activity of the conjugates (**Table 2.6**) revealed the multivalent character of carbon nanostructures.

For the conjugates prepared by the “click” reaction, the activity is in general higher for Gram-positive bacteria. However, for some compounds, the activity for Gram-negative *E.coli* has been significantly increased. For carbon dots conjugates (**CQDs-3.4a**; **CQDs-3.4b**; **CQDs-3.5a**; **CQDs-3.5b**) we can observe 5 fold increase of activity and 4-fold increase in case of nanodiamonds (**ND-3.4a**; **ND-3.4b**; **ND-3.5a**; **ND-3.5b**) with the MIC values ranging between  $6.02\mu\text{g mL}^{-1}$ -  $6.59\mu\text{g mL}^{-1}$  (CQDs) and  $7.65\mu\text{g mL}^{-1}$  –  $8.22\mu\text{g mL}^{-1}$  (NDs) respectively. The additional amino acid and the position of the propargyl group does not seem to alter the MIC values. This contrast to the presence of the metallocene group (conjugates: **6a-7b**) where the activity in case of ND was slightly decreased, and carbon dots showed no activity in the studied range.

Considering Gram-positive bacteria *S.aureus* (MRSA) 5-fold increase for carbon dots and a 4-fold increase in the activity is also observed (**conjugates: 6a-7b**). In the case of peptides containing ferrocene or ruthenocene, the activity increases 3-fold for CQDs being approx.  $12\mu\text{g mL}^{-1}$  with an exception for compound **CQDs-3.7a** where the MIC value ( $6.34\mu\text{g mL}^{-1}$ ) is close to the value of the free peptide ( $8\mu\text{g mL}^{-1}$ ). Nanodiamond conjugates showed a 2-fold increase in case of **ND-3.6b** and **ND-3.7b**, no significant difference for **ND-3.6a** and decreased

activity for the compound **ND-3.7a** was observed. Lower activity compared to CQDs can be attributed to the higher loading of ND, resulting in a higher amount of ferrocene/ ruthenocene presented on the surface. Therefore, increasing the lipophilicity of the compounds.

Additionally, CuSO<sub>4</sub> that was used as a catalyst during the click reaction (compounds **4a-7b**) was tested, showing no inhibition of growth in case of both bacterial strains.

**Table 2.6:** Antibacterial properties of carbon nanostructures (CQDs-3, ND-3) and carbon nanoconjugates prepared by Cu(I) catalysed azide-alkyne cycloaddition (CuAAC) (CQDs-3.4a-3.7b; ND-3.4a-ND-3.7b). MIC value for the conjugates: [μg/ml] NP // [μg/ml] of the peptide conjugated on the surface

Compound	Sequence	MIC [μg/ml]	
		Gram-negative <i>E.coli</i> DSM 30083	Gram-positive <i>S.aureus</i> (MRSA) ATCC 43300
<b>CQDs-3</b>	-	n.a.	n.a.
<b>4a</b>	<b>CHC</b> CH <sub>2</sub> CH <sub>2</sub> C(O)-RWRWRW-NH <sub>2</sub>	<b>32</b>	<b>16</b>
<b>CQDs-3.4a</b>	<b>CHC</b> CH <sub>2</sub> CH <sub>2</sub> C(O)-RWRWRW-NH <sub>2</sub>	64 // <b>6.02</b>	32 // <b>3.01</b>
<b>4b</b>	<b>CHC</b> CH <sub>2</sub> CH <sub>2</sub> C(O)-WRWRWR-NH <sub>2</sub>	<b>32</b>	<b>16</b>
<b>CQDs-3.4b</b>	<b>CHC</b> CH <sub>2</sub> CH <sub>2</sub> C(O)-WRWRWR-NH <sub>2</sub>	64 // <b>6.08</b>	32 // <b>3.04</b>
<b>5a</b>	H-RWRWRWG(CH <sub>2</sub> <b>CCH</b> )-NH <sub>2</sub>	<b>32</b>	<b>16</b>
<b>CQDs-3.5a</b>	H-RWRWRWG(CH <sub>2</sub> <b>CCH</b> )-NH <sub>2</sub>	64 // <b>6.46</b>	32 // <b>3.23</b>
<b>5b</b>	H-WRWRWRWG(CH <sub>2</sub> <b>CCH</b> )-NH <sub>2</sub>	<b>32</b>	<b>16</b>
<b>CQDs-3.5b</b>	H-WRWRWRWG(CH <sub>2</sub> <b>CCH</b> )-NH <sub>2</sub>	64 // <b>6.59</b>	32 // <b>3.3</b>
<b>6a</b>	FcCO-WRWRWG(CH <sub>2</sub> <b>CCH</b> )-NH <sub>2</sub>	<b>64</b>	<b>32</b>
<b>CQDs-3.6a</b>	FcCO-WRWRWG(CH <sub>2</sub> <b>CCH</b> )-NH <sub>2</sub>	512 // <b>51.2</b> >	128 // <b>12.8</b>
<b>6b</b>	FcCO-RWRWRWG(CH <sub>2</sub> <b>CCH</b> )-NH <sub>2</sub>	<b>128</b>	<b>32</b>
<b>CQDs-3.6b</b>	FcCO-RWRWRWG(CH <sub>2</sub> <b>CCH</b> )-NH <sub>2</sub>	512 // <b>49.7</b> >	128 // <b>12.4</b>
<b>7a</b>	RcCO-WRWRWG(CH <sub>2</sub> <b>CCH</b> )-NH <sub>2</sub>	<b>128</b>	<b>8</b>
<b>CQDs-3.7a</b>	RcCO-WRWRWG(CH <sub>2</sub> <b>CCH</b> )-NH <sub>2</sub>	512 // <b>50.07</b> >	64 // <b>6.34</b>
<b>7b</b>	RcCO-RWRWRWG(CH <sub>2</sub> <b>CCH</b> )-NH <sub>2</sub>	<b>128</b>	<b>32</b>
<b>CQDs-3.7b</b>	RcCO-RWRWRWG(CH <sub>2</sub> <b>CCH</b> )-NH <sub>2</sub>	512 // <b>50.07</b> >	128 // <b>12.7</b>
<b>ND-3</b>	-	n.a.	n.a.
<b>4a</b>	<b>CHC</b> CH <sub>2</sub> CH <sub>2</sub> C(O)-RWRWRW-NH <sub>2</sub>	<b>32</b>	<b>16</b>
<b>ND-3.4a</b>	<b>CHC</b> CH <sub>2</sub> CH <sub>2</sub> C(O)-RWRWRW-NH <sub>2</sub>	32 // <b>7.78</b>	16 // <b>3.89</b>
<b>4b</b>	<b>CHC</b> CH <sub>2</sub> CH <sub>2</sub> C(O)-WRWRWR-NH <sub>2</sub>	<b>32</b>	<b>16</b>
<b>ND-3.4b</b>	<b>CHC</b> CH <sub>2</sub> CH <sub>2</sub> C(O)-WRWRWR-NH <sub>2</sub>	32 // <b>7.65</b>	16 // <b>3.82</b>
<b>5a</b>	H-RWRWRWG(CH <sub>2</sub> <b>CCH</b> )-NH <sub>2</sub>	<b>32</b>	<b>16</b>
<b>ND-3.5a</b>	H-RWRWRWG(CH <sub>2</sub> <b>CCH</b> )-NH <sub>2</sub>	32 // <b>8.22</b>	16 // <b>4.11</b>
<b>5b</b>	H-WRWRWRWG(CH <sub>2</sub> <b>CCH</b> )-NH <sub>2</sub>	<b>32</b>	<b>16</b>
<b>ND-3.5b</b>	H-WRWRWRWG(CH <sub>2</sub> <b>CCH</b> )-NH <sub>2</sub>	32 // <b>8.19</b>	16 // <b>4.1</b>
<b>6a</b>	FcCO-WRWRWG(CH <sub>2</sub> <b>CCH</b> )-NH <sub>2</sub>	<b>64</b>	<b>32</b>
<b>ND-3.6a</b>	FcCO-WRWRWG(CH <sub>2</sub> <b>CCH</b> )-NH <sub>2</sub>	512 // <b>134</b> >	128 // <b>33.4</b>
<b>6b</b>	FcCO-RWRWRWG(CH <sub>2</sub> <b>CCH</b> )-NH <sub>2</sub>	<b>128</b>	<b>32</b>
<b>ND-3.6b</b>	FcCO-RWRWRWG(CH <sub>2</sub> <b>CCH</b> )-NH <sub>2</sub>	512 // <b>140</b> >	64 // <b>17.5</b>
<b>7a</b>	RcCO-WRWRWG(CH <sub>2</sub> <b>CCH</b> )-NH <sub>2</sub>	<b>128</b>	<b>8</b>
<b>ND-3.7a</b>	RcCO-WRWRWG(CH <sub>2</sub> <b>CCH</b> )-NH <sub>2</sub>	512 // <b>138</b> >	64 // <b>17.2</b>
<b>7b</b>	RcCO-RWRWRWG(CH <sub>2</sub> <b>CCH</b> )-NH <sub>2</sub>	<b>128</b>	<b>32</b>
<b>ND-3.7b</b>	RcCO-RWRWRWG(CH <sub>2</sub> <b>CCH</b> )-NH <sub>2</sub>	512 // <b>132</b> >	64 // <b>16.5</b>

Indicated in **orange**: alkyne group necessary for the click reaction; Indicated in **blue**: conjugates that showed increased antibacterial activity.

## 2.6. Conclusions

A set of 28 different carbon- peptide nanostructure conjugates were successfully prepared, and their antibacterial activity was assessed by determining the MIC values against Gram-negative *E.coli* DSM 30083 and *S.aureus* ATCC 43300. The first group of compounds obtained by covalent linking showed no antibacterial activity against studied strains (conjugates: **1a-3b**) while the second group where click chemistry was applied (conjugates: **4a-7b**) showed a significant decrease in the minimal inhibitory concentrations for Gram-negative and Gram-positive bacteria. Amongst them, conjugates **4a-5b** showed the best MIC values for the tested strains being 5-fold lower for peptide modified CQDs and 4-fold higher for peptide modified ND when compared to the peptide in solution.

The lack of activity in some particle-conjugates in the tested range is associated with the molecules loaded on the surface rather than particles themselves. The data collected in the (Table 2.3) and (Table 2.5) indicate that charge is a significant factor in the antibacterial activity. Even though the zeta potentials were decreased towards less negative charges indicating successful incorporation of peptides, it did not increase as much as expected, like for the “clicked” compounds suggesting that some if not all of the positive charge in the backbone of the loaded peptides was blocked.

In addition, it was shown that the position of the propargyl group, as well as the reverse order of amino acids in the sequence, does not influence the activity of tested compounds. This contrast the results obtained for the conjugates where the organometallic moiety was present. The presence of ferrocene or ruthenocene results in loss of activity for the Gram-negative bacteria and only 2-3 fold higher for Gram-positive *S.aureus* with an exception for the conjugate **7a** where the MIC value did not improve. This might be explained by the increased lipophilicity on the surface of nanoparticles due to the presence of ferrocene or ruthenocene. Which indicated that the existence of organometallic moiety in case of as prepared conjugates is not favourable and better MIC values are obtained for the “simple” peptides.



## 2.7. References

1. Cheng, G., et al., *Antimicrobial Drugs in Fighting against Antimicrobial Resistance*. Frontiers in microbiology, 2016. **7**: p. 470-470.
2. O'Neill, J. *Antimicrobial Resistance: Tackling a crisis for the health and wealth of nations*. December 2014; Available from: <https://amr-review.org/Publications.html>.
3. Huh, A.J. and Y.J. Kwon, "Nanoantibiotics": *A new paradigm for treating infectious diseases using nanomaterials in the antibiotics resistant era*. Journal of Controlled Release, 2011. **156**(2): p. 128-145.
4. Weir, E., et al., *The use of nanoparticles in anti-microbial materials and their characterization*. Analyst, 2008. **133**(7): p. 835-845.
5. Allaker, R.P. and G. Ren, *Potential impact of nanotechnology on the control of infectious diseases*. Transactions of The Royal Society of Tropical Medicine and Hygiene, 2008. **102**(1): p. 1-2.
6. Li, Q., et al., *Antimicrobial nanomaterials for water disinfection and microbial control: Potential applications and implications*. Water Research, 2008. **42**(18): p. 4591-4602.
7. Mühling, M., et al., *An investigation into the effects of silver nanoparticles on antibiotic resistance of naturally occurring bacteria in an estuarine sediment*. Marine Environmental Research, 2009. **68**(5): p. 278-283.
8. Pal, S., Y.K. Tak, and J.M. Song, *Does the Antibacterial Activity of Silver Nanoparticles Depend on the Shape of the Nanoparticle? A Study of the Gram-Negative Bacterium <em>Escherichia coli</em>*. Applied and Environmental Microbiology, 2007. **73**(6): p. 1712.
9. Huang, Z., et al., *Toxicological Effect of ZnO Nanoparticles Based on Bacteria*. Langmuir, 2008. **24**(8): p. 4140-4144.
10. Kim, J.S., et al., *Antimicrobial effects of silver nanoparticles*. Nanomedicine: Nanotechnology, Biology and Medicine, 2007. **3**(1): p. 95-101.
11. Rabea, E.I., et al., *Chitosan as Antimicrobial Agent: Applications and Mode of Action*. Biomacromolecules, 2003. **4**(6): p. 1457-1465.
12. Zhang, L., et al., *Development of Nanoparticles for Antimicrobial Drug Delivery*. Current Medicinal Chemistry, 2010. **17**(6): p. 585-594.
13. Zhang, L., et al., *Nanoparticles in Medicine: Therapeutic Applications and Developments*. Clinical Pharmacology & Therapeutics, 2008. **83**(5): p. 761-769.
14. Santos-Magalhães, N.S. and V.C.F. Mosqueira, *Nanotechnology applied to the treatment of malaria*. Advanced Drug Delivery Reviews, 2010. **62**(4): p. 560-575.
15. Mengesha, A.E. and B.B.C. Youan, *8 - Nanodiamonds for drug delivery systems*, in *Diamond-Based Materials for Biomedical Applications*, R. Narayan, Editor. 2013, Woodhead Publishing. p. 186-205.
16. Szunerits, S., A. Barras, and R. Boukherroub, *Antibacterial Applications of Nanodiamonds*. International journal of environmental research and public health, 2016. **13**(4): p. 413-413.
17. Mishra, V., et al., *Carbon dots: emerging theranostic nanoarchitectures*. Drug Discovery Today, 2018. **23**(6): p. 1219-1232.
18. Zheng, M., et al., *Integrating Oxaliplatin with Highly Luminescent Carbon Dots: An Unprecedented Theranostic Agent for Personalized Medicine*. Advanced Materials, 2014. **26**(21): p. 3554-3560.

19. Moore, L., et al., *Biocompatibility Assessment of Detonation Nanodiamond in Non-Human Primates and Rats Using Histological, Hematologic, and Urine Analysis*. ACS Nano, 2016. **10**(8): p. 7385-7400.
20. Zhu, Y., et al., *The biocompatibility of nanodiamonds and their application in drug delivery systems*. Theranostics, 2012. **2**(3): p. 302.
21. Marcon, L., et al., *Cellular and in vivo toxicity of functionalized nanodiamond in Xenopus embryos*. Journal of Materials Chemistry, 2010. **20**(37): p. 8064-8069.
22. Liu, K.-K., et al., *Biocompatible and detectable carboxylated nanodiamond on human cell*. Nanotechnology NANOTECHNOLOGY Nanotechnology, 2007. **18**71: p. 325102-10.
23. Krueger, A. and D. Lang, *Functionality is key: recent progress in the surface modification of nanodiamond*. Advanced Functional Materials, 2012. **22**(5): p. 890-906.
24. Krueger, A., *New Carbon Materials: Biological Applications of Functionalized Nanodiamond Materials*. Chemistry – A European Journal, 2008. **14**(5): p. 1382-1390.
25. Mochalin, V.N., et al., *The properties and applications of nanodiamonds*. Nature Nanotechnology, 2012. **7**(1): p. 11-23.
26. Yang, S.-T., et al., *Carbon Dots for Optical Imaging in Vivo*. Journal of the American Chemical Society, 2009. **131**(32): p. 11308-11309.
27. Wei, W., et al., *Non-Enzymatic-Browning-Reaction: A Versatile Route for Production of Nitrogen-Doped Carbon Dots with Tunable Multicolor Luminescent Display*. Scientific Reports, 2014. **4**: p. 3564.
28. Weng, C.-I., et al., *One-step synthesis of biofunctional carbon quantum dots for bacterial labeling*. Biosensors and Bioelectronics, 2015. **68**: p. 1-6.
29. Wang, Q., et al., *Hollow luminescent carbon dots for drug delivery*. Carbon, 2013. **59**: p. 192-199.
30. Lai, C.-W., et al., *Facile synthesis of highly emissive carbon dots from pyrolysis of glycerol; gram scale production of carbon dots/mSiO<sub>2</sub> for cell imaging and drug release*. Journal of Materials Chemistry, 2012. **22**(29): p. 14403-14409.
31. Gogoi, N. and D. Chowdhury, *Novel carbon dot coated alginate beads with superior stability, swelling and pH responsive drug delivery*. Journal of Materials Chemistry, 2014. **2**: p. 4089.
32. Thakur, M., et al., *Antibiotic Conjugated Fluorescent Carbon Dots as a Theranostic Agent for Controlled Drug Release, Bioimaging, and Enhanced Antimicrobial Activity*. Journal of Drug Delivery, 2014. **2014**: p. 9.
33. Sarkar, N., et al., *Carbon quantum dot tailored calcium alginate hydrogel for pH responsive controlled delivery of vancomycin*. European Journal of Pharmaceutical Sciences, 2017. **109**: p. 359-371.
34. Shai, Y., *Mode of action of membrane active antimicrobial peptides*. Peptide Science, 2002. **66**(4): p. 236-248.
35. Zhang, L.J., A. Rozek, and R. Hancock, *Interaction of Cationic Antimicrobial Peptides with Model Membranes*. The Journal of biological chemistry, 2001. **276**: p. 35714-22.
36. Jenssen, H., P. Hamill, and R.E.W. Hancock, *Peptide Antimicrobial Agents*. Clinical Microbiology Reviews, 2006. **19**(3): p. 491.
37. Brogden, K.A., *Antimicrobial peptides: pore formers or metabolic inhibitors in bacteria?* Nature Reviews Microbiology, 2005. **3**(3): p. 238-250.
38. Brumfitt, W., M.R.J. Salton, and J.M.T. Hamilton-Miller, *Nisin, alone and combined with peptidoglycan-modulating antibiotics: activity against methicillin-resistant*

- Staphylococcus aureus* and vancomycin-resistant enterococci. Journal of Antimicrobial Chemotherapy, 2002. **50**(5): p. 731-734.
39. Strøm, M.B., et al., *The Pharmacophore of Short Cationic Antibacterial Peptides*. Journal of Medicinal Chemistry, 2003. **46**(9): p. 1567-1570.
40. Strøm, M.B., Ø. Rekdal, and J.S. Svendsen, *Antimicrobial activity of short arginine- and tryptophan-rich peptides*. Journal of Peptide Science, 2002. **8**(8): p. 431-437.
41. Liu, Z., et al., *Length effects in antimicrobial peptides of the (RW)<sub>n</sub> series*. Antimicrobial agents and chemotherapy, 2007. **51**(2): p. 597-603.
42. Wenzel, M., et al., *Small cationic antimicrobial peptides delocalize peripheral membrane proteins*. Proceedings of the National Academy of Sciences of the United States of America, 2014. **111**(14): p. E1409-E1418.
43. Wenzel, M., et al., *Towards Profiles of Resistance Development and Toxicity for the Small Cationic Hexapeptide RWRWRW-NH<sub>2</sub>*. Frontiers in cell and developmental biology, 2016. **4**: p. 86-86.
44. Chantson, J.T., et al., *Solid-Phase Synthesis, Characterization, and Antibacterial Activities of Metallocene–Peptide Bioconjugates*. ChemMedChem, 2006. **1**(11): p. 1268-1274.
45. Albada, H.B., et al., *Modulating the activity of short arginine-tryptophan containing antibacterial peptides with N-terminal metallocenoyl groups*. Beilstein journal of organic chemistry, 2012. **8**: p. 1753-1764.
46. Albada, B. and N. Metzler-Nolte, *Highly Potent Antibacterial Organometallic Peptide Conjugates*. Accounts of Chemical Research, 2017. **50**(10): p. 2510-2518.
47. Zhu, S., et al., *Highly Photoluminescent Carbon Dots for Multicolor Patterning, Sensors, and Bioimaging*. Angewandte Chemie International Edition, 2013. **52**(14): p. 3953-3957.
48. Wang, S., et al., *The dual roles of functional groups in the photoluminescence of graphene quantum dots*. Nanoscale, 2016. **8**(14): p. 7449-7458.
49. Kim, T.H., et al., *Yellow-Emitting Carbon Nanodots and Their Flexible and Transparent Films for White LEDs*. ACS App. Mater. Interfaces, 2016. **8**: p. 33102–33111.
50. Cui, X., et al., *A fluorescent biosensor based on carbon dots-labeled oligodeoxyribonucleotide and graphene oxide for mercury (II) detection*. Biosensors and Bioelectronics, 2015. **63**: p. 506-512.
51. Zhu, L., et al., *Fluorescence immunoassay based on carbon dots as labels for the detection of human immunoglobulin G*. Analytical Methods, 2014. **6**(12): p. 4430-4436.
52. Jarre, G., et al., *Synthesis of nanodiamond derivatives carrying amino functions and quantification by a modified Kaiser test*. Beilstein journal of organic chemistry, 2014. **10**: p. 2729-2737.

## CHAPTER 3

### On-demand antimicrobial releasing platform triggered by near-infrared light

*The content below was done in collaboration work with Laura Chambre from Prof. Amitav Sanyal group (Boğaziçi University, Istanbul, Turkey). Cryogels were fabricated by Laura Chambre. The author performed or coordinated most of the experiments including the biological assays.*

#### 3.1. Introduction

Advances in controlled drug release systems and devices have addressed many of the challenges encountered in traditional drug delivery [1-7]. Controlled drug release can be triggered either by internal or external stimuli [8-11]. These systems may provide a long-term solution to the main drawbacks of drug resistance development which is a widespread problem encountered in many treatments, especially in bacterial infections therapy due to increasing antibacterial resistance and severity of side effects [12, 13].

Stimuli-responsive systems are considered to be effective for “on-demand” drug delivery under the influence of a particular stimulus, which can be endogenous or exogenous in nature [14]. Endogenous systems are systems that result in drug release upon changes in pH, temperature change, redox state etc. [8-11]. The limited control over drug release is the main obstacle in designing and in the efficient use of such systems. Exogenous stimuli like light, magnetic field, electric field and ultrasound have been successfully utilised helping to overcome these limitations [15]. Among them, light is considered the most attractive stimulus due to ease and spatiotemporal control [16-19]. Near-infrared (NIR) light has good tissue penetration due to limited attenuation. It is also considered safe for cells and tissues [17, 20]. Therefore systems that are NIR light-responsive can be utilised as a potential drug carrier for drug delivery in clinical application [4]. In such systems, the release of a drug is achieved upon exposure to NIR light where photothermally active material convert absorbed light radiation into heat. Depending on the material, the local application of heat will result in either physical or chemical change in the system, subsequently resulting in enhanced drug release [21]. Several thermoresponsive nanomaterials have been successfully applied in on-demand release systems such as gold nanorods, metallic nanoparticles, organic chromophores and carbon nanomaterials notable graphene-based materials [1, 17, 22]. Graphene oxide (GO) and its derivatives, notably reduced graphene oxide (rGO) have been used to fabricate drug delivery platforms either as

discrete nanocarriers or have been incorporated into composite nanomaterial [23]. Modifications with nontoxic polymers enhance its biocompatibility and dispersibility.

Embedding GO into hydrogels would have in addition several advantages such as high loading capacity, protection of an active molecule together with on-demand release possibilities [21, 24, 25]. While hydrogels have been extensively explored, in recent years, the focus has shifted towards utilisation of the macroporous member of hydrogel family- cryogel [26]. The advantage of using cryogel over traditional hydrogel is its exceptional combination of highly porous characteristic with sufficient osmotic stability, better drug release due to higher porosity and swellability which allows for better transport of medium into their interiors [27].

We envisioned that graphene oxide (rGO) loaded cryogel patch, where the release of antibacterial agent can be triggered photothermally, might be an effective on-demand delivery platform with antibacterial properties for the ablation of skin related pathogens. The increased temperature during NIR irradiation is used in this approach to promote the release of the loaded drug either through enhanced diffusion out of the gel or by the disruption of the structure (**Figure 3.1**). For that purpose, we utilise a photothermal active cryogels consisting of rGO embedded in a gel composed of hydrophilic poly(ethylene glycol) (PEG) and hydrophobic furfuryl groups. The furan groups served a dual-mode providing hydrophobic pockets and covalent linkage sites for maleimide-modified antimicrobial peptide. We took advantage of thermally controlled equilibrium of the Diels-Alder reaction, which at elevated temperature induce the reverse reaction and the reformation of maleimide and furan moieties whereas lower temperature favours the adduct formation.

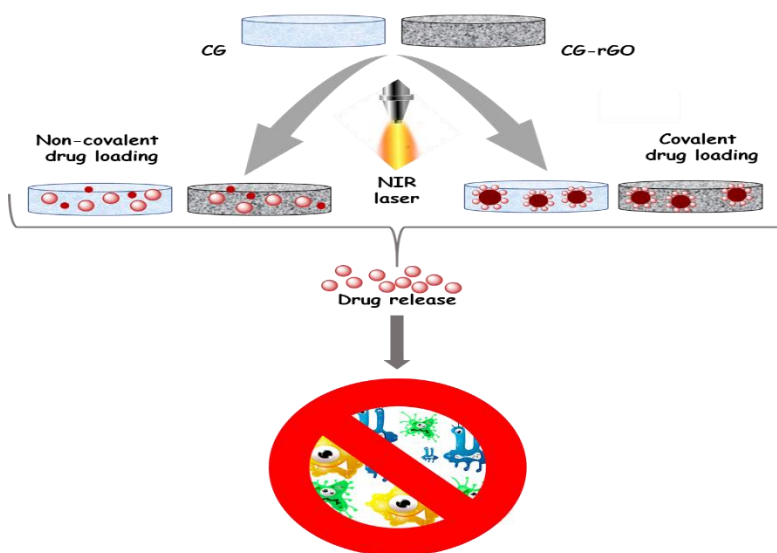


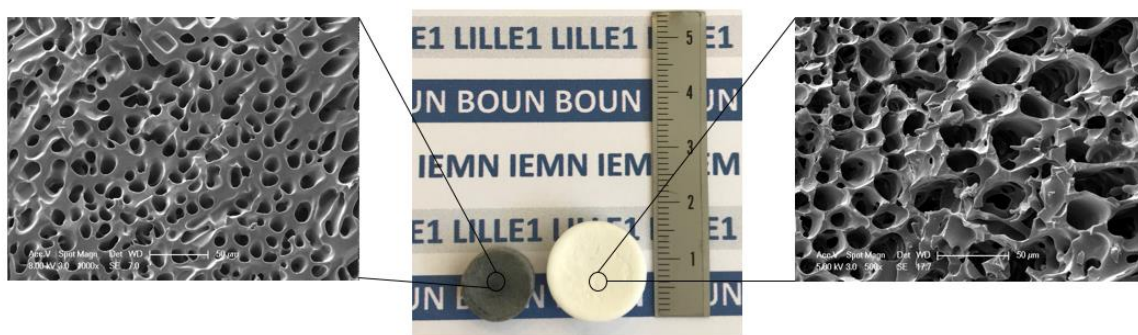
**Figure 3.1:** Schematic illustration of different furan-based cryogels loaded non-covalently as well as covalently via Diels-Alder reaction with an antimicrobial agent for the killing of bacteria triggered by near-infrared laser.



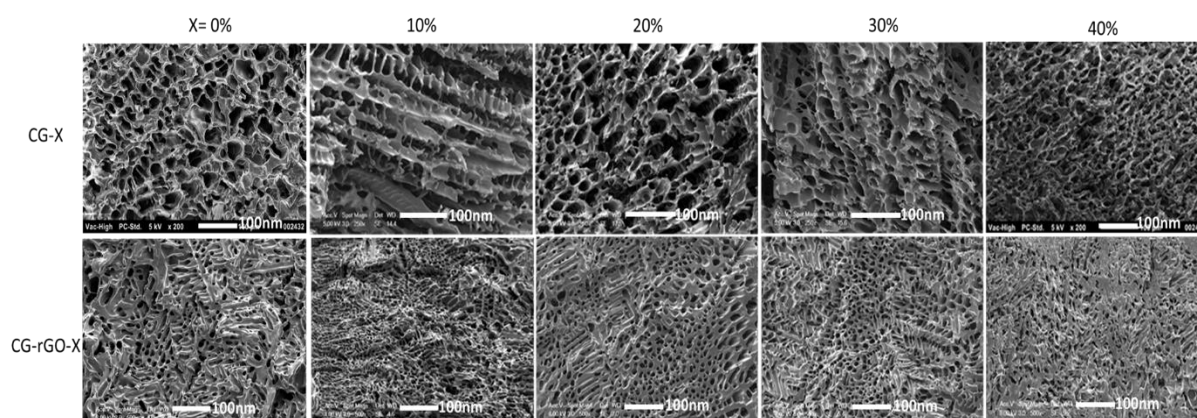
### 3.2. Fabrication and photothermal properties of furan-modified cryogels with and without embedded rGO

A series of maleimide reactive cryogels with and without embedded rGO (**Figure 3.2B**) were synthesised using varying amounts of poly(ethylene glycol) methyl ethermethacrylate (PEGMEMA) and furfuryl methacrylate (FuMA) monomers and an aqueous dispersion of rGO. The fabrication of cryogels was carried out at  $-13^{\circ}\text{C}$  under UV irradiation (365nm). 2,2-dimethoxy-2-phenylacetophenone (DMPA) was used as a photoinitiator and poly(ethylene glycol) dimethacrylate (PEGDMA) as a crosslinker (**Figure 3.2B**). As can be seen from **Table 3.1**), increasing the FuMA/PEDMEM ratio resulted in a decrease of pore size diameter; likewise, the presence of rGO is causing the reduction of pore size. Additionally, the presence of rGO changes the morphology of the cryogels (**Figures 3.2B-C**) significantly. The successful incorporation of rGO is validated by the colour change of cryogel (**Figure 3.2A**).

(A)



(B)





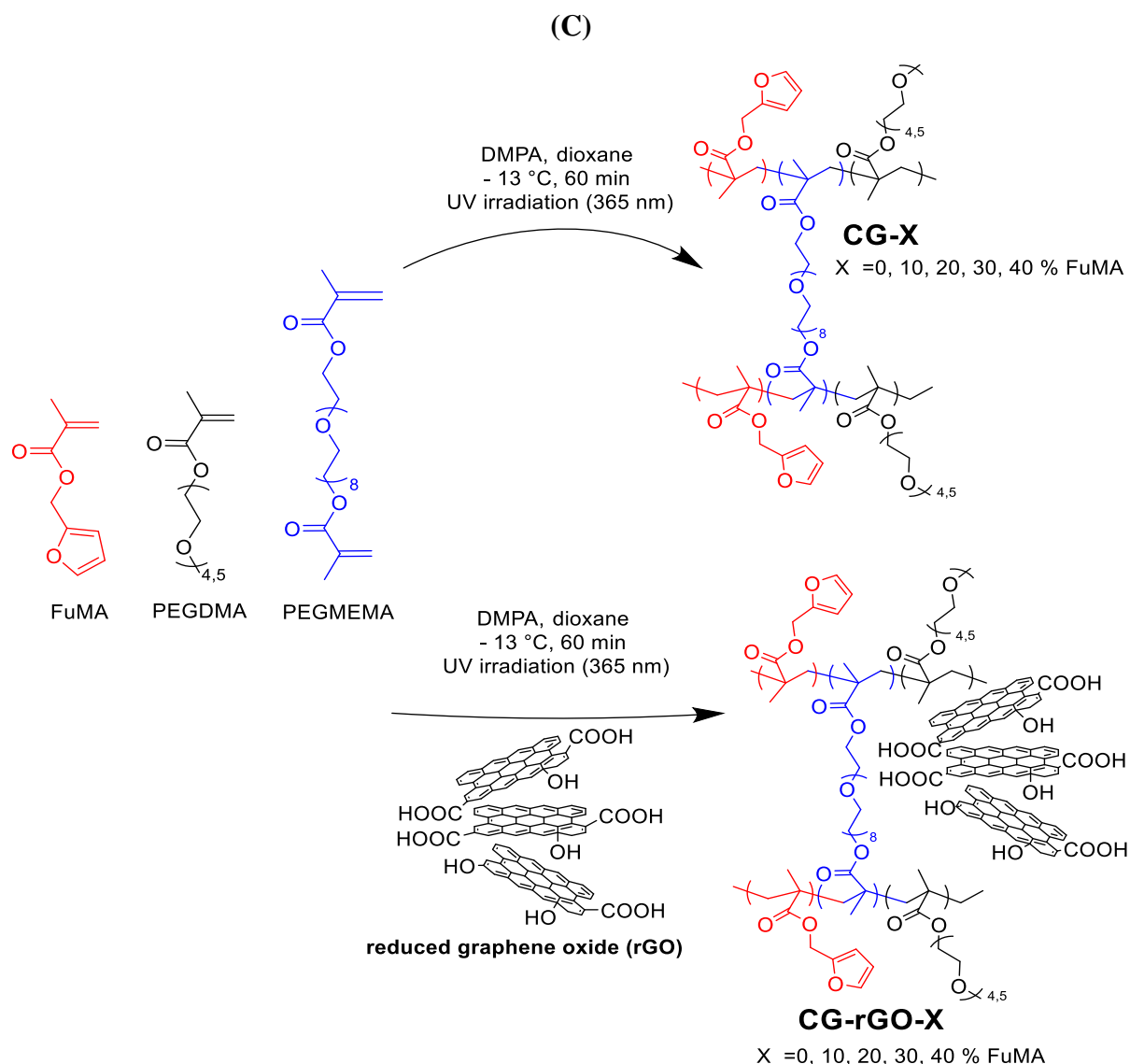


**Figure 3.2:** (A) Hydrogel samples prepared using a FuMA/PEDMEM= 20/80 with (left) and without (right) embedded rGO; (B) SEM picture of furan-containing cryogels with (up) and without (down) embedded rGO (scale bar: 100nm); (C) Schematic illustration of the fabrication of furan containing cryogels.

**Table 3.1:** Composition, pore size and swelling capacity of cryogels fabricated by photo-crosslinking

Cryogel No embedded rGO	FuMA/PEGMEMA	Pore size / $\mu\text{m}$	Swelling capacity
<b>CG-0</b>	0/100	$36.4 \pm 9.6$	$1123 \pm 18$
<b>CG-10</b>	10/90	$26 \pm 10.8$	$992 \pm 30$
<b>CG-20</b>	20/80	$23.9 \pm 5.1$	$934 \pm 28$
<b>CG-30</b>	30/70	$16.2 \pm 4.0$	$808 \pm 33$
<b>CG-40</b>	40/60	$13.5 \pm 2.7$	$759 \pm 38$
Cryogel rGO embedded	FuMA/PEGMEMA	Pore size / $\mu\text{m}$	Swelling capacity
<b>CG-rGO-0</b>	0/100	$13.1 \pm 1.6$	$468 \pm 7$
<b>CG-rGO-10</b>	10/90	$10.3 \pm 2.9$	$428 \pm 5$
<b>CG-rGO-20</b>	20/80	$9.5 \pm 2.6$	$317 \pm 5$
<b>CG-rGO-30</b>	30/70	$7.7 \pm 1.9$	$303 \pm 7$
<b>CG-rGO-40</b>	40/60	$6.5 \pm 1.6$	$278 \pm 8$

The swelling capacity of the cryogels was investigated by recording the water uptake as a function of time (**Figure 3.3**). In general, all cryogels showed a decrease in swelling capacity with increased hydrophobic content (FuMA). Addition of rGO in the structure of as-prepared cryogels decreases the overall water uptake.

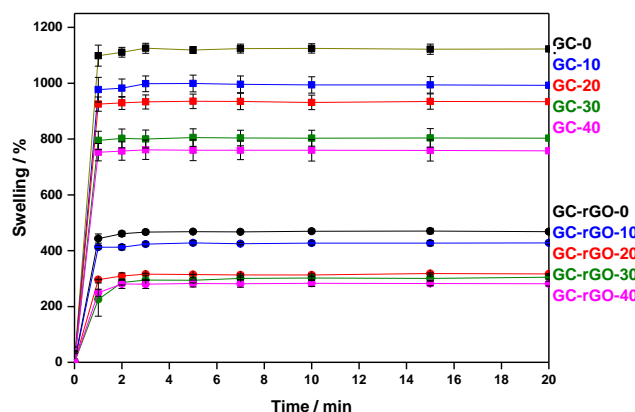


**Figure 3.3: Swelling behaviour of the different cryogels:** Water uptake of different cryogels at 24 °C without and with rGO (1 weight %) embedded into the cryogels.

As we can see from the UV-Vis absorption spectrum (**Figure 3.4A**), the presence of rGO causes a strong absorption in the NIR region. This indicated the potential use of the cryogel for NIR based photothermal heating. Therefore, the photothermal properties of cryogels containing rGO were explored. As expected, the increasing amount of rGO embedded in the cryogel leads to an increase in the temperature during NIR irradiation. Cryogels containing different amount of rGO were irradiated with a continuous wave laser at 980 nm at  $1\text{Wcm}^{-2}$ , resulting in the maximum surface temperature of  $70\pm 3\text{ }^{\circ}\text{C}$  (**Figure 3.4B**).

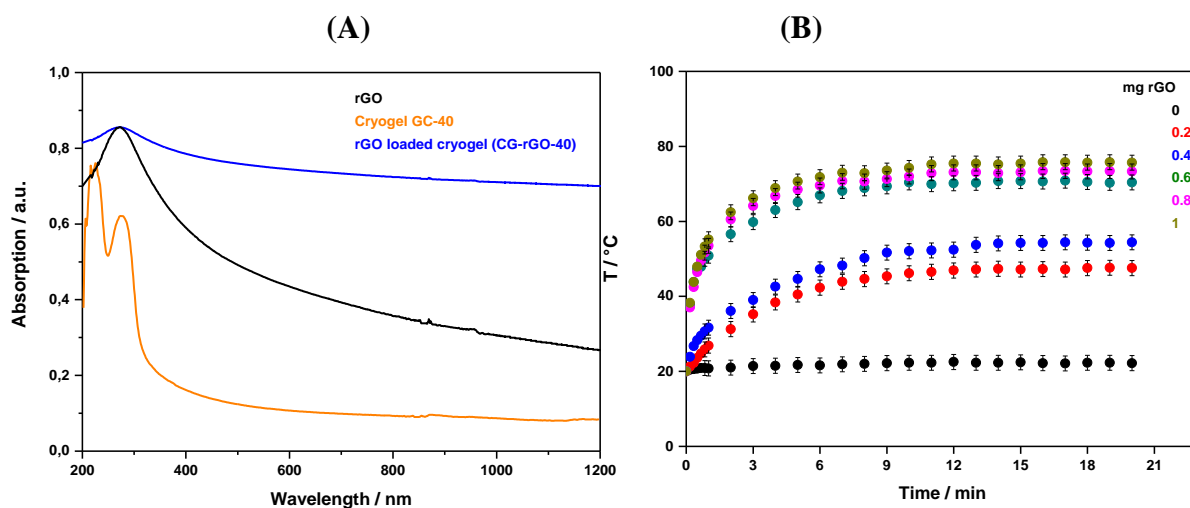


**Figure 3.4: (A)** UV/Vis absorption spectra of cryogel CG-40 without rGO and rGO embedded CG-40; **(B)** Photothermal heating curves of cryogels with different amount of rGO when immersed in PBS (0.1 M, pH 7.4) and exposed to laser light of 980 nm for 10 min at  $1\text{W cm}^{-2}$ .

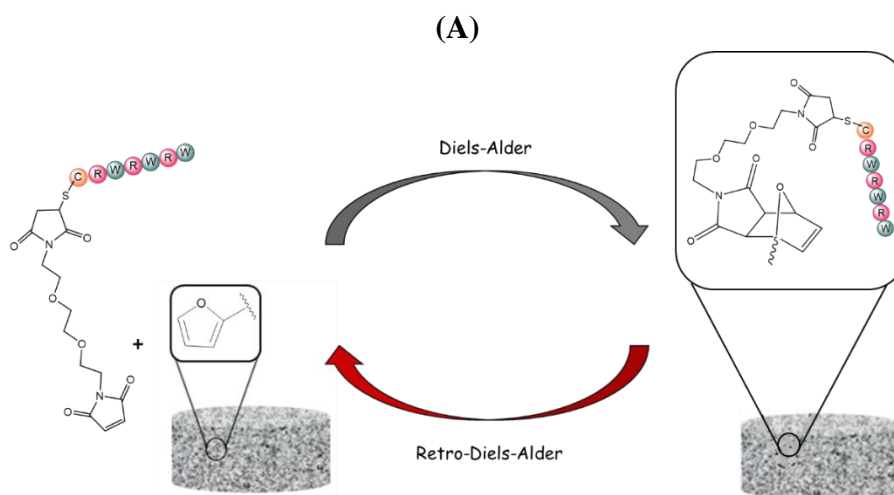
### 3.3. Loading of cryogels with antimicrobial agents

Loading of antimicrobials was accomplished in two ways : a) by simple absorption of the drug inside the gels via gel immersion into an aqueous solution of the antimicrobial agents; b) by Diels-Alder reaction between the furan containing cryogel and a maleimide containing antimicrobial (**Figure 3.5A**)

#### 3.3.1. Loading of the antibacterial drug via absorption and subsequent release

The loading capacity of cryogel CG-rGO-40 for ampicillin was investigated first. The amount of antibiotic-loaded onto the gel was calculated from the solution before and after the loading using a calibration curve on HPLC. From **Figure 3.5B**, we can see that the concentration of antibiotic used in the initial solution is proportional to the amount loaded inside the cryogel. When  $800 \mu\text{g mL}^{-1}$  of the antibiotic was used for loading,  $114 \mu\text{g mL}^{-1}$  (14%) of ampicillin was found to be loaded into the CG-rGO-40 gel.

To trigger the release of ampicillin (**Figure 3.5C**), a laser at a power density of  $1 \text{ W cm}^{-2}$  was used and resulted in a total release of  $56 \mu\text{g mL}^{-1}$ . In comparison, the passive release of extensively washed cryogels was low. The minimal inhibitory concentration for Gram-negative bacteria *E.coli K12* was determined to be  $10 \mu\text{g mL}^{-1}$ . The amount of released antimicrobial was higher than the minimum concentration inhibiting the growth of the bacteria (**Figure 3.5C**). In addition, **Figure 3.5D** shows that already after 5 minutes of irradiation, the amount of released antibiotic is sufficient for complete bacterial ablation, while passively released amount is below the MIC value for the tested bacteria, which shows the importance of combining laser irradiation with rGO embedded cryogels in “on-demand” antibiotic release.



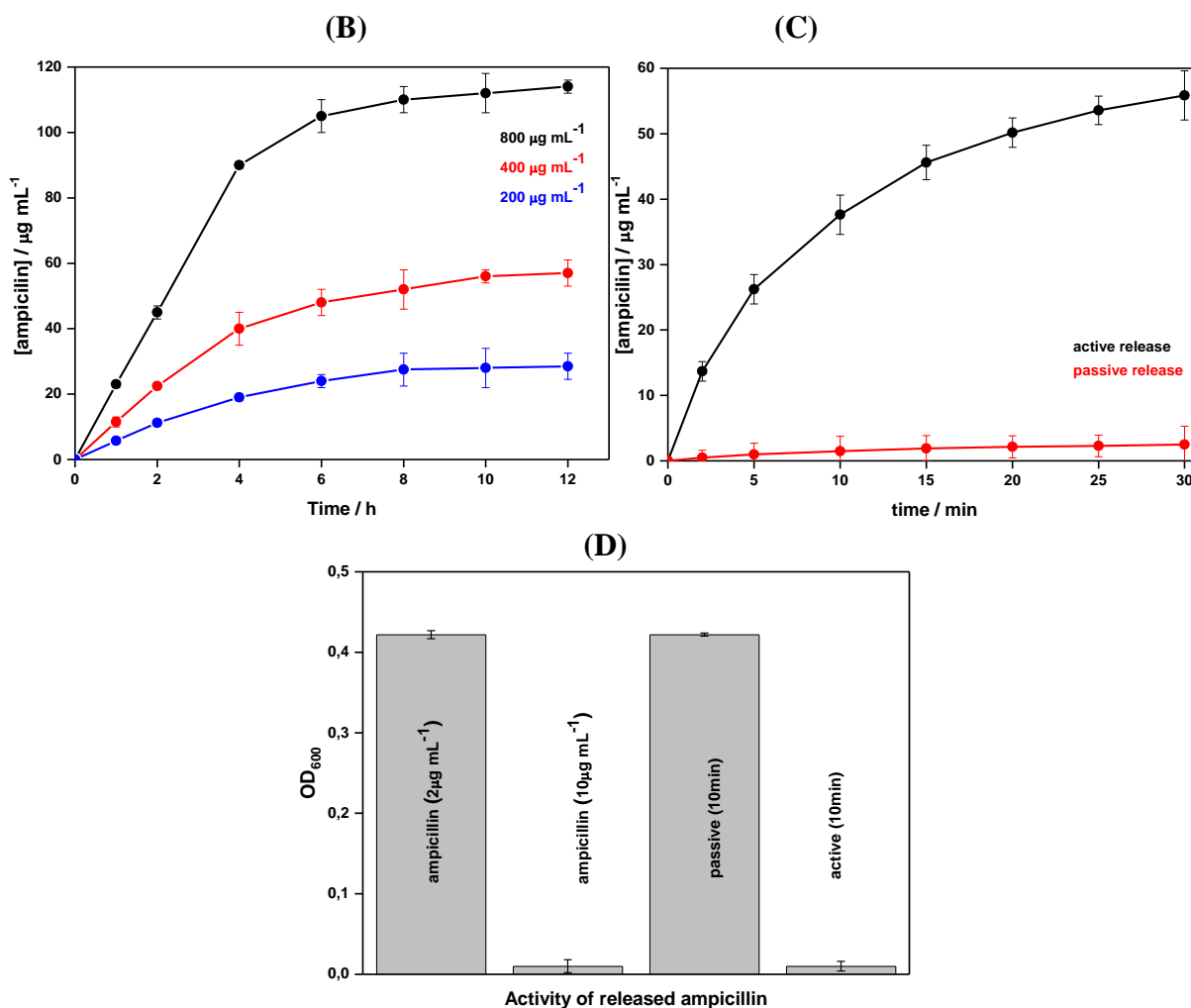


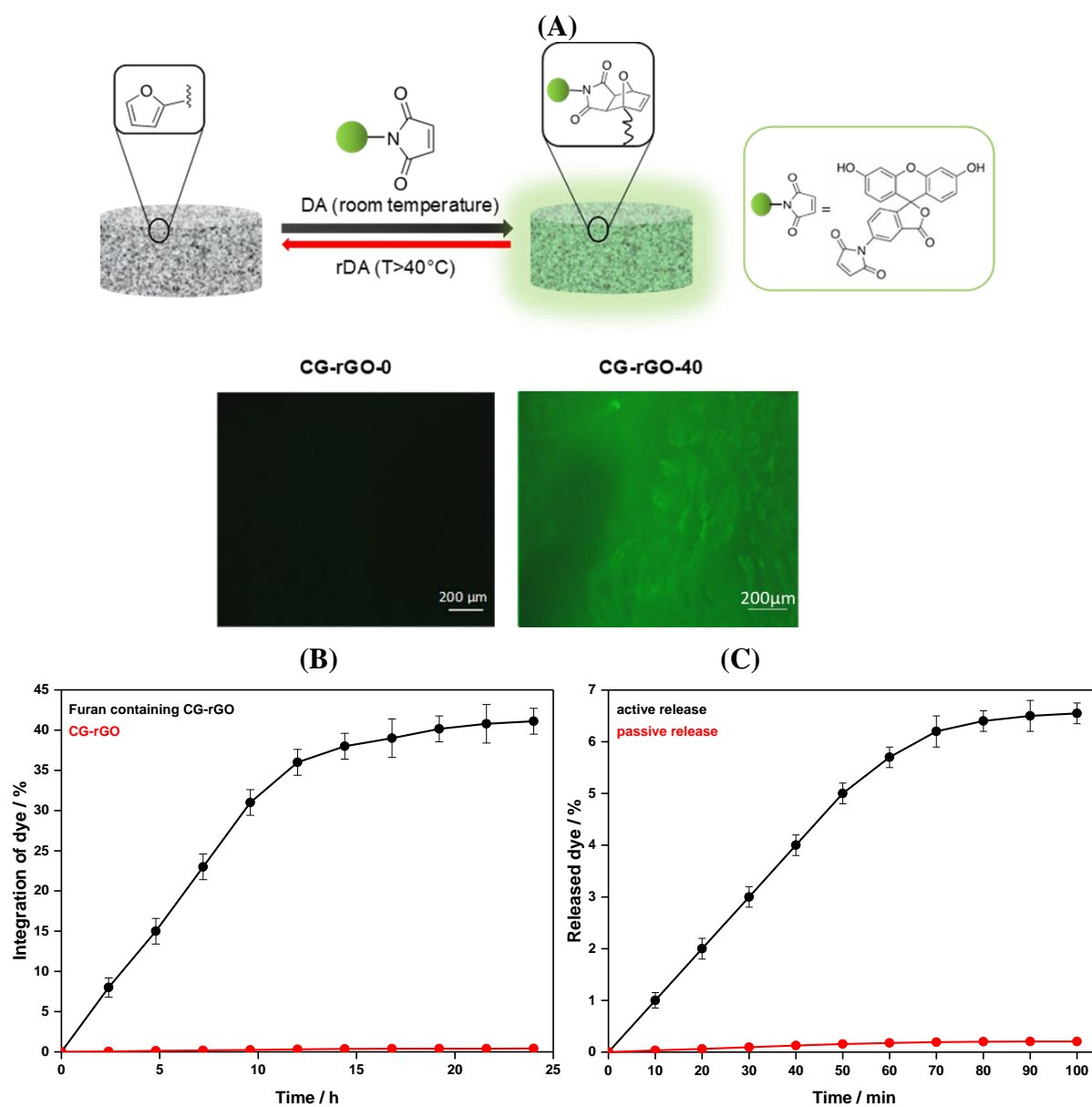
**Figure 3.5:** (A) Furan-maleimide chemistry; (B) Loading capacity of CG-rGO-40 (3 mg) for ampicillin using different initial concentrations; (C) Release behaviour of ampicillin from CG-rGO-40 loaded with 114  $\mu\text{g mL}^{-1}$  of antibiotic under 10 min laser activation (1 W  $\text{cm}^{-2}$ ) and passively at 24°C; (D) Comparison of the action of free ampicillin (2  $\mu\text{g mL}^{-1}$ , negative control), ampicillin (10  $\mu\text{g mL}^{-1}$ ; positive control) and released ampicillin after 10 min upon activation and passively when incubated with *E. coli* ( $1 \times 10^8$  CFU  $\text{mL}^{-1}$ ).

### 3.3.2. Loading of the antibacterial agent via Diels-Alder reaction and subsequent release

Another way of incorporating biologically active molecule into the cryogels is the possibility of furfuryl interaction with maleimide modified antimicrobial. In this section, we evaluated loading efficiency using HPLC calibration curve or fluorescent microscopy of the solution before and after loading. Fluorescent- maleimide dye was used as a model to validate the loading mechanism. Cryogel CG-rGO-40 was immersed in a solution of the dye for 24h, resulted in fluorescent cryogel with the loading efficiency of  $40 \pm 2\%$  (**Figure 3.6B**). To confirm that the dye is covalently bonded to the furan moiety, the same amount of the dye was

loaded onto furan depleted cryogel (CG-rGO-0) for the same amount of time. Proving that, no dye was left inside the gel as no fluorescent signal could be observed (**Figure 3.6A**).

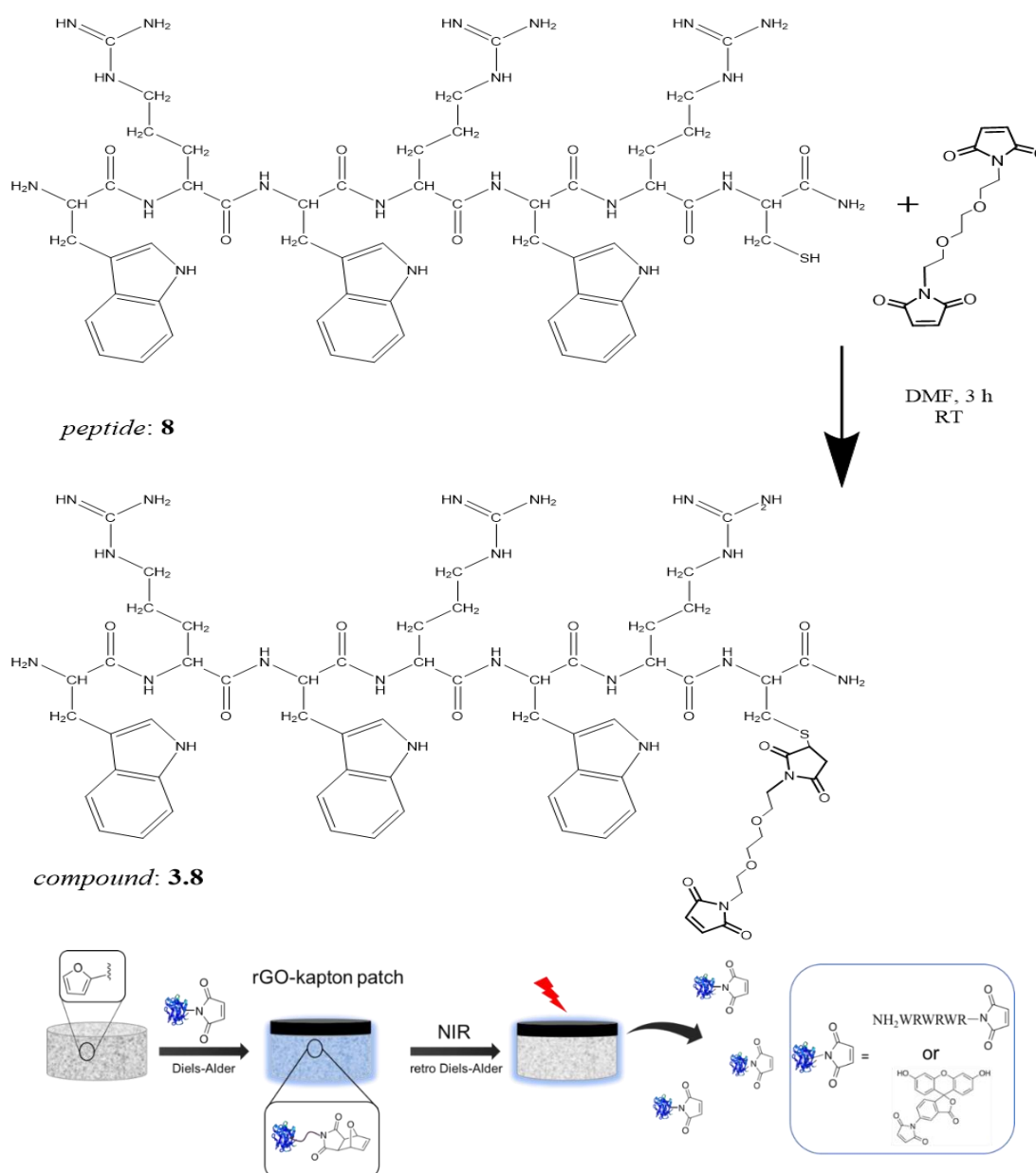
The release mechanism is based on the temperature-dependent equilibrium between Diels-Alder (DA) and reverse reaction (rDA), where at a lower temperature, the adduct formation is favoured (**Figure 3.6A**). During the irradiation of the cryogel, the polymer network is exposed to an increased temperature which affects the equilibrium rate between DA-rDA, resulting in an increased release of maleimide-dye compared to release at 37 °C without irradiation.



**Figure 3.6:** (A) Schematic representation of dye loading and microscopy images of CG-rGO-0(control) and CG-rGO-40 (CG-Furan) after treatment with maleimide dye; (B) Capacity of furan free CG-rGO-0 (control) and furfuryl-containing CG-rGO-40 cryogels for the integration *N*-(5-fluoresceinyl)maleimide via Diels-Alder cycloaddition; (C) Release of fluorescein maleimide dye via retro Diels Alder from CG-rGO in % using a laser (active) and at 37 °C (passive).

We decided to investigate the possibility of loading a short synthetic antimicrobial peptide (AMP) onto the cryogel. The AMP chosen is a maleimide-modified cationic peptide containing three arginine units serving as a positive charge donor and three tryptophan serving as a bulky lipophilic part- necessary to obtain the optimum antibacterial activity (**Figure 3.7A**). This small peptide targets the bacterial membrane and inhibits cellular respiration and cell wall synthesis [28, 29] and was shown to be effective against Gram-positive bacteria including methicillin-resistance *S. aureus* while being moderately active against Gram-negative bacteria. MIC values obtained for the peptide and the peptide-maleimide conjugate remain unchanged, indicating that the modification did not alter the antibacterial activity of AMP.

(A)





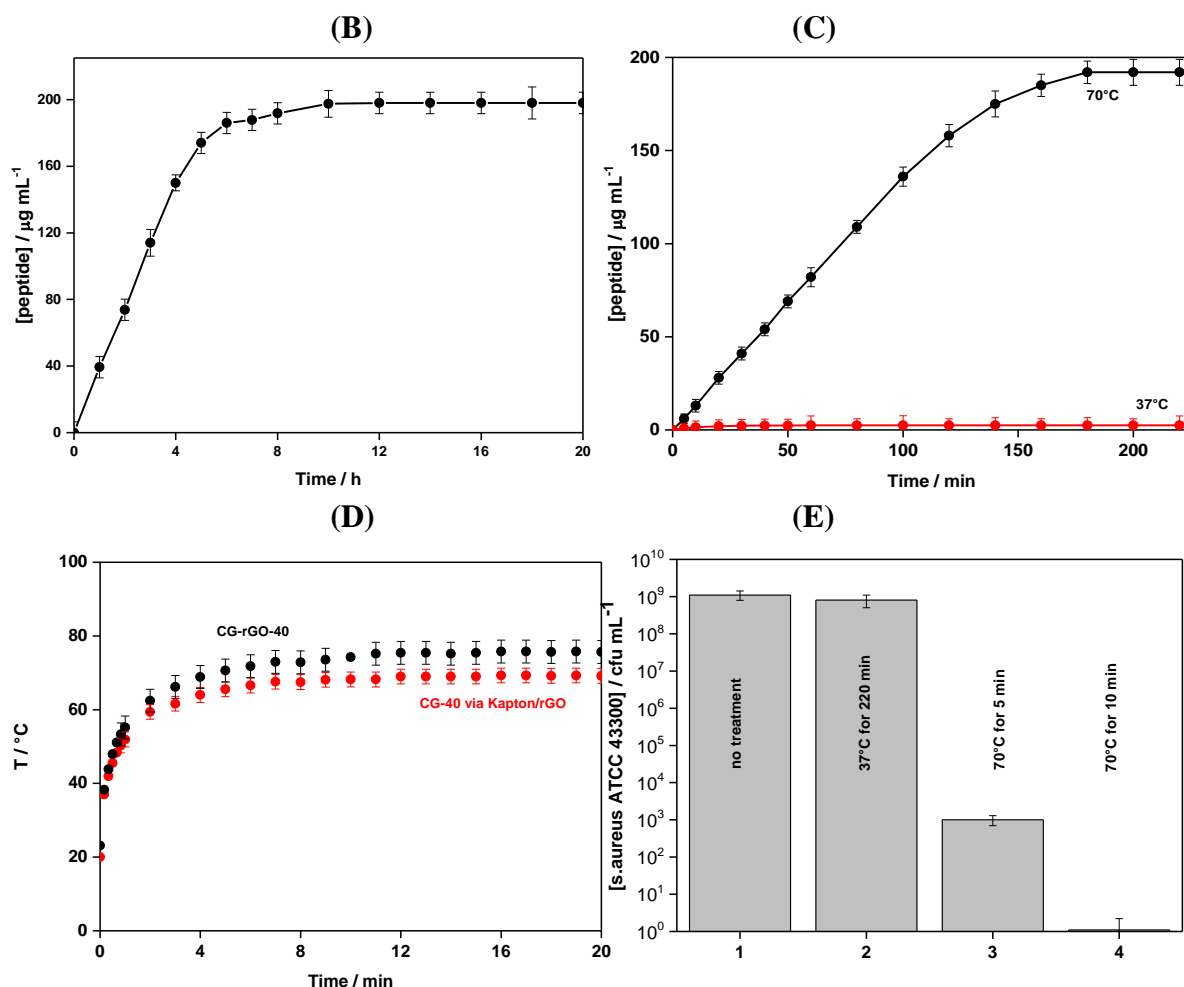


**Figure 3.7:** (A) Synthesis of maleimide modified peptide via Thiol Michael addition reaction between a PEG bis-maleimide and the cysteine end and Schematic representation of loading and release of maleimide containing molecules based on Diels Alder based linkage and retro Diels Alder based cleavage at Temperature > 42 °C; (B) Loading capacity of CG-rGO-40 cryogel with time from a stock solution of maleimide-modified peptide of 600  $\mu\text{g mL}^{-1}$ ; (C) Release of maleimide containing peptide via retro Diels Alder from cryogel at 37 °C (passive) and 70 °C (active); (D) Photothermal heating curves of CG-40 via Kpaton/rGO and CG-rGO-40 when immersed in PBS (0.1 M, pH 7.4) and exposed to laser light of 980 nm for 10 min at 1W cm<sup>-2</sup>; (E) Activity of maleimide-modified peptide released from cryogel under different conditions against *S. aureus* ATCC4300.

The amount of peptide integrated into CG-rGO-40 was calculated to be 198  $\mu\text{g mL}^{-1}$  (33%) (**Figure 3.7B**) after 20h incubation (HPLC). Unfortunately, the release from the cryogel was <1% even after irradiation for 30 min at 70 °C. These findings are comparable to those of using *N*-(5-fluoresceinyl)maleimide, where only 6% of the loaded dye was released (0.6% at 37 °C without radiation) (**Figure 3.6C**). One possible explanation could be the strong  $\pi$ - $\pi$  stacking interaction between the peptide and the rGO inside the gel and/or electrostatic interaction between positively charged peptide and negatively charged reduce graphene oxide. To validate this theory, an rGO-free gel (CG-40), was loaded with the peptide/dye, and photothermal release was achieved by using an rGO-covered Kapton patch on top of the cryogel (**Figure 3.7A**). Such a construct does not influence significantly the max temperature of the

solution reached during the irradiation (**Figure 3.7D**) but affects the release efficiency of the loaded molecules. As shown in (**Figure 3.7C**) the peptide release was almost 100% ( $194 \pm 6 \mu\text{g mL}^{-1}$ ) when heated to  $70^\circ\text{C}$  for 240 min, while only  $2.4 \mu\text{g mL}^{-1}$  (1.4 %) was released at  $37^\circ\text{C}$ - as for the dye, using such a construct allows us to release 28% while heating and only 1,4% at  $37^\circ\text{C}$ .

The activity of the released antibacterial peptide was tested on Gram-positive bacteria *S. aureus ATCC43300*. The MIC value for the maleimide-modified peptide was determined by microdilution method, and the obtained value was the same as for the peptide itself ( $16 \mu\text{g mL}^{-1}$ ). While the amount of the released AMP at  $37^\circ\text{C}$  was not efficient to inhibit the growth of tested bacteria strain, the amount of the peptide-maleimide released upon heating of the cryogel up to  $70^\circ\text{C}$  already after 10min of irradiation was enough to reach the MIC value and ultimately decrease bacteria cell viability (**Figure 3.7E**).

Before applying this approach for real application (e.g. wound healing platform), the cell toxicity of the cryogel was determined using a HeLa cell line and the CCK-8 viability assay. As shown in the (**Figure 3.8**), none of the prepared cryogels shows any cytotoxicity. As expected for a PEG-based matrix [30].

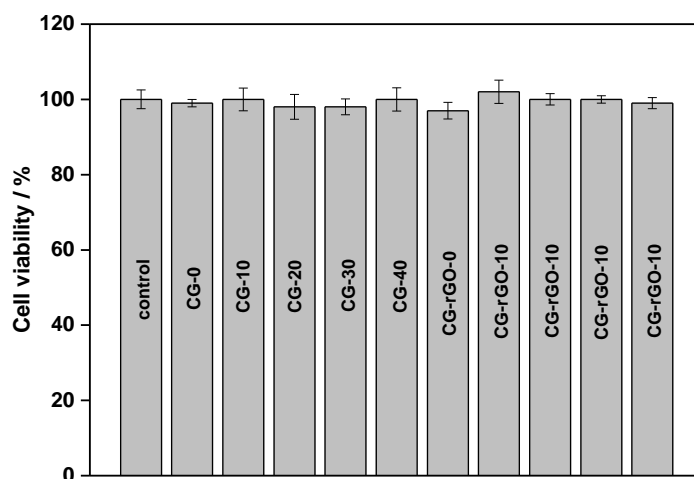


**Figure 3.8:** HeLa cell viability of after 24h incubation with different cryogels with and without incorporated rGO.

### 3.4. Conclusions

Cryogels were fabricated using photo-polymerisation leading to embedded matrix comprised of hydrophilic poly(ethylene glycol) and hydrophobic furfuryl groups. Furfuryl groups were incorporated as control over the hydrophobicity as well as a handle for Diels-Alder conjugation. Ampicillin was loaded inside the matrix via adsorption, while a maleimide-containing anti-microbial peptide was conjugated via the Diels-Alder reaction.

While the system performed as expected for the release of conventional antibiotic like ampicillin, the study reveals that integration of rGO inside the cryogels hindered the release of AMPs due to the strong  $\pi$ - $\pi$  interactions between the anti-microbial peptide and the rGO. To overcome this problem, a bilayer device structure was employed. The furan containing the rGO-depleted hydrogel was interfaced with NIR responsive Kapton patch modified with rGO. In case of cryogel loaded via absorption of commercially available ampicillin- total eradication of *E.coli* bacteria is achieved after 10 min. of NIR irradiation. Cryogels loaded via Diels-Alder reaction with AMP inhibited the growth of bacteria by 75% after 10 min. Increasing the irradiation time resulted in the higher release of a peptide, and after 30min, no bacteria could be detected. In order to apply this approach in the clinical application, the cytotoxicity of the cryogels was tested. Obtained results revealed no toxicity against HeLa cells. In addition to cytotoxicity, the antibacterial activity of as-prepared cryogels was tested showing no activity before antimicrobial loading.

### 3.5. References

1. Blum, A.P., et al., *Stimuli-Responsive Nanomaterials for Biomedical Applications*. Journal of the American Chemical Society, 2015. **137**(6): p. 2140-2154.
2. Deng, L., et al., *Magnetothermally responsive star-block copolymeric micelles for controlled drug delivery and enhanced thermo-chemotherapy*. Nanoscale, 2015. **7**(21): p. 9655-9663.
3. Ge, J., et al., *Drug Release from Electric-Field-Responsive Nanoparticles*. ACS Nano, 2012. **6**(1): p. 227-233.
4. Mura, S., J. Nicolas, and P. Couvreur, *Stimuli-responsive nanocarriers for drug delivery*. Nature Materials, 2013. **12**: p. 991.
5. Peer, D., et al., *Nanocarriers as an emerging platform for cancer therapy*. Nature Nanotechnology, 2007. **2**(12): p. 751-760.
6. Spizzirri, U.G., et al., *Recent Advances in the Synthesis and Biomedical Applications of Nanocomposite Hydrogels*. Pharmaceutics, 2015. **7**(4): p. 413-437.
7. Wolinsky, J.B., Y.L. Colson, and M.W. Grinstaff, *Local drug delivery strategies for cancer treatment: Gels, nanoparticles, polymeric films, rods, and wafers*. Journal of Controlled Release, 2012. **159**(1): p. 14-26.
8. Fleige, E., M.A. Quadir, and R. Haag, *Stimuli-responsive polymeric nanocarriers for the controlled transport of active compounds: Concepts and applications*. Advanced Drug Delivery Reviews, 2012. **64**(9): p. 866-884.
9. de la Rica, R., D. Aili, and M.M. Stevens, *Enzyme-responsive nanoparticles for drug release and diagnostics*. Advanced Drug Delivery Reviews, 2012. **64**(11): p. 967-978.
10. Ganta, S., et al., *A review of stimuli-responsive nanocarriers for drug and gene delivery*. Journal of Controlled Release, 2008. **126**(3): p. 187-204.
11. Rapoport, N., *Physical stimuli-responsive polymeric micelles for anti-cancer drug delivery*. Progress in Polymer Science, 2007. **32**: p. 962-990.

12. Lobanovska, M. and G. Pilla, *Penicillin's Discovery and Antibiotic Resistance: Lessons for the Future?* The Yale journal of biology and medicine, 2017. **90**(1): p. 135-145.
13. Melander, R.J. and C. Melander, *The Challenge of Overcoming Antibiotic Resistance: An Adjuvant Approach?* ACS Infectious Diseases, 2017. **3**(8): p. 559-563.
14. Hang, C., et al., *NIR and UV-responsive degradable hyaluronic acid nanogels for CD44-targeted and remotely triggered intracellular doxorubicin delivery.* Colloids and Surfaces B: Biointerfaces, 2017. **158**: p. 547-555.
15. Wang, Y. and D.S. Kohane, *External triggering and triggered targeting strategies for drug delivery.* Nature Reviews Materials, 2017. **2**(6): p. 17020.
16. Liu, G., W. Liu, and C.-M. Dong, *UV- and NIR-responsive polymeric nanomedicines for on-demand drug delivery.* Polymer Chemistry, 2013. **4**(12): p. 3431-3443.
17. Yang, G., et al., *Near-infrared-light responsive nanoscale drug delivery systems for cancer treatment.* Coordination Chemistry Reviews, 2016. **320-321**: p. 100-117.
18. Sahu, A., et al., *Nanographene oxide as a switch for CW/pulsed NIR laser triggered drug release from liposomes.* Materials Science and Engineering: C, 2018. **82**: p. 19-24.
19. Rahoui, N., et al., *Spatio-temporal control strategy of drug delivery systems based nano structures.* Journal of Controlled Release, 2017. **255**: p. 176-201.
20. Li, A., et al., *NIR-laser switched ICG/DOX loaded thermo-responsive polymeric capsule for chemo-photothermal targeted therapy.* European Polymer Journal, 2017. **92**: p. 51-60.
21. Teodorescu, F., et al., *Photothermally triggered on-demand insulin release from reduced graphene oxide modified hydrogels.* Journal of Controlled Release, 2017. **246**: p. 164-173.
22. Matteini, P., et al., *Graphene as a photothermal switch for controlled drug release.* Nanoscale, 2014. **6**(14): p. 7947-7953.
23. Liu, J., L. Cui, and D. Losic, *Graphene and graphene oxide as new nanocarriers for drug delivery applications.* Acta Biomaterialia, 2013. **9**(12): p. 9243-9257.
24. Robinson, J.T., et al., *Ultrasmall Reduced Graphene Oxide with High Near-Infrared Absorbance for Photothermal Therapy.* Journal of the American Chemical Society, 2011. **133**(17): p. 6825-6831.
25. Teodorescu, F., et al., *Transdermal skin patch based on reduced graphene oxide: A new approach for photothermal triggered permeation of ondansetron across porcine skin.* Journal of Controlled Release, 2017. **245**: p. 137-146.
26. Aydin, D., et al., *Hooked on Cryogels: A Carbamate Linker Based Depot for Slow Drug Release.* Bioconjugate Chemistry, 2017. **28**(5): p. 1443-1451.
27. Memic, A., et al., *Latest Advances in Cryogel Technology for Biomedical Applications.* Advanced Therapeutics, 2019. **2**(4): p. 1800114.
28. Wenzel, M., et al., *Toards Profiles and Resistance Development and Toxicity for the small cationic hexapeptide RWRWRW-NH<sub>2</sub>.* Frontiers in cell and Dev. Biol., 2016. **4**: p. 86.
29. Wenzel, M., et al., *Small cationic antimicrobial paptides delocalized peripheral memebrane proteins.* Procc. Nat. Acad. Sci., 2014: p. E1408.
30. Chen, S.-L., et al., *A PEG-Based Hydrogel for Effective Wound Care Management.* Cell transplantation, 2018. **27**(2): p. 275-284.

## CHAPTER 4

### Functional carbon quantum dots as a medical countermeasure to human coronavirus (HCoV)

*Much of the content below served as a basis for a publication [1]. The author conceived and performed all syntheses and performed or coordinated all experiments. Antiviral assays were performed in collaboration with Dr. Karin Seron in the group of Dr. Jean Dubuisson (Institut Pasteur de Lille, U1019- UMR8204- CIIL- Center for Infection and Immunity of Lille).*

#### 4.1. Introduction

The eradication of viral infections is an ongoing challenge in the medical field, not only due to the problem of spreading but also owing to virus ability to escape therapy by genetic mutations. The lack of targeted antiviral therapeutics, as well as the constant emergence of new viruses, make the search for antiviral agents a challenging and extremely needed research task [2]. As part of a global strategy to prevent epidemics, some severe emerging pathogens with great epidemic potential have been identified by the World Health Organization (WHO) [3], including, next to Ebola virus disease, the highly pathogenic human coronavirus (HCoV) infections. While circulating HCoVs (HCoV-229E, HCoV-OC43, HCoV-NL63 and HKU1) cause relatively mild common cold-like respiratory tract infections, severe acute respiratory syndrome coronavirus (SARS-CoV) and Middle-East respiratory syndrome coronavirus (MERS-CoV) lead to pneumonia, which requires hospitalisation and intensive care [4]. A total of 2266 laboratory-confirmed cases of MERS-CoV, including 804 associated deaths, have been declared to WHO until now, with a high case-fatality rate (35%) [5]. As the virus is circulating in animals and humans, it may undergo further adaptation and cause a pandemic. Therefore, therapeutic options are urgently needed.

The current treatments for MERS-CoV are extrapolated from SARS-CoV and H1N1 influenza outbreaks [6-8]. These include different combinations of small molecules with broad antiviral activity (*e.g.* ribavirin, corticosteroids, interferons (IFN)), and monoclonal or polyclonal antibody therapies [8, 9]. The membrane-anchored glycoprotein S was found lately to be essential for the interaction between MERS-CoV and the host cell [9, 10], and the development of MERS-CoV entry/fusion inhibitors targeting the S1 subunit is nowadays considered as a viable antiviral strategy.

Recently, nanoscale materials have emerged as promising and efficient platforms to modulate the viral infection cycle [11]. Given that the attachment of viruses to host cells is favoured by multivalent interactions, the multivalent character of nanostructures and their high surface-to-volume ratio, both allowing the attachment of several ligands, make them well adapted to interfere with the viral attachment and to block the viral entry into cells.

We investigate here the potential of functional carbon quantum dots (CQDs) as inhibitors of host cell infections by HCoV-229E coronavirus as the model virus (**Figure 4.1**). CQDs with an average diameter below 10 nm and excellent water dispersibility are highly attractive for nanomedical applications due to a lack of visible signs of toxicity in animals [12]. They can be synthesised quickly via several different, inexpensive and simple methods, and their excellent optical properties offer *in vivo* tracking possibilities. It was recently demonstrated that CQDs are suitable scaffolds to interfere with the entry of viruses into cells [13-15]. As an example, boronic acid-modified CQDs were able to inhibit HIV-1 entry by suppressing syncytium formation [14]. Additionally, CQDs functionalised with boronic acid and amine moieties have been demonstrated to interfere with the entry of herpes simplex virus type 1 [13]. Han and co-workers also reported the potential of CQDs as viral inhibitors by activation of type I interferon responses [15].

The present study reveals that boronic acid functions can be responsible for the anti-HCoV activity. CQDs derived from citric acid and ethylenediamine, further conjugated by “click” chemistry with boronic acid functions ( $-B(OH)_2$ ), display an effective 50% inhibition concentration  $EC_{50}=52\pm8\ \mu\text{g mL}^{-1}$ . Likewise, CQDs derived from 4-aminophenylboronic acid and phenylboronic acid without any further modification exhibit antiviral behaviour with an effective  $EC_{50}$  lowered down to  $5.2\pm0.7\ \mu\text{g mL}^{-1}$ . The underlying mechanism of action of these CQDs proved to be their interaction with the HCoV-229E S protein. Surprisingly, an equally large inhibition activity was observed at the viral replication step.



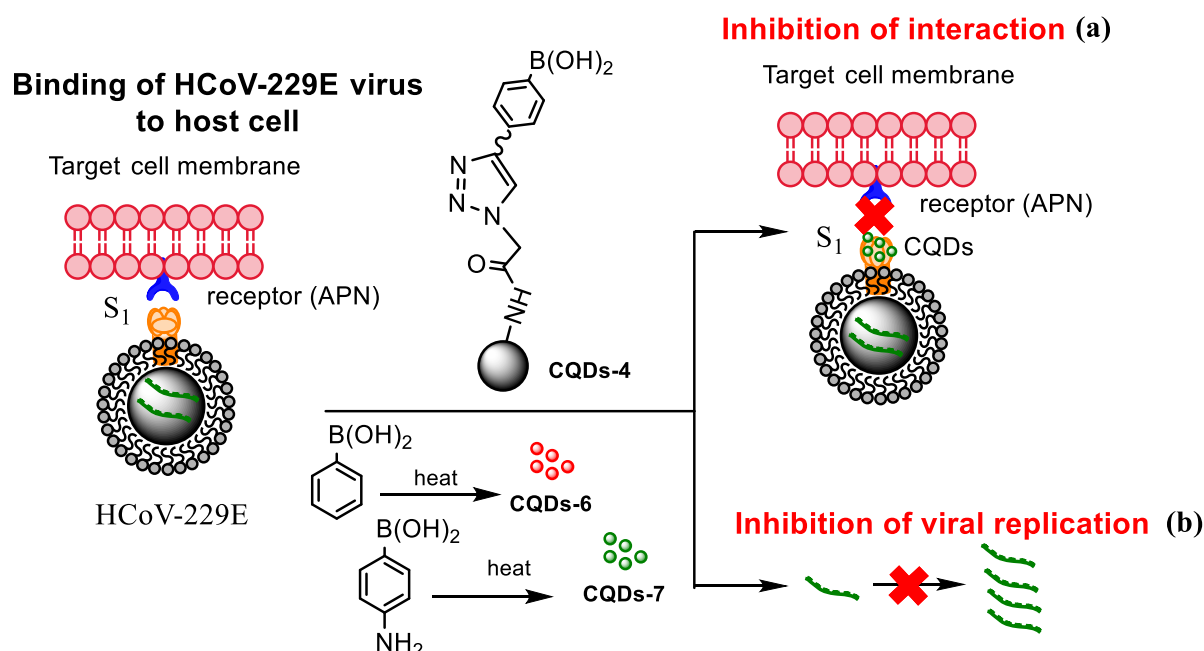
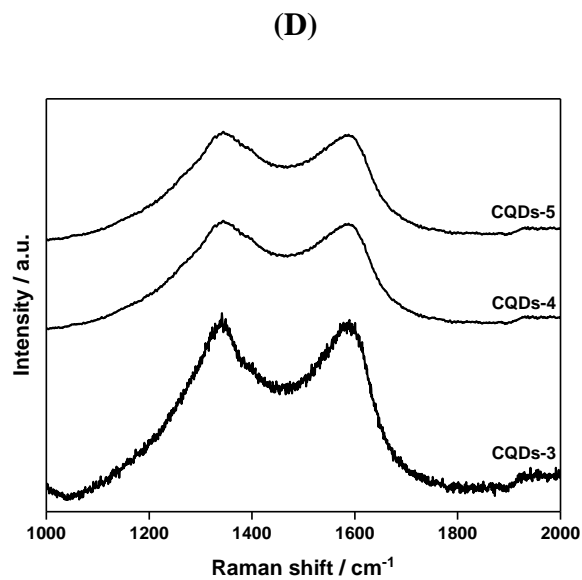
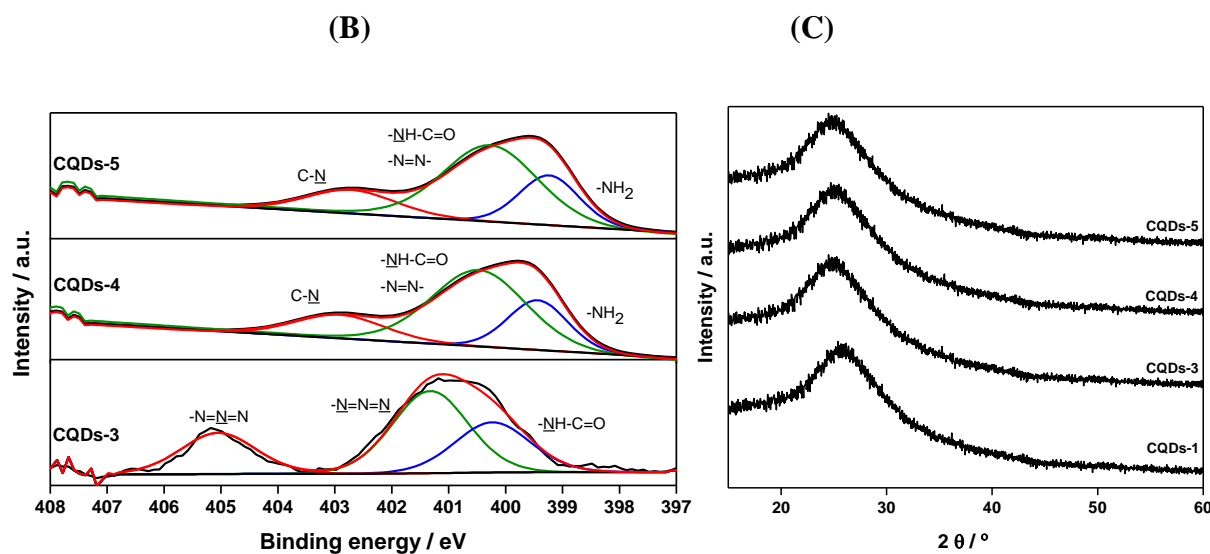
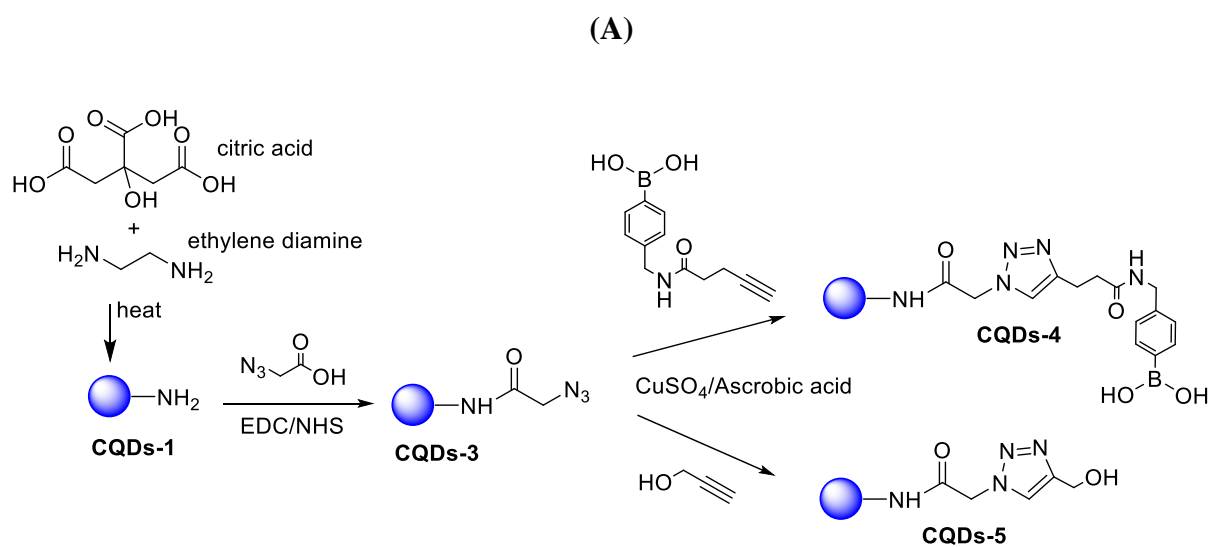


**Figure 4.1:** Influence of CQDs, prepared by hydrothermal carbonisation, on the binding of HCoV-229E virus to cells: (a) inhibition of protein S receptor interaction, (b) inhibition of viral RNA genome replication.

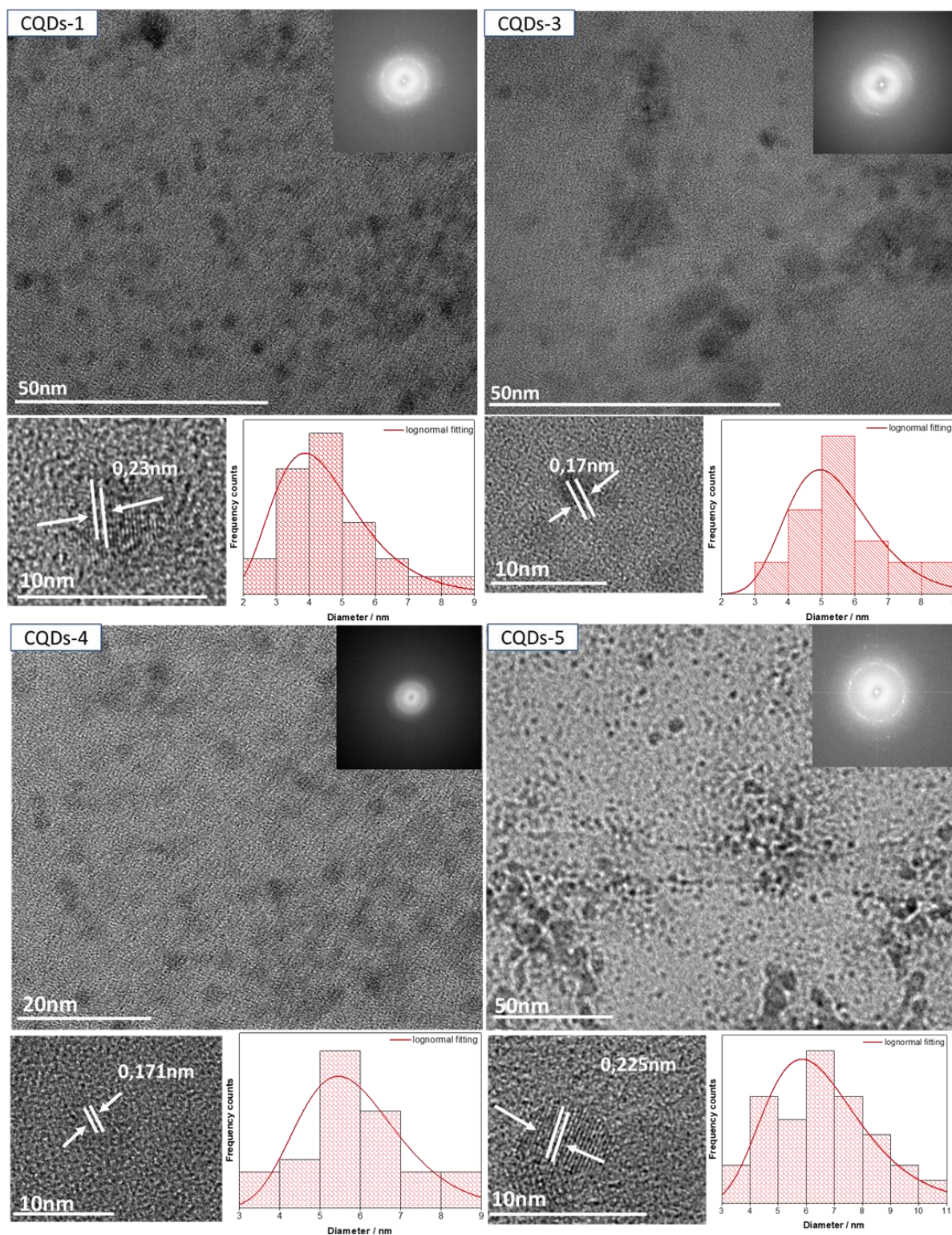
## 4.2. First-generation of CQDs inhibitors of host cell infections by HCoV-229E coronavirus: Boronic acid-modified CQDs

### 4.2.1. Formation, functionalization and characterisation

Boronic acid derivatives have been proposed as low-toxicity agents for inhibiting the interaction of various viruses with cells [16, 17]. To test if such concepts can be extrapolated to human coronavirus HCoV-229E infections, boronic acid functional groups were chemically integrated onto CQDs formed through the hydrothermal carbonisation of ethylenediamine and citric acid (**CQDs-1**, **Figure 4.2A**). Synthesis and characterisation of as-prepared CQDs have already been discussed in details in **CHAPTER 2**.



(E)



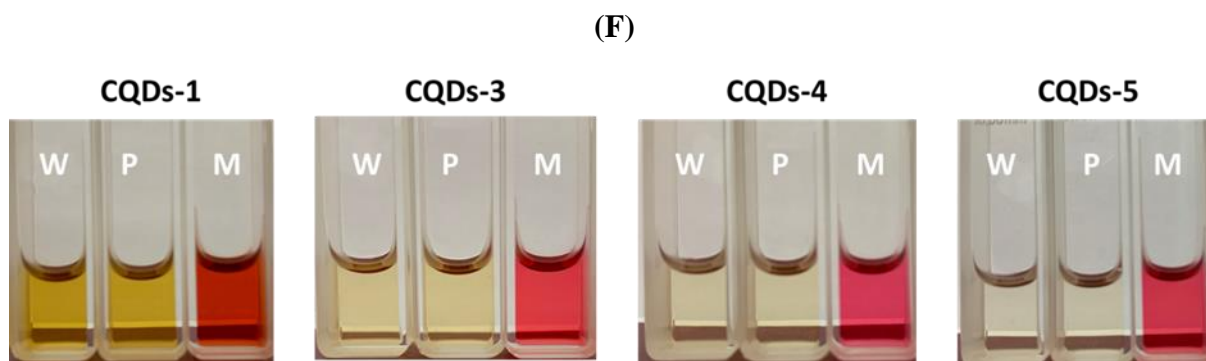


**Figure 4.2:** (A) Schematic representation of the synthesis of **CQDs-1**, **-3**, **-4** and **-5**; (B)  $N_{1s}$  high resolution XPS spectra of **CQDs-3**, **-4** and **-5**; (C) XRD diffractograms of **CQDs-1**, **-3**, **-4**, **-5**; (D) Raman spectra of **CQDs-3**, **-4**, and **-5**; (E) TEM, magnified TEM, HR-TEM images and size distribution histograms of **CQDs-1**, **-3**, **-4** and **-5**; (F) Photographs of **CQDs-1**, **-3**, **-4** and **-5** suspensions ( $1 \text{ mg mL}^{-1}$ ) after 1 month in water (W), PBS (0.01 M, P) and Dulbecco's Modified Eagle's medium (M).

**Table 4.1:** Physico-chemical properties of **CQDs-1**, **-3**, **-4** and **-5**

CQDs	$\zeta$ (mV) <sup>1</sup>	Size (nm)	Hydrodynamic size (nm) <sup>2</sup>	PDI <sup>3</sup>	C1s <sup>4</sup> (at. %)	O1s <sup>4</sup> (at. %)	N1s <sup>4</sup> (at. %)	B1s <sup>4</sup> (at. %)
<b>CQDs-1</b>	$-9.9 \pm 3.4$	$4.5 \pm 0.2$	$11 \pm 0.1$	$0.22 \pm 0.11$	72.6	12.5	14.9	-
<b>CQDs-3</b>	$-7.9 \pm 2.7$	$5.5 \pm 0.3$	$12 \pm 0.1$	$0.23 \pm 0.11$	68.8	13.9	17.3	-
<b>CQDs-4</b>	$-15.9 \pm 4.3$	$6.3 \pm 0.4$	$12 \pm 0.25$	$0.15 \pm 0.10$	67.9	7.3	20.3	4.5
<b>CQDs-5</b>	$-15.9 \pm 1.3$	$6.5 \pm 0.4$	$11 \pm 0.19$	$0.13 \pm 0.10$	68.5	13.6	17.9	-

<sup>1</sup> $\zeta$ : zeta potential; <sup>2</sup>The hydrodynamic size was recorded at  $37^\circ\text{C}$ ; <sup>3</sup>PDI Polydispersity index; <sup>4</sup>XPS was used to determine the respective atomic percentages of the indicated elements.

The formation of **CQDs-4** is based on a two-step chemical process. In a first step, azido-functionalized **CQDs-3** are prepared by coupling 2-azido acetic acid to **CQDs-1**. The  $N_{1s}$  signal of **CQDs-3** shows signals at 405.2 ( $-\text{N}=\text{N}^+=\text{N}^-$ ) and 401.6 eV ( $\text{N}=\text{N}^+=\text{N}^-$ ) in a 1:2 ratio, as theoretically expected (**Figure 4.2B**). The azide functions in **CQDs-3** quantitatively react with alkyne functions as indicated by the absence of the azide band at 405.2 eV in the relevant spectra of **CQDs-4** and **CQDs-5** (**Figure 4.2B**). The band at 399.2 eV ( $-\text{NH}_2$ ) is most likely resulting from partial hydrolysis of surface-linked 2-azido acetamide functions. **CQDs-5** were synthesised as a control to check whether the triazole function acts as a passive linker or not [18, 19].

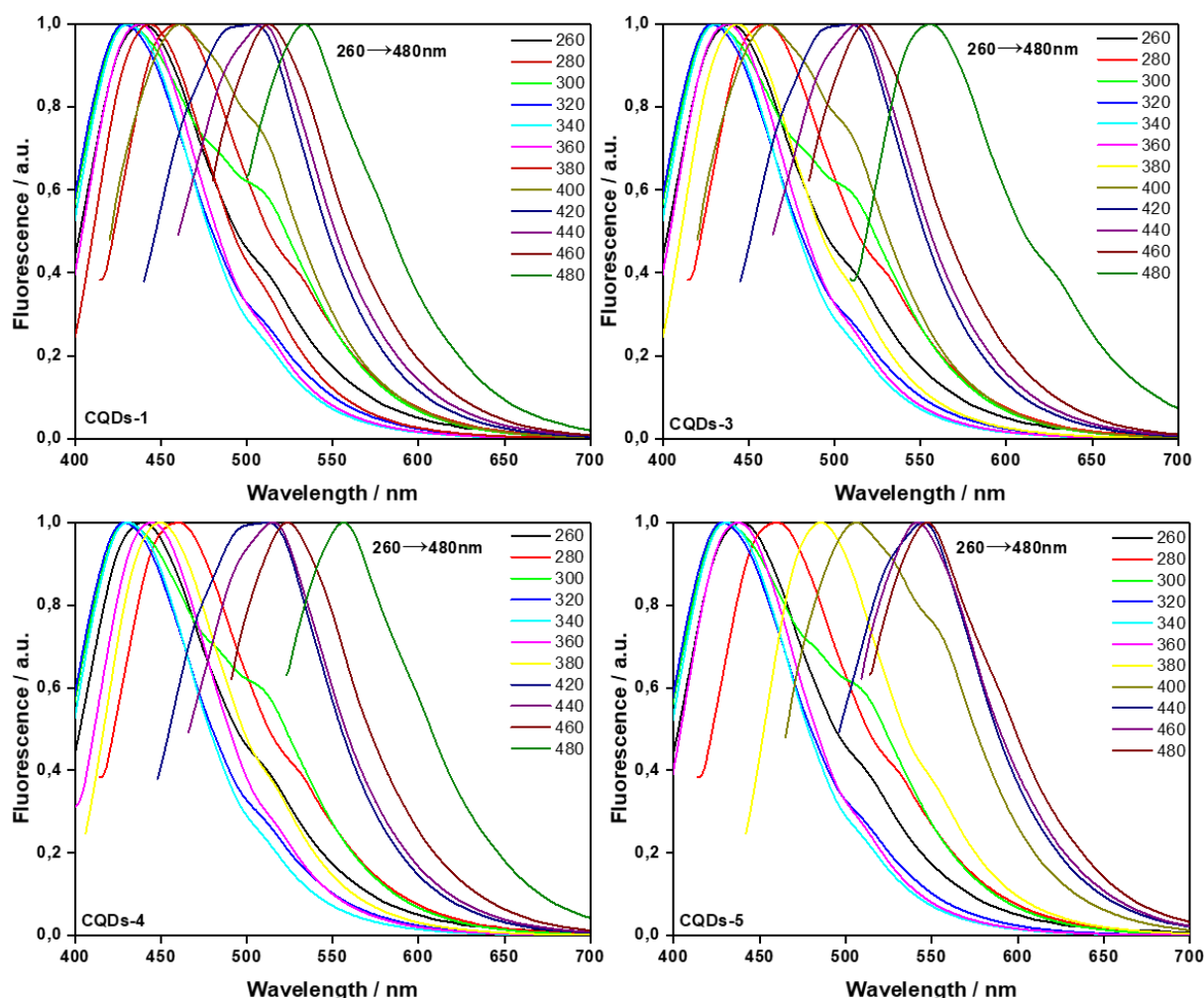
The morphologies of **CQDs-4** and **CQDs-5** are comparable to that of **CQDs-1** with an average diameter of  $6.25 \pm 0.17 \text{ nm}$  (**Figure 4.2E**) and a diffraction peak centred at  $25.3^\circ$  for **CQDs-4** (**Figure 4.3C**), and an average diameter of  $6.50 \pm 0.40 \text{ nm}$  and a diffraction peak centred at  $25.4^\circ$  for **CQDs-5**. The Raman spectra of the **CQDs-3**, **-4**, **-5** (**Figure 4.2D**) do not show any significant difference compared to that of **CQDs-1**, displaying the characteristic G and D bands with  $I_D/I_G = 0.93 \pm 0.15$  [20]. The colloidal stability of **CQDs-1** and **CQDs-3**, **-4**, **-5** in water, phosphate buffer (PBS, 10 mM) and Dulbecco's Modified Eagle's medium (M) was



also examined. All the particles had good long-term colloidal stability as seen from the photographs in **Figure 4.2F**.

The UV/Vis spectra of **CQDs-3**, **-4**, **-5** reveal the same features as the one of **CQDs-1** (**Figure 4.3B**), which are: an absorption maximum at  $\approx 242$  nm attributed to a  $\pi\text{-}\pi^*$  transition of C=C and a band at 344 nm attributed to  $n\text{-}\pi^*$  transition of C=O and C=N bonds [21, 22]. However, CQDs exhibit different fluorescent quantum yields: 61% (**CQDs-1**), 34% (**CQDs-3**), 9.8 (**CQDs-4**) and 7.3 (**CQDs-5**) with respect to that of quinine sulphate as a reference (**Figure 4.3C**). The wavelength-dependent fluorescence emission properties of the CQDs are similar (**Figure 4.3A**).

(A)



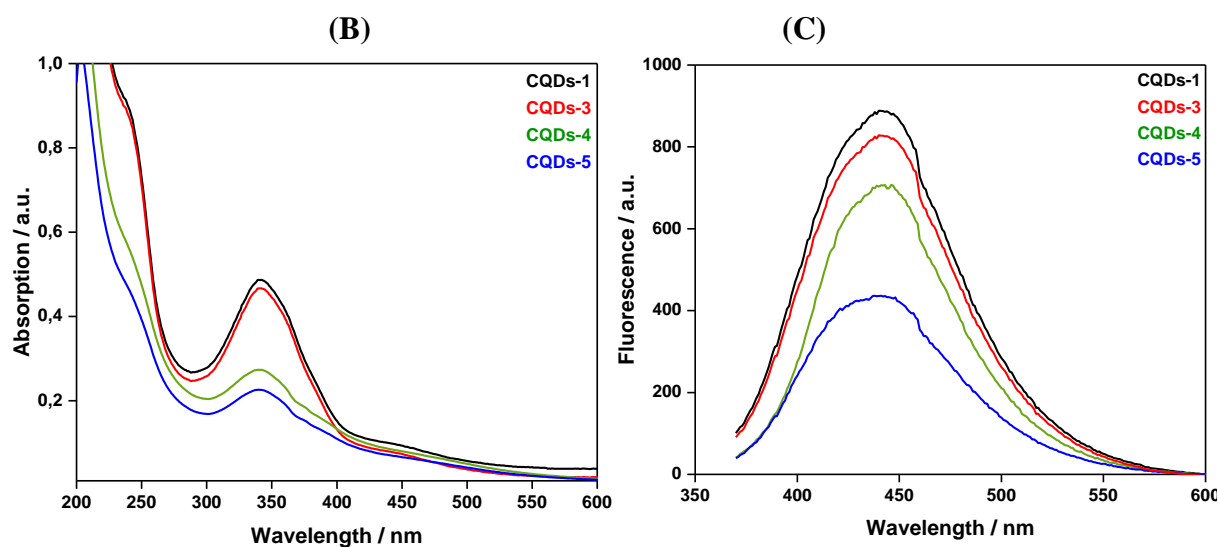


**Figure 4.3:** (A) Wavelength-dependent fluorescence emission of **CQDs-1**, **-3**, **-4** and **-5**; (B) UV-Vis absorption spectra of 100  $\mu\text{g mL}^{-1}$  dispersions of **CQDs-1**, **-3**, **-4** and **-5**; (C) Fluorescence spectra of **CQDs-1**, **-3**, **-4** and **-5** upon excitation at 350 nm.

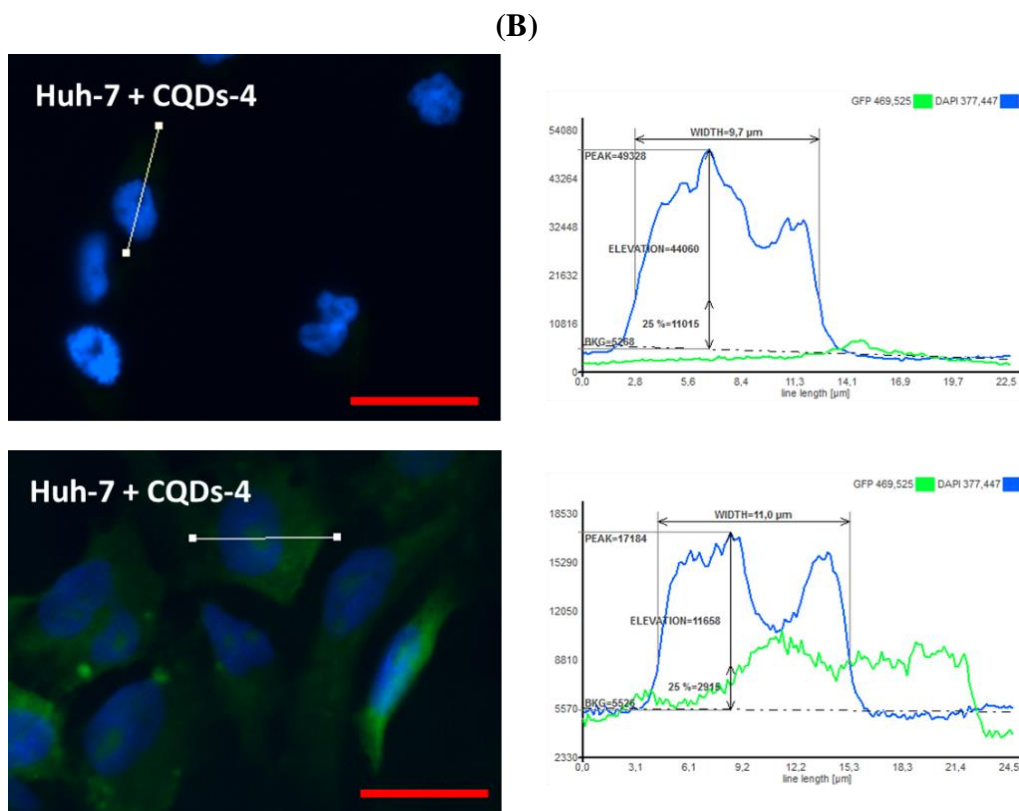
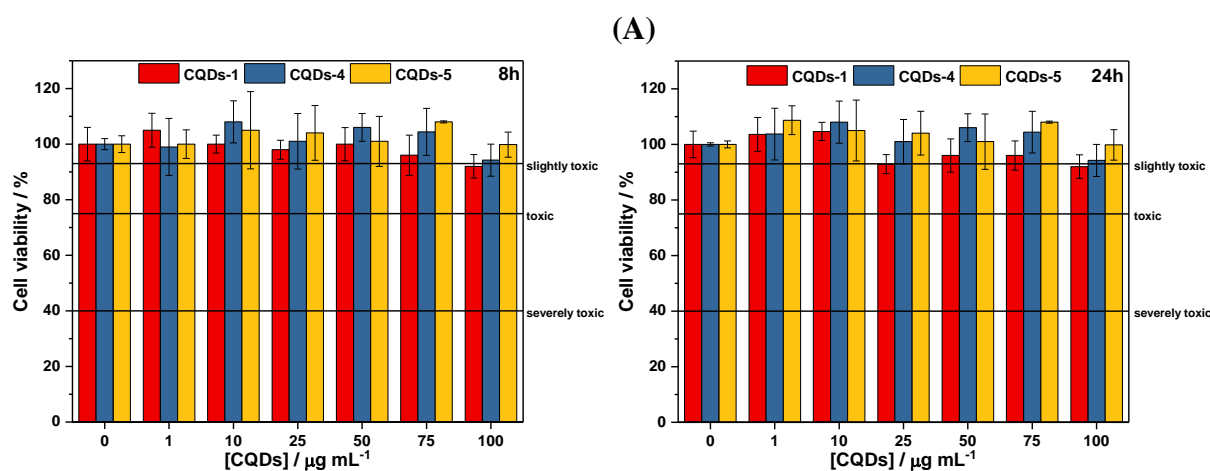
#### 4.2.2. Cytotoxicity assay

The cell toxicity of **CQDs-1**, **CQDs-4** and **CQDs-5** were established on Huh-7 cell lines after 8 h (time points corresponding to HCoV-229E infections) and 24 h incubation. The CQDs toxicity was evaluated using cell viability assessment by the resazurin assay, based on the conversion of a non-fluorescent dye to a fluorescent molecule by mitochondrial and cytoplasmic enzymes. All CQDs are non-toxic to Huh-7 cells even at the highest concentration (100  $\mu\text{g mL}^{-1}$ ) investigated when incubated for 8 and 24 h (**Figure 4.4A**). Neither the presence of boronic acid nor triazole units had a negative effect on cell toxicity.

The uptake mechanism proved to be the same for all of the nanostructures. Taking the example of **CQDs-4** (which later proves to have antiviral activity), Huh-7 cells were fixed after 1 h incubation at 4 °C and 37 °C. Then nuclei were stained with Hoechst 33342, a fluorescent dye for labelling DNA in fluorescence microscopy (**Figure 4.4B**). The green fluorescence, attributed to **CQDs-4**, is homogeneously distributed in the cytoplasm after 1 h when incubated at 37 °C, which confirms the internalisation of **CQDs-4** in the cells. The reduction of green fluorescence, observed in the cytoplasm after 1 h incubation at 4 °C, suggests that the active internalisation mechanism may be partially blocked and a small portion of CQDs was internalised by passive penetration.



The endocytosis of **CQDs-4** was in addition quantitatively evaluated using flow cytometry by treating Huh-7 cells with  $100 \mu\text{g mL}^{-1}$  of **CQDs-4** for 1 h at  $4^\circ\text{C}$  and for 1 h, 3 h and 6 h at  $37^\circ\text{C}$  (**Figure 4.4C**). The excitation fluorescence of **CQDs-4** at 488 nm allowed the analysis of intracellular CQDs. A progressive shift in the cell population towards higher fluorescence values was observed along with the increase of the incubation time, due to the time-dependent cellular uptake, most likely through endocytosis. Lower fluorescence intensity was observed upon incubation at  $4^\circ\text{C}$  for 1 h, where an active uptake process is blocked. The low percentage of green cells (0.8%) observed after 1 h at  $4^\circ\text{C}$  suggests that only a very low quantity of **CQDs-4** penetrates via passive uptake.



(C)

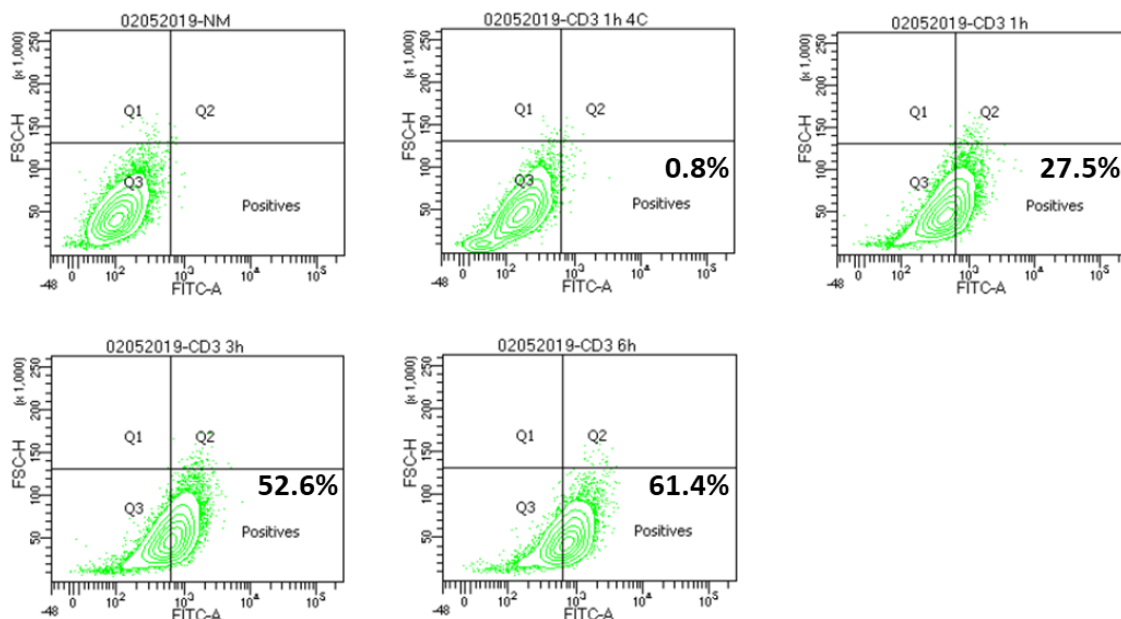


**Figure 4.4: Characterization of post-functionalized CQDs:** (A) Viability of Huh-7 cells treated with the different CQDs: Huh-7 cells were grown in 96-well plates ( $15 \times 10^3$  cells/well) with 100  $\mu$ L of culture medium containing increasing concentrations of CQDs for 8 h (left) and 24 h (right). The results, expressed as the percentage of viability, are the mean value of two independent experiments with each treatment performed in triplicate. Negative control: without CQDs; (B) Fluorescence microscopy of Huh-7 cells treated with 100  $\mu$ g mL<sup>-1</sup> of **CQDs-4** for 1 h at 4 °C (upper image) and 37 °C (lower image). The blue signal corresponds to the nuclei stained with Hoechst 33342, while the green signal is attributed to **CQDs-4**. Scale bars = 50  $\mu$ m. (C) Flow cytometry analysis of cellular uptake of CQDs in Huh-7 cells treated with 100  $\mu$ g mL<sup>-1</sup> of **CQDs-4** for 1 h at 4 °C and 1 h, 3 h and 6 h at 37 °C.

#### 4.2.3. Antiviral assay of first-generation CQDs

The antiviral activity of **CQDs-1**, **CQDs-4** and **CQDs-5** was evaluated on Huh-7 cells monolayers, infected with HCoV-229E-Luc (**Figure 4.5A**). Addition of **CQDs-1** 1 h after the infection and further incubation for 6 h at 37 °C shows no inhibition of the infection. This contrasts to **CQDs-4**, where a concentration-dependent virus inactivation is observed with an estimated  $EC_{50} = 52 \pm 8$   $\mu$ g mL<sup>-1</sup> (**Figure 4.5B**). Addition of mannose to **CQDs-4** results in a complete loss of antiviral activity of the latter at low particle concentrations, with some antiviral activity above 50  $\mu$ g mL<sup>-1</sup> CQDs. These data reveal two important findings. First, it highlights that boronic acid functions, the mode of action of which is the selective and reversible formation of tetravalent boronate complexes with *cis*-diols – and thus glycan units [23] – are interacting with HCoV-229E. **CQDs-4** are in this context speculated to be pseudolectins, targeting the S protein of HCoV-229E via a lectin-carbohydrate binding mechanism, similar to that of the oligomannose-specific lectin Griffithsin [24]. Thus, the addition of mannose blocking the

antiviral activity is in favour of this mechanistic assumption. The remaining little antiviral activity of **mannose-saturated CQDs-4** might be due to the presence of the triazole function at the particles' surface. Indeed, control particles **CQDs-5**, bearing no boronic acid function but a triazole ring, display some antiviral activity, even though largely decreased when compared to **CQDs-4**.

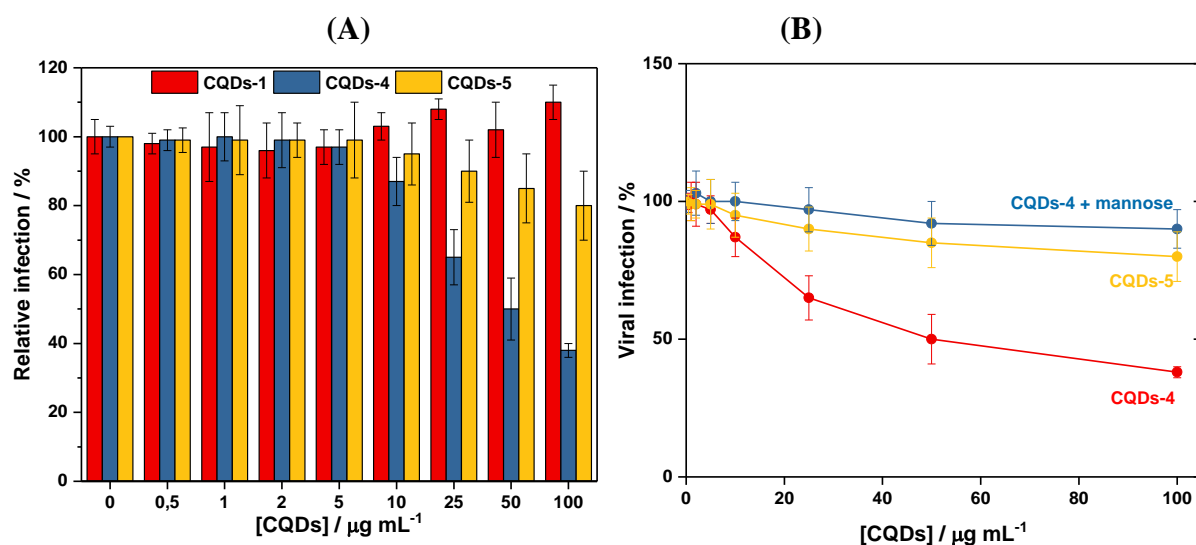


**Figure 4.5. Viral infection inhibition in the presence of CQDs:** (A) Viral inhibition using CQDs at various concentrations. Huh-7 cells ( $1.5 \times 10^4$  cells/well) were inoculated with HCoV-229E-Luc for 1 h (in an atmosphere with 5%  $\text{CO}_2$  at 37  $^\circ\text{C}$ ) in the presence or absence of different CQDs in medium without FBS for 1 h. Afterwards, the inoculum was removed and replaced with DMEM with FBS for 6 h. Cells were lysed, and luciferase activity quantified. The results expressed as the percentage of infection normalised to the control without CQDs, which is expressed as 100% infection. Data are means of two independent experiments with each treatment performed in triplicate. (B) Determination of  $\text{EC}_{50}$  for **CQDs-4** and **CQDs-5**, and the effect of viral inhibition using **CQDs-4** after incubation with mannose (2:1) overnight at 4  $^\circ\text{C}$ .

### 4.3. Second- generation of CQDs inhibitors of host cell infections by HCoV-229E coronavirus

#### 4.3.1. Formation and characterisation of CQDs-6, -7, -8

To validate if boronic acid functions can be formed directly on CQDs, hydrothermal carbonisation of phenylboronic acid and 4-aminophenylboronic acid were performed, resulting in **CQDs-6** and **CQDs-7**, respectively (**Figure 4.6A**). As a control, hydrothermal carbonisation of aniline and poly(ethylene glycol) PEG<sub>600</sub>, both lacking boronic acid functions, was conducted. Unfortunately, several attempts to prepare CQDs from aniline as a starting material failed.

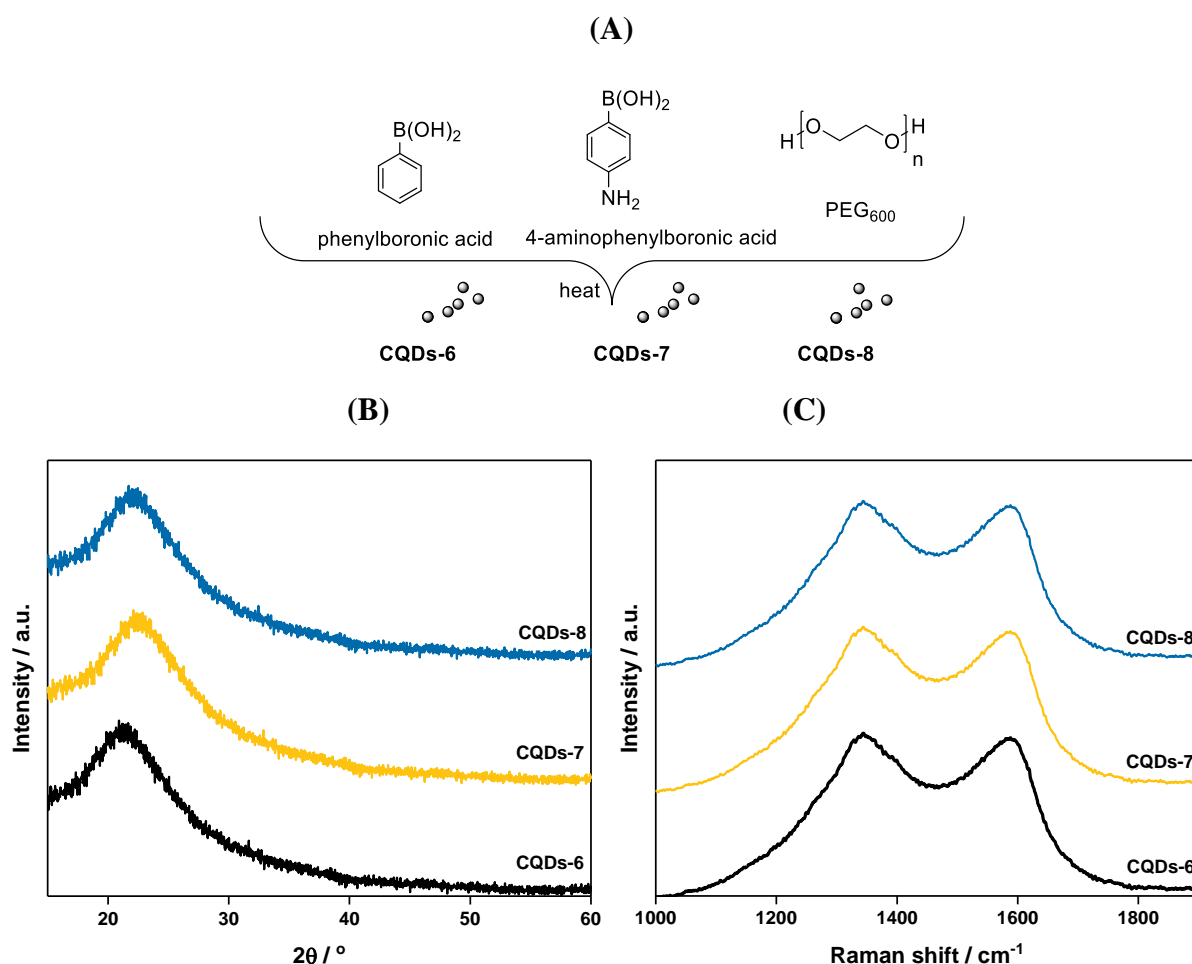


**Figure 4.6:** (A) Schematic representation of the hydrothermal carbonisation of the different organic precursors employed for the synthesis of **CQDs-6**, **-7**, **-8**; (B) XRD diffractograms of **CQDs-6**, **-7**, **-8**; (C) Raman spectra of **CQDs-6**, **-7**, **-8**; (D) TEM, magnified TEM and size distribution histograms of **CQDs-6**, **-7**, **-8**.

The TEM images of **CQDs-6**, **-7** and **-8** appear in **Figure 4.7**. **CQDs-6** have an average diameter of  $9.2 \pm 0.3$  nm, somehow larger than **CQDs-7**, which have a size distribution centred on  $7.6 \pm 0.2$  nm (**Table 4.2**). The particles formed from PEG (**CQDs-8**) display a spherical shape, with an average diameter of  $8.0 \pm 0.2$  nm. The XRD diffractograms (**Figure 4.6B**) display broad diffraction peaks centred at  $21.3^\circ$  for **CQDs-6**,  $22.6^\circ$  for **CQDs-7**, and  $22.1^\circ$  for **CQDs-8**, corresponding to an interlayer spacing of 0.42 nm (**CQDs-6**), 0.40 nm (**CQDs-7**), and 0.39 nm (**CQDs-8**). Raman spectra of **CQDs-6**, **-7** and **-8** (**Figure 4.6C**) remain similar to that of **CQDs-1**, displaying the characteristic G and D bands with  $I_D/I_G = 0.93 \pm 0.15$  for all particles.

The UV/Vis absorption spectra of the CQDs are depicted in **Figure 4.8B**. The absorption shoulders at 250-300 nm correspond to the typical absorption of an aromatic  $\pi$

system, in accordance with the literature data [25]. The CQDs exhibit different fluorescence quantum yields (QY) of 0.03 (CQDs-6), 0.05 (CQDs-7), and 0.09 (CQDs-8) (Figure 4.8C). The wavelength-dependent fluorescence emission properties of the CQDs are comparable (Figure 4.8A). The zeta potential and hydrodynamic size of CQDs-6, -7 and -8 are summarised in Table 4.2.

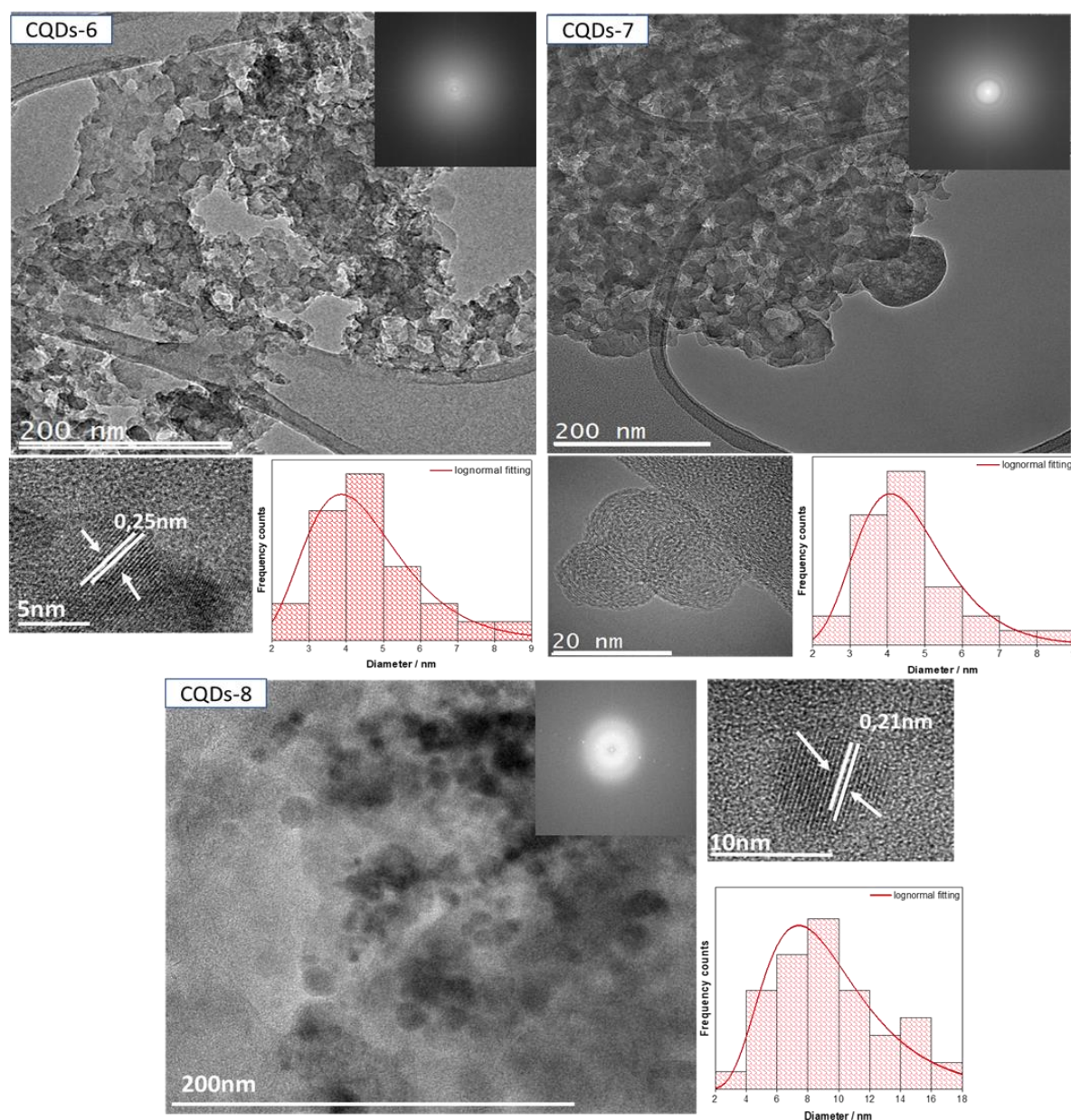
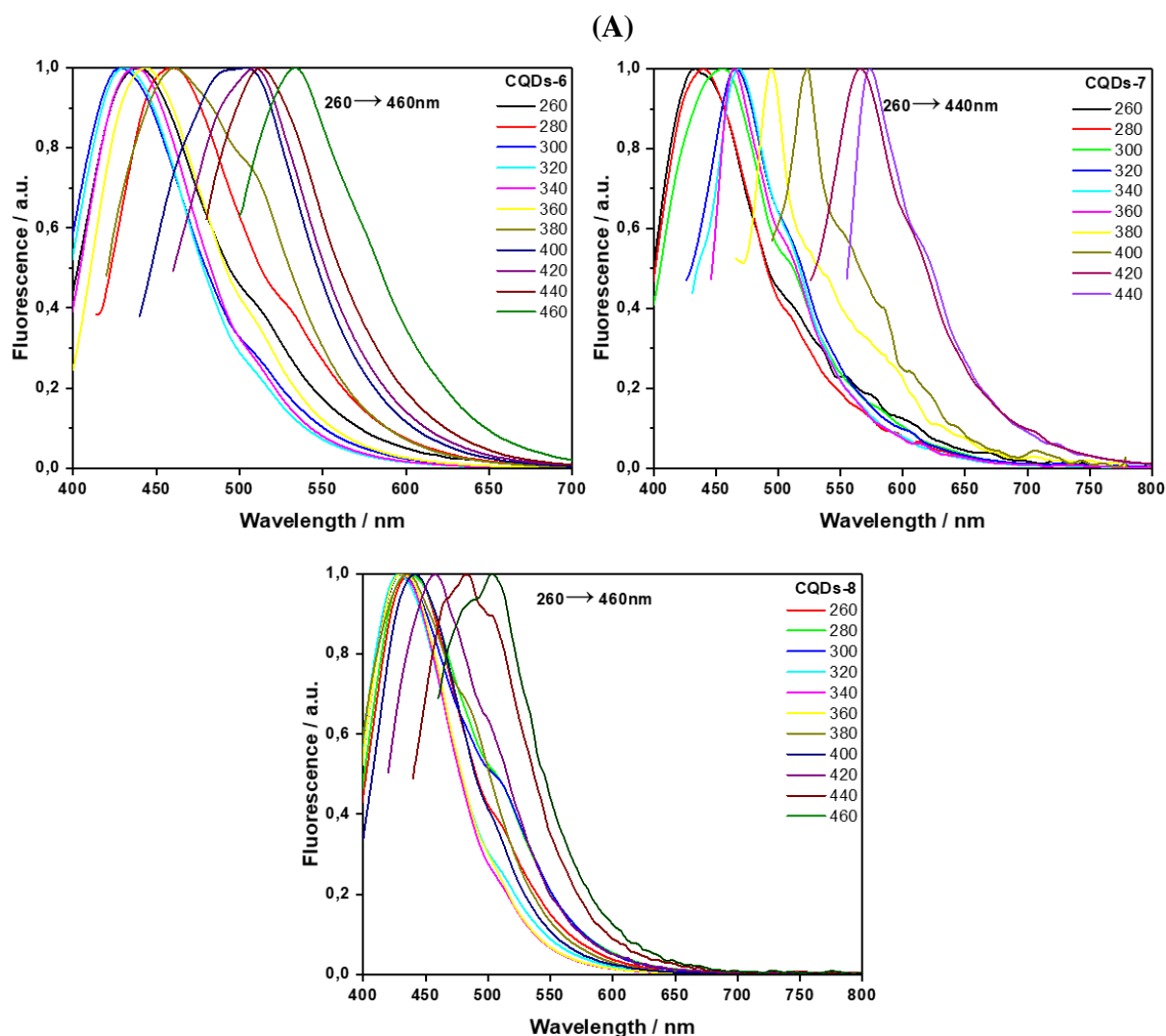


**Figure 4.7:** TEM, magnified TEM and size distribution histograms of CQDs-6, -7, -8.

The chemical composition of the particles was further assessed using X-ray photoelectron spectroscopy and  $^{11}\text{B}$  boron NMR. The XPS survey spectra of the different CQDs (Table 4.2) indicate the presence of  $\text{C}_{1s}$ ,  $\text{O}_{1s}$ ,  $\text{N}_{1s}$  and  $\text{B}_{1s}$  in agreement with the chemical



composition of the precursors. Deconvolution of the  $C_{1s}$  XPS spectrum of **CQDs-6** reveals bands located at 284.3 eV (C=C,  $sp^2$ ); 285.1 eV (C-H, C-B) and a small contribution centred at 287.0 eV (C=O) (**Figure 4.9C**). The boron content is lower than that reported by Shen and Xi [26] but comparable to that reported by Wang *et al.* [27]. This indicates that some of the phenylboronic acid groups were carbonised under our experimental conditions. The low B content might also indicate doping rather than the presence of boronic acid functions. **CQDs-7** particles depict binding energy bands at 284.3 eV (C=C,  $sp^2$ ), 285.2 eV (C-H, C-B), 287.3 eV (C=O) and a band at 290.3 eV due to O–C=O functions. In the case of **CQDs-8**, the  $C_{1s}$  XPS spectrum comprises three different carbon features: the graphitic C=C at 283.4 eV, 284.9 eV (C-H) and 286.4 eV (C-O, C-N). Analysis of the  $N_{1s}$  high resolution spectrum of **CQDs-7** reveals the presence of surface  $-NH_2$  groups (**Figure 4.9B**).





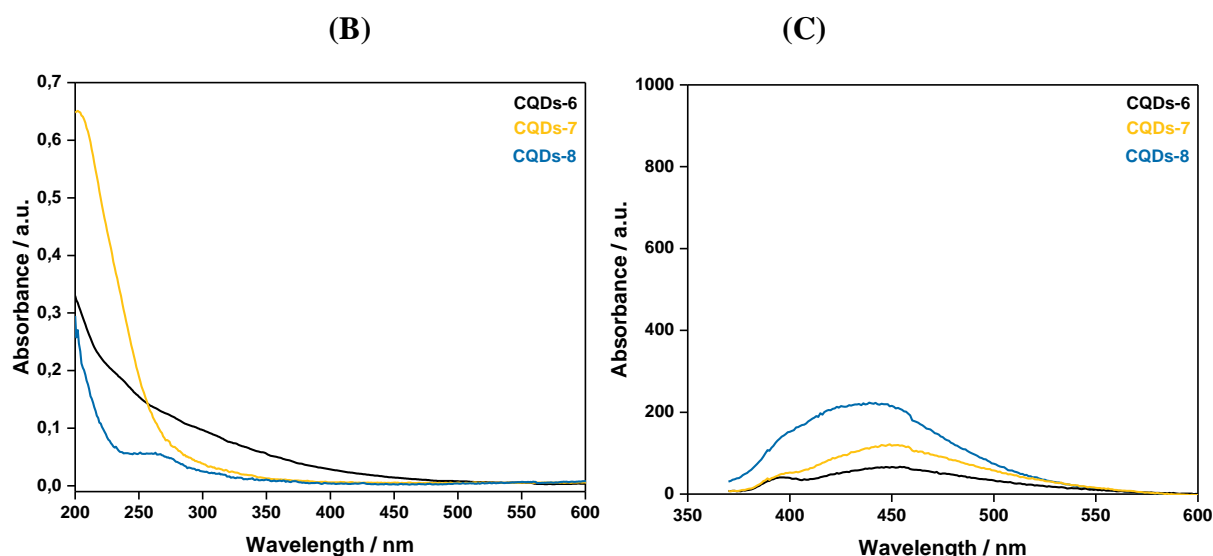


**Figure 4.8:** (A) Wavelength-dependent fluorescence emission properties of **CQDs-6, -7, -8**; (B) UV-Vis absorption spectra of 100  $\mu\text{g mL}^{-1}$  suspensions of **CQDs-6, -7, -8**; (C) Fluorescence spectra of **CQDs-6, -7, -8** upon excitation at 350 nm.

**Table 4.2:** Physico-chemical characteristics of **CQDs-6, -7, and -8**.

CQDs	$\zeta$ (mV) <sup>1</sup>	Size (nm)	Hydrodynamic size (nm) <sup>2</sup>	PDI <sup>3</sup>	C <sub>1s</sub> <sup>4</sup> (at. %)	O <sub>1s</sub> <sup>4</sup> (at. %)	N <sub>1s</sub> <sup>4</sup> (at. %)	B <sub>1s</sub> <sup>4</sup> (at. %)
<b>CQDs-6</b>	$-20.0 \pm 5.5$	$7.6 \pm 0.2$	$13 \pm 1.8$	$0.14 \pm 0.09$	77.4	21.7	-	0.9
<b>CQDs-7</b>	$-41.2 \pm 1.0$	$9.2 \pm 0.3$	$12 \pm 0.2$	$0.11 \pm 0.06$	69.4	21.5	7.4	1.7
<b>CQDs-8</b>	$-39.2 \pm 1.5$	$8.0 \pm 0.2$	$13 \pm 3.1$	$0.28 \pm 0.34$	60.8	39.2	-	-

<sup>1</sup> $\zeta$ : zeta potential; <sup>2</sup>The hydrodynamic size was recorded at 37 °C; <sup>3</sup>PDI: Polydispersity index; <sup>4</sup>XPS was used to determine the atomic percentage of the elements respectively.

The FTIR spectra (**Figure 4.9A**) of **CQDs-6, -7, -8** exhibit a distinct band at  $3465\text{ cm}^{-1}$  attributed to the stretching vibration of -OH groups and bands around  $2874$  and  $2924\text{ cm}^{-1}$ , due to  $\text{CH}_2$  stretching. The sharp band at  $1618\text{ cm}^{-1}$  is assigned to graphitic  $\text{C}=\text{C}$ , and the C-H deformation mode is observed at  $1460\text{ cm}^{-1}$ . The  $\text{C}=\text{O}$  band at  $\sim 1780\text{-}1650\text{ cm}^{-1}$  is also visible in all cases. In the case of **CQDs-7**, the band at  $1090\text{ cm}^{-1}$  might be due to C-B stretching modes. This band is less defined in the case of **CQDs-6**, which might underline doping rather than the presence of boronic acid functions. The FTIR spectrum of **CQDs-8** displays the C-O-C bands of the PEG units at  $1043\text{ cm}^{-1}$ .

**CQDs-6, -7, -8** exhibited a negative zeta potential in water (pH 7.4) at room temperature and showed excellent long-term stability even in a biological medium such as Dulbecco's Modified Eagle's medium (**Figure 4.9D**).

The cytotoxicity of CQDs 5-7 (**Figure 4.10A**) is comparable to the CQDs discussed before (**Figure 4.4A**), with CQDs-7 being slightly more toxic at concentrations  $>25\text{ }\mu\text{g mL}^{-1}$  after 24

h incubation. This might be due to the presence of  $\text{NH}_2$  groups on these particles. The uptake mechanism of these particles was comparable and is exemplified using CQDs-7 in **Figure 4.10B**. Due to the low intrinsic fluorescence of CQDs-7 particles, they were labelled with fluorescein-NHS.

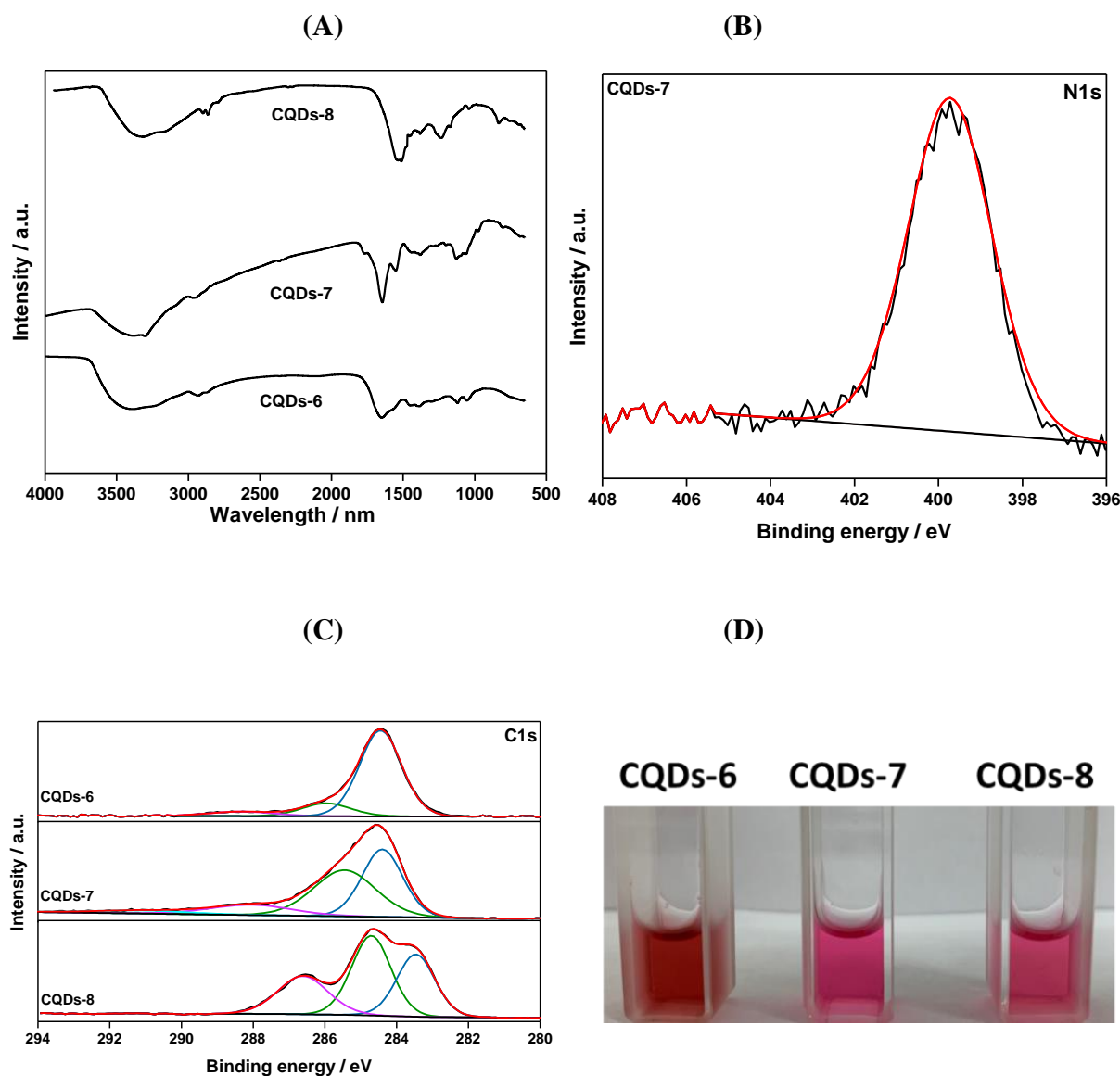


**Figure 4.9:** (A) FTIR spectra of CQDs-6, -7, -8; (B) N<sub>1s</sub> high resolution XPS spectrum of CQDs-7; (C) C<sub>1s</sub> high resolution XPS spectrum of CQDs-6, -7, -8; (D) Photographs of CQDs CQDs-6, -7, -8 suspensions (1mg mL<sup>-1</sup>) after 1 month in Dulbecco's Modified Eagle's medium.

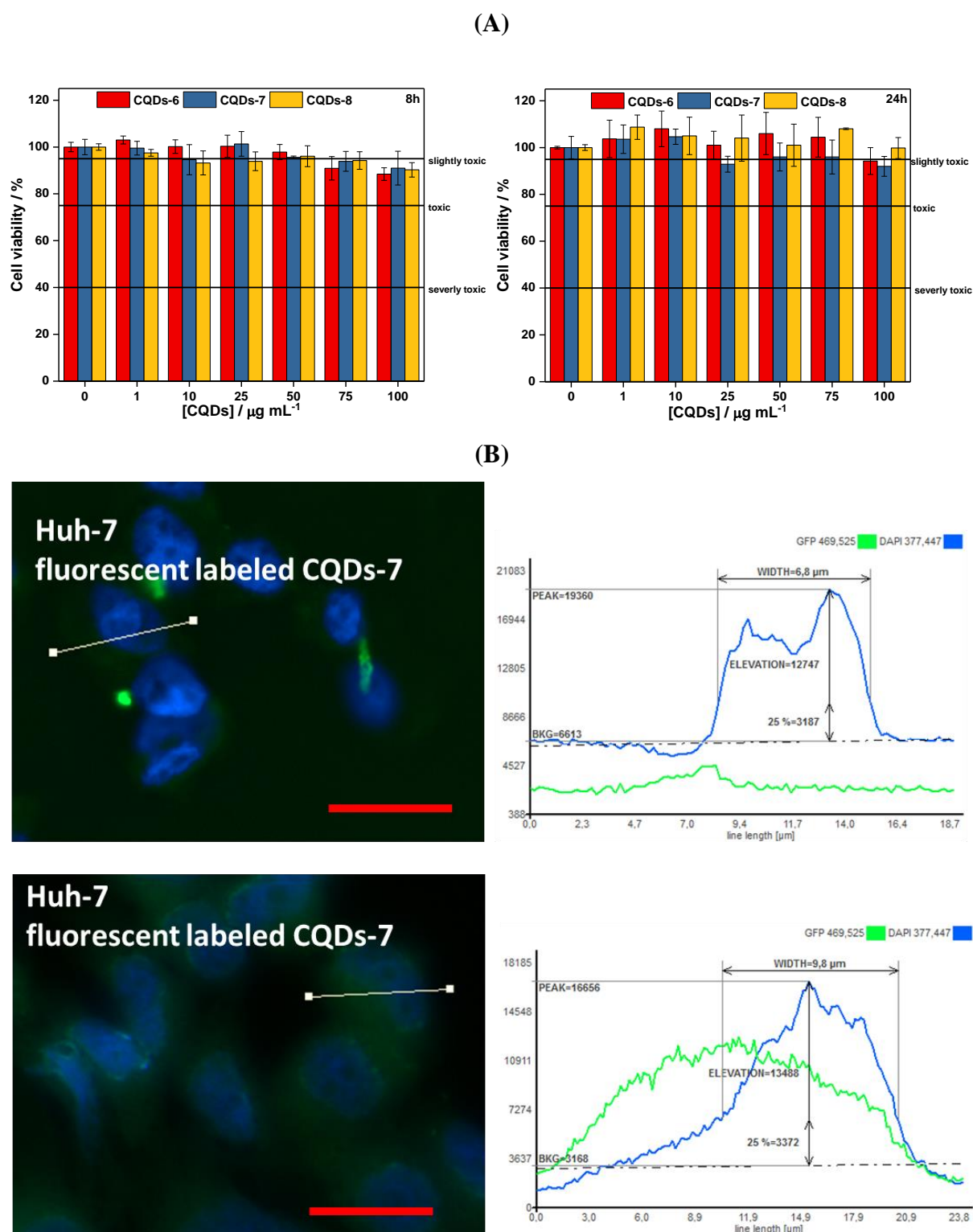


**Figure 4.10: Cell viability of CQDs-6, -7, -8:** (A) Viability of Huh-7 cells grown in 96-well plates ( $15 \times 10^3$  cells/well) with 100  $\mu\text{L}$  of culture medium containing an increasing concentration of **CQDs-6, -7, -8** labelled for 8 and 24 h. The results, expressed as the percentage of viability, are the mean value of two independent experiments with each treatment performed in triplicate. Negative control: without CQDs; (B) **Fluorescence microscopy** of Huh-7 cells treated with 100  $\mu\text{g mL}^{-1}$  of **CQDs-6** labelled with fluorescein for 1 h at 4 °C (upper) and 37 °C (lower). The blue signal corresponds to the nuclei stained with Hoechst 33342, while the green signal is attributed to CQDs. Scale bars = 50  $\mu\text{m}$ .

### 4.3.2. Antiviral assay of second-generation CQDs-6, -7, -8

Addition of **CQDs-8** 1 h after infection and further incubation for 6 h at 37 °C showed no inhibition of infection (**Figure 4.11A**), indicating that these particles are not interfering with HCoV-229E-Luc entry or replication. **CQDs-6** and **CQDs-7** display a concentration-dependent virus inactivation. The dose-response curve (**Figures 4.11B**) reveals that the effective concentration to achieve 50% inhibition ( $EC_{50}$ ) against HCoV-229E-Luc infection is  $5.2 \pm 0.7 \mu\text{g mL}^{-1}$  for **CQDs-7** and  $11.6 \pm 1.1 \mu\text{g mL}^{-1}$  for **CQDs-6**. Surprisingly, the addition of mannose did not result in a loss of the antiviral activity (**Figure 4.11C**), as observed previously for **CQDs-4**.

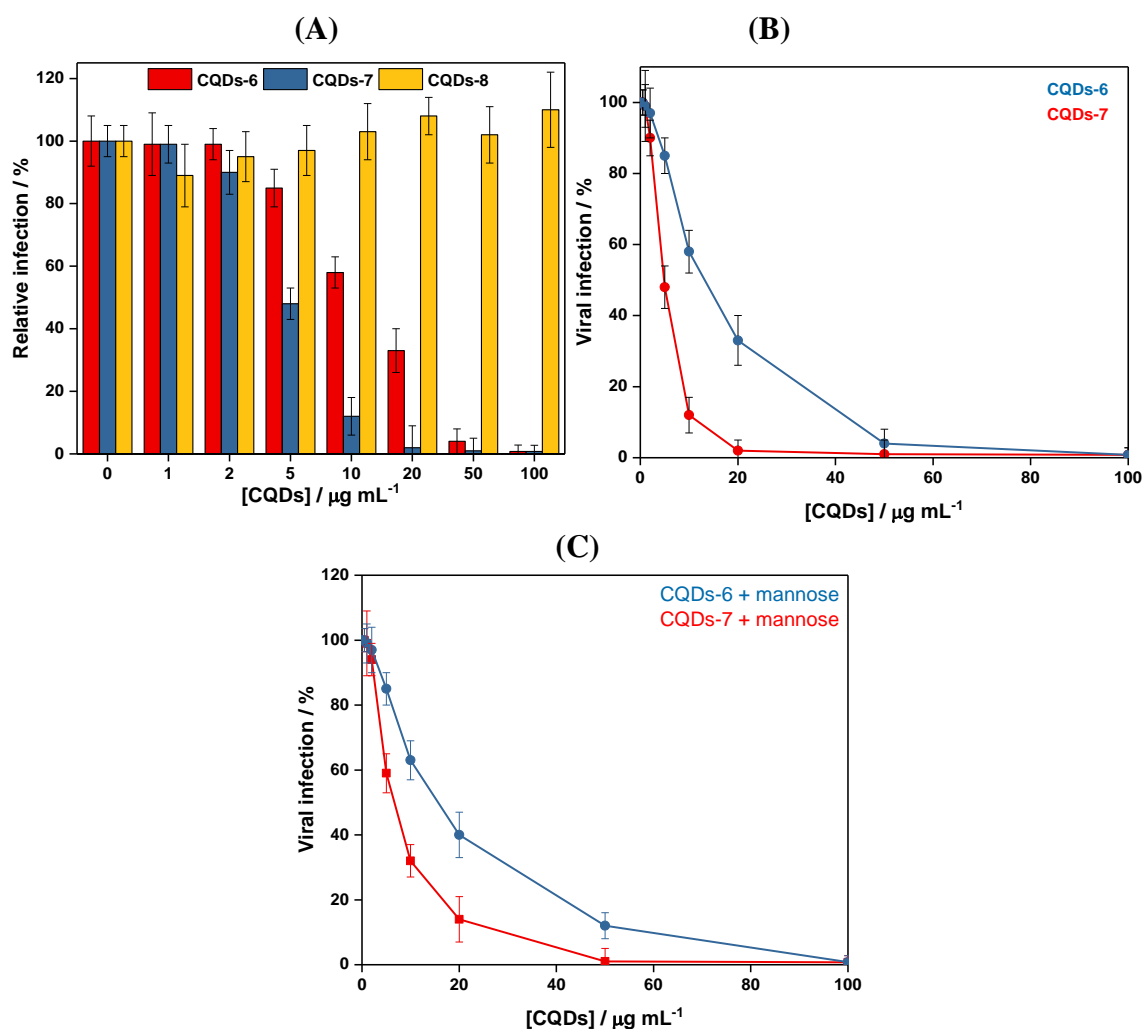


**Figure 4.11: Viral infection inhibition in the presence of CQDs-6, -7, -8:** (A) Viral inhibition using **CQDs-6**, -**7**, -**8** at various concentrations. Huh-7 cells ( $1.5 \times 10^4$  cells/well) were inoculated with HCoV-229E-Luc for 1 h (in an atmosphere with 5%  $\text{CO}_2$  at 37 °C) in the presence or absence of different CQDs in medium without FBS for 1 h. Afterwards, the inoculum was removed and replaced with DMEM with FBS for 6 h. Cells were lysed, and luciferase activity quantified. The results expressed as the percentage of infection normalised to the control without CQDs, which is expressed as 100% infection. Data are means of two independent experiments with each treatment performed in triplicate; (B) Determination of  $EC_{50}$  for **CQDs-6** and **CQDs-7**; (C) Viral inhibition using **CQDs-6** and **CQDs-7** after incubation with mannose (2:1) overnight at 4 °C.

Performing  $^{11}\text{B}$  NMR analysis of **CQDs-6** and **CQDs-7** (**Figure 4.12**) and comparing the resulting spectra to those of the respective starting materials, 4-aminophenylboronic acid (4APBA) and phenylboronic acid (PBA) (**Figure 4.12**), reveals large differences in the chemical composition. 4-aminophenylboronic acid and phenylboronic acid both exhibit a strong signal at around 29 ppm, in accordance with literature data for  $-\text{B}(\text{OH})_2$  functions [28, 29]. The small-signal at about 20 ppm arises most likely from residual  $\text{B}(\text{OR})_3$  often used in boronic acid synthesis [30]. The  $^{11}\text{B}$  NMR spectra of **CQDs-6** and **CQDs-7** display, on the other hand, peaks at 13 ppm (**CQDs-6**) and a band at 10 ppm with a shoulder at 12 ppm for **CQDs-7**. This means that, during the hydrothermal reaction, boron was incorporated through doping rather than in the form of a surface function. Indeed, one-pot solvothermal synthesis using aminophenylboronic acid as a precursor was reported by Wang *et al.* to result in N and B co-doped CQDs. [31] They reported the presence of 0.7 at.% B measured by XPS, which is comparable to the amount obtained in the present work (**Table 4.2**).

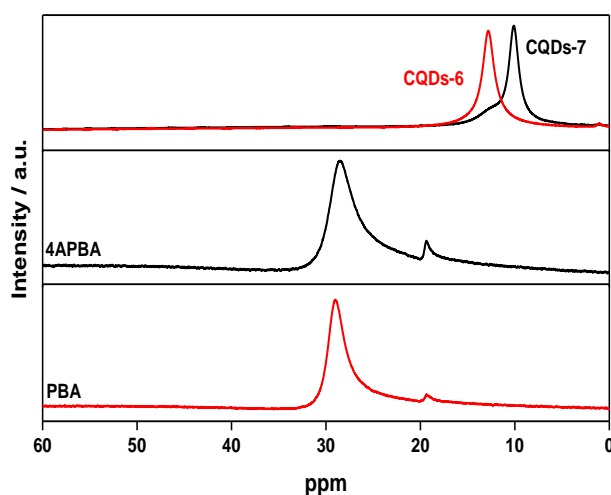


**Figure 4.12:**  $^{11}\text{B}$  NMR spectra of **CQDs-6** and **CQDs-7** prepared by hydrothermal method from phenylboronic acid (PBA) and 4-aminophenylboronic acid (4-APBA) precursors respectively, and  $^{11}\text{B}$  NMR spectra of 4-aminophenylboronic acid (4-APBA) and phenylboronic acid (PBA) starting materials.

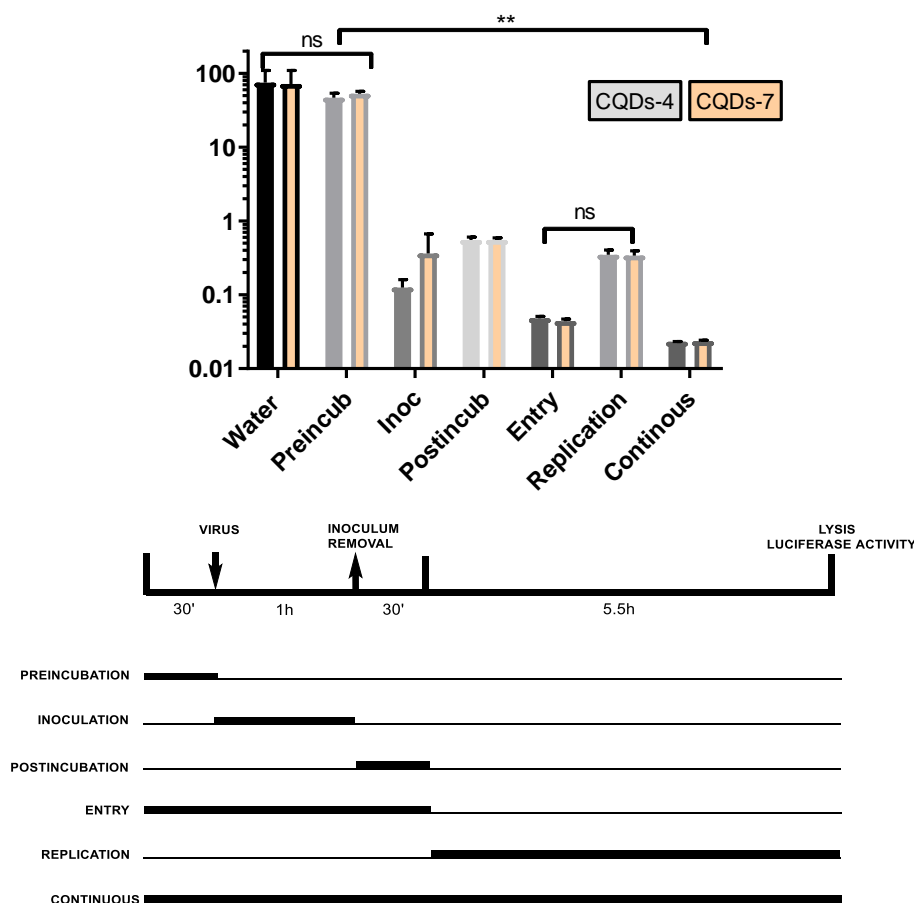
#### 4.4. Mechanism of action

We further investigated the mechanism of action of **CQDs-4** and **CQDs-7** on viral infection by performing a time-of-addition assay. CQDs (at  $10 \mu\text{g mL}^{-1}$ ) were added at different time points during infection, as represented in **Figure 4.13A**. As expected, a strong inhibition of the infection was observed when CQDs were added 1 h after inoculation. Moreover, the inhibition activity of CQDs was stronger when the nanoparticles were added during the entry step, i.e. 30 min before and after inoculation and during inoculation. These results are in agreement with our hypothesis of the interaction of CQDs with HCoV-229E S protein, or the interaction of CQDs with entry factors. Surprisingly, a strong inhibitory activity of CQDs was also observed when they were added 5.5 h after the entry step, that is at the replication step. The inhibition is not significantly different for the entry step compared to the replication step. It suggests that, in addition to its major effect on HCoV-229E entry, CQDs can also affect the genomic replication of this virus. It could potentially be explained by an interaction between the CQDs and a cell surface protein leading to signal transduction affecting viral replication, or by interaction with cytosolic proteins as CQDs are internalised.

To determine if CQDs are interacting directly with viral particles, HCoV-229E-Luc was incubated with CQDs at  $10 \mu\text{g mL}^{-1}$  for 30 min at  $37^\circ\text{C}$  before inoculation. The inoculum was diluted ten times, leading to a final concentration of CQDs of  $1 \mu\text{g mL}^{-1}$ , and an infection assay was performed. In parallel, Huh-7 cells were inoculated with HCoV-229E-Luc in the presence of CQDs at 1 or  $10 \mu\text{g mL}^{-1}$ . The inoculum titers were kept constant in different conditions. The results showed that the pre-incubation of the virus with CQDs at high concentration does not impair HCoV-229E infection, meaning that CQDs are not interacting with the virus before infection (**Figure 4.13B**). Taken together, our results are in favour of an interaction of the CQDs with cellular factors, which could also explain that their antiviral effects occur at different steps of the infection.



(A)



(B)

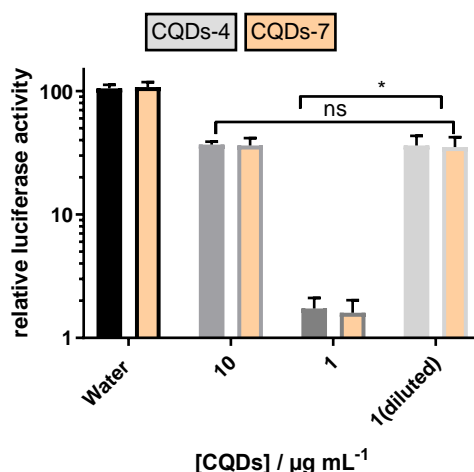


**Figure 4.13: Time-of-addition assay of CQDs-4 and -7 during HCoV-229E infection.** (A) CQDs at  $10 \mu\text{g mL}^{-1}$  were added at different time points during infection of Huh-7 cells with HCoV-229E-Luc as shown below the graph. Cells were lysed, and luciferase activity quantified. Results are representative of 3 experiments performed in triplicate. Error bars represent SD of three independent values; (B) Virus HCoV-229E-Luc was pre-incubated with CQDs at  $10 \mu\text{g mL}^{-1}$  for 30 min at  $37^\circ\text{C}$ . The mixture was diluted 10 times in culture medium leading to a final concentration of CQDs of  $1 \mu\text{g mL}^{-1}$  and inoculated on Huh-7 cells for 1 h. In parallel, Huh-7 cells were inoculated with HCoV-229E-Luc in the presence of CQDs at 1 and  $10 \mu\text{g mL}^{-1}$  for 1 h. Cells were lysed 7 h post-infection, and luciferase activity quantified. Results are means of 3 experiments performed in triplicate. Error bars represent means of three independent values. Statistic evaluation (confidence interval of 95%), ns ( $p > 0.99$ ); \* ( $p < 0.1$ ); \*\* ( $p < 0.01$ ).

## 4.5. Conclusions

The viral infection cycle produces important biological and structural changes in the host cell, resulting in cell damage. The possibility to interfere with viral attachment to cells as well as with viral replication to reduce viral infection and spreading is an appropriate antiviral approach. We presented here the antiviral performance of seven different CQDs with their main features summarised in **Table 4.3**. Three of these CQDs (**CQDs-4, -6, -7**) proved to interfere significantly with HCoV-229E-Luc infection in a concentration-dependent manner. While **CQDs-6** showed the most modest antiviral activity, the estimated  $EC_{50}$  value decreased considerably from **CQDs-4** (boronic acid-modified quantum dots, derived from ethylenediamine/citric acid as carbon precursors;  $EC_{50} = 52 \pm 8 \mu\text{g mL}^{-1}$ ) to **CQDs-7** ( $5.2 \pm 0.7 \mu\text{g mL}^{-1}$ ). The presence of boronic acid functions proved to be essential for **CQDs-4** to exhibit antiviral activity, whereas **CQDs-6** and **CQDs-7** did not carry any substantial amount of boronic acid functions, as revealed by  $^{11}\text{B}$  NMR and confirmed by mannose addition experiments. These findings reveal the complex nature of the identification of viral inhibitors for human coronaviruses such as HCoV-229E-Luc. Mechanistic studies suggest that the particles are acting at the early stage of the virus infection, especially through the inhibition of the virus entry which could itself be due to the inhibition of protein S-receptor interaction with the host cell membrane. In addition, all of the three different particles interfere with the viral replication step, something less common. These results are extremely encouraging to replace currently used antiviral agents such as ribavirin, and IFN is known to have major side effects such as confusion, short-term memory loss, deficits in executive functions, as well as extrapyramidal effects. Further experimental confirmations are required to know if this approach can be extrapolated to other coronaviruses (notably to the clinically relevant MERS-CoV) and to validate the potential of these nanostructures as alternative anti-MERS therapeutics or anti-MERS approaches able to confront this severe and life-threatening disease. Additionally, the precise *in vivo* behaviour of such particles needs to be understood in the future, so that the different possible inhibition mechanisms can be elucidated.

**Table 4.3:** Summary of the main features of CQDs-1 to -8.

CQDs	Size (nm)	charge	functions	antiviral	EC <sub>50</sub> / $\mu\text{g mL}^{-1}$
CQDs-1	4.5 $\pm$ 0.2	-9.9	NH <sub>2</sub> , COO <sup>-</sup>	-	
CQDs-3	5.5 $\pm$ 0.3	-7.9	N <sub>3</sub>	-	
CQDs-4	6.3 $\pm$ 0.4	-15.9	triazole, R-B(OH) <sub>2</sub>	++	52 $\pm$ 8
CQDs-5	6.5 $\pm$ 0.4	-15.9	triazole, OH	+	n.d.
CQDs-6	7.6 $\pm$ 0.2	-20.0	R-B(OH) <sub>2</sub>	+++	11.6 $\pm$ 1.1
CQDs-7	9.2 $\pm$ 0.3	-41.2	R-B(OH) <sub>2</sub> , NH <sub>2</sub>	++++	5.2 $\pm$ 0.7
CQDs-8	8.0 $\pm$ 0.3	-39.2	PEG	-	

n.d. not determinable

## 4.6. References

1. Loczechin, A., et al., *Functional Carbon Quantum Dots as Medical Countermeasures to Human Coronavirus (HCoV)*. ACS Applied Materials & Interfaces, 2019.
2. Nii-Trebi, N.I., *Emerging and Neglected Infectious Diseases: Insights, Advances, and Challenges*. BioMed Research International, 2017. **2017**: p. 15.
3. <http://www.who.int/csr/research-and-development/meeting-report-prioritization.pdf>.
4. Al Hajjar, S., Z.A. Ziad A. Memish, and K. McIntosh, *Middle East Respiratory Syndrome Coronavirus (MERS-CoV): A Perpetual Challenge*. Ann Saudi Med. , 2013. **33**: p. 427–436.
5. <http://www.emro.who.int/pandemic-epidemic-diseases/mers-cov/mers-situation-update-november-2017.html>.
6. Mo, Y. and D. Fisher, *A review of treatment modalities of Middle Respiratory Syndroms*. J. Antimicrob. Chemother., 2016. **71**: p. 3340-3350.
7. Uyeki, T.M., et al., *Development of Medical Countermeasures to Middle East Respiratory Syndrome Coronavirus*. Emerging Infect. Disease, 2016. **22**: p. e1.
8. Zumla, A., et al., *Coronavirus-drug discovery and therapeutic options*. Nat. Rev., 2016. **15**: p. 327.
9. Du, L., et al., *MERS-CoV spike protein: a key target for antivirals*. Exp. Opin. Ther. Targets, 2017. **21**: p. 131-143.
10. Lu, L., et al., *Structures-based discovery of Middle East respiratory syndrome coronavirus fusion inhibitor*. Nat. Commun., 2014. **5**: p. 3067.
11. Szunerits, S., et al., *Nanostructures for the Inhibition of Viral Infections*. Molecules 2015. **20**: p. 14051
12. Lim, S.Y., W. Shen, and Z. Gao, *Carbon quantum dots and their applications*. Chem. Soc. Rev. , 2015. **44**: p. 362.
13. Barras, A., et al., *High Efficiency of Functional Carbon Nanodots as Entry Inhibitors of Herpes Simplex Virus Type 1*. ACS Appl. Mater. Interfaces 2016. **8**: p. 9004.
14. Fahmi, M.Z., et al., *Design of boronic acid-attributed carbon dots on inhibits HIV-1 entry*. RSC Adv., 2016. **6**: p. 92996-93002
15. Du, T., et al., *Carbon dots as inhibitors of virus by activation of type I interferon response*. Carbon, 2016. **110**: p. 278-285.
16. P. C. Trippier, et al.
17. Khanal, M., et al., *Boronic acid-modified lipid nanocapsules: a novel platform for the highly efficient inhibition of hepatitis C viral entry*. Nanoscale, 2015. **7**: p. 1392.
18. Agalave, S.G., S.R. Maujan, and V.S. Pore, *Click Chemistry: 1,2,3-Triazoles as Pharmacophores*. Chem. Asian J., 2011. **6**: p. 2696-2718.

19. Hilimire, T.A., et al., *HIV-1 Frameshift RNA-Targeted Triazoles Inhibit Propagation of Replication-Competent and Multi-Drug-Resistant HIV in Human Cells*. ACS Chem Biol., 2017. **12**: p. 1674–1682.
20. Yaoping, H., et al., *How do nitrogen-doped carbon dots generate from molecular precursors? An investigation of the formation mechanism and a solution-based large-scale synthesis*. J. Mater. Chem. B, 2015. **3**: p. 5608-5614
21. Wang, S., et al., *The dual roles of functional groups in the photoluminescence of graphene quantum dots*. Nanoscale, 2016. **8**(14): p. 7449-7458.
22. Kim, T.H., et al., *Yellow-Emitting Carbon Nanodots and Their Flexible and Transparent Films for White LEDs*. ACS App. Mater. Interfaces, 2016. **8**: p. 33102–33111.
23. Yan, J., H. Fang, and B. Wang, *Boronolactams and fluorescent boronolactams: an examination of the detailed chemistry issues important for the design*. Med. Res. Rev., 2005. **25**: p. 490-520.
24. O'Keefe, B.R., et al., *Broad-Spectrum In Vitro Activity and In Vivo Efficacy of the Antiviral Protein Griffithsin against Emerging Viruses of the Family Coronaviridae*. J. Virol., 2010. **84**: p. 2511-2521.
25. Li, H., et al., *Water-Soluble Fluorescent Carbon Quantum Dots and Photocatalyst Design*. Angew. Chem. Int. Ed., 2010. **49**: p. 4430-4434.
26. Shen, P. and Y. Xia, *Synthesis-Modification Integration: One-Step Fabrication of Boronic Acid Functionalized Carbon Dots for Fluorescent Blood Sugar Sensing*. Anal. Chem., 2014. **86**: p. 5323.
27. Wang, Y., et al., *Multi-doped carbon dots with ratiometric pH sensing properties for monitoring enzyme catalytic reactions*. Chem. Commun., 2016. **52**: p. 9247-9250.
28. De Moor, J.E. and P. Van Der Kelen, *Studies on trivalent boron compounds II. Dipole moment measurements*. J. Organomet. Chem. , 1967. **9**: p. 23-29.
29. Beachell, H.C. and D.W. Beistel, *Nuclear Magnetic Resonance Spectra of Phenylboronic Acids*. Inorg. Chem., 1964. **3**: p. 1028.
30. Good, C.D. and D.M. Ritter, *Alkenylboranes. II. Improved Preparative Methods and New Observations on Methylvinylboranes*. J. Am. Chem. Soc. , 1962. **84**: p. 1162.
31. Wang, Y., et al., *Multi-doped carbon dots with ratiometric pH sensing properties for monitoring enzyme catalytic reactions*. Chem. Commun., 2016. **52**: p. 9247-9250.

## CHAPTER 5

### Conclusions and perspectives

Unprecedented antibacterial resistances, as well as new and more aggressive viruses, are continuously emerging, with a global impact on public health and society at large. This has made the search for antibacterial and antiviral drugs or therapeutics a very challenging research task. In the case of viral infections, the general absence of availability of specific antiviral therapeutics for a variety of viruses represents a considerable threat to the body's immune system as they hide inside cells, making it difficult for antibodies to reach them. In contrast to bacterial infections, which are mostly treated using antibiotics, immunisation against viral infections is not always possible. While vaccines against serious viral infections such as measles, mumps, hepatitis A, and hepatitis B do exist, some viruses are capable of mutating from one person to the next, making vaccination a difficult task as the viruses have already changed their format by the time the corresponding vaccines become available. We considered both antiviral and antibacterial aspects of this thesis.

Special attention was given to carbon nanomaterials, considered as promising candidates for various biological applications because of their biocompatible nature and rich surface chemistry. Among the possible candidates, diamond particles (NDs), were considered as they represent an important class of highly stable nanomaterials limiting their decomposition or transformation to materials with potential toxicity and decreased activity. Furthermore, carbon quantum dots (CQDs), formed by green synthetic methods without the need of a metal catalyst were investigated as they show good biocompatibility, small hydrodynamic size (5-20 nm in diameter) and excellent hydrophilic character. These nanostructures were modified with short cationic synthetic antimicrobial peptides (synAMP) that are rich in arginine (Arg) and tryptophan (Trp). The peptides were coupled either through a condensation reaction or via a copper(I)-catalyzed azide-alkyne cycloaddition (CuAAC) using an azido group originating from a previous chemical modification at the nanoparticle surface. Among the 28 investigated structures, conjugates **4a-5b** showed the best MIC values for the tested bacteria strains (Gram-negative *E.coli* DSM 30083 and *S.aureus* ATCC 43300) with a 5-fold lower MIC value for peptide modified CQDs and 4-fold lower for peptide modified NDs, when compared to the free peptides in solution, reaching MIC values of ca. 3  $\mu\text{g mL}^{-1}$  and 4  $\mu\text{g mL}^{-1}$  respectively.

The collected data indicated that charge is a significant factor in the antibacterial activity as well as the presence of metallocenoyl group.

Additionally, rGO-embedded furan-modified cryogels conjugated with maleimide-modified ampicillin and synAMP were formed, and the possibility of on-demand release of the antibacterial agent to ablate bacteria was investigated. The cryogels were fabricated using photo-polymerisation reaction using hydrophilic poly(ethylene glycol) and hydrophobic furfuryl elements, where maleimide-containing anti-microbial peptide could be linked via the Diels-Alder reaction. While the system performed as expected for the release of ampicillin, the study reveals that integration of rGO inside the cryogels hindered the release of AMPs due to the strong  $\pi$ - $\pi$  interactions between the anti-microbial peptide and the rGO.

We also considered CQDs as antiviral agents. We have developed a first and second generation of functional antiviral CQDs prepared by one-pot synthesis or by subsequent surface post-modification. The structure showed a concentration-dependent virus inactivation with an estimated  $EC_{50}$  of  $52 \pm 8 \mu\text{g mL}^{-1}$  for the first generation, and  $5.2 \pm 0.7 \mu\text{g mL}^{-1}$  for the second. Our mechanistic studies revealed that the particles interact with the virus already at the early stage of the viral infection, inhibiting the virus entry. This behaviour could be due to the inhibition of the protein S-receptor interaction with the host cell membrane. In addition, the existence of another interaction occurring during the replication step was discovered. As-prepared CQDs could thus be a potential substitute for currently used antiviral agents. However, further experimental confirmations are required to validate their potential as alternative therapeutics as well as the possibility of this approach can to be extrapolated to other coronaviruses, notably the clinically relevant MERS-CoV.

Overall, the scope of application of the different carbon-based nanostructures is certainly broad. The third generation of functional antiviral CQDs is under development, using MERS-CoV specific peptides as surface anchors. This will allow specific targeting of the inhibition of MERS-CoV cell interactions. The concept will be also expanded to other nanostructures (NDs,  $\text{MoS}_2$  nanosheets, etc.) to see if the concept is specific to CQDs or not. Additionally, this will also allow answering questions concerning the importance of the size of these nanostructures in the inhibition process.

In the case of antibacterial nanostructures, further work will be devoted to understanding the mechanism of conjugates **4a-5b** to ablate Gram-negative *E.coli* DSM 30083 and



Gram-positive *S.aureus* ATCC 43300. In addition, no *in vivo* studies have been performed in this work, essential for establishing pharmacokinetic parameters of these nanostructures and elucidating their real potential for antibacterial applications. This is also true for the proposed antibacterial cryogels where testing on *ex vivo* infected skin will be one of the next steps. The healing of diabetic foot ulcers is targeted with these gels where the effect of heat and local antibacterial release might be of great advantage for treating such chronic wounds. The future of this interdisciplinary research that brings organic chemistry, nanotechnology and biology together is thus brighter than ever.

## APPENDIX

### EXPERIMENTAL PART

#### 6.1. Materials

Rink amid resin, Fmoc-Arg(Pbf)-OH, Fmoc-Trp(BOC)-OH, Fmoc-propargyl-Gly-OH, Fmoc-Cys(Trt)-OH, triisopropyl silane (TIS), *N,N*-diisopropylethylamine (DiPEA), 2-(1H-benzotriazole-1-yl)-1,1,3,3-tetramethylammonium tetrafluoroborate (TBTU), *N,N'*-diisopropylcarbodiimide (DIC), 1-hydroxy benzotriazole hydrate (HOBt), were purchased from Iris Biotech or Novabiochem.

2,6-dichlorobenzoyl chloride, 1,2-dimethoxyethane, anhydrous aluminium chloride ( $\text{AlCl}_3$ ), sodium sulfate ( $\text{Na}_2\text{SO}_4$ ), potassium *tert*-butoxide (KOtBu), ascorbic acid, copper sulfate pentahydrate ( $\text{CuSO}_4 \cdot 5 \text{H}_2\text{O}$ ), phenol, potassium cyanide (KCN), ninhydrin, *N*-hydroxysuccinimide (NHS), 4-pentynoic acid, 4-dimethylaminopyridine (DMAP), *N*-(3-dimethylaminopropyl)-*N'*-ethylcarbodiimide hydrochloride (EDC•HCl), quinine sulfate, acetic acid, sodium acetate, propargyl alcohol, 2-azidoacetic acid, ethylenediaminetetraacetic acid (EDTA), sodium hydroxide (NaOH), hydrochloric acid (HCl), potassium bromide (KBr), phenylboronic acid (PBA), 4-aminophenylboronic acid (4APBA), poly(ethylene glycol) (PEG600, molecular weight 570-630  $\text{g.mol}^{-1}$ ), citric acid, ethylenediamine, ampicillin, *N,N'*-dicyclohexyl carbodiimide (DCC), sodium chloroacetate ( $\text{ClCH}_2\text{COONa}$ ), *para*-formaldehyde, 5/6-carboxyfluorescein succinimidyl ester (fluorescein-NHS), *N*-(5-fluoresceinyl)maleimide, 1,8-bismaleimidodiethyleneglycol (BM(PEG)<sub>2</sub>), Bis(cyclopentadienyl)-ruthenium(II), dimethylformamide (DMF), dichloromethane (DCM), isopropanol (IPA), piperidine, trifluoroacetic acid (TFA), formic acid (FA), *n*-hexane, diethyl ether ( $\text{Et}_2\text{O}$ ), acetonitrile (MeCN), ethyl acetate (EtOAc), pyridine, sulfuric acid; deuterated solvents: dimethylsulfoxide-*d*<sub>6</sub> (DMSO), chloroform ( $\text{CDCl}_3$ ), water ( $\text{D}_2\text{O}$ ); Muller Hinton Broth (MHB), Muller Hinton agar (MHA), brain heart infusion medium and agar (BHI), Luria-bertani medium and broth (LB) were purchased from Sigma Aldrich, Thermofisher or Fisher Scientific.

4-azidobenzoic acid (TCI Europe), ferrocenecarboxylic acid (Alfa Aesar), Dulbecco's modified Eagle's medium (DMEM, Gibco®), fetal bovine serum (FBS, Gibco®), penicillin-

streptomycin (Gibco®), renilla lysis buffer (Promega, Madison, USA), renilla luciferase assay system kit (Promega, Madison, USA), disposable PD10 columns G-25 PD-10 desalting columns (GE Healthcare) and all the dialysis membranes were purchased from Spectrum laboratories. Kapton® HN polyimide foils with a thickness of 125 µm were obtained from DuPont™. Graphene oxide (GO) was purchased from Graphenea, Spain. Amino- and carboxyl-terminated nanodiamonds were purchased from International Technology Center (Raleigh, NC, USA).

All the solvents used for solid-phase peptide synthesis were peptide grade solvents. Ultrapure water (Milli-Q, 18 MWcm) was used for all the experiments. All the chemicals were used as received unless otherwise noted.

## 6.2. Synthesis

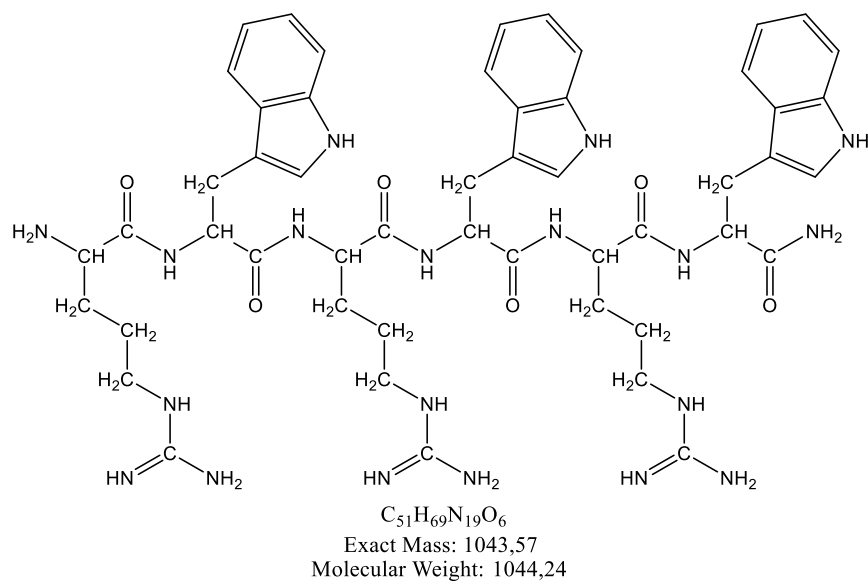
### 6.2.1. General procedure for solid-phase peptide synthesis (SPPS)

Solid-phase peptide synthesis (SPPS) was performed manually using the Fmoc protection strategy on a Rink amid resin. The resin was left to swell for 30 min in dichloromethane (DCM) before use. Removal of Fmoc protection was achieved using 20% (v/v) piperidine in dimethylformamide (DMF), deprotection was performed in duplicate in the course of 5 min. For each coupling step, a mixture of Fmoc-aa-OH (4 eq); TBTU (4 eq); HOBt (4 eq); DIPEA (8 eq) in DMF was used (metalloenes were attached using [Ru(Cp)(C<sub>5</sub>H<sub>4</sub>-COOH)] or [Fe(Cp)(C<sub>5</sub>H<sub>4</sub>-COOH)] (2 eq); TBTU (2 eq); HOBt (2 eq); DIPEA (4 eq)). Each coupling reaction was carried out 2 times for 60 min. In case of unsuccessful coupling, the reagents were changed to Fmoc-aa-OH (4 eq); DIC (4 eq); HOBt (4 eq). After attaching the last aa, the Fmoc group was removed, the resin was washed and dried under vacuum. Side-protecting groups were removed along with the cleavage of the peptide from the resin in the course of 3 h with a treatment of:

- TFA:water:TIS (95:2.5:2.5) for peptides *1a*, *1b*, *3a-5b*, *7a*, *7b*.
- TFA:phenol:TIS (95:2.5:2.5) for ferrocene-containing peptides *2a*, *2b*, *6a*, *6b*.
- TFA:TIS:EDT (95:2.5:2.5) for peptide *8*.

The cleavage cocktail was filtered, and the crude peptide was precipitated and washed with ice-cold Et<sub>2</sub>O/hexane (v/v). Peptides were dissolved in a water/acetonitrile mixture and lyophilised to be further purified by RP-HPLC.

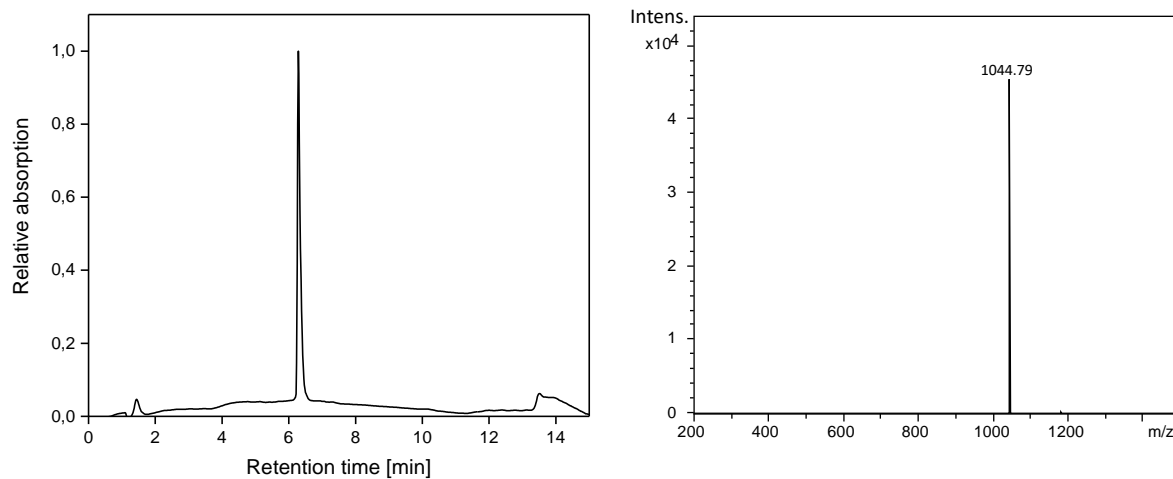
### 6.2.1.1. *Synthesis of H-RWRWRW-NH<sub>2</sub>: 1a*



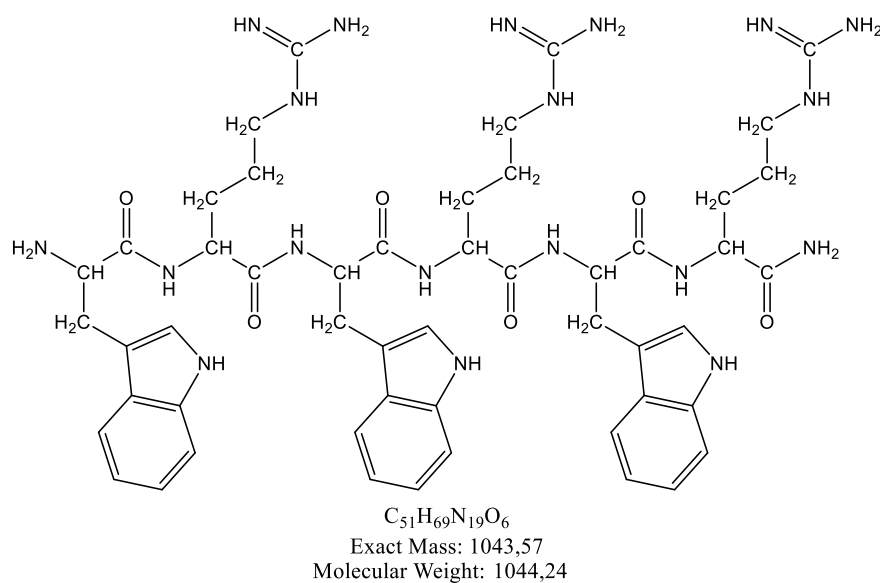
The peptide was synthesised by solid-phase peptide synthesis as described in the general SPPS procedure.

MS (ESI,  $m/z$ ): 1044.79 (calc. 1044.24 for  $[M+H]^+$ ).

HPLC ( $t_R$ , min): 6.28.



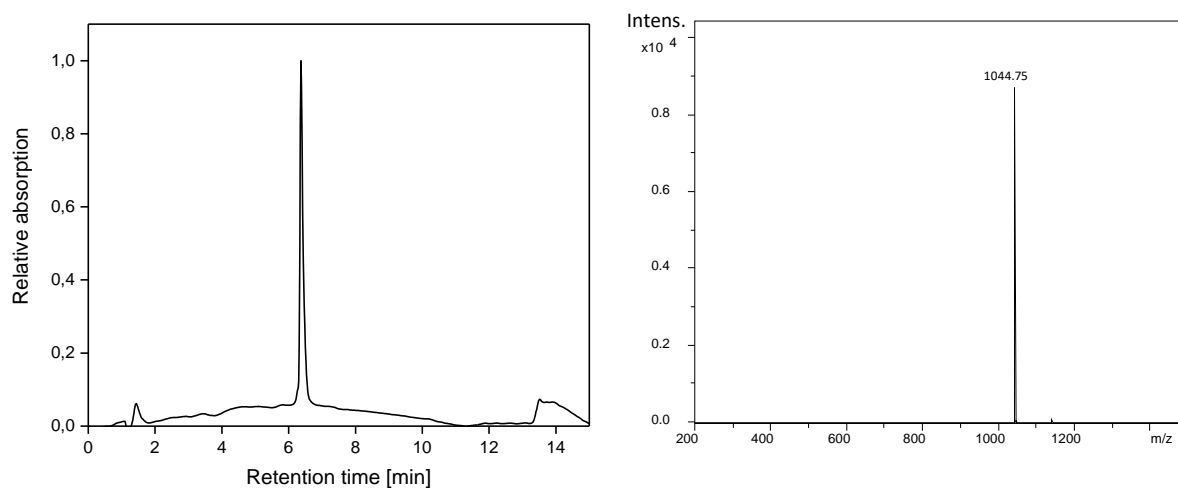
### 6.2.1.2. Synthesis of *H*-WRWRWR-NH<sub>2</sub>: *1b*

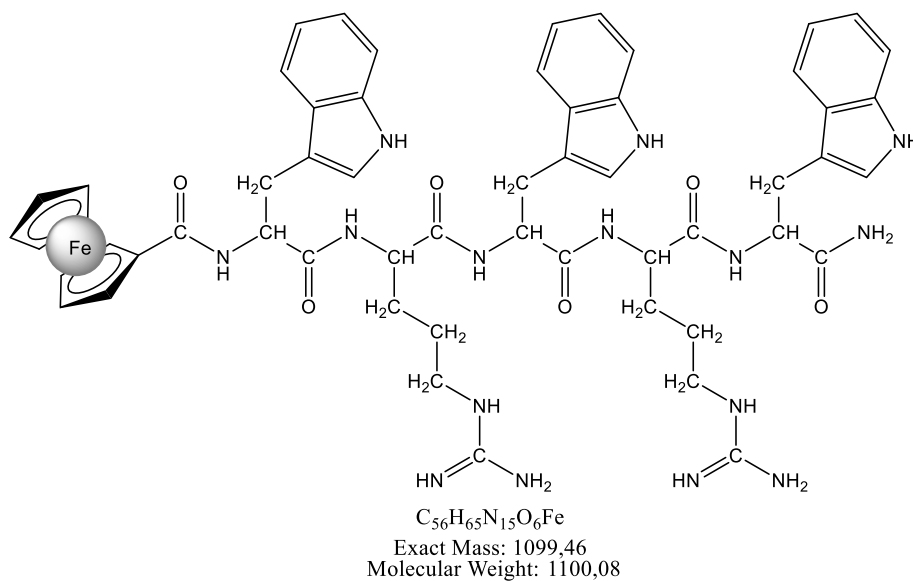


The peptide was synthesised by solid-phase peptide synthesis as described in the general SPPS procedure.

MS (ESI,  $m/z$ ): 1044.75 (calc. 1044.24 for  $[M+H]^+$ ).

HPLC ( $t_R$ , min): 6.36.

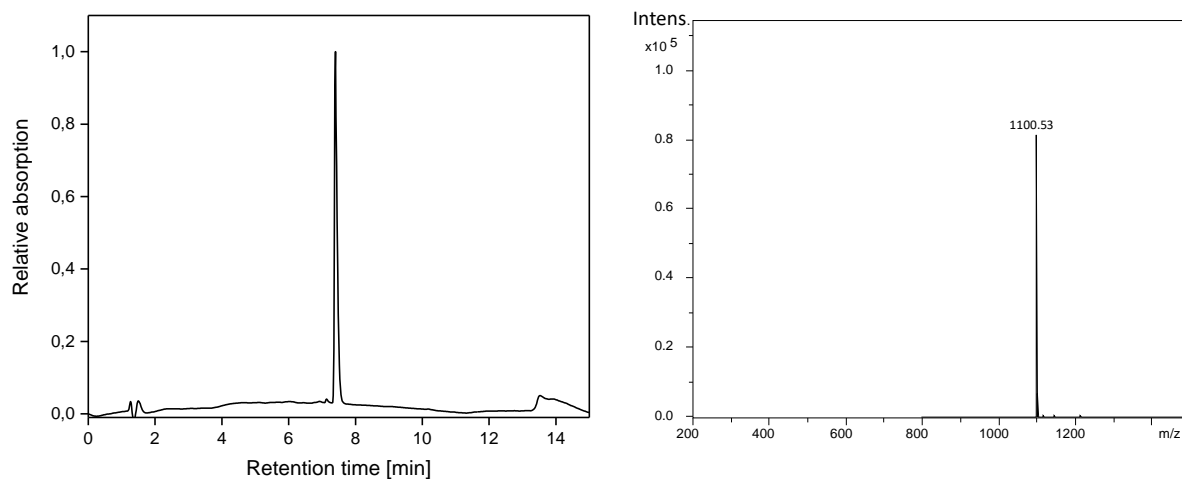


**6.2.1.3.** *Synthesis of FcCO-WRWRW-NH<sub>2</sub>: 2a*

The peptide was synthesised by solid-phase peptide synthesis as described in the general SPPS procedure.

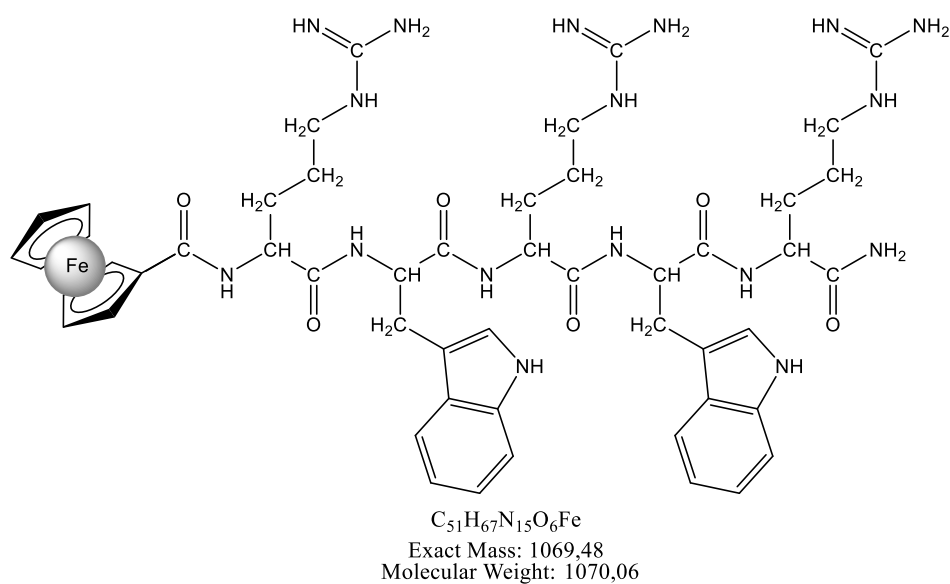
MS (ESI,  $m/z$ ): 1100.53 (calc. 1100.08 for  $[M+H]^+$ ).

HPLC ( $t_R$ , min): 7.4.





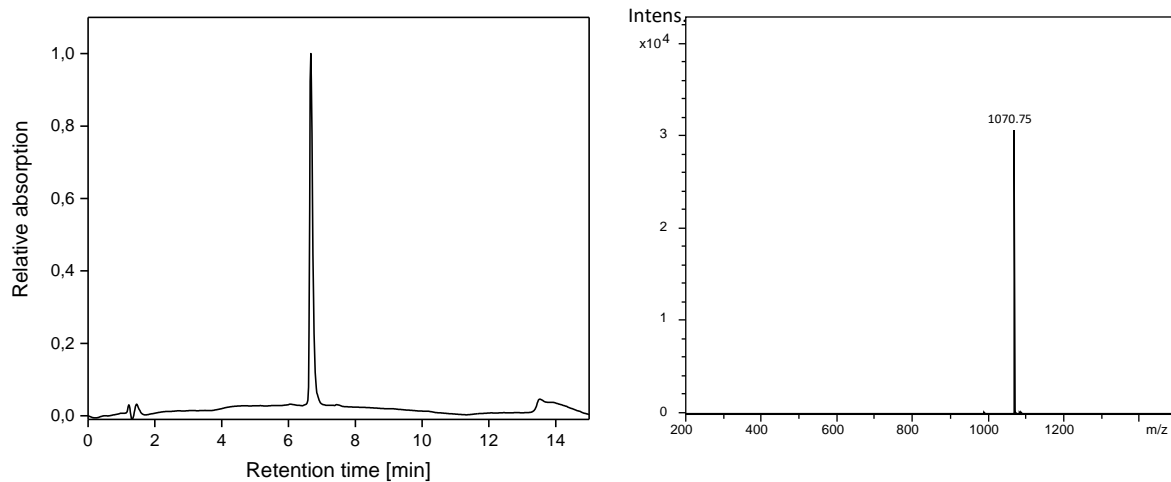
#### 6.2.1.4. Synthesis of *FcCO-RWRWR-NH<sub>2</sub>*: *2b*



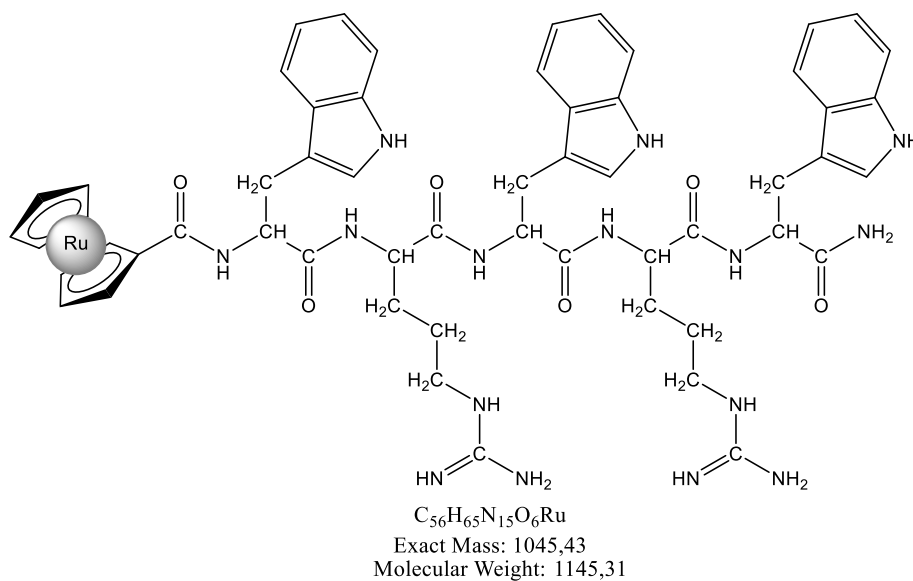
The peptide was synthesised by solid-phase peptide synthesis as described in the general SPPS procedure.

MS (ESI,  $m/z$ ): 1070.75 (calc. 1070.06 for  $[M+H]^+$ ).

HPLC ( $t_R$ , min): 6.63.



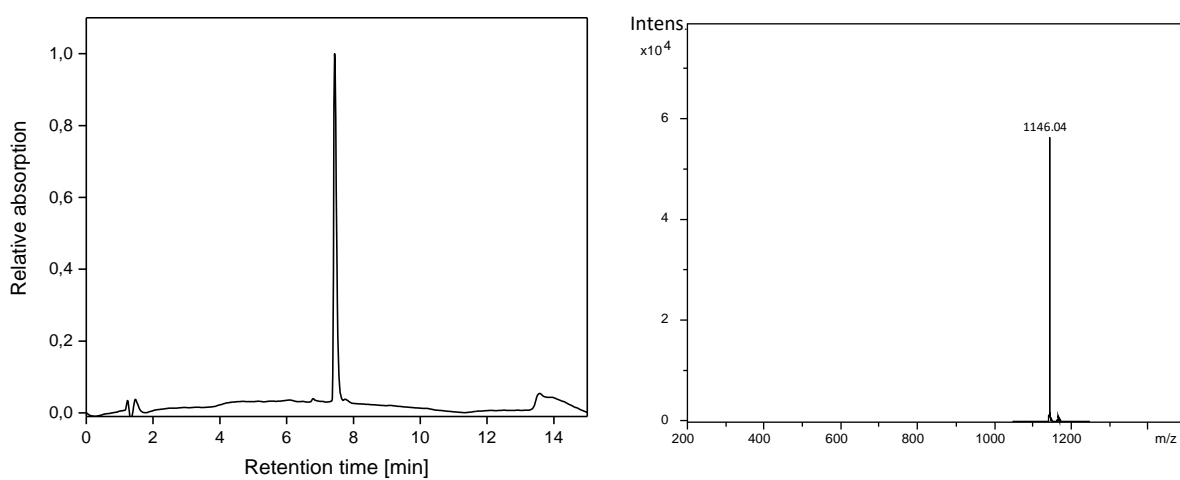
### 6.2.1.5. Synthesis of *RcCO-WRWRW-NH<sub>2</sub>*: **3a**



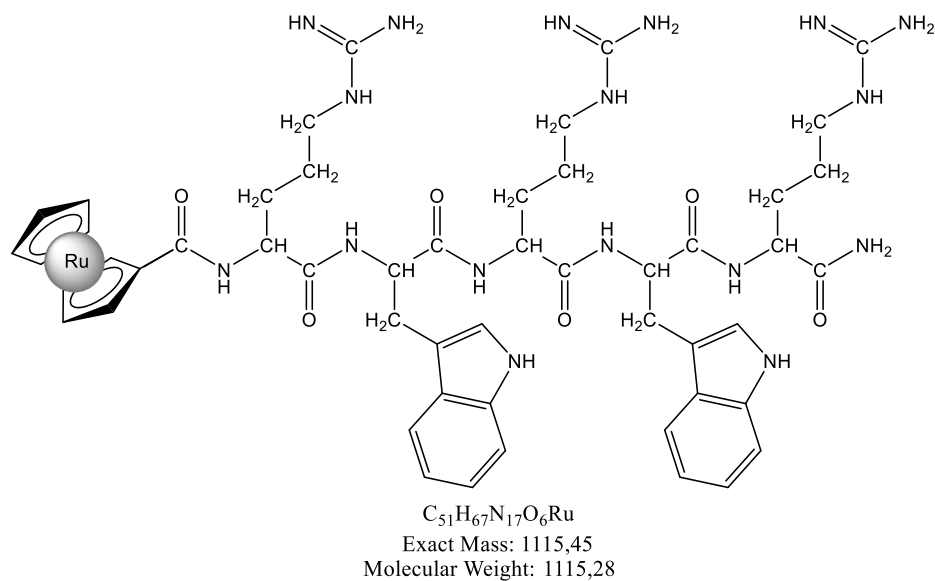
The peptide was synthesised by solid-phase peptide synthesis as described in the general SPPS procedure.

MS (ESI,  $m/z$ ): 1146.04 (calc. 1145.31 for  $[\text{M}+\text{H}]^+$ ).

HPLC ( $t_R$ , min): 7.43.



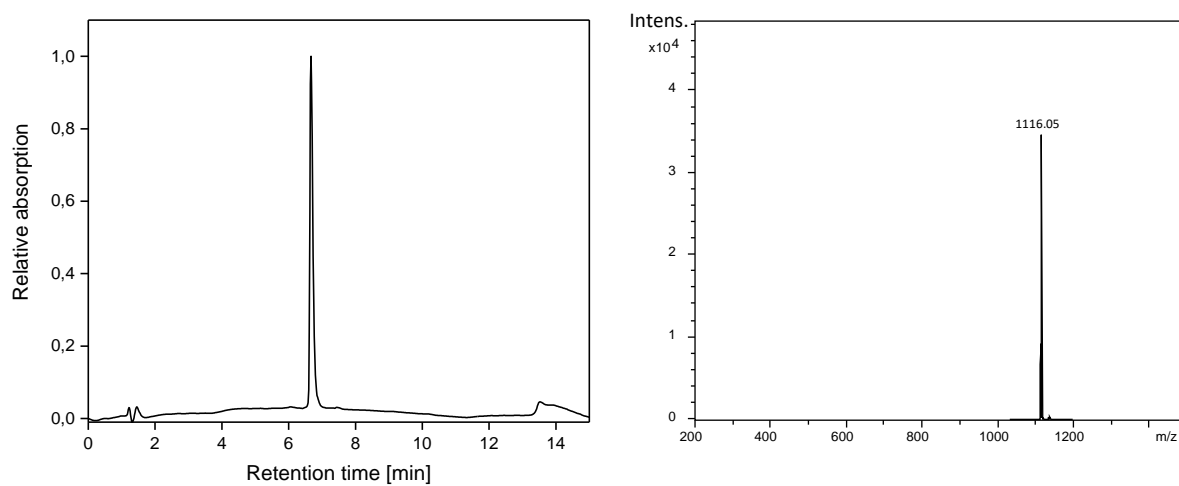
### 6.2.1.6. Synthesis of *RcCO-RWRWR-NH<sub>2</sub>*: **3b**



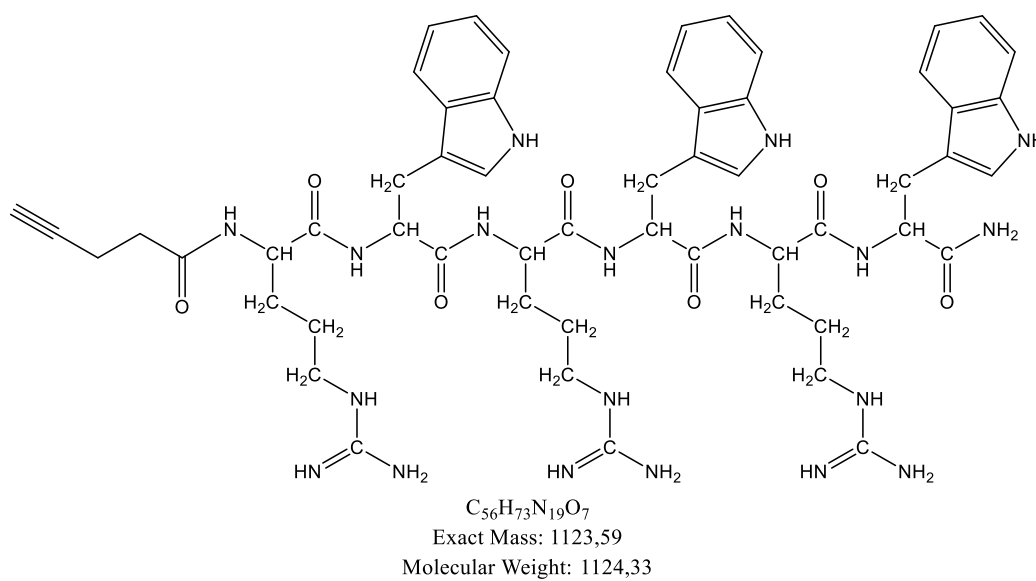
The peptide was synthesised by solid-phase peptide synthesis as described in the general SPPS procedure.

MS(ESI,  $m/z$ ): 1116.05 (calc. 1115.28 for  $[M+H]^+$ ).

HPLC ( $t_R$ , min): 6.66.



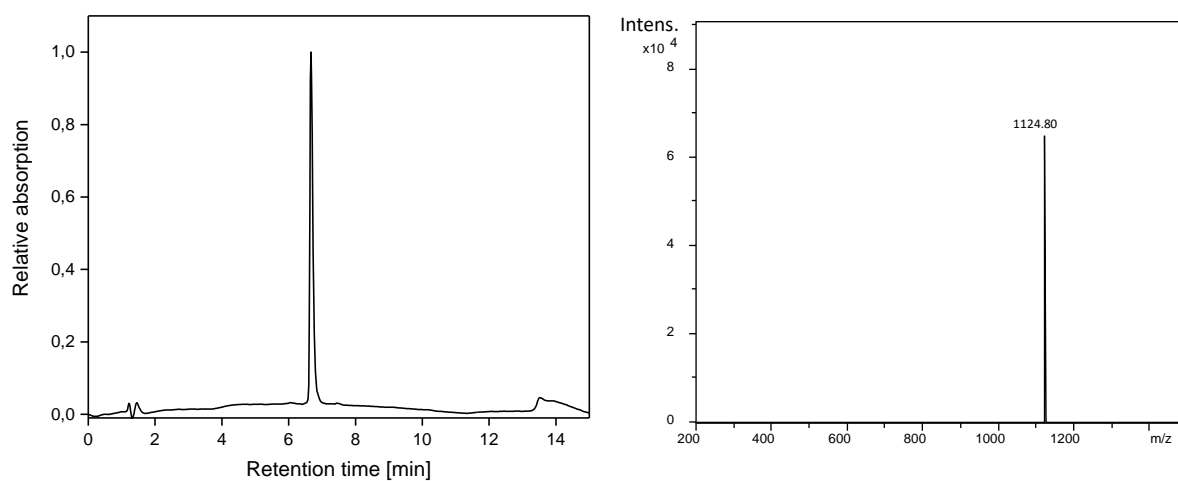
### 6.2.1.7. Synthesis of $\text{CHCCH}_2\text{CH}_2\text{C(O)-RWRWRW-NH}_2$ : *4a*



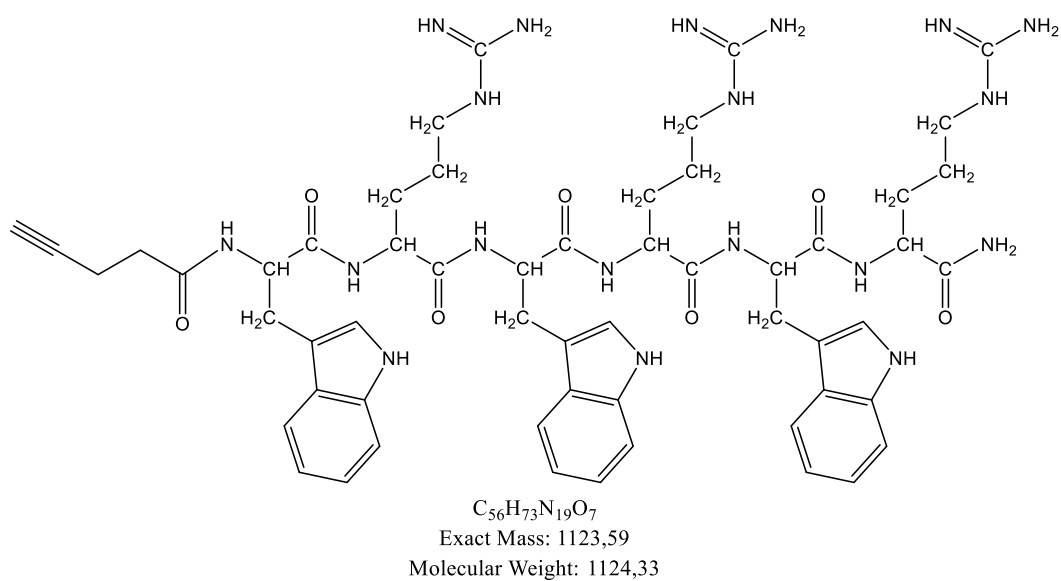
The peptide was synthesised by solid-phase peptide synthesis as described in the general SPPS procedure.

MS (ESI,  $m/z$ ): 1124.80 (calc. 1124.33 for  $[\text{M}+\text{H}]^+$ ).

HPLC ( $t_R$ , min): 6.61.



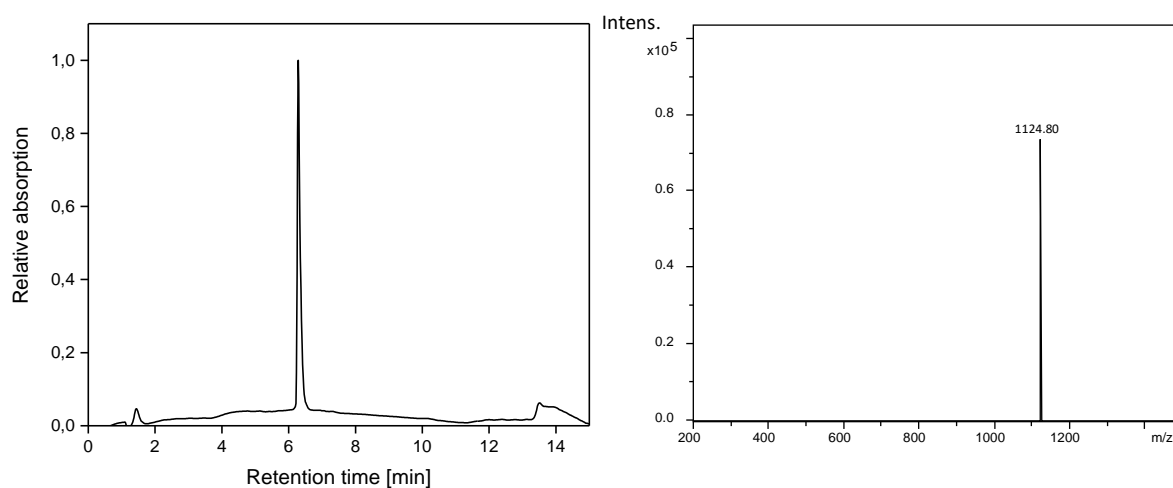
### 6.2.1.8. Synthesis of $CHCCH_2CH_2C(O)-WRWRWR-NH_2$ : *4b*



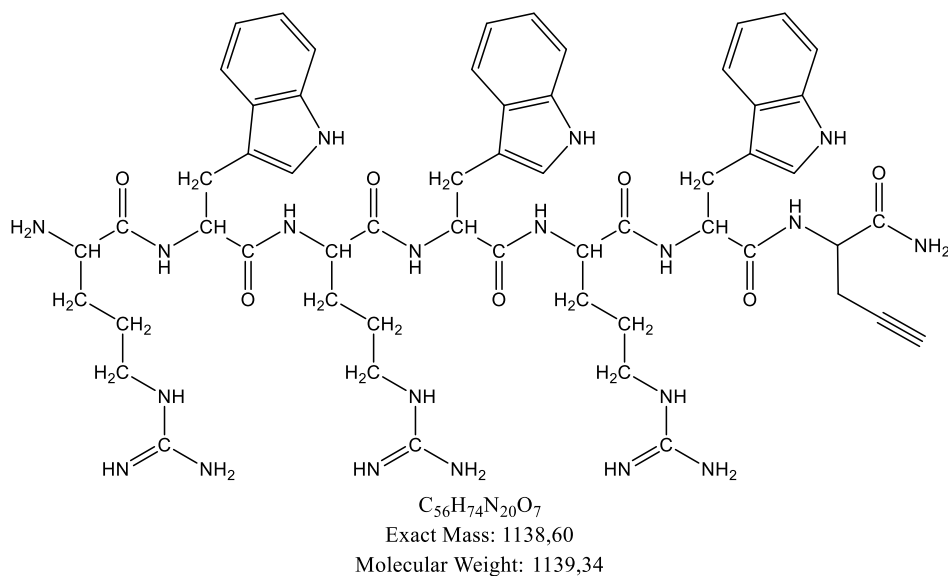
The peptide was synthesised by solid-phase peptide synthesis as described in the general SPPS procedure.

MS (ESI,  $m/z$ ): 1124.80 (calc. 1124.33 for  $[M+H]^+$ ).

HPLC ( $t_R$ , min): 6.68.



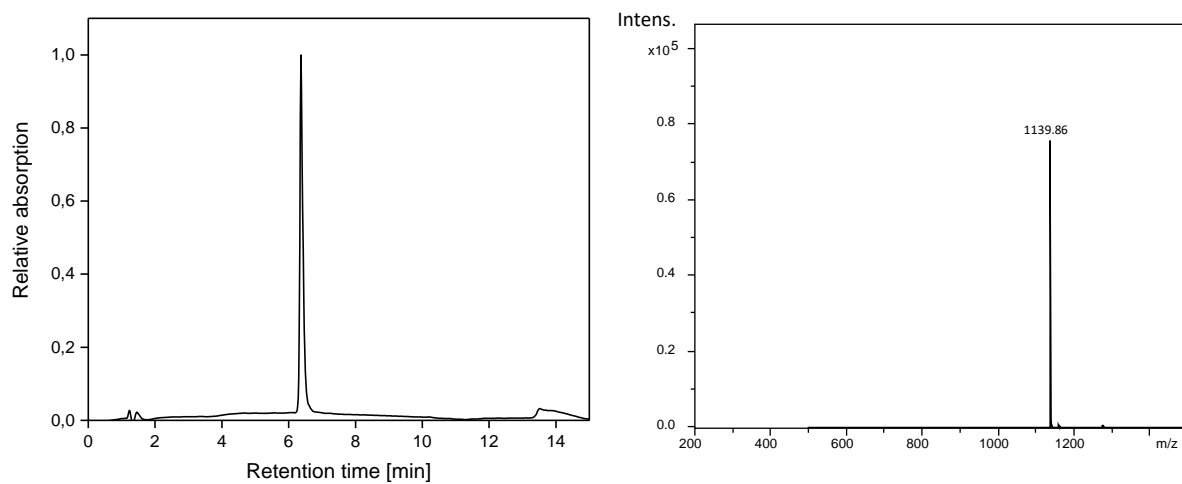
### 6.2.1.9. Synthesis of *H*-RWRWRWG(CH<sub>2</sub>CCH)-NH<sub>2</sub>: 5a



The peptide was synthesised by solid-phase peptide synthesis as described in general procedure for SPPS.

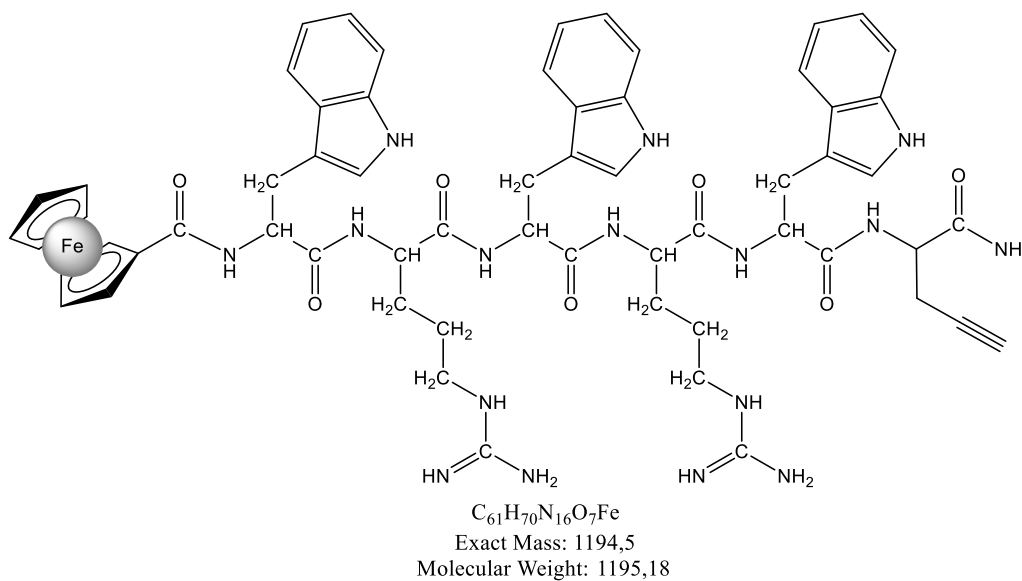
MS (ESI,  $m/z$ ): 1139.86 (calc. 1139.34 for  $[M+H]^+$ ).

HPLC ( $t_R$ , min): 6.36.





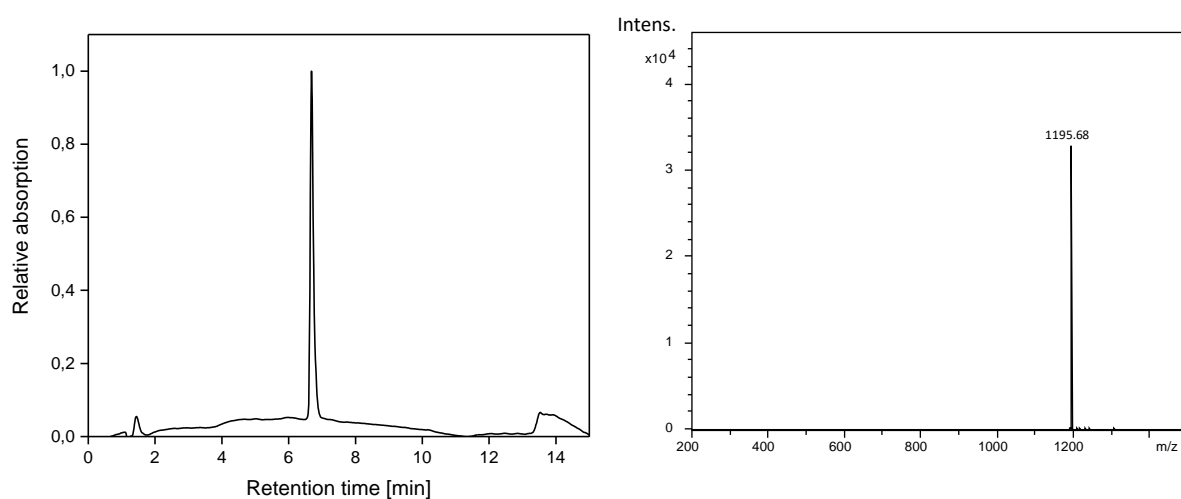


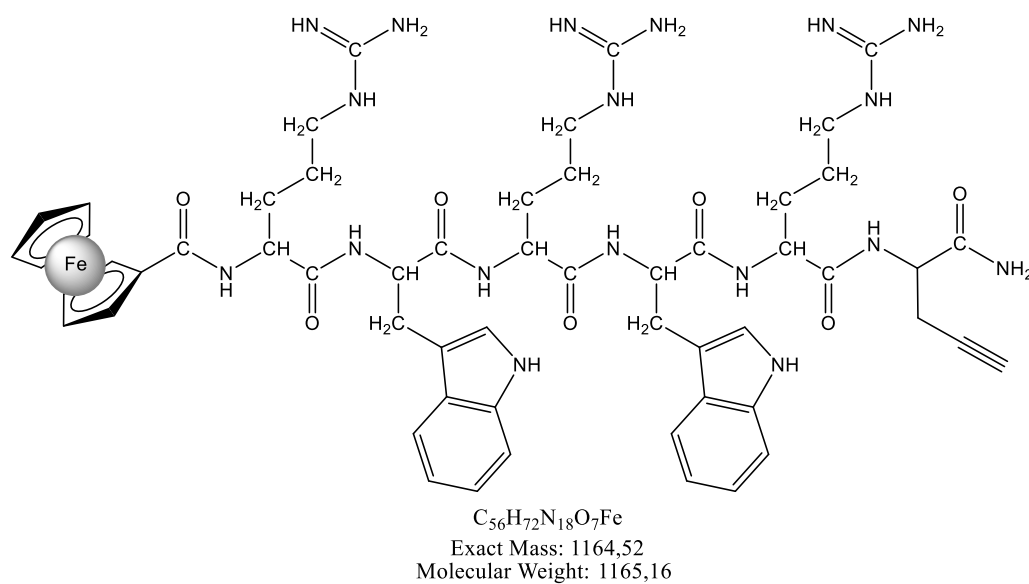
**6.2.1.11. Synthesis of  $\text{FcCO-WRWRWG}(\text{CH}_2\text{CCH})\text{-NH}_2$ : 6a**

The peptide was synthesised by solid-phase peptide synthesis as described in the general SPPS procedure.

MS (ESI,  $m/z$ ): 1195.68 (calc 1195.18 for  $[\text{M}+\text{H}]^+$ ).

HPLC ( $t_R$ , min): 7.43min

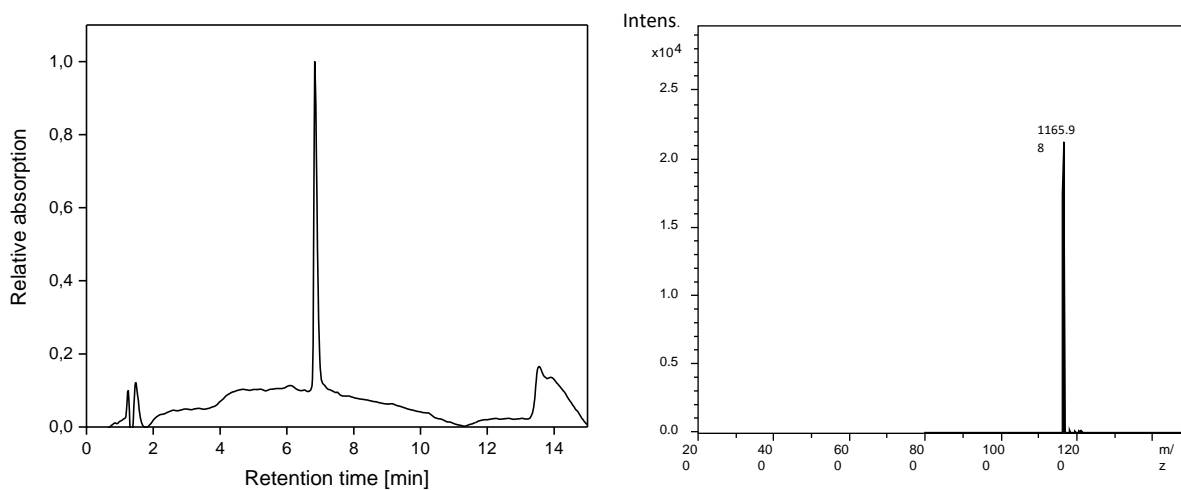


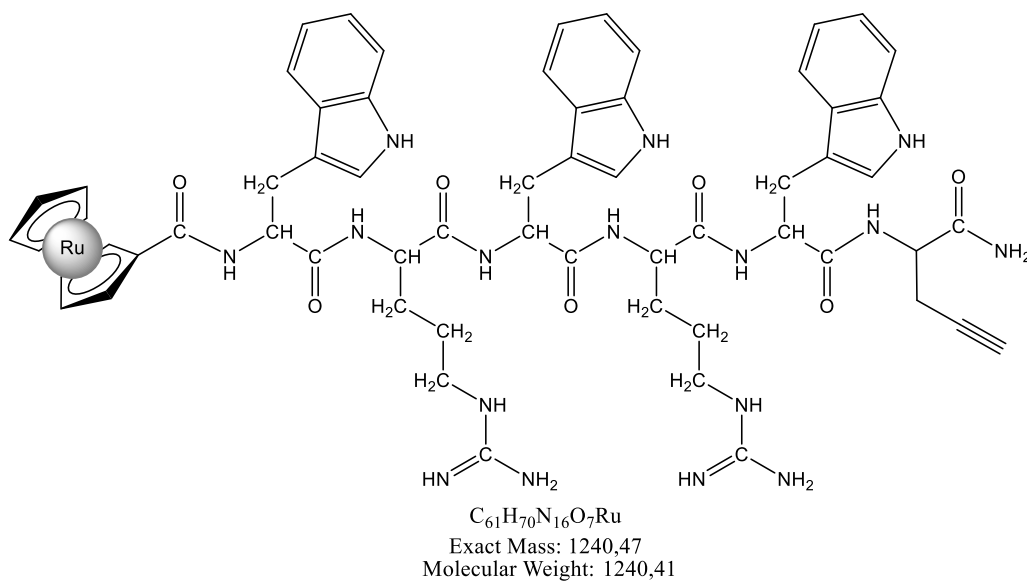
**6.2.1.12.** *Synthesis of  $\text{FcCO-RWRWRG}(\text{CH}_2\text{CCH})\text{-NH}_2$ : 6b*

The peptide was synthesised by solid-phase peptide synthesis as described in the general SPPS procedure.

MS (ESI,  $m/z$ ): 1165.98 (calc. 1165.16 for  $[\text{M}+\text{H}]^+$ ).

HPLC ( $t_R$ , min): 6.83.

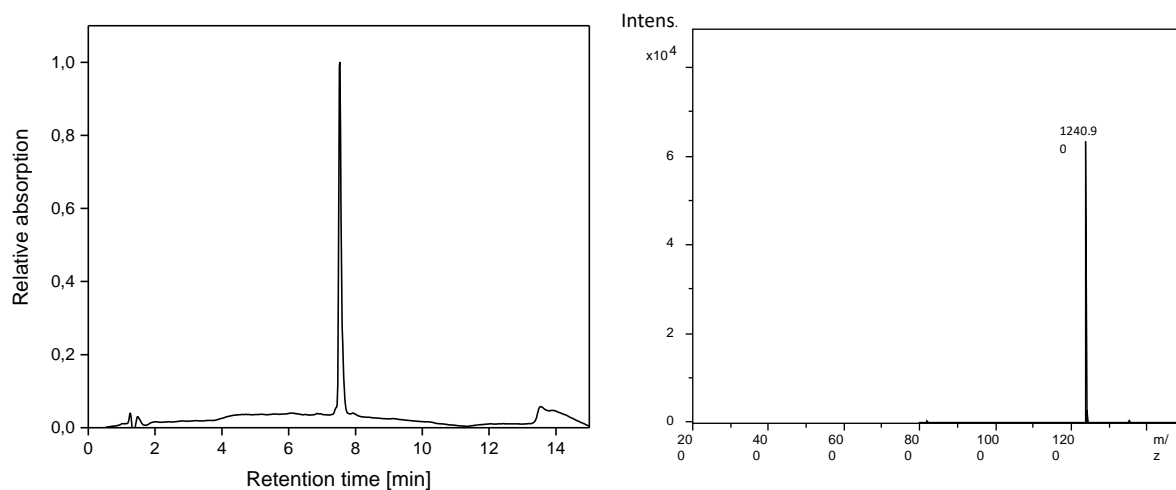


**6.2.1.13.** *Synthesis of  $RcCO-WRWRWG(CH_2CCH)-NH_2$ : 7a*

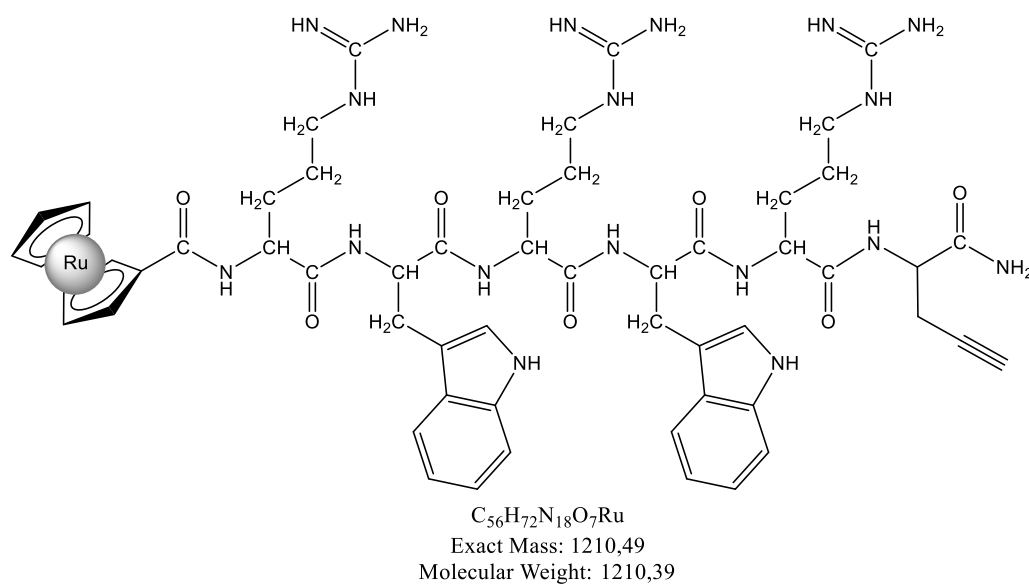
The peptide was synthesised by solid-phase peptide synthesis as described in the general SPPS procedure.

MS(ESI,  $m/z$ ): 1240.9 (calc. 1240.41 for  $[M+H]^+$ ).

HPLC ( $t_R$ , min): 7.51.



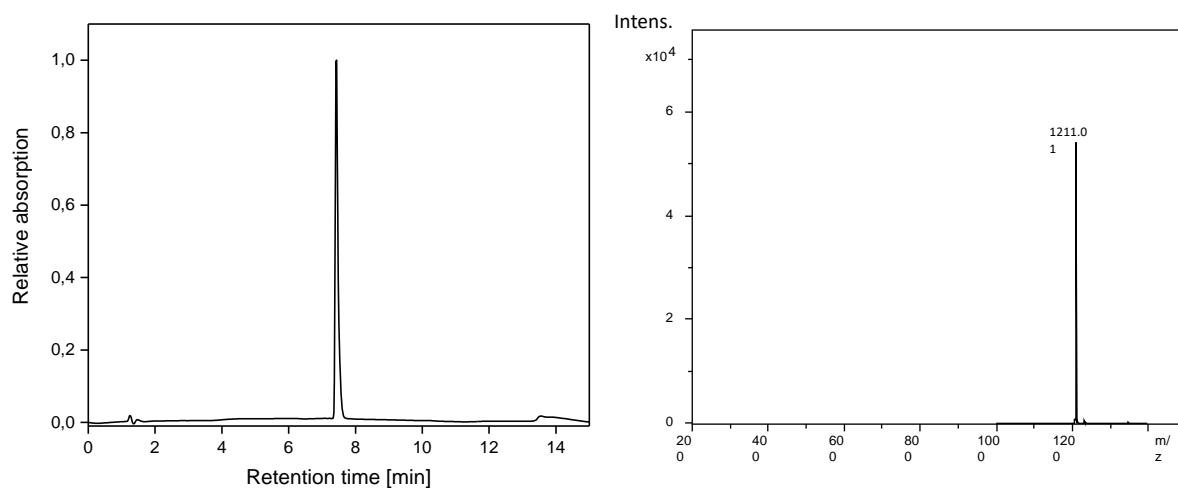
### 6.2.1.14. Synthesis of $RcCO-RWRWRG(CH_2CCH)-NH_2$ : **7b**



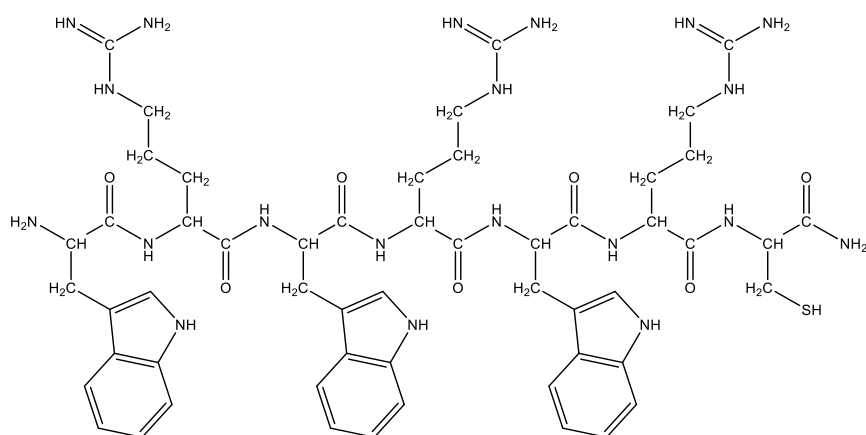
The peptide was synthesised by solid-phase peptide synthesis as described in the general SPPS procedure.

MS (ESI,  $m/z$ ): 1211.01 (calc. 1210.39 for  $[M+H]^+$ ).

HPLC ( $t_R$ , min): 7.41.



### 6.2.1.15. Synthesis of *H*-WRWRWRC-NH<sub>2</sub>: 8



Chemical Formula: C<sub>54</sub>H<sub>74</sub>N<sub>20</sub>O<sub>7</sub>S

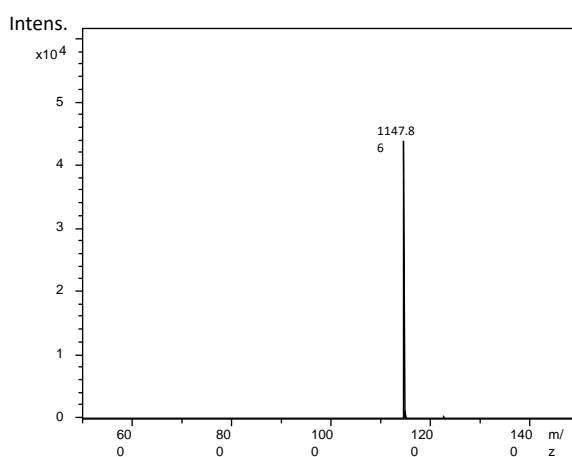
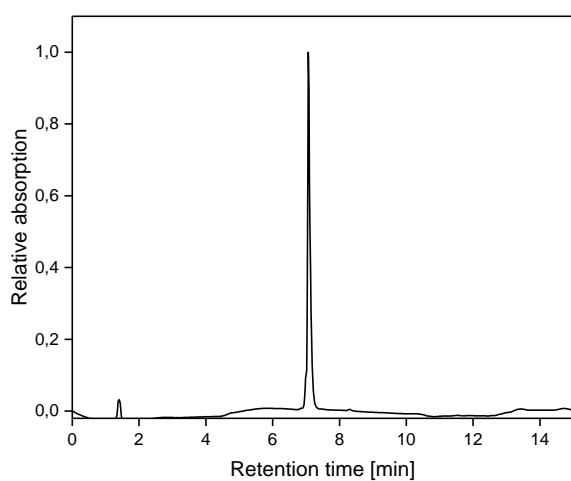
Exact Mass: 1146,58

Molecular Weight: 1147,38

The peptide was synthesised by solid-phase peptide synthesis as described in the general SPPS procedure.

MS (ESI, *m/z*): 1147.86 (calc. 1147.38 for [M+H]<sup>+</sup>).

HPLC (*t<sub>R</sub>*, min): 7.06.

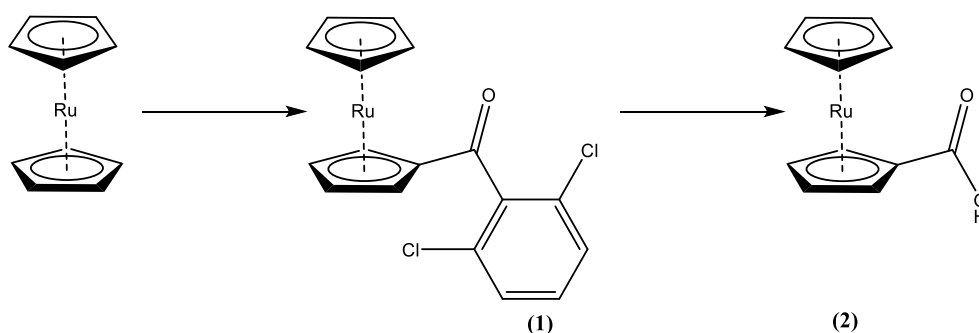


## 6.2.2. Organic compounds

### 6.2.2.1. Synthesis of *H*-WRWRWRC-maleimide

BM(PEG)<sub>2</sub> (2.62  $\mu$ mol, 3 eq) was dissolved in a minimum volume of DMF (200  $\mu$ L). Peptide **8** (0.871  $\mu$ mol, 1 eq) was added to the solution. The reaction mixture was stirred overnight at room temperature. The next day, the solution was precipitated in ice-cold diethyl ether and centrifuged at 13,000 rpm for 5min, resulting in the desired maleimide-modified peptide (yield 73%).

### 6.2.2.2. Ruthenocenecarboxylic acid

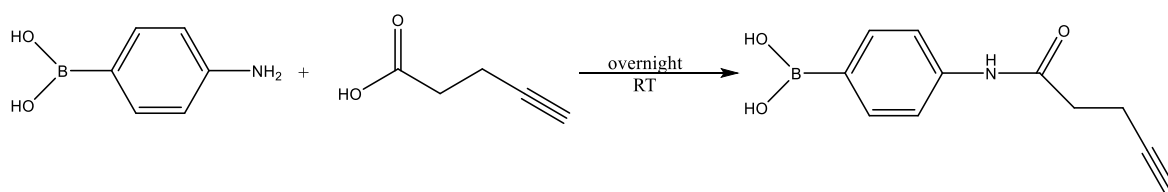


Ruthenocenecarboxylic acid was prepared by Friedel-Crafts acylation (1) followed by hydrolysis of the ketone, resulting in the desired carboxylic acid (2). The synthesis was performed according to the literature with minor modifications [1]. For the synthesis of compound (1): ruthenocene (2.16 mmol) was suspended in freshly distilled dry DCM (20 mL), and 2,6-dichlorobenzoyl chloride (2.16 mmol) was added. The mixture was cooled down in an ice salt bath, and anhydrous AlCl<sub>3</sub> (2.16 mmol) was added. Stirring was continued overnight at room temperature. The reaction mixture was cooled down to 0 °C and water (3.5 mL) was added. After separation of the layers, the organic phase was concentrated under reduced pressure, and EtOAc was added. The solution was washed with brine, and the organic layer was dried over Na<sub>2</sub>SO<sub>4</sub>. The product was purified using column chromatography (silica; eluent: *n*-hexane/EtOAc 10:1, v/v) resulting in 2,6-dichlorobenzoylruthenocene (yellow solid: 389 mg, 0.96 mmol, 45% yield). <sup>1</sup>H NMR (CDCl<sub>3</sub>):  $\delta$  7.32-7.14 (m, 3H, aromatic H), 4.89-4.8 (m, 2H, Cp-R), 4.76-4.70 (m, 2H, Cp-R), 4.61-4.53 (s, 5H, C<sub>5</sub>H<sub>5</sub>). <sup>13</sup>C NMR(CDCl<sub>3</sub>):  $\delta$  194.5, 138.1, 132.1, 130.2, 128.3, 84.5, 73.6, 72.5, 71.4.



For the synthesis of (2), compound (1) (0.91 mmol) was dissolved in 1,2-dimethoxyethane (8 mL). KOtBu (10 eq) and water were added, and the reaction mixture was stirred under reflux until the next day. The solution was diluted with 10 mL of water and left to cool down to room temperature. Et<sub>2</sub>O was added, and ruthenocenecarboxylate was extracted using 1 N NaOH. Aqueous layers were combined, acidified with 1 N HCl, and the desired carboxylic acid was extracted using Et<sub>2</sub>O. The organic phase was dried over Na<sub>2</sub>SO<sub>4</sub> and concentrated under reduced pressure, resulting in the final product as a yellow solid (230 mg; 0.82 mmol; 91% yield). <sup>1</sup>H NMR (DMSO):  $\delta$  12.04 (s, 1H, COOH), 5.03 (t, <sup>3</sup>J<sub>HH</sub> = 1.8 Hz, 2H, Cp-R), 4.75 (t, <sup>3</sup>J<sub>HH</sub> = 1.8 Hz, Cp-R, 2H), 4.65-4.59 (s, 5H, C<sub>5</sub>H<sub>5</sub>).

#### 6.2.2.3. 4-[(1-oxo-4-pentyn-1-yl)amino]phenylboronic acid



4-[(1-oxo-4-pentyn-1-yl)amino]phenylboronic acid was synthesised according to the literature with small modifications [2]. 4-pentynoic acid (1.5 mmol) was dissolved in water (5 mL), and the pH of the solution was adjusted to 4.8 using 1N NaOH. 4-aminophenylboronic acid hydrochloride (1.8 mmol) was dissolved in water (5 mL), and the pH was adjusted to 4.8 with 1N NaOH. EDC hydrochloride (1.5 mmol) was added to the 4-aminophenylboronic acid solution, and the mixture was stirred for 20 min at 0 °C. The solution of 4-pentynoic acid was added dropwise, and the mixture was kept for another hour in ice then overnight at room temperature. A white/grey precipitate appeared and was collected by filtration. The precipitate was washed with ice-cold water and dried under vacuum, resulting in a grey powder (yield: 59%).

<sup>1</sup>H NMR (DMSO):  $\delta$  9.97 (s, 1H, O=CNH), 7.87 (s, 2H, B-OH), 7.73 (d, J = 8.1 Hz, 2H, Ar-H), 7.55(d, J = 8.1Hz, 2H, Ar-H), 2.79 (t, J = 2.5 Hz, 1H, HCCR), 2.6-2.4 (m, 4H, CH<sub>2</sub>-CH<sub>2</sub>).

<sup>13</sup>C NMR (DMSO):  $\delta$  138.8, 117, 39.77, 35.22.

### 6.2.3. Nanoparticles

#### 6.2.3.1. Carbon dots: CQDs

##### 6.2.3.1.1. CQDs-1: $NH_2$ -rich CQDs

Carbon dots were prepared following a method reported previously by Zhu et al. [3] with some modifications. Citric acid (2.1014 g) was dissolved in Milli-Q water (20 mL), and ethylenediamine was added (670  $\mu$ L). The mixture was transferred into a Teflon-lined autoclave (125 mL acid digestion vessel n° 4748, Parr, France) and heated at 250 °C for 5 h. The resulting product was dialysed against Milli-Q water for 24 h (SpectraPor, pore size 1 kDa). To obtain the powder, carbon dots were lyophilised and stored at 4 °C.

##### 6.2.3.1.2. CQDs-2: CQDs-COOH

To introduce carboxyl groups at the surface of CQDs-1, a simple method was used similar to the one reported to Zu *et al.* [4]. Briefly, 100 mg of CQDs-1 were dispersed in 50 mL of Milli-Q water containing 2.5 g NaOH and 2.5 g  $ClCH_2COONa$ . The mixture was sonicated for several hours, left shaking overnight and neutralised with 1 N HCl to obtain CQDs-COOH. The suspension was dialysed against Milli-Q water using a cellulose ester dialysis membrane (Biotech CE N°131093, pore size 500-1000 Da) for 2 days to remove all ions.

##### 6.2.3.1.3. CQDs-3: CQDs- $N_3$

Azide-terminated carbon dots were prepared from CQDs-1 using carbodiimide chemistry. To a solution of 2-azidoacetic acid (1 mg in 1 mL, 0.1 X PBS) were added equimolar amounts of EDC•HCl and NHS. The solution was stirred for 20 min in order to activate the carboxyl groups. To this solution, CQDs-1 (1 mg in mL, 0.1X PBS) were added in a 1:2 ratio (v/v). The reaction was carried out for 5 h at room temperature, and the resulting suspension was then dialysed against Milli-Q water using a cellulose ester dialysis membrane for 24 h (Biotech CE N°131093, pore size 500-1000 Da) to remove all unreacted material.

##### 6.2.3.1.4. CQDs-4: CQDs-BA

A dispersion of CQDs-3 (1 mg  $mL^{-1}$ , 5 mL) was mixed with previously prepared 4-[(1-oxo-4-pentyn-1-yl)amino]phenylboronic acid (2 mM), copper sulphate pentahydrate (200  $\mu$ M) and ascorbic acid (300  $\mu$ M). The reaction mixture was stirred for 24 h at room temperature.

EDTA was added to the mixture prior to dialysis (SpectraPor 1, pore size: 1000 Da) against Milli-Q water for 48 h.

#### 6.2.3.1.5. CQDs-5

A suspension of CQDs-3 (1 mg mL<sup>-1</sup>, 5 mL) was mixed with propargyl alcohol (2 mM), copper sulphate pentahydrate (200 µM) and ascorbic acid (300 µM). The reaction mixture was stirred for 24 h at room temperature. EDTA was added to the mixture prior to dialysis (SpectraPor 1, pore size: 1000 Da) against Milli-Q water for 48 h.

#### 6.2.3.1.6. CQDs-6

CQDs-6 particles were prepared according to the protocol described recently by our group [5]. Phenylboronic acid (200 mg) was dissolved in water (20 mL), and the pH was adjusted to 9.0 with NaOH (1 M). The solution was degassed with nitrogen gas for 1 h in order to remove dissolved oxygen and heated in a Teflon-lined autoclave chamber (125 mL – acid digestion vessel n°4748, Parr, France) for 8 h at 160 °C. After cooling to room temperature, the suspension was dialysed against Milli-Q water for 24 h, water being changed every 6 h (SpectraPor 1, pore size: 1000 Da). The formed functional CQDs-2 (200 µL) were dried and then weighed with a Sartorius microbalance (TG 209 F3 Tarsus®, Netzsch) to estimate the exact mass concentration. Particles were lyophilised and stored at 4 °C until use.

#### 6.2.3.1.7. CQDs-7

CQDs-7 were prepared in a similar way to CQDs-6. In short, 4-aminophenylboronic acid (200 mg) was dissolved in Milli-Q water (20 mL), and the pH of the solution was adjusted to 9.0 with NaOH (1 M). The solution was degassed with nitrogen gas for 1 h in order to remove dissolved oxygen and heated in a Teflon-lined autoclave chamber (125 mL – acid digestion vessel n°4748, Parr, France) for 8 h at 160 °C. After cooling to room temperature, the solution was centrifuged at 10,000 rpm for 30 min to remove large precipitates and dialysed against water for 24 h with Milli-Q water, water being changed every 6 h (SpectraPor 1, pore size: 1000 Da). The formed functional CQDs-7 (200 µL) were dried and then weighed with a Sartorius microbalance (TG 209 F3 Tarsus®, Netzsch) to estimate the exact mass concentration. The suspension was further lyophilised and stored at 4 °C.

#### 6.2.3.1.8. CQDs-8

Particles were prepared in a similar manner to CQDs-6 and CQDs-7 by dissolving PEG600 (200 mg) in water (20 mL) and adjusting the pH to 9.0 by using NaOH (0.5 M). The solution was degassed with nitrogen gas for 1 h to remove dissolved oxygen and heated in a Teflon-lined autoclave chamber (125 mL – acid digestion vessel n°4748, Parr, France) for 72 h at 120 °C. After cooling to room temperature, the solution was dialysed against Milli-Q water for 24 h, water being changed every 6 h (SpectraPor 1, pore size: 3500 Da).

#### 6.2.3.1.9. Fluorescently labelled CQDs-7

CQDs-7 were dispersed in PBS buffer (pH 7.4) at the concentration of 2 mg mL<sup>-1</sup>. Fluorescein-NHS was dissolved in DMF (10 mg mL<sup>-1</sup>). The CQDs-7 dispersion was cooled down to 0 °C, and 10 µL of freshly prepared fluorescein was added. The reaction was stirred on ice for another 3 h. After that, a Sephadex G-25 PD-10 desalting column was used to remove the dye in excess. The formed fluorescent CQDs-7 were dried (200 µL) and then weighed with a Sartorius microbalance (TG 209 F3 Tarsus®, Netzsch) to estimate the exact mass concentration. Particles were stored as a dispersion.

#### 6.2.3.1.10. CQDs-peptide conjugates: CQDs-2.1a; -2.1b; -2.2a; -2.2b; -2.3a; -2.3b

A suspension of CQDs-COOH was prepared in PBS buffer (pH 7.4) at the concentration of 2 mg in 1 mL (10 mg). To this suspension, a two-fold excess of EDC and a 2.5-fold excess of NHS (dissolved in the minimum amount of PBS) were added, and the mixture was stirred for 20 min in order to activate the carboxyl groups. The peptide (1a-3b) (5 mg, 1 eq), dissolved in the minimum amount of Milli-Q water or DMSO, was added and the reaction was stirred overnight. 1 mL of the mixture was lyophilised to obtain powder and indirectly quantify the free peptide by quantifying the unbounded one. The rest of the mixture was dialysed against Milli-Q water for 24 h using a cellulose membrane (Spectra/Por 6 Standard RC Pre-wetted Dialysis Tubing, MWCO 3.5 kDa). The sample collected before dialysis was weighed on a microbalance (Mettler Toledo, XPR6UD5), dispersed in 1 mL Milli-Q water and dropped off on a size exclusion PD10 disposable column (GE Healthcare) in order to separate the free peptide from the particles. Some of the particles stayed at the top of the column, indicating the formation of aggregates. Therefore, this method was not used for purification purposes. The

separated peptide was lyophilised and quantified by HPLC using the corresponding calibration curve.

*6.2.3.1.11. CQDs-peptide conjugates: CQDs-3.4a; -3.4b; -3.5a; -3.6b; -3.7a; -3.7b*

CQDs-N<sub>3</sub> were dispersed in water at the concentration of 3 mg in 1 mL (9 mg). 5 eq of copper sulphate pentahydrate, 10 eq of ascorbic acid and *ca.* 3 mg (1 eq) of the peptide (4a-7b) were added. The reaction mixture was stirred for 24 h. 1 mL of the reaction mixture was collected in order to quantify the free peptide. To the rest of the solution, 1 mM solution of EDTA was added, and the mixture was dialysed against Milli-Q water for 24 h using a cellulose membrane (Spectra/Por 6 Standard RC Pre-wetted Dialysis Tubing, MWCO 3.5 kDa). The sample collected before dialysis was weighed on a microbalance (Mettler Toledo, XPR6UD5), dispersed in 1 mL of Milli-Q water and dropped off on a size exclusion column (GE Healthcare, disposable PD10 columns) in order to separate the free peptide from the particles. Some of the particles stayed at the top of the column, indicating the formation of aggregates. Therefore, this method was not used for purification purposes. The separated peptide was lyophilised and quantified by HPLC using the adequate calibration curve.

**6.2.3.2. Nanodiamonds: ND**

*6.2.3.2.1. ND-3: ND-N3*

ND-NH<sub>2</sub> were suspended in dry ACN at a concentration of 5 mg in 1 mL (10 mL). Particles were sonicated for 30 min before the addition of 4-azidobenzoic acid (0.2 mmol), DCC (0.22 mmol) and DMAP (0.066 mmol). The reaction mixture was stirred for 24 h under a nitrogen atmosphere. The particles were purified via several washing/centrifugation cycles at 12,500 rpm with ACN (3 times), ethanol (3 times), dried under vacuum and finally stored until further use.

*6.2.3.2.2. Nanodiamonds-peptide conjugates: ND-1.1a; -1.1b; -1.2a; -1.2b; -1.3a; -1.3b*

ND-COOH (ND-1) were dispersed in acetonitrile at the concentration of 1 mg in 1 mL (5 mg). The particles were sonicated for 30 min before addition of DIC (4 eq), HOBt (4 eq) and the peptide (1a-3b, approx. 3 mg, 1 eq) dispersed in the minimum amount of water. The reaction was carried out for 12 h at room temperature. The particles were purified by repeated washing/centrifugation cycles at 12,500 rpm with ACN (2 times) and water (until the

absorbance at 214 nm = 0). The supernatants collected from the washing steps were lyophilised, and the amount of the free peptide was quantified by HPLC (calibration curve).

6.2.3.2.3. *Nanodiamonds- peptide conjugates: ND-3.4a; -3.4b; -3.5a; -3.5b; -3.6a; -3.6b; -3.7a; -3.7b*

ND-N<sub>3</sub> (ND-3) were dispersed in Milli-Q water at the concentration of 2.5 mg in 1 mL (5 mg). The particles were sonicated for 1 h before the addition of 5 eq of copper sulphate pentahydrate, 10 eq of ascorbic acid and 3 mg (1 eq) of a peptide. The reaction mixture was stirred for 24 h at room temperature, and the particles were purified by several washing/centrifugation cycles at 12,500 rpm with water (until the absorbance at 214 nm = 0) and EDTA (3 times). Supernatants collected from the washing steps in water were lyophilised, and the amount of the free peptide was quantified by HPLC using a calibration curve.

#### 6.2.3.3. **Reduced graphene oxide: rGO**

A GO aqueous suspension (150 mg, 3 mg mL<sup>-1</sup>) was prepared by sonication and hydrazine hydrate (50  $\mu$ L, 1.03 mmol) was added to this suspension. The mixture was heated in an oil bath at 100 °C for 24 h over which reduced GO gradually precipitated out the suspension. The product was isolated by filtration over a PVDF membrane with a 0.45  $\mu$ m pore size, washed copiously with water (5  $\times$  20 mL) and methanol (5  $\times$  20 mL), and dried in an oven.

#### 6.2.4. **Preparation of flexible patch photothermal heaters**

Kapton foils (10  $\times$  10 mm<sup>2</sup>) were cleaned with acetone in an ultrasonic water bath for 30 min, followed by isopropanol for 10 min and then dried under a nitrogen flow. The cleaned Kapton foils were modified with rGO using a drop-casting procedure (100  $\mu$ L) repeated three times and dried at room temperature for several hours.

#### 6.2.5. **Fabrication of furfuryl-containing cryogels**

A mixture of all monomers and crosslinkers (FuMA, PEGMEMA, PEGDMA, DMPA) at the appropriate ratios were prepared in 1,4-dioxane. Gelation was undertaken at -13 °C under UV irradiation exposure (365 nm). After 1 h, cryogels were thawed at room temperature, washed with 1,4-dioxane and rinsed with water to remove unreacted monomers. The cryogels were dried under vacuum to yield spongy materials.

### **6.2.6. Synthesis of rGO embedded furfuryl containing cryogels**

rGO was introduced into the reaction mixture, and the synthesis remains the same. Resulting in a black crosslinked material after drying in vacuo

## **6.3. Swelling of cryogels**

Swelling studies were conducted by sampling a circular piece of a dried hydrogel in a vial containing distilled/deionised water at room temperature. After removing the hydrogel from water and absorbing excess surface adhered water with a tissue paper, the mass increase of the cryogel sample was recorded at periodic time points. The water uptake percentage was obtained using the following equation:

$$\text{Percentage of swelling (\%)} = (W_{\text{wet}} - W_{\text{dry}}) / W_{\text{dry}} \times 100$$

where  $W_{\text{wet}}$  and  $W_{\text{dry}}$  are the weights of the hydrogels in their swollen and dried states, respectively.

## **6.4. Drug loading**

### **6.4.1. Non-covalent interaction with ampicillin**

The cryogels (30 mg) were loaded with ampicillin (ampicillin, 1 mL, 800  $\mu\text{g mL}^{-1}$ ) under shaking for 12 h at 4 °C. The concentration of ampicillin loaded onto the gel was determined using HPLC analysis.

### **6.4.2. Diels-Alder reaction**

#### **6.4.2.1. Conjugation of N-(5-fluoresceinyl)maleimide**

A solution of *N*-(5-fluoresceinyl)maleimide in PBS (30  $\mu\text{g mL}^{-1}$ ) was loaded into the cryogels CG-40 (30 mg) and left to react for 24 h at room temperature. Any unbound dye was washed with PBS. A solution of PBS was analysed by fluorescence to ensure total removal of the dye.



#### **6.4.2.2. Conjugation of maleimide-functionalized antibacterial peptides**

Maleimide-modified peptides ( $1\ \mu\text{L}$ ,  $600\ \mu\text{g mL}^{-1}$ ) were loaded into CG-40 (30 mg) for 24 h at room temperature. Any unbound peptide was washed with water. Washing solution was analysed by UV-Vis to ensure the total removal of the free peptide.

### **6.5. High-Performance Liquid Chromatography for quantification**

#### **6.5.1. AMP loading and release**

The concentration of AMP loaded onto CG-GrGO-40 was determined by an HPLC system (Shimadzu, Tokyo, Japan) equipped with a  $5\ \mu\text{m}$  C<sub>4</sub> QS Uptisphere<sup>®</sup> 300 Å,  $250\ \text{mm} \times 4.6\ \text{mm}$  column (Interchim, Montluçon, France) heated to  $40\ ^\circ\text{C}$ . Mobile phase: A (water:0.1% TFA); B (MeCN:0.1% TFA); flow rate of  $1\ \text{mL min}^{-1}$ . The samples were injected at a volume of  $40\ \mu\text{L}$ , and the detection wavelength was 214 nm. First, a calibration curve of a series of AMP solutions of different concentrations was generated. The concentration of AMP remaining in the supernatant solution used for loading was measured, allowing the determination of the AMP concentration in CG-rGO. The concentration of an aliquot removed at a different time interval during the photothermal and passive release was measured using the same parameters as above to determine the amount and % of released AMP.

#### **6.5.2. Quantification of peptides incorporated into the nanostructures of carbon nanoparticles**

The concentration of AMP loaded onto CQDs and NDs was determined by HPLC. Calibration curves were recorded on HPLC system (Shimadzu, Tokyo, Japan) equipped with a  $5\ \mu\text{m}$  C18AQ Uptisphere<sup>®</sup> column (Interchim, Montluçon, France) heated to  $40\ ^\circ\text{C}$  at a flow rate  $1\ \text{mL min}^{-1}$ . As a mobile phase: 100% A (water: 0.1% FA); 100% B (MeCN: 0.1% FA) was used.

### **6.6. Fluorescent plate reader for quantification of dye loading and release**

The concentration of *N*-(5-fluoresceinyl)maleimide loaded onto CG-rGO-40 was determined using a plate reader (BioTek Instruments SAS, France). First, a calibration curve of a series of dye solutions of different concentrations was generated. The concentrations of dye

remaining in the supernatant used for loading and washing solutions were measured, allowing the determination of the dye concentration in CG-GrGO. The concentration of an aliquot removed at different time intervals during the photothermal treatment and passive release was measured using the same parameters as above to determine the amount and % of released dye.

### 6.7. Purification and purity assessment of peptides: 1a-8

For purification purposes, semi-preparative HPLC was performed on a Knauer instrument. A Macherey Nagel Nucleodur 100-5 C18 reverse phase column was used at a flow rate of 5 mL min<sup>-1</sup>. The gradient used was changed as a function of the impurities of the crude product. Chromatograms were recorded at  $\lambda = 214$  nm and  $\lambda = 254$  nm.

Purity was assessed by analytical HPLC, performed on Knauer instrument. Macherey Nagel Nucleodur 100-5 Pyramid C18 reverse phase column was used at a flow rate of 1 mL min<sup>-1</sup>. With the linear gradient of buffer B (95% in 7min) from 95% buffer A with a total run time of 15min (**Table 6.1**). Chromatograms were recorded at  $\lambda = 214$  nm and  $\lambda = 254$  nm.

**Table 6.1:** Gradient for analytical HPLC (A = 100% Millipore-Q water, 0.1% TFA; B=100% acetonitrile, 0.1% TFA).

T [min]	15 min gradient	
	% A	% B
0	95	5
2	95	5
9	5	95
11	5	95
13	95	5
15	95	5

### 6.8. Quantification of the amino groups by a modified Keiser test

The primary amino groups onto the surface of CQDs were quantified using a modified photometric assay based on the Kaiser test reported by [65]. CQDs carrying amino groups (0.1-0.5 mg of powder) were dispersed in 1 mL Milli-Q water. To this suspension, 1 mL of the buffer solution (A) was added, followed by 15 min sonication. 1 mL of solution (C) and 1 mL of solution (D) were added, and the dispersion was heated at 120 °C for 10 min; 1 mL of solution (B) was added, and the mixture was heated for another 10 min. After cooling to room temperature, 5 mL of the ethanol solution (E) were added. As a reference sample, benzylamine was used at different concentrations in aqueous solution. The calibration curve is shown in (**Figure 6.1**).

A) Buffer pH 5.5: 36 g of sodium acetate were dissolved in 6.9 mL of acetic acid and completed with Milli-Q water to a volume of 100 mL.

B) 5 % ninhydrin solution: 5 g of ninhydrin was dissolved in 100 mL of ethanol.

C) KCN solution: 2 mL of 0.03 M KCN solution was diluted to a final of the volume of 100 mL with pyridine.

D) Phenol solution: 80 g phenol were dissolved in 20 mL of ethanol.

E) 60 % ethanol solution.

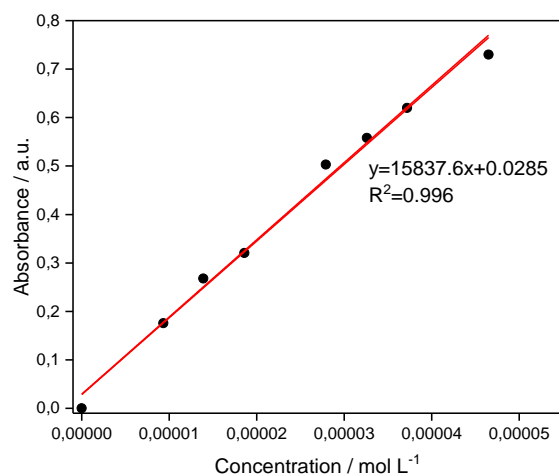


**Figure 6.1:** UV-Vis calibration curve of benzylamine.

**Table 6.2:** Surface loading of different CQDs (mmol/g) obtain by modified Keiser method

Sample	Sample mass (mg)	Absorbance at 570nm	Surface loading (mmol/g)
CQDs-1	0.1375	0.343	0.144
CQDs-3	0.056	0.068	0.0445
CQDs-2	0.099	0.116	0.055

## 6.9. Quantum yield measurements

The quantum yields ( $\Phi$ ) of the CQDs were calculated by comparing their fluorescence intensities (excitation at 350 nm) and absorbance values at 350 nm with those of quinine sulphate using the following equation:

$$\Phi = \Phi_{\text{REF}} \times (I/I_{\text{REF}}) \times (A_{\text{REF}}/A) \times (\eta^2/\eta_{\text{REF}}^2)$$

Where  $\Phi$  is the quantum yield,  $A$  is the optical density,  $I$  is the measured integrated emission fluorescence intensity, and  $\eta$  is the refractive index. Quinine sulfate (quantum yield of 0.54 at 350 nm) was chosen as standard and dissolved in 0.1 M  $\text{H}_2\text{SO}_4$  (refractive index: 1.33), and the CQDs were dissolved in water (refractive index: 1.33). Absorbance values of the CQDs suspensions were kept under 0.05 at the excitation wavelength in order to minimise re-absorption effects.

## 6.10. Photothermal release studies

Release experiments were performed into 1 mL PBS buffer. The cryogels were irradiated with laser in a continuous mode (Gbox model, Fournier Medical Solution) with an output light at 980 nm ( $1\text{ W cm}^{-2}$ ) for various time intervals (1-60 min). Thermal images were captured by an Infrared Camera (Thermovision A40) and treated using ThermoCam Researcher Pro 2.9 software. The amount of released antibiotic was evaluated by HPLC. The quantity of *N*-(5-fluoresceinyl)maleimide released was evaluated by fluorescence spectroscopy (BioTek Instruments SAS, France).

## 6.11. Biological assays

### 6.11.1. Cytotoxicity assay – Huh-7 cells

The Huh-7 hepatocarcinoma cell line was cultured and maintained in Dulbecco's Modified Eagle's medium (DMEM, Gibco®) supplemented with 10% fetal bovine serum (FBS, Gibco®) and 1% penicillin-streptomycin (Gibco®) in a humidified incubator at 37 °C and 5% CO<sub>2</sub>. Cells were seeded at a density of  $15 \times 10^3$  cells/well in a 96-well plate and grown for 24 h before assay. The culture medium was replaced with a fresh medium that contains increasing concentrations of CQDs for 2 h and 8 h from 1 to 100  $\mu\text{g mL}^{-1}$ . Then, the old medium was aspirated, and the cells were washed with PBS. The cell viability was evaluated using resazurin cell viability assay. Briefly, 100  $\mu\text{L}$  of the resazurin solution ( $11 \mu\text{g mL}^{-1}$ ) in DMEM/10% FBS were added to each well, and the plate was incubated for 4 h in the humidified incubator. The fluorescence emission of each well was measured at 593 nm (20-nm bandwidth) with an excitation at 554 nm (18-nm bandwidth) using a Cytation™ 5 Cell Imaging Multi-Mode Reader (BioTek Instruments SAS, France). Each condition was replicated three times, and the mean fluorescence value of non-exposed cells was taken as 100% cellular viability.

### 6.11.2. Cytotoxicity assay – HeLa cells

The HeLa cell line derived from the cervical carcinoma of a 31-year-old female [ATCC® CCL-2™, ECACC, Sigma Aldrich, Saint-Quentin Fallavier, France] were cultured and maintained in Dulbecco's Modified Eagle's medium (DMEM, Gibco®) supplemented with 10% fetal bovine serum (FBS, Gibco®) and 1% penicillin-streptomycin (Gibco®) in a humidified incubator at 37 °C and 5% CO<sub>2</sub>. Cells were grown for 24 h before the assay to be treated with the cryogel for another 24 h. The cell viability was assessed by using CCK-8

viability assay. Briefly, the cells were washed, CCK-8 was added, and cells were incubated for an additional 2 h at 37°C. The absorbance values were then measured at 450 nm. The results were expressed as a percentage compared to controls.

#### **6.11.3. Uptake mechanism: fluorescently labelled CQDs-7**

Cells were seeded at a density of  $15 \times 10^4$  cells/well in a 24-well plate with sterile coverslips at the bottom and grown for 24 h before assay. The culture medium was replaced with a fresh medium that contained  $100 \mu\text{g mL}^{-1}$  of CQDs. After 1 h incubation at 4 °C and 37 °C, the Huh-7 cells were washed with PBS (three times), fixed with 4% *para*-formaldehyde for 10 min at room temperature and then stained with  $10 \mu\text{g mL}^{-1}$  Hoechst 33342 in PBS for 10 min at room temperature in the dark. After washing with PBS, the coverslips were mounted on glass slides and recorded using a Cytation™ 5 Cell Imaging Multi-Mode Reader (BioTek Instruments SAS, France) equipped with a 40× objective (Plan Fluorite WD 2.7 NA 0.6). The fluorescence images were acquired with the same exposure using DAPI (377/447 nm) and GFP (469/525 nm) excitation/emission filter sets. All the images were processed using Gen5 Image+ software.

For cellular uptake, cells were seeded at a density of  $15 \times 10^4$  cells/well in a 6-well plate and grown for 48 h before assay. The culture medium was replaced with a fresh medium that contained  $100 \mu\text{g mL}^{-1}$  of CQDs. After 1 h incubation at 4 °C and 1, 3, and 6 h incubation at 37 °C, the Huh-7 cells were washed with PBS (three times) and collected by trypsinisation. The cells suspensions were resuspended in PBS/PFA 0.5% and analysed through a flow cytometer (BD LSR Fortessa) with FITC channel. The data were collected ( $10^4$  cells per sample) and analysed using BD FACSDiva 8.0.1 software.

#### **6.11.4. Antiviral assay: HCoV-229E-Luc**

We used a modified HCoV-229E containing a renilla luciferase reporter gene HCoV-229E-Luc. The viral stocks were produced in Huh-7 cells. Huh-7 cells were infected with a pre-stock of HCoV-229E-Luc in flasks. After 5 days, the supernatants of flasks were collected. For the infection assay, Huh-7 cells,  $15,000/\text{well}$  seeded in 96-well plate, were inoculated with HCoV-229E-Luc at a multiplicity of infection (MOI) of 1 for 1 h at 37 °C in DMEM without serum, then the inoculum was removed and cells were incubated in complete culture medium for 6 h at 37 °C. CQDs were added to cells during the 1-h infection. Cells were lysed in  $20 \mu\text{L}$

of renilla lysis buffer (Promega, Madison, USA) and luciferase activity quantified using a renilla luciferase assay system kit (Promega, Madison, USA) as recommended by the manufacturer and a Tristar LB 941 luminometer (Berthold Technologies, Bad Wildbad, Germany). To measure  $EC_{50}$ , the dose-response experiment was performed with CQDs added at different concentrations during the inoculation step and post-inoculation step. For time-of-addition assays, CQDs were added at different time points at  $10 \mu\text{g mL}^{-1}$ . For all experiments, water was used as a control because CQDs are suspended in water.

#### **6.11.5. Time-of-addition assay**

Huh-7 cells were infected with a pre-stock of HCoV-229E-Luc in flasks. After 5 days, the supernatants of flasks were collected. For the infection assay, Huh-7 cells, 15,000/well seeded in 96-well plate, were inoculated with HCoV-229E-Luc at a multiplicity of infection (MOI) of 1 for 1 h at  $37^\circ\text{C}$  in DMEM without serum, then the inoculum was removed and cells were incubated in complete culture medium for 6 h at  $37^\circ\text{C}$ . CQDs were added to cells at a different time during the infection of Huh-7 with HCoV-229E-Luc. Cells were lysed in  $20 \mu\text{L}$  of renilla lysis buffer (Promega, Madison, USA) and luciferase activity quantified using a renilla luciferase assay System kit (Promega, Madison, USA) as recommended by the manufacturer and a Tristar LB 941 luminometer (Berthold Technologies, Bad Wildbad, Germany). All the conditions were performed in triplicates.

#### **6.11.6. Virus-nanoparticles interaction assay**

Virus HCoV-229E-Luc was pre-incubated with CQDs at  $10 \mu\text{g mL}^{-1}$  for 30 min at  $37^\circ\text{C}$ . The mixture was diluted 10 times in culture medium leading to a final concentration of CQDs of  $1 \mu\text{g mL}^{-1}$  and inoculated on Huh-7 cells for 1 h. In parallel, Huh-7 cells were inoculated with HCoV-229E-Luc in the presence of CQDs at 1 and  $10 \mu\text{g mL}^{-1}$  for 1 h. Cells were lysed 7 h post-infection, and luciferase activity quantified. All the experiments were performed in triplicates.

#### **6.11.7. Competitive assay with mannose**

The suspensions of **CQDs-4** and **CQDs-7** were prepared at the concentration of  $1 \text{mg mL}^{-1}$ . pH was adjusted to 9 with 1N NaOH and excess of mannose (2:1) was added. The mixture was incubated overnight at  $4^\circ\text{C}$  to be further dialysed against water for 24 h (SpectraPor 1, pore size: 1000 Da). As prepared CQDs were added to cells during the 1-h

infection. Cells were lysed in 20  $\mu\text{L}$  of renilla lysis buffer (Promega, Madison, USA) and luciferase activity quantified using a renilla luciferase assay System kit (Promega, Madison, USA) as recommended by the manufacturer and a Tristar LB 941 luminometer (Berthold Technologies, Bad Wildbad, Germany). All the experiments were performed in triplicates.

#### **6.11.8. Susceptibility testing – MIC values determination**

*E. coli* DSM 30083 and *S. aureus* ATCC 43300 (MRSA) were used. 3-5 morphologically similar colonies from a fresh agar plate were transferred into a sterile tube containing sterile broth. The bacteria were incubated overnight at 37 °C. The next day OD<sub>600</sub> of the overnight culture was adjusted to reach OD<sub>600</sub> 0.1 and was left to continue growing until reaching the mid-log phase. After preparing the inoculum at the concentration of  $5 \times 10^5$  CFU mL<sup>-1</sup>, the bacterial suspension was used within 30 min to prevent changes in the cell number. Peptides and peptide-carbon conjugates were tested. MIC values were established in a microtiter plate assay according to CSLI guidelines [66]. Briefly, the peptide and the peptide conjugate were dissolved in DMSO at the concentration of 10 mg mL<sup>-1</sup>. Serial dilution was prepared in MH (Muller-Hinton) medium, inoculated with  $5 \times 10^5$  CFU mL<sup>-1</sup> and incubated for 16 h at 37 °C. Inoculated medium without the sample served as a growth control and uninoculated medium as a sterility control. The lowest visible growth was reported as a MIC value. Visual counting of the number of colonies upon overnight incubation at 37 °C allowed reading out the initial and final concentrations of the bacteria strain in CFU mL<sup>-1</sup>. All the experiments were performed in triplicates.



## 6.12. Instrumentation

### 6.12.1. NMR Spectroscopy

$^1\text{H}$  NMR and  $^{13}\text{C}$  NMR spectra were recorded at room temperature on a Bruker DPX 200 ( $^1\text{H}$ : 200 MHz,  $^{13}\text{C}$ : 50 MHz) spectrometer. Chemical shifts are given in ppm relative to tetramethylsilane (TMS). Coupling constant  $J$  are reported in Hz. Multiplicities are noted as singlet (s), doublet (d), triplet (t), multiplet (m).

$^{11}\text{B}$  NMR spectra were recorded on a Bruker Avance II 400MHz. All the spectra were recorded in deuterated solvents.

### 6.12.2. Mass Spectrometry

ESI-MS spectra were measured on a Bruker Esquire 6000.

### 6.12.3. High-Performance Liquid Chromatography (HPLC)

**Semi-preparative** HPLC was performed on a Knauer instrument. A Macherey Nagel VP Nucleodur 125/10 100-5 C18ec reverse phase column was used at a flow rate of  $5\text{ mL min}^{-1}$ . As a mobile phase A (water:0.1% TFA); B (MeCN:0.1% TFA) was used.

**Analytical** HPLC was performed on a Knauer instrument. A Nagel EC 125/4 Nucleodur C18 pyramid,  $5\mu\text{m}$  reverse phase column was used at a flow rate of  $1\text{ mL min}^{-1}$ . As a mobile phase A (water:0.1% TFA); (MeCN:0.1% TFA) was used. With the linear gradient of buffer B (95% in 7min) from 95% buffer A with a total run time of 15min.

Calibration curves obtained for the loading and release studies were recorded on an **HPLC system (Shimadzu, Tokyo, Japan)** equipped with a  $5\mu\text{m}$  C<sub>4</sub> QS Uptisphere<sup>®</sup> 300 Å,  $250\text{ mm} \times 4.6\text{ mm}$  column (Interchim, Montluçon, France) heated to  $40\text{ }^\circ\text{C}$  at a flow rate  $1\text{ mL min}^{-1}$ . As a mobile phase: A (water:0.1% TFA); B (MeCN:0.1% TFA) was used. With the linear gradient of buffer B (80% in 15min) from 100% buffer A with a total run time of 23min.

Calibration curves obtained for peptide quantification on the surface of nanoparticles were recorded on **HPLC system (Shimadzu, Tokyo, Japan)** equipped with a  $5\mu\text{m}$  C18AQ Uptisphere<sup>®</sup> column (Interchim, Montluçon, France) heated to  $40\text{ }^\circ\text{C}$  at a flow rate  $1\text{ mL min}^{-1}$ . As a mobile phase 100%A (water: 0.1%FA); 100B (MeCN: 0.1%FA) was used. With the linear gradient of buffer B (80% in 15min) from 100% buffer A with a total run time of 23min.

#### **6.12.4. Fourier Transform Infrared (FTIR) Spectroscopy**

FTIR spectra were recorded using a ThermoScientific FTIR instrument (Nicolet 8700) in the 550 - 4000  $\text{cm}^{-1}$  range at a spectral resolution of 6  $\text{cm}^{-1}$ . 1 mg of dried sample was mixed with 200 mg of KBr powder in an agate mortar. The mixture was pressed into a pellet under 7 tons of load for 2-4 min, and the spectrum was recorded immediately. A total of 64 accumulative scans were collected. The signal from a pure KBr pellet was subtracted as the background.

#### **6.12.5. X-ray Photoelectron Spectroscopy (XPS)**

XPS measurements were carried out using a ESCALAB 220 XL spectrometer from Vacuum Generators featuring a monochromatic Al  $K\alpha$  X-ray source (1486.6 eV) and a spherical energy analyser operated in the CAE (constant analyser energy) mode (CAE = 100 eV for survey spectra and CAE = 40 eV for high-resolution spectra), using the electromagnetic lens mode. The angle between the incident X-rays and the analyser was  $58^\circ$ , and the detection angle of the photoelectrons was  $30^\circ$ .

#### **6.12.6. Raman Spectroscopy**

Raman spectroscopy measurements were performed on a LabRam HR Micro-Raman system (Horiba Jobin Yvon) using a 473-nm laser diode as an excitation source. Visible light is focused by a 100 $\times$  objective. The scattered light is collected by the same objective in backscattering configuration, dispersed by an 1800 mm focal length monochromator and detected by a CCD camera.

#### **6.12.7. UV-Vis Spectroscopy**

UV-Vis measurements were performed with a Perkin-Elmer Lambda 950 dual-beam spectrophotometer (resolution of 1 nm) in a 1-cm quartz cuvette.

#### **6.12.8. X-Ray Diffraction (XRD)**

XRD patterns of the CQDs powders were recorded in the range of  $10^\circ$ - $90^\circ$  on a Bruker AXS D8-advance X-ray diffractometer using the Cu  $K\alpha$  radiation ( $\lambda = 1.54 \text{ \AA}$ ) at 40 kV and 40 mA.

#### **6.12.9. Transmission Electron Microscopy (TEM)**

TEM images were recorded on a JEOL JEM-2800 electron microscope operated at an accelerating voltage of 200 kV.

#### **6.12.10. Scanning Electron Microscopy (SEM)**

Scanning electron microscope (SEM) images were obtained using an ESEM-FEG/EDAX Philips XL-30 (Philips, Eindhoven, The Netherlands) instrument operated at an accelerating voltage of 10 kV.

#### **6.12.11. Emission fluorescence Spectroscopy**

Emission fluorescence spectra were recorded between 340 and 800 nm using a Cary Eclipse spectrometer (Agilent, France). Samples were excited at 350 nm, and different wavelengths (excitation and emission slit: 10 nm, scan rate: 600 nm min<sup>-1</sup>).

#### **6.12.12. Particle Size and Zeta Potential Measurements**

The average **hydrodynamic diameter**, the polydispersity index (PDI), and the **zeta-potential** were recorded on a Zetasizer® Nano ZS (Malvern Instruments S.A., Worcestershire, UK). All the batches were diluted to 100 µg mL<sup>-1</sup> in water and analysed in triplicate. The size of suspended nanoparticles was measured at 25 °C or 37 °C in the 173° scattering geometry, and zeta potentials were measured using the electrophoretic mode.

#### **6.12.13. Photothermal Effect Measurements**

All irradiations were performed in 12 or 6 well plates. The temperature changes were captured by an infrared camera (ThermoVision A40) and treated using ThermoCam Researcher Pro 2.9 software.

### 6.13. References

1. Slootweg, J.C., et al., *Efficient Reagent-Saving Method for the N-Terminal Labeling of Bioactive Peptides with Organometallic Carboxylic Acids by Solid-Phase Synthesis*. *Organometallics*, 2016. **35**(18): p. 3192-3196.
2. Kanayama, N. and H. Kitano, *Interfacial Recognition of Sugars by Boronic Acid-Carrying Self-Assembled Monolayer*. *Langmuir*, 2000. **16**(2): p. 577-583.
3. Zhu, S., et al., *Highly Photoluminescent Carbon Dots for Multicolor Patterning, Sensors, and Bioimaging*. *Angewandte Chemie International Edition*, 2013. **52**(14): p. 3953-3957.
4. Zhu, L., et al., *Fluorescence immunoassay based on carbon dots as labels for the detection of human immunoglobulin G*. *Analytical Methods*, 2014. **6**(12): p. 4430-4436.
5. Barras, A., et al., *High Efficiency of Functional Carbon Nanodots as Entry Inhibitors of Herpes Simplex Virus Type 1*. *ACS Appl. Mater. Interfaces* 2016. **8**: p. 9004.
6. Approved Standard, M.A., *Methods for Dilution Antimicrobial Susceptibility Tests for Bacteria That Grow Aerobically*; vol 29, no. 2, 2009, 8th edition., 2009.

## SCIENTIFIC ACTIVITY

### LIST OF PUBLICATIONS

- Loczechin A, Seron K, Barras A, Giovanelli E, Belouzard S, Chen YT, Metzler-Nolte N, Boukherroub R, Debuissou J, Szunerits S; (2019) Functional Carbon Quantum Dots as medical Countermeasures to Human Coronavirus (HCoV). ACS Applied Materials & Interfaces (accepted)  
DOI: 10.1021/acsami.9b15032

### RESEARCH VISITS

- April 2017- October 2017; May 2018- August 2018; October 2018- April 2019- three PhD mobilities at Ruhr University Bochum, Germany.

### MEMBER GRANTS

- Pathogen and Graphene (September 2016- December 2019); funding from the European Union's Horizon 2020 Research and Innovation Staff Exchange (RISE) Marie Skłodowska-Curie Actions under grant agreement No 69083

## RESUME

La résistance croissante aux antibiotiques et les limitations dans le développement de nouveaux médicaments nécessitent la recherche de stratégies alternatives afin d'éradiquer les infections bactériennes. Des problèmes semblables apparaissent dans le développement de thérapeutiques antivirales, en raison de l'émergence constante de nouveaux virus et leur capacité à contourner les thérapies par des mutations génétiques.

Ce travail de recherche examine la potentielle activité antibactérienne et/ou antivirale de nanostructures à base de carbone telles que les nanoparticules de diamant et les points quantiques carbonés (*carbon quantum dots*, CQDs), ainsi que l'oxyde de graphène réduit (*reduced graphene oxide*, rGO) combiné à des cryogels. Les CQDs produits par synthèse hydrothermale à partir de l'acide 4-aminophénylboronique comme précurseur carboné se sont montrés efficace en tant qu'inhibiteurs de l'attachement du coronavirus humain HCoV-229E-Luc aux cellules avec une  $EC_{50}$  de  $5,2 \pm 0,7 \mu\text{g mL}^{-1}$ . Les études mécanistiques suggèrent que les CQDs agissent lors des tout premiers stades de l'infection virale ainsi que lors de l'étape de réplication du virus. En parallèle, nous avons tiré parti du caractère multivalent des CQDs et des nanodiamants pour les modifier en y fixant de courts peptides synthétiques antimicrobiens (*antimicrobial peptides*, AMPs). Ces nanostructures ont été testées contre des bactéries pathogènes à Gram positif *Staphylococcus aureus* et à Gram négatif *Escherichia coli* et ont montré une activité antibactérienne plus élevée que celle des AMPs seuls. Dans le cas du rGO combiné à des cryogels chargés en AMPs, l'éradication des bactéries a été réalisée efficacement et à la demande en utilisant une irradiation infrarouge comme activateur externe permettant le relargage des AMPs.

## ABSTRACT

Increasing antibiotic resistance and limited development of new drugs necessitate the search for alternative strategies to eradicate bacterial infections. Similar problems are faced in the development of antiviral therapeutics, due to the constant emergence of new viruses and their ability to escape therapy by genetic mutations.

This work investigates the potential antibacterial and/or antiviral activity of carbon-based nanostructures such as diamond nanoparticles and carbon quantum dots (CQDs) as well as reduced graphene oxide (rGO) in combination with cryogels. CQDs formed by hydrothermal synthesis from 4-aminophenylboronic acid as the carbon precursor showed to be efficient in the inhibition of the viral attachment of human coronavirus HCoV-229E-Luc to cells with an  $EC_{50}$  of  $5.2 \pm 0.7 \mu\text{g mL}^{-1}$ . Mechanistic studies suggest that the CQDs are acting at the early stage of virus infection as well at the viral replication step. In parallel, we took advantage of the multivalent character of CQDs as well as nanodiamonds and modified them with short synthetic antimicrobial peptides (AMPs). Tests of these nanostructures against Gram-positive *Staphylococcus aureus* and Gram-negative *Escherichia coli* pathogens showed increased antibacterial activity when compared to AMPs alone. In the case of rGO combined with cryogels loaded with AMPs, bacterial eradication was achieved efficiently and on-demand using near-infrared light as external trigger to release AMPs.